The Dissertation Committee for Sezgin Kucukcoban
certifies that this is the approved version of the following dissertation:

The inverse medium problem in PML-truncated elastic media

Committee:

Loukas F. Kallivokas, Supervisor

Leszek F. Demkowicz

Omar Ghattas

Spyros A. Kinnas

Gregory J. Rodin

Kenneth H. Stokoe II

Carlos Torres-Verdin

The inverse medium problem in PML-truncated elastic media

by

Sezgin Kucukcoban, B.S., M.S.C.E.

DISSERTATION

Presented to the Faculty of the Graduate School of

The University of Texas at Austin

in Partial Fulfillment

of the Requirements

for the Degree of

DOCTOR OF PHILOSOPHY

THE UNIVERSITY OF TEXAS AT AUSTIN

December 2010

Dedicated to my beloved family.

Acknowledgments

I would like to express my deepest gratitude and appreciation to my advisor Prof. Loukas F. Kallivokas, who has the attitude and the substance of a genius: he continually and convincingly conveyed a spirit of adventure in regard to research and scholarship, and an excitement in regard to teaching. This dissertation would not have been possible without his invaluable help and supervision. I would also like to thank Professors Leszek F. Demkowicz, Omar Ghattas, Spyros A. Kinnas, Gregory J. Rodin, Kenneth H. Stokoe II, and Carlos Torres-Verdin for serving on my dissertation committee and for their helpful suggestions. Partial support provided by the US National Science Foundation under grant awards CMMI-0348484 and CMMI-0619078 is gratefully acknowledged.

I would like to thank my officemates who gave me the joy of working with such a creative and inspiring group. I owe sincere and earnest thankfulness to Ibrahim Erdem, Cengiz Nergiz, Serdar Ozcan, Gokhan Ozdemir, Bayezid Ozden, Basar Ozler, Onur Pekcan, Seval Pinarbasi, and Koray Sigirtmac for their heartfelt encouragement and long-distance friendship. I am truly indebted and wholeheartedly thankful to Merve Celen, Nevin Kahriman, Pinar Yazicioglu, and Duygu & Cengizhan Yenerim, as they give me a warm happiness that blooms the cheek. I cannot find words to express my heartfelt gratitude to my extended family in Austin: Erkin Bahceci, Ipek Nese Sener, and Didem & Umut Unver. During ups and downs of this challenging journey, you have always been there for me with your love, sympathy, patience, and emotionally comforting support. My motivation has always been at its peak thanks to Ipek and Didem since they prepare *out of this world* traditional Turkish cuisine dishes.

Last but not least, heartiest thanks goes to my immediate family, who has been an important and indispensable source of love and spiritual support. This dissertation is dedicated to you, as you have always stood by me and borne all my absence from many family occasions with a smile.

I offer my regards and blessings to all of those who supported me in any respect during the completion of this dissertation.

The inverse medium problem in PML-truncated elastic media

Publication No. ____________________

Sezgin Kucukcoban, Ph.D.
The University of Texas at Austin, 2010

Supervisor: Loukas F. Kallivokas

We introduce a mathematical framework for the inverse medium problem arising commonly in geotechnical site characterization and geophysical probing applications, when stress waves are used to probe the material composition of the interrogated medium. Specifically, we attempt to recover the spatial distribution of Lamé's parameters (λ and μ) of an elastic semi-infinite arbitrarily heterogeneous medium, using surface measurements of the medium's response to prescribed dynamic excitations. The focus is on characterizing near-surface deposits, and to this end, we develop a method that is implemented directly in the time-domain, is driven by the full waveform response collected at receivers on the surface, while the domain of interest is truncated using Perfectly-Matched-Layers (PMLs) to limit the originally semi-infinite extent of the physical domain.

There are two key issues associated with the problem at hand: (a) the forward problem, namely the numerical simulation of the wave motion in the domain of interest; and (b) the framework and strategies for tackling the inverse problem.

To address the forward problem, it is necessary that the domain of interest be truncated, and the resulting finite domain be forced to mimic the physics of the original problem: to this end, we introduce unsplit-field PMLs, and develop and implement two new formulations, one fully-mixed and one hybrid (mixed coupled with a non-mixed approach) that model wave motion within the, now PML-truncated, domain. To address the inverse problem, we adopt a partial-differential-equation-constrained optimization framework that results in the usual triplet of an initial-and-boundary-value forward problem, a final-and-boundary-value adjoint problem, and a time-independent boundary-value control problem. This triplet of boundary-value-problems is used to guide the optimizer to the target profile of the spatially distributed Lamé parameters. Given the multiplicity of solutions, we assist the optimizer, by deploying regularization schemes, continuation schemes (regularization factor and source-frequency content), as well as a physics-driven simple procedure to bias the search directions.

We report numerical examples attesting to the quality, stability, and efficiency of the forward wave modeling. We also report moderate success with numerical experiments targeting inversion of both smooth and sharp profiles in two dimensions.

Table of Contents

List of Tables

List of Figures

List of Algorithms

Chapter 1

Introduction

Recent advances in both algorithms and computer hardware architecture have renewed hope that problems associated with the non-invasive condition assessment of physical and biological systems are becoming more tractable with present means. From a mathematical point of view, at the center of such problems lies, typically, an inverse problem. That is, a problem, for example, where the geometry of the medium, the loads acting on it, and the medium's response may be known, but the medium's material composition is unknown. This, in fact, is the very definition of the *inverse medium problem*, which is treated in this dissertation.

The last thirty years have seen various developments aiming at the solution of such a mathematically, algorithmically, and computationally challenging inverse problem that arises in various application domains ranging from seismic to medical imaging. The primary battleground where such developments have primarily emerged from is the geophysical exploration arena, where, however, despite considerable industrial commitment and academic involvement, the problem remains, by and large, *open*.

This dissertation seeks to address the inverse medium problem in the context of geotechnical site characterization, where we try to reconstruct the soil's material profile, i.e., the spatial distribution of the elastic material properties as the latter are expressed by the Lamé parameters λ and μ (or, to an extent, equivalently, by the P-wave and S-wave velocities, c_p and c_s, respectively). To this end, we discuss a mathematical framework for a full-waveform-based inversion that uses stress waves for interrogation, and is driven by the measurements collected directly in the time-domain at receivers on the soil's surface.

The main issues we tackle in this dissertation are as follows: (a) since geotechnical site characterization is a target application, the interest is in the profile reconstruction of the near-surface deposits for which the truncation of the, otherwise, semi-infinite extent of the physical domain becomes necessary: we, thus, introduce perfectly-matched-layers (PMLs) to convert the semi-infinite physical domain to a finite computational model, and discuss the implications of their introduction to the simulation of the wave motion. Specifically, we address, with two new formulations, the numerical simulation of elastic wave motion in PML-truncated arbitrarily heterogeneous media (*the forward problem*). (b) Armed with an efficient methodology for the forward wave simulation, we address next the reconstruction of the spatially-distributed material properties λ and μ of a heterogeneous medium (*the inverse problem*), using the systematic framework of partial-differential-equation-constrained optimization.

We report on numerical results demonstrating the stability and efficacy of the forward modeling; we also report fairly satisfactory results for the inverse problem. Computationally, the problems are quite challenging: the various algorithms we report here have been implemented on sequential platforms only. Substantial gains can be attained if the implementations were to be extended to parallel architectures. Though the presentation in this dissertation is limited to geotechnical applications, the overall methodology is systematic and quite general, and could be adopted as a solution approach for a broader class of inverse problems.

1.1 Problem definition

We are concerned with a non-destructive exploration/characterization methodology that aims at the reconstruction of the material properties of an arbitrarily heterogeneous semi-infinite medium using surficial measurements of its response to known dynamic excitations applied on the soil's surface, as schematically shown in Figs. 1.1(a) and 1.1(b). The problem is akin to medical imaging, without, however, the benefit of a medical scanning device that typically circumscribes the probed structure with sources and receivers.

1.2 Research objectives

The primary research goal is to arrive at a viable methodology for solving the inverse medium problem in elastic semi-infinite media with an eye towards geotechnical site characterization applications. The primary interest is in the algorithmic robustness of the inverse problem solution approach.

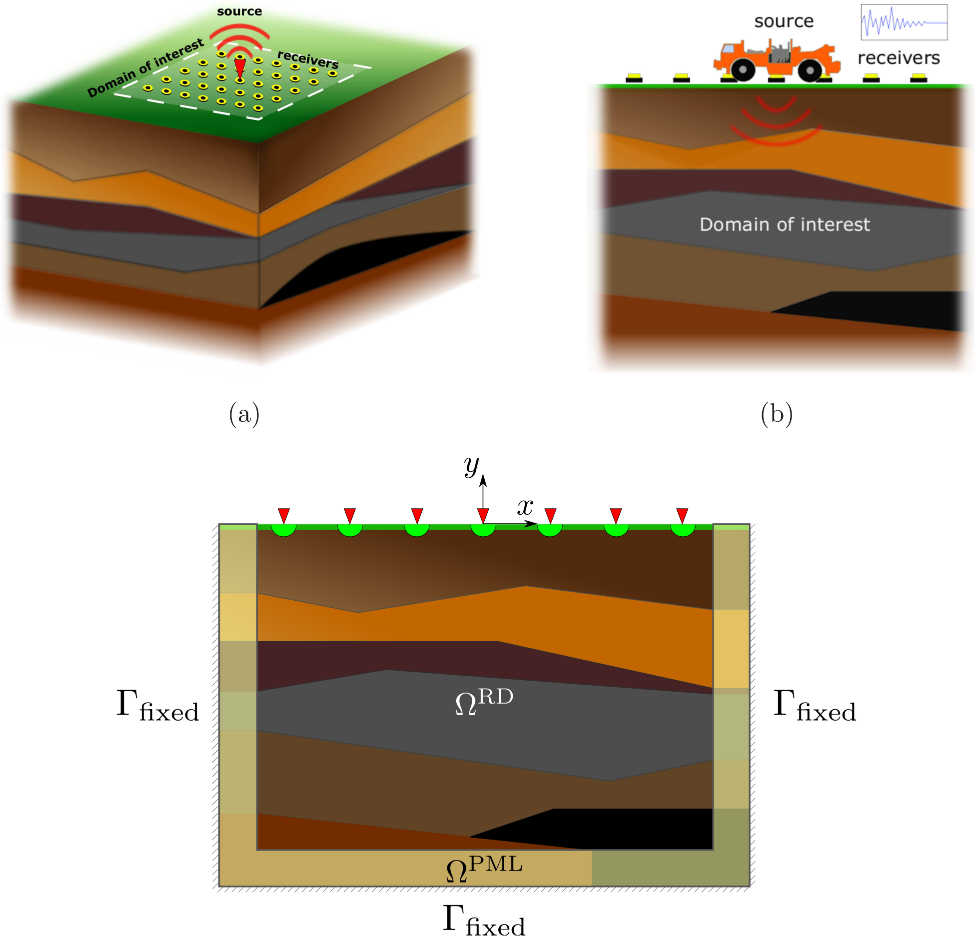

(a) (b)

(c)

Figure 1.1: Problem definition: (a) interrogation of a heterogeneous semi-infinite domain by an active source; (b) a two-dimensional cross-section of the domain showing one source and multiple receivers; and (c) equivalent two-dimensional computational model truncated from the semi-infinite medium via the introduction of Perfectly-Matched-Layers

The mathematical framework of the inverse medium problem must address two key components, namely, the *forward problem* and the *inverse problem*. Solution of the inverse problem usually necessitates multiple solutions of the forward problem, and thus, an efficient methodology that addresses the forward problem is of importance. Such an efficient approach for forward wave simulations constitutes an equally important objective of the research reported in this dissertation.

1.3 Review of related research

We discuss prior research related to both the forward and the inverse problem. Of relevance to the approach undertaken in this dissertation is the means by which one truncates infinite and/or semi-infinite domains; this is discussed first.

1.3.1 Perfectly-Matched-Layers - the forward problem

The simulation of wave motion in unbounded heterogeneous media requires negotiation of the infinite or semi-infinite extent of the unbounded domain. When domain discretization methods are used, the reduction of the physical to a finite domain through truncation is the only available computational strategy[1]. Truncation introduces artificial (non-physical) boundaries surrounding the finite computational domain. These boundaries require spe-

---

[1] Domain discretization methods are, essentially, the only possibility when the domain is heterogeneous.

cial treatment in order for the finite domain of interest to mimic the physical behavior of the non-truncated domain, while minimizing spurious reflections that may pollute the solution within the finite computational domain.

Two distinctly different strategies are possible for dealing with truncation boundaries: either to truncate the semi-infinite extent by introducing a transparent condition at the truncation interface, or to truncate by introducing an absorbing condition or absorbing buffer/layer. A transparent condition allows the passage of waves with, ideally, no or minimal reflections from the interface. An absorbing condition will typically force the decay of the wave motion within a buffer zone, while, ideally, annihilating any interface reflections as well[2].

Both categories, transparent and absorbing/layer conditions, have their own strengths and limitations. Broadly classified, transparent conditions are either local or non-local, where the non-locality refers to the temporal (convolution) and spatial (boundary integral) coupling of the response at the truncation interface. The published literature on the subject is considerable: Tsynkov in [158] provides an excellent review of both local and non-local truncation conditions. Non-local conditions typically attempt to simulate exactly the effect of the infinite (or semi-infinite) medium [72, 73, 75], while assuming that the domain excluded from the computations is homogeneous. However, the

---

[2] Transparent conditions are sometimes termed absorbing too, and also, silent, non-transmitting, non-reflecting, etc. Here, we adhere to a terminology based on whether there is a zone where the waves are forcibly absorbed (absorbing) or not (transparent).

benefit derived by providing an exact condition comes at a computationally expensive, difficult to implement, scheme. In addition, non-local conditions cannot handle arbitrary heterogeneity. To overcome the difficulties arising with non-local conditions, local conditions tend to relax both the spatial and temporal non-locality, but result in approximate forms that allow for reflections [20, 59, 74, 84, 91]. Local conditions are less accurate, but computationally efficient, and easy to implement when they are of low-order (higher-order local conditions become more complicated). Though, local conditions are often used at truncation boundaries of heterogeneous domains without sufficient theoretical justification, the errors due to reflections are compounded.

Absorbing/layer methods typically entail surrounding a truncated finite computational domain with a layer of uniform thickness within which the waves are forced to decay (Fig. 1.1(c)). Such absorbing boundary layers presently offer the best possible alternative for domain truncation in heterogeneous domains, due, by and large, to the successful introduction of the perfectly-matched-layer (PML) by Bérenger in the context of electromagnetic waves [26, 27]. PMLs, by construction, attenuate outwardly propagating waves without reflection from the truncation interface for all angles of incidence and frequencies. Once the waves enter the PML zone, they decay with distance according to a user-defined decay function. Although, in the continuous case, the PML can be shown to be reflection-less at the truncation interface, the spatial discretization introduces numerical reflections. However, the PML's tunable parameters enable the minimization of these reflections and allow increased accuracy even within thin layers, thereby reducing the overall computational cost. Applications of PMLs span a broad spectrum[3], and the last fifteen years have seen a wide range of applications, including, for example, the linearized Euler equations [85], the simulation of high-power microwaves (HPM) [162], Helmholtz equation [80, 159], seismic wave propagation in poroelastic media [173], fluid-filled pressurized boreholes [112], nonlinear and matter waves [62], acoustics [172], etc.

The literature on PMLs is fairly extensive: to place in context the present development, we discuss, in chronological order, developments on PMLs, by focusing on electromagnetics, for which PMLs were first developed, and elastodynamics, which is the focus of this work. In 1994, Bérenger [26] led the way by introducing the idea of a perfectly-matched-medium in electromagnetics. Bérenger's PML was formulated based on field-splitting in order to avoid convolutional operations in the time-domain, when the resulting forms are inverted back from the frequency-domain. The contribution of a spatial derivative in each coordinate direction was isolated, resulting in non-physical components for each field (as the name split-field implies; the number of non-physical components equals the dimensionality of the problem). Chew and Weedon [41] suggested a reinterpretation of the PML in the context of complex coordinate-stretching –a change of variables where spatial coordinates are mapped onto the complex space via *complex stretching functions*. Their

---

[3] free-space simulation problems, radiation and scattering problems, soil-structure interaction, seismic survey problems, computational fluid dynamics, geophysical subsurface sensing, waveguides, non-destructive evaluation applications, etc.

viewpoint transformed the PML into a superior tool by endowing it with a straightforward and consistent formulation. Even though the split-field formulation doubles the number of unknowns, its remarkable absorptive performance compensated for the added cost.

However, the field-splitting alters the initial form of the system, and results in a non-Maxwellian system of equations that makes implementations into existing Maxwell-based codes difficult. An alternative (also true for elastodynamics) that maintains the original Maxwellian form of the governing equations, is to reinterpret the medium as anisotropic, while simultaneously avoiding the field-splitting, as suggested by Gedney [70]. The interpretation of PML as an artificially anisotropic material necessitated the verification of causality. Kuzuoglu and Mittra [108] claimed that the anisotropic PML is not causal, and proposed a correction by introducing a frequency-dependent real part for the stretching functions. The discussion of causality that ensued showed that Kuzuoglu and Mittra's claim was based on an error in their application of the Kramers-Krönig relationships [154]; however, their proposed correction, though not needed for causality purposes, introduced an innovative formulation of the PML, the, so called, "complex-frequency-shifted PML" (CFS-PML). The frequency-dependent real part of the stretching functions proved onerous when inverting the resulting equations back into time-domain. By means of specialized convolutional operations, the difficulty was overcome, yielding an efficient implementation of the CFS-PML in electromagnetics, referred to as "convolution PML" (CPML) [138]. The relations between the various PML formulations (up to about 2000) were nicely summarized by Texeira and Chew in [155]. The equivalence between the complex coordinate-stretching and the anisotropic formulation was shown also in [99].

Most of the PML developments are predicated upon straight-edge or planar boundaries. But for certain problems where the domain of interest is more naturally associated with a non-cartesian coordinate system, the generalization of PML formulations to other coordinate systems is of importance. Maloney in [116] provided an extension to cylindrical coordinates, based on geometric arguments. Using the complex coordinate-stretching viewpoint, the cartesian PML was extended to cylindrical and spherical coordinates in [39, 151–153]. A theoretical analysis of Bérenger's system in curvilinear coordinates was performed by Collino and Monk [46], and optimal PML parameters were studied for the best computational performance in [47]. In [111], Liu and He pointed out that the straightforward extension of the original PML formulation to cylindrical coordinates (quasi-PML) was not reflection-less in cylindrical coordinates even in the continuum limit. The quasi-PML was simpler and computationally less demanding when compared to other PML implementations in cylindrical coordinates, since the same stretching functions were used in both the radial and angular directions. Later on, the same authors introduced a true PML formulation with different stretching functions for the radial and angular directions, and compared its performance against the quasi-PML [82]. A systematic derivation of the PML in curvilinear coordinates was also presented by Zhao [177]. Next, the generalization of PML to cartesian, cylindrical, and spherical coordinates was reviewed in [155]. Recently, for transient Maxwell equations, Donderici and Teixeira [56] developed a mixed finite element time-domain implementation of PML in doubly dispersive media, and in [55], a conformal PML was introduced for which the late-time stability and energy conservation properties have been verified numerically. The conformal PML allowed for a considerable reduction of buffer space by tightly circumscribing the scattering source.

Most PMLs are, by construction, excellent absorbers of propagating waves. Though evanescent waves too are absorbed efficiently [27], there is evidence that, for some frequencies, the strong attenuation might produce reflections caused by inadequately meshed PML zones [28]. In [137], Roden and Gedney showed that the CFS-PML implementation is highly absorptive of evanescent waves as well. A comparison of the split, unsplit, and CFS-PMLs revealed that split and unsplit formulations perform identically, whereas the CFS-PML forces a rapid decay of evanescent waves [30]. However, at low-frequencies, the CFS-PML suffers from degrading absorption of propagating waves. In [29], Bérenger discussed optimal CFS-PML parameters in order to absorb both evanescent and propagating waves. The CFS-PML was also effective in eliminating the observed long-time linear growth (instability) behavior of the unsplit PML [25]. Although the CFS-PML has several advantages over the standard PML, the low-frequency propagating waves are absorbed better in the standard PML. A recently developed second-order PML [49] allowed the combination of the best properties of the standard and CFS-PMLs in one PML, by simply using a stretching function that is the product of a standard and a CFS-PML stretching function. The resulting PML is as good as the CFS-PML in absorbing evanescent waves, while better attenuating the low-frequency propagating waves for waveguide problems [50]. Lou in [114] presented a successful finite element time-domain implementation of this second-order PML.

Chew and Liu in [40] were the first to extend the PML developments from electromagnetics to elastodynamics using a split-field, velocity-stress formulation, implemented using finite differences. Concurrently, Hastings [81] developed a PML for elastic waves using displacement potentials and a velocity-stress formulation, implemented using finite differences, which, however, could not be used in the presence of interface boundaries, such as those arising in layered media. Liu in [110] introduced a PML in cylindrical and spherical coordinates in elastodynamics based on split-fields. Later on, Collino and Tsogka [48] discussed a finite difference, time-domain, velocity-stress, split-field formulation and implementation, which appears identical to Chew and Liu [40], but was also used for applications involving anisotropic media. A mixed finite element implementation of the velocity-stress split-field formulation, in the context of a fictitious domain method, was discussed by Bécache et al. in [23]. All of the above key developments were based on velocity-stress schemes that are first-order in time.

In [101], Komatitsch and Tromp introduced a new split-field approach, whereby stress terms are eliminated, but the displacement field is split into four components, resulting in either third-order (in time) semi-discrete forms for the four displacement fields, or a second-order system coupled with one first-order equation for one of the displacement fields. Despite its complexity, their scheme was the first to create a displacement-only PML formulation in elastodynamics.

Since split-field formulations result in substantial computational cost, there is clear need for unsplit-field developments. An unsplit-field finite difference PML formulation was introduced by Wang and Tang [164] for elastodynamics, using the recursive convolution method of CPML developed originally for electromagnetics. However, in [164], the authors used standard stretching functions for their PML implementation, by contrast to the complex-frequency-shifted stretching functions of the original CPML formulation.

In [18], Basu and Chopra developed an unsplit-field PML for time-harmonic elastodynamics and implemented it using finite elements. Shortly thereafter, they also presented the time-domain implementation, using a rather complicated time integration scheme [19]. Recently, in [17], Basu used an explicit scheme to improve on the implicit time integration scheme previously used, but, despite the computational gain, the complexity remains. In [45], Cohen and Fauqueux discussed a formulation, based on a novel decomposition of the elastodynamics equations as a first-order system, which was implemented using a mixed finite element approach and spectral elements. To arrive at the first-order decomposition, the authors split the strain tensor, and introduced independent stress variables to account for the split strain tensor components. In [64], Festa and Vilotte, also discussed mixed formulations (velocity-displacement, and velocity-stress), the use of spectral elements, and a time-staggering scheme for marching in time. Their formulation differs decidedly from Cohen and Fauqueux: the authors in [64] followed classical lines for reducing the second-order displacement-only elastodynamic problem to a first-order in time system, and used split-fields for both the velocity and stress components (as opposed to the splitting of the strain tensor).

Recently, in [58], Drossaert and Giannopoulos discussed an alternative implementation of the unsplit PML that is based on recursive integration (RIPML), rather than the explicit computation of convolutions. Later, in [57], they implemented the CPML for elastodynamics using the complex-frequency-shifted stretching functions, and reported better performance than the RIPML.

The majority of the developments in elastodynamics refer to the isotropic case. Notable exceptions include the earlier work by Collino and Tsogka [48], where they showed that the split-field standard PML can also handle heterogeneous and anisotropic media. However, the stability of the PML and the effect of anisotropy was studied later by Bécache et al. [21], where it was shown that, while the standard PML is stable for isotropic applications, it is conditionally unstable for anisotropic applications. The authors proposed necessary conditions for stability in the form of inequalities implicating the material constants. More recently, in [120], Meza-Fajardo and Papageorgiou discussed a novel PML approach, termed M-PML, which results from the introduction of coordinate-stretching and associated decay functions along all coordinate directions, that is, not only along the direction normal to the PML interface, as has been the norm to date. Their resulting split-field, non-convolutional M-PML exhibits superior performance when compared to the standard PML formulations, especially for waves propagating at grazing angles. They also showed that the M-PML is capable of handling anisotropy, without the long-time instability reported earlier for the CPML and standard PML formulations.

The performance of the PML has been investigated also for Rayleigh and interface waves [63]. It was shown that both were attenuated remarkably well. Komatitsch and Tromp in [101] also confirmed the efficiency of PML in absorbing surface waves, but the performance of the discrete PML at grazing incidence was rather poor. This limitation was also reported in [58], but has been removed, owing to the CPML formulation reported by Komatitsch and Martin in [100].

Any PML implementation entails user-chosen values for a number of PML parameters. There are very few comprehensive parametric studies reported in the literature that provide guidance on parameter selection. A notable exception is the work by Harari and Albocher [80], where the authors studied, using dispersion analysis, the effect of PML parameters for the time-harmonic elastic case, and presented guidelines for the proper choice of PML parameter values. Guidelines on the discretization of the PML, for any choice of the PML parameters, were also given in [121].

Table 1.1 summarizes the key developments to date for time-domain elastodynamics, classified depending on whether the primary unknowns are split or not, and whether the implementation is done using finite differences (FD), or finite/spectral elements (FE/SE). In general, when the PML formulation involves split-fields, almost always the resulting scheme is mixed [23, 40, 45, 48, 64, 81, 110, 120], i.e., both displacements/velocities *and* stresses become unknowns. The one exception is the approach by Komatitsch and Tromp [101], where the displacement field was the only unknown, albeit split into four components. On the other hand, unsplit-field schemes require, in general, the evaluation of convolutions [57, 58, 100, 164], which, despite the use of recursive evaluation schemes, remain expensive. One exception here is the work by Basu and Chopra [19], and by Basu [17], where the authors, though they came close to defining a mixed problem (with unsplit displacement and stresses as unknowns), they ended up departing considerably from it at the discrete level, in favor of implementing a complicated time-marching scheme. We note that, in general, the penalty one pays for a purely displacement-only formulation is an increase in the temporal complexity, which, as a result, calls for specialized time integration schemes. The temporal complexity arises from the structure of the PML, and in particular, from the choice of the stretching function. The mixed approach relaxes the temporal complexity, and as will be shown here, leads to second-order in time semi-discrete forms in the two-dimensional case, and in third-order in time semi-discrete forms in the axisymmetric and three-dimensional cases. In a recent work by Martin et al.

[118], the authors presented a formulation, where the interior is treated using a standard displacement-only formulation, retaining a mixed velocity-stress form for the PML (CPML in this case), and an *ad hoc* coupling at the interface –all resolved using finite differences. Their approach reduces considerably the overall number of degrees-of-freedom, due to the non-mixed form of the interior problem. To an extent, the hybrid method developed here, independently of [118], is similar to [118], but is cast in a true variational setting using finite elements, and avoids the staggering scheme used in [118] for time-marching.

For completeness, Table 1.1 includes also references to our own recently published work, which was based on the research reported in this dissertation.

Table 1.1: PML implementations in time-domain elastodynamics

	Split-field	**Unsplit-field**
FD	Chew and Liu [40] Hastings et al. [81] Liu [110] Collino and Tsogka [48]	Wang and Tang [164] Drossaert and Giannopoulos [57, 58] Komatitsch and Martin [100]
FE/SE	Bécache et al. [23] Komatitsch and Tromp [101] Cohen and Fauqueux [45] Festa and Vilotte [64] Meza-Fajardo and Papageorgiou [120]	Basu and Chopra [19] Basu [17] Kucukcoban and Kallivokas [103–105]

Since most PML developments to date, including the ones we will be discussing herein, lead to mixed formulations, we provide next a brief overview of mixed finite element formulations; a comprehensive review is well outside the scope of this dissertation. In [4], Arnold presented an outstanding introductory level discussion of mixed methods, their advantages and disadvantages, and the concepts of convergence, approximability and stability. Whereas standard single-field finite elements require approximants for a single distributed variable, mixed schemes require approximants for two (or more) fields. For stability, the choice of the approximants in mixed problems cannot be arbitrary, and must satisfy an *inf-sup* condition (also referred to as Ladyzhenskaya-Babuška-Brezzi (LBB) condition).

In an interesting review by Brezzi in [32], the author pointed out that there exist two possible variational forms for treating a mixed problem such as the one arising in elasticity; the two forms result in *decidedly different* regularity requirements for the approximants. In the first form, the regularity required for the stress approximants is higher than that of the displacement approximants; this is the classic mixed method. The first family of mixed finite elements related to this variational form was introduced by Raviart and Thomas for second-order elliptic problems (RT elements) [135]. Later on, several other special mixed finite elements were introduced: Johnson-Mercier [89], Brezzi-Douglas-Marini (BDM) [33], MINI element [10], PEERS (plane elasticity element with reduced symmetry) [9], etc. Other related developments can be found in [6, 11–15, 22, 24, 34, 38, 67, 117, 122, 124–126, 148].

On the other hand, in the second form, which differs from the first simply by an integration by parts, the regularity requirements are somewhat reversed: the regularity for the displacement approximants should be higher than that of the stress approximants. The latter requirements are less onerous for implementation purposes and do not require any special element types, such as the RT, BDM, etc. In this work, we favor this second, and largely unexplored, variational form. Thus, in short, we use *unsplit-fields* resulting in a *non-convolutional mixed PML*, where both displacements and stresses are treated as unknowns, and employ *finite elements* to resolve the unknowns.

To date, there are four developments that are closely related to ours, but they all differ in substantial ways: Bécache et al. in [23] used a classic mixed method, but split-fields; Cohen and Fauqueux [45] used a unique mixed method, unlike any other in the literature, and split the strain tensor fields; Festa and Vilotte [64] used the same non-classic mixed method as ours, but ended up using split-fields; and finally Basu and Chopra [19] came close to casting the problem in a mixed form using unsplit fields similar to ours, but ended up with a discrete implementation that destroyed the mixed form, in favor of a complicated time-marching scheme. Their semi-discrete forms are *almost* second-order in time, but include an internal force term, whose computation requires both the storage of strains (thus, effectively, rendering the scheme mixed), as well as the temporal integration of the strains at every time step, unless, at the expense of accuracy, some form of linearization is adopted. We remark that, as is the case with any mixed form, there always results an increase in the number of unknowns, when compared to non-mixed methods. However, in light of the fact that most developments to date employ mixed split-fields, where the unknowns include the split-fields of both velocities and stresses, the first formulation proposed herein results in computational savings, even though, when compared to interior displacement-only methods it is expensive. But, then again, purely displacement-only methods capable of handling arbitrary heterogeneity for infinite or semi-infinite domains, directly in the time-domain, have yet to appear.

By contrast to all preceding developments, the second formulation we discuss herein, termed hybrid, combines a displacement-only interior with a mixed PML domain: the hybrid approach is optimal in terms of computational cost.

1.3.2 Full waveform inversion

The past thirty years have witnessed rapid advances in extracting the geophysical properties of the Earth, for example, directly from seismic data ([16, 35, 44, 144, 150]). Broadly classified, there exist two strategies one could pursue to tackle the inverse problem: *migration velocity analysis* (MVA) [36, 44, 129], and *full waveform inversion*[4] [31, 35, 134, 144]. The MVA approach is based on a decomposition of the sought properties into slowly-varying and fast-varying components, referred to as the background and reflectivity components. Each component is determined separately, which increases the complexity and overall computational cost of the approach: the background component necessitates a travel-time inversion, whereas the reflectivity component requires a prestack migration. On the other hand, full-waveform-based inversion schemes rely typically on a least-squares (or other norm) data fitting

---

[4] The complete waveform record is used in a full waveform inversion approach, also known as full waveform tomography.

process, and their robustness depends, to an extent, on having a good initial guess (see also [128] for a short overview). The issue was discussed in a recent comprehensive review of MVA and waveform inversion by Symes [149], where it was emphasized that full waveform inversion schemes require a good initial guess to avoid spurious local minima. There are, however, strategies to alleviate the inherent solution multiplicity: these can be roughly grouped into direct regularization approaches (e.g. Tikhonov [156], Total Variation [139]), and continuation schemes (e.g. [60, 123]). Overall, many issues pertaining to inversion remain, by and large, open. However, advances in both computer architecture and optimization algorithms have already enabled large-scale three-dimensional full waveform inversion in acoustic and, to an extent, in elastic media as well using synthetic data [37, 60].

Waveform inversion, in general, has been pursued in many technical areas (e.g., medical imaging, non-destructive testing, oil-exploration, etc.), in both the frequency-domain [132, 145], and the time-domain [127, 146], owing to the significance of the underlying applications. For example, Pratt and Shipp [132, 133], Operto et al. [127], Gao et al. [68], and Choi et al. [42, 43] explored full waveform inversion using either real or synthetic data sets to reconstruct complicated earth velocity structures. However, a systematic and robust time-domain methodology, consistent with the incomplete nature of the data typically collected in field applications, remains elusive.

In this dissertation, we favor a full waveform inversion approach embedded within a PDE-constrained least-squares optimization framework, similar to the recent work by Epanomeritakis et al. [60], and Kang and Kallivokas [92, 96]. The key conceptual difference between [60] and what we discuss here is the adoption of a PML as the truncation condition, which, in turn, adds complexity in both the forward and the inverse modeling. There are also two essential differences between this work and that of Kang and Kallivokas [92, 96]: a) in this work we treat the elastic case, whereas in [92, 96] only the acoustic (or SH) case was treated, requiring inversion for a single distributed parameter; and b) the approach in [92, 96] for the forward and the inverse problem rested on a fully-mixed formulation, whereas here we have developed and adopted for both problems a more efficient hybrid formulation.

1.4 Solution approach

The steps taken to address the research objectives outlined earlier can be divided into the two key components, the forward and inverse problem, respectively; the steps are summarized below.

On the forward problem:

- We discuss the formulation of a new mixed unsplit-field PML for direct transient analysis in two-dimensional elastic, semi-infinite, arbitrarily heterogeneous media. We provide details on the mixed finite element implementation, where both displacements and stress histories are the primary unknowns. The formulation results in second-order in time semi-discrete forms. We report on numerical results, involving both homogeneous and heterogeneous domains, to demonstrate the stability and efficacy of the approach.

- We extend the new PML formulation to axisymmetric problems and to three dimensions. Axisymmetric problems arise in elastic, semi-infinite, horizontally-layered media and are of interest in geophysical borehole applications and pavement design/assessment problems. We discuss the details of the mixed finite element implementation that results in a semi-discrete form containing a jerk or jolt term for the displacements. To integrate in time the semi-discrete forms, we provide an extension to the classical Newmark-β scheme. We present numerical simulations exhibiting stability and demonstrating efficacy of the proposed PML in homogeneous and heterogeneous axisymmetric media. Three-dimensional results are not reported, since the implementation of the three-dimensional formulation was beyond the scope of this dissertation. We remark that this first formulation retains the displacement and stress unknowns everywhere within both the interior domain and the PML buffer, and is, thus, computationally expensive, especially when considering the need for its repeated use in the context of the inverse problem.

- To overcome the above shortcoming, we discuss next a new hybrid, fully symmetric, variational formulation (mixed unsplit-field PML, coupled with a non-mixed approach for the interior domain) that reduces the number of unknowns by as much as 60%, and leads to optimal computational cost. We provide the formulation and implementation details:

we show that existing displacement-based codes can easily be modified to accommodate PMLs as a means of domain truncation. We study numerically the stability, efficacy, and cost-effectiveness of the hybrid formulation in both homogeneous and heterogeneous media, and report the results.

On the inverse problem:

We seek to recover the spatial distribution of the Lamé parameters $\lambda(\mathbf{x})$ and $\mu(\mathbf{x})$ in an elastic PML-truncated domain. The data of the problem consist of the surface loads (sources) and the observed[5] response at a few receivers (measuring stations) on the surface. In simple terms, we solve the forward problem (wave motion in the PML-truncated elastic domain) under a known excitation and for a trial distribution of the Lamé parameters, and then iteratively update the parameters until the misfit between the computed and observed responses at the measuring stations is minimized. The minimization problem is subject to the satisfaction of the governing partial differential equations (PDEs), initial, and boundary conditions, which together describe the underlying physics of the problem. Consequently:

- To address the inverse medium problem, we adopt a PDE-constrained optimization framework. We cast the profile reconstruction problem as a PDE-constrained least-squares misfit optimization problem, and then

---

[5] The terms "observed" and "measured" are used interchangeably throughout the dissertation.

recast it with the aid of a Lagrangian, whereby the misfit functional is augmented with the side-imposition of the PML-endowed PDEs, initial, and boundary conditions via Lagrange multipliers. To enforce the stationarity of the Lagrangian, we derive next the first-order optimality conditions that lead to a *state* (forward), an *adjoint*, and *control* problems. Upon discretization, the coupled system results in a classic KKT (Karush-Kuhn-Tucker) system. To solve, we pursue a *reduced-space approach* in which the coupled system of PDEs are solved in the reduced space of the control variables –the Lamé parameters. Typically, we start with an assumed initial spatial distribution of λ and μ and solve the state problem. Then, we solve the adjoint problem using the previously computed state solutions. By doing so, we satisfy the first and second optimality conditions. Then, we iteratively update λ and μ until the misfit between measured and computed responses reduces to a preset tolerance, using the control problems; this, effectively, forces the satisfaction of the third optimality conditions.

- As it is commonly the case with all inverse problems, the inverse medium problem too is afflicted by solution multiplicity. To alleviate the difficulties associated with solution multiplicity, we explore both Tikhonov (TN) and Total Variation (TV) regularization schemes, and report on the effect they have on the quality of the recovered profiles.
- Regularization by itself is not sufficient for guiding the optimizer to the true profile. We discuss additional remedies in the form of continuation

schemes to aid the inversion process in reconstructing high-quality material profiles: specifically, we discuss regularization factor continuation and source-frequency continuation schemes. In the first scheme, we adjust the regularization factor dynamically so that it takes a large value at the beginning of the inversion process (to narrow down the initial feasibility space of the solution), and, as iterations progress, it is continuously reduced in order to relax the penalty the regularization imposes on the inversion process.

  In the second scheme, we use, initially, probing signals with low-frequency content to avoid multiple attraction basins; this results in profiles that can be used as initial guesses to subsequent problems driven by signals with higher-frequency content. The scheme progressively allows for the fine tuning of the profile. Finally, we also developed and use a search-direction biasing scheme that recognizes the relation between the Lamé parameters, and accelerates the optimizer's convergence.

- We discuss our experience in reconstructing heterogeneous profiles involving layered systems and smoothly-varying profiles, as well as layered systems containing inclusions to demonstrate the performance of the proposed inversion approach and associated algorithms.

1.5 Dissertation outline

This dissertation is organized as follows:

In Chapter 2, we discuss the developments pertaining to the forward problem. Specifically, in section 2.1, we review key ideas in the development of the PML and discuss the central concept of complex coordinate-stretching without particular reference to any specific coordinate system. Then, in section 2.2, we develop a new fully-mixed unsplit-field PML formulation in two dimensions, provide implementation details, and report on numerical results for both homogeneous and arbitrarily heterogeneous media. Next, in sections 2.3 and 2.4, we extend the fully-mixed formulation to the axisymmetric and three-dimensional cases. We report numerical simulations for the axisymmetric case only.

In section 2.5, we discuss the alternative hybrid, symmetric, variational formulation (mixed unsplit-field PML, coupled with a non-mixed approach for the interior domain) that leads to optimal computational cost. We provide two numerical experiments to discuss the stability, accuracy, and cost-effectiveness of the hybrid approach.

In Chapter 3, we present the mathematical modeling framework for the full waveform inversion in which we determine the unknown Lamé parameters λ and μ of a PML-truncated two-dimensional elastic medium. We report numerical experiments to discuss the performance of the various schemes we used.

Chapter 4 summarizes the findings and suggests future directions and enhancements to this work. Lastly, the various Appendices include details of the theoretical development presented in earlier chapters.

Chapter 2

Wave motion modeling in PML-truncated domains

2.1 The Perfectly-Matched-Layer (PML)

Following its introduction by Berénger [26] in electromagnetics, Chew and Weedon [41] suggested a reinterpretation of the PML in the context of complex coordinate-stretching, which allowed for the PML's wide adoption (e.g., free-space simulation problems, radiation and scattering problems, soil-structure interaction, borehole acoustic measurements, seismic survey, computational fluid dynamics, geophysical subsurface sensing, non-destructive evaluation applications etc.) and refined development.

The PML is a truly absorbing condition, capable of handling heterogeneity, unlike any other competing methodology. The PML attenuates propagating waves without reflection from the interface for all non-zero angles-of-incidences and frequencies. At the interface, the material properties of PML match with the ones in the regular domain. Thus, the interface becomes invisible to waves incident at all angles and frequencies. Once the wave enters PML, it decays exponentially with distance into the layer. The attenuation is applied in the direction normal to the interface with a rate specified by the selected attenuation profile. In addition, corners in the PML do not require any special treatment. Although, in the continuum, the PML has been shown to be reflection-less, the spatial discretization introduces numerical reflections. However, the PML's tunable parameters enable the minimization of these reflections and allow increased accuracy even with thin PMLs.

In the following sections, we describe the usual formulation of a PML based on complex coordinate-stretching [41, 155]. The key idea of complex coordinate-stretching is based on analytic continuation of the solutions of wave equations [155], and is realized via a mapping of the spatial coordinates onto the complex space via complex stretching functions. This is accomplished by a simple change of coordinate variables from the real to their complex-stretched counterparts. The coordinate change is applied to the equations written for the frequency-domain and, if required, the resulting complex-transformed equations are inverted back into the time-domain for transient applications. Parts of the material discussed in this chapter is not new (see cited references), but is provided here to allow for context, completeness, and illumination of differences.

2.1.1 Complex coordinate-stretching in PML development

Without reference to any specific coordinate system (the system needs to be orthogonal), let s denote the coordinate along a coordinate axis normal to the interface between the PML and the regular (interior) domain. Assuming that the interface is located at s_o, the computational domain of interest is the region $0 \leq s < s_o$, whereas $s_o < s \leq s_t$ is the PML with a layer thickness of L_{PML}, as depicted in Fig. 2.1.

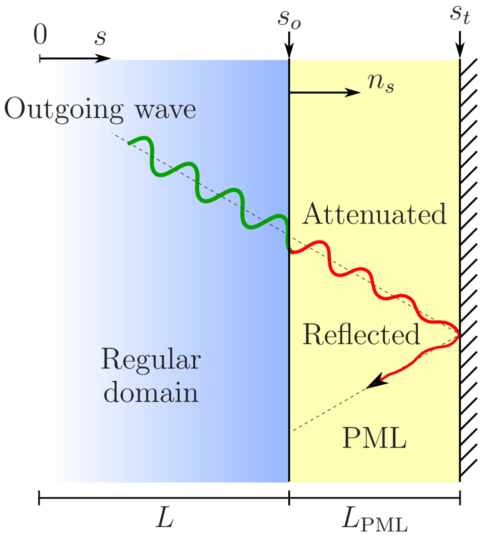

Figure 2.1: A PML-truncated computational domain in the direction of coordinate s. The outgoing waves pass through the interface located at s_o without reflections, and decay exponentially with distance within the layer.

The original coordinate variable s is replaced by the "stretched" coordinate $\tilde{s}$ in any equation s appears, where $\tilde{s}$ is defined as

$$\tilde{s} = \int_0^s \varepsilon_s(s', \omega)\, ds' = s_o + \int_{s_o}^s \varepsilon_s(s', \omega)\, ds'. \tag{2.1}$$

In the above, ω denotes circular frequency, and ε_s is a "complex stretching function" in the direction of coordinate s. Though various forms of stretching functions have been proposed, here we adopt the most-widely used form of a stretching function due to its straightforward implementation and improved performance with low-frequency propagating waves. Accordingly,

$$\varepsilon_s(s, \omega) = \alpha_s(s) + \frac{\beta_s(s)}{i\omega}, \tag{2.2}$$

where α_s and β_s are commonly referred to as scaling (or stretching) and attenuation functions, respectively (both are real-valued). As the names imply, the real part of ε_s scales the coordinate s, and, thus, acts as a real-valued "stretch", effectively resulting in artificial geometric damping. However, the amount of attenuation imposed by the scaling function is not enough to attenuate the propagating waves. It is the imaginary part of ε_s that is responsible for the exponential decay of the propagating wave, once it enters the PML. The role of α_s is reversed in the case of evanescent waves, where it, instead of β_s, becomes responsible for their amplitude decay post-PML-entry. Specifically, for waves propagating outwardly along s, their amplitude is proportional to e^{-iks}, which, after the substitution of s by $\tilde{s}$, becomes:

$$e^{-ik\tilde{s}} = e^{-ik\int_0^s \alpha(s')ds'} e^{-\frac{k}{\omega}\int_0^s \beta(s')ds'}, \tag{2.3}$$

and similarly, for evanescent waves:

$$e^{-k\tilde{s}} = e^{-k\int_0^s \alpha(s')ds'} e^{i\frac{k}{\omega}\int_0^s \beta(s')ds'}. \tag{2.4}$$

Thus, to enforce both propagating and evanescent waves to be attenuated within the PML, we require that α_s and β_s are monotonically increasing functions of s; moreover:

$$\alpha_s(s) > 1 \quad \text{and} \quad \beta_s(s) > 0, \quad s_o < s \leq s_t,$$

whereas, in the regular domain we require that

$$\alpha_s(s) = 1 \quad \text{and} \quad \beta_s(s) = 0, \quad 0 \leq s < s_o,$$

so that $\tilde{s} \equiv s$ in the regular domain (no scaling or attenuation within the regular domain). At the interface, continuity between the two domains is maintained by setting $\alpha_s(s_o) = 1$ and $\beta_s(s_o) = 0$. The latter conditions are responsible for ensuring that the interface becomes invisible to the waves entering the PML. Since the scaling and attenuation functions do not depend on frequency, the rate of decay in the PML is frequency-independent. Although α_s is usually taken equal to one, using a value larger than one within the PML improves the attenuation of strong evanescent waves [110].

An alternative form of the stretching function was proposed by Kuzuoglu and Mittra [108], giving rise to the, so-called, frequency-shifted stretching, where

$$\varepsilon_s(s,\omega) = \alpha_s(s) + \frac{\beta_s(s)}{\kappa_s(s) + i\omega\gamma}. \tag{2.5}$$

Using (2.5) results in the CFS-PML formulation where both the real and imaginary parts of ε_s are now frequency-dependent. In transient implementations of the unsplit-field PML, the use of (2.5) results in convolutional operations. It has been shown that the CFS-PML outperforms the standard PML in attenuating evanescent waves, though, with a degrading absorption of low-frequency propagating waves [29, 30, 137]. In an effort to combine the best of both stretching functions, a second-order PML was introduced in [49] where

$$\varepsilon_s(s,\omega) = \left(\alpha_s(s) + \frac{\beta_s(s)}{i\omega\gamma}\right)\left(\alpha_s^*(s) + \frac{\beta_s^*(s)}{\kappa_s(s) + i\omega\gamma}\right). \tag{2.6}$$

Although the implementation of (2.6) is not trivial in the time-domain, the second-order PML is the best choice when both low-frequency propagating waves and strong evanescent waves are present [50]. In this dissertation, the stretching function defined in (2.2) is preferred since it leads to a straightforward implementation and exhibits better performance with low-frequency propagating waves.

Lastly, with the aid of the fundamental theorem of calculus, there also holds that

$$\frac{d\tilde{s}}{ds} = \frac{d}{ds}\int_0^s \varepsilon_s(s', \omega)\, ds' = \varepsilon_s(s, \omega) \qquad \Rightarrow \qquad \frac{d}{d\tilde{s}} = \frac{1}{\varepsilon_s(s, \omega)}\frac{d}{ds}. \tag{2.7}$$

Relation (2.7) will be used to transform the governing equations. For notational brevity, the functional dependence of ε_s will be henceforth omitted.

It is important to note that, by construction, the particular form of the stretching function (2.2) used herein clearly fails for the static case, i.e. for $\omega = 0$. Therefore, using this stretching function, one cannot obtain a PML suitable for truncating a semi-infinite domain, and recover displacement and stress fields corresponding to static loading. All subsequent derivations are predicated upon the exclusion of the zero frequency from consideration.

2.1.2 The PML's stretching function

There is no rigorous methodology suggested in the literature for choosing the scaling and attenuation functions α_s and β_s, respectively, but the key idea is to have a profile varying smoothly with distance within the PML. To minimize reflections, generally, either quadratic or linear profiles have been recommended [40], though, we have found linear profiles to result in sharp profiles, sharper than higher-order polynomials, thus exacting the mesh requirements within the PML. On the other hand, quadratic profiles have been broadly used in PML elastodynamics [45, 48, 64, 101]. In general, the commonly adopted form of the attenuation profile can be cast, for arbitrary polynomial degree m, as

$$\beta_s(s) = \begin{cases} 0, & 0 \leq s \leq s_o, \\ \beta_o \left[\frac{(s-s_o)n_s}{L_{\text{PML}}} \right]^m, & s_o < s < s_t, \end{cases} \tag{2.8}$$

where β_o is a user-chosen scalar parameter, m is the degree of the polynomial attenuation, and n_s is the s-th component of the outward normal to the interface between the PML and the regular domain. For ε_s to remain dimensionless, parameter β_o must have units of frequency. Based on one-dimensional wave propagation ideas, β_o can be shown to assume the form

$$\beta_o = \frac{(m+1)c_p^{\text{ref}}}{2L_{\text{PML}}} \log\left(\frac{1}{|R|}\right), \tag{2.9}$$

where R is user-tunable reflection coefficient controlling the amount of reflections from the outer PML boundary that is typically set as fixed, and c_p^{ref} is the P-wave velocity (in general, a reference velocity, not necessarily the P-wave velocity of the medium). Once a polynomial degree is specified for the attenuation profile, the strength of decay in the PML can be tuned by controlling R, or even β_o (since c_p^{ref} and R are floating parameters).

The scaling function (α_s) controls the decay of evanescent waves and affects the performance of the PML. It is common practice to use similar profiles for both scaling and attenuation functions. Since α_s is required to be unity in the regular domain, a form similar to the attenuation profile β_s

requires that α_s be expressed as

$$\alpha_s(s) = \begin{cases} 1, & 0 \leq s \leq s_o, \\ 1 + \alpha_o \left[\frac{(s-s_o)n_s}{L_{\text{PML}}}\right]^m, & s_o < s < s_t, \end{cases} \tag{2.10}$$

where α_o is, similar to β_o, a user-chosen dimensionless scalar parameter. To avoid having two different tuning parameters, here, we employ a form similar to β_o

$$\alpha_o = \frac{(m+1)b}{2L_{\text{PML}}} \log\left(\frac{1}{|R|}\right), \tag{2.11}$$

where b is a characteristic length of the domain (e.g., element size).

The general expression for $\tilde{s}$ in (2.1) can be easily computed by substituting (2.10) and (2.8) in (2.2). The stretched coordinate $\tilde{s}$ then becomes:

$$\tilde{s} = \int_0^s \left(\alpha_s(s') + \frac{\beta_s(s')}{i\omega}\right) ds' \quad \Rightarrow \quad \tilde{s} = \bar{\alpha}_s + \frac{\bar{\beta}_s}{i\omega}, \tag{2.12}$$

where $\bar{\alpha}_s(s)$ and $\bar{\beta}_s(s)$ denote the integrated quantities:

$$\bar{\alpha}_s(s) = \begin{cases} s, & 0 \leq s \leq s_o, \\ s + \alpha_o \left(\frac{n_s}{L_{\text{PML}}}\right)^m \frac{(s-s_o)^{m+1}}{m+1}, & s_o < s < s_t, \end{cases} \tag{2.13a}$$

$$\bar{\beta}_s(s) = \begin{cases} 0, & 0 \leq s \leq s_o, \\ \beta_o \left(\frac{n_s}{L_{\text{PML}}}\right)^m \frac{(s-s_o)^{m+1}}{m+1}, & s_o < s < s_t. \end{cases} \tag{2.13b}$$

In this work, we favor quadratic profiles ($m = 2$), even though higher-order profiles enforce more gradual attenuation within the PML. In summary, we use

$$\alpha_s(s) = \begin{cases} 1, & 0 \leq s \leq s_o, \\ 1 + \frac{3b}{2L_{\mathrm{PML}}} \log\left(\frac{1}{|R|}\right) \left[\frac{(s-s_o)n_s}{L_{\mathrm{PML}}}\right]^2, & s_o < s < s_t, \end{cases} \tag{2.14a}$$

$$\beta_s(s) = \begin{cases} 0, & 0 \leq s \leq s_o, \\ \frac{3c_p^{\mathrm{ref}}}{2L_{\mathrm{PML}}} \log\left(\frac{1}{|R|}\right) \left[\frac{(s-s_o)n_s}{L_{\mathrm{PML}}}\right]^2, & s_o < s < s_t, \end{cases} \tag{2.14b}$$

$$\bar{\alpha}_s(s) = \begin{cases} s, & 0 \leq s \leq s_o, \\ s + \frac{b\, n_s^2}{2L_{\mathrm{PML}}^3} \log\left(\frac{1}{|R|}\right) (s-s_o)^3, & s_o < s < s_t, \end{cases} \tag{2.14c}$$

$$\bar{\beta}_s(s) = \begin{cases} 0, & 0 \leq s \leq s_o, \\ \frac{c_p^{\mathrm{ref}}\, n_s^2}{2L_{\mathrm{PML}}^3} \log\left(\frac{1}{|R|}\right) (s-s_o)^3, & s_o < s < s_t. \end{cases} \tag{2.14d}$$

Guided by the numerical experiments that appear later in this dissertation, a variable α_s parameter shows no significant improvement over a constant α_s of value 1 and we have thus used $\alpha_s(s) = 1$, $0 \leq s < s_t$. However, we note that in the presence of strong evanescent waves there may be an advantage in using a spatially varying α_s.

We also note that, in general, the polynomial order m in (2.8) controls the shape of the attenuation profile within the PML: depending on the order, a sharper transition could be imposed either closer to the PML-regular domain interface, or closer to the fixed PML boundary. This, in turn, drives the meshing within the PML so that the sharper profile portion of the attenuation profile is adequately resolved. Moreover, the scalar factor in front of the polynomial term in the expression (2.14b) for β_s controls the intensity of the imposed attenuation: thus, the reference velocity c_p^{ref}, the PML length L_{PML}, and the reflection coefficient R all play an equal role in controlling the attenuation. To quantify our observations, we turn our attention to the amplitude decay factor (ADF) for the propagating waves first introduced in (2.3):

$$(\text{ADF}) = e^{-\frac{k}{\omega}\int_0^s \beta(s')ds'} = e^{-\gamma_o n_s^m \left(\frac{s-s_o}{L_{\text{PML}}}\right)^{m+1}}, \tag{2.15}$$

where

$$\gamma_o = \frac{c_p^{\text{ref}}}{2c_p}\log\left(\frac{1}{|R|}\right). \tag{2.16}$$

Figure 2.2(a) shows the amplitude decay of the propagating waves within the PML for a fixed polynomial order ($m = 2$): with increasing γ_o (i.e., increasing c_p^{ref}/c_p ratio or decreasing reflection coefficient R), the decay profile becomes sharper close to the regular domain-PML interface. By contrast, Fig. 2.2(b) shows that the profile becomes sharper closer to the outer fixed PML boundary with increasing polynomial order.

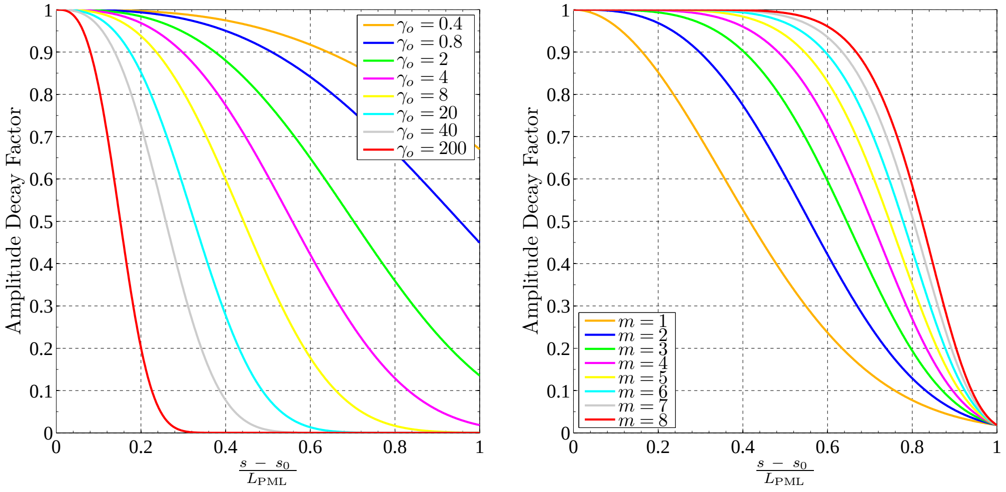

(a) (b)

Figure 2.2: Amplitude decay of the propagating waves within the PML for: (a) different γ_o, fixed $m = 2$, (b) fixed $\gamma_o = 4$, different m

For a fixed polynomial order m, any of γ_o (or equivalently c_p^{ref}/c_p or R) or β_o can be used to control the attenuation intensity within the PML. Here, for most of the numerical results, we use R to control the attenuation strength; in section 2.5, we use β_o.

2.2 Fully-mixed 2D elastic wave modeling

In section 2.1, we introduced the basics of PML and reviewed the concept of complex coordinate-stretching to place this development in context. In this section, we discuss the formulation of a new fully-mixed unsplit-field PML for direct transient analysis in 2D elastic, semi-infinite, arbitrarily heterogeneous media. To mimic the semi-infinite physics of the problem, we surround a truncated finite computational domain (i.e., the domain of interest) with a uniform thickness layer (i.e., the PML) in which the waves are attenuated.

In coordinate-system-independent form, the propagation of linear elastic waves is governed by the equations of motion, the generalized Hooke's law, and the kinematic conditions:

$$\mathbf{div}\,\mathcal{S}^T + \mathbf{f} = \rho\ddot{\mathbf{u}}, \tag{2.17a}$$

$$\mathcal{S} = \mathcal{C} : \mathcal{E}, \tag{2.17b}$$

$$\mathcal{E} = \frac{1}{2}\left[\nabla\mathbf{u} + (\nabla\mathbf{u})^T\right], \tag{2.17c}$$

where $\mathcal{S}$, $\mathcal{E}$, and $\mathcal{C}$ are the stress, strain, and elasticity tensors, respectively; ρ is the density of the elastic medium, $\mathbf{u}$ is the displacement vector, $\mathbf{f}$ is the load vector, (:) denotes tensor inner product, the superscript T denotes the transpose operation, and a dot $(\dot{\ })$ denotes differentiation with respect to time of the subtended function. The spatial and temporal dependence of the displacement vector, stress, and strain tensors is implicit in the above expressions. For a cartesian system, the components of the gradient (∇) and divergence $(\mathbf{div})$ operators are defined as

$$(\nabla \mathbf{u})_{ij} = \frac{\partial u_i}{\partial j}, \qquad (\mathbf{div}\, \mathcal{S})_i = \sum_j \frac{\partial \mathcal{S}_{ij}}{\partial j}, \qquad i, j = x, y(, z). \tag{2.18}$$

The PML formulation results from the application of complex coordinate-stretching to the governing equations so that the resulting system governs the motion within both the regular and PML domains. To this end, equations (2.17a-2.17c) must first be Fourier-transformed, then stretched, and finally inverted back into the time-domain for transient implementations. Within the regular domain, the stretched equations reduce, by construction of the stretching function ε_s, to the original, undisturbed, system of governing equations.

2.2.1 In the frequency-domain

First, the equilibrium, constitutive, and kinematic equations (2.17a-2.17c) are Fourier-transformed into the frequency-domain, to obtain

$$\mathbf{div}\, \hat{\mathcal{S}}^T + \hat{\mathbf{f}} = -\omega^2 \rho \hat{\mathbf{u}}, \tag{2.19a}$$

$$\hat{\mathcal{S}} = \mathcal{C} : \hat{\mathcal{E}}, \tag{2.19b}$$

$$\hat{\mathcal{E}} = \frac{1}{2} \left[\nabla \hat{\mathbf{u}} + (\nabla \hat{\mathbf{u}})^T \right], \tag{2.19c}$$

where a caret $(\hat{\ })$ denotes the Fourier transform of the subtended function. In deriving (2.19a), we assumed initially silent conditions for the displacement field. Moreover, implicit in the above expressions is the spatial and frequency dependence of the displacement vector, stress, and strain tensors. Next, we introduce the coordinate-stretched form for each coordinate,

$$\tilde{s} = \int_0^s \varepsilon_s(s')ds', \qquad \varepsilon_s(s,\omega) = \alpha_s(s) + \frac{\beta_s(s)}{i\omega}, \qquad s = x, y. \tag{2.20}$$

The stretching is applied first to the equations of motion (2.19a) by replacing x and y with the stretched coordinates $\tilde{x}$ and $\tilde{y}$; to clarify, we make use of unabridged notation:

$$\frac{\partial \hat{\sigma}_{xx}}{\partial \tilde{x}} + \frac{\partial \hat{\sigma}_{yx}}{\partial \tilde{y}} + \hat{f}_x = -\omega^2 \rho \hat{u}_x, \tag{2.21a}$$

$$\frac{\partial \hat{\sigma}_{xy}}{\partial \tilde{x}} + \frac{\partial \hat{\sigma}_{yy}}{\partial \tilde{y}} + \hat{f}_y = -\omega^2 \rho \hat{u}_y, \tag{2.21b}$$

where σ_{ij} denotes the stress tensor component in the j direction on the plane whose normal is along i ($\sigma_{ij} = (\mathcal{S})_{ij}$). Making use of (2.7), (2.21) can be written in terms of the non-stretched coordinates as

$$\frac{1}{\varepsilon_x}\frac{\partial \hat{\sigma}_{xx}}{\partial x} + \frac{1}{\varepsilon_y}\frac{\partial \hat{\sigma}_{yx}}{\partial y} + \hat{f}_x = -\omega^2 \rho \hat{u}_x, \tag{2.22a}$$

$$\frac{1}{\varepsilon_x}\frac{\partial \hat{\sigma}_{xy}}{\partial x} + \frac{1}{\varepsilon_y}\frac{\partial \hat{\sigma}_{yy}}{\partial y} + \hat{f}_y = -\omega^2 \rho \hat{u}_y. \tag{2.22b}$$

Next, we multiply both sides of (2.22) by $\varepsilon_x\varepsilon_y$; there results

$$\mathbf{div}\left(\hat{\mathcal{S}}^T \tilde{\Lambda}\right) + \varepsilon_x\varepsilon_y \hat{\mathbf{f}} = -\omega^2 \rho \varepsilon_x \varepsilon_y \hat{\mathbf{u}}, \tag{2.23}$$

in which the tensor $\tilde{\Lambda}$ is defined as (the definition is identical to that used in [19])

$$\tilde{\Lambda} = \begin{bmatrix} \varepsilon_y & 0 \\ 0 & \varepsilon_x, \end{bmatrix} = \begin{bmatrix} \alpha_y & 0 \\ 0 & \alpha_x \end{bmatrix} + \frac{1}{i\omega}\begin{bmatrix} \beta_y & 0 \\ 0 & \beta_x \end{bmatrix} = \tilde{\Lambda}_e + \frac{1}{i\omega}\tilde{\Lambda}_p, \tag{2.24}$$

and the subscripts "e" and "p" refer to attenuation functions associated with evanescent and propagating waves, respectively. In the regular domain, $\tilde{\Lambda}_e$ reduces to the identity tensor, whereas $\tilde{\Lambda}_p$ vanishes identically. After substituting (2.24) and (2.20) into (2.23), rearranging and grouping like-terms, there results

$$\begin{aligned}\mathbf{div}\left(\hat{\mathbb{S}}^T\tilde{\Lambda}_e + \frac{1}{i\omega}\hat{\mathbb{S}}^T\tilde{\Lambda}_p\right) + \left[a\hat{\mathbf{f}} + \frac{b}{i\omega}\hat{\mathbf{f}} + \frac{c}{(i\omega)^2}\hat{\mathbf{f}}\right]& \\ = \rho\left[(i\omega)^2 a\hat{\mathbf{u}} + i\omega b\hat{\mathbf{u}} + c\hat{\mathbf{u}}\right],& \quad (2.25)\end{aligned}$$

where

$$a = \alpha_x\alpha_y, \qquad b = \alpha_x\beta_y + \alpha_y\beta_x, \qquad c = \beta_x\beta_y. \tag{2.26}$$

We note that, within the regular domain, $a \equiv 1, b \equiv 0, c \equiv 0$, and since the body forces $\mathbf{f}$ are non-vanishing only within the regular domain, (2.25) reduces further to

$$\mathbf{div}\left(\hat{\mathbb{S}}^T\tilde{\Lambda}_e + \frac{1}{i\omega}\hat{\mathbb{S}}^T\tilde{\Lambda}_p\right) + a\hat{\mathbf{f}} = \rho\left[(i\omega)^2 a\hat{\mathbf{u}} + i\omega b\hat{\mathbf{u}} + c\hat{\mathbf{u}}\right]. \tag{2.27}$$

Similarly, we apply complex coordinate-stretching to the kinematic equation (2.19c); there results

$$\hat{\mathcal{E}} = \frac{1}{2}\left\{(\nabla\hat{\mathbf{u}})\begin{bmatrix}\frac{1}{\varepsilon_x} & 0\\ 0 & \frac{1}{\varepsilon_y}\end{bmatrix} + \begin{bmatrix}\frac{1}{\varepsilon_x} & 0\\ 0 & \frac{1}{\varepsilon_y}\end{bmatrix}(\nabla\hat{\mathbf{u}})^T\right\}. \tag{2.28}$$

Next, we pre-multiply (2.28) by $i\omega\varepsilon_x\varepsilon_y$ to obtain

$$i\omega\varepsilon_x\varepsilon_y\hat{\mathcal{E}} = \frac{1}{2}i\omega\left[(\nabla\hat{\mathbf{u}})\tilde{\Lambda} + \tilde{\Lambda}(\nabla\hat{\mathbf{u}})^T\right], \tag{2.29}$$

where the stretching tensor $\tilde{\Lambda}$ is defined in (2.24). Substituting (2.24) and (2.20) into (2.29), rearranging and grouping like-terms, results in

$$\begin{aligned} & i\omega a\hat{\mathcal{E}} + b\hat{\mathcal{E}} + \frac{c}{i\omega}\hat{\mathcal{E}} \\ & \qquad = \frac{1}{2} i\omega \left[(\nabla\hat{\mathbf{u}})\tilde{\Lambda}_e + \tilde{\Lambda}_e(\nabla\hat{\mathbf{u}})^T \right] + \frac{1}{2}\left[(\nabla\hat{\mathbf{u}})\tilde{\Lambda}_p + \tilde{\Lambda}_p(\nabla\hat{\mathbf{u}})^T \right], \end{aligned} \tag{2.30}$$

where a, b, and c are defined in (2.26). Equations (2.27), (2.19b), and (2.30), constitute the stretched form of the governing frequency-domain equations of the unsplit-field PML formulation:

$$\mathbf{div}\left(\hat{\mathcal{S}}^T\tilde{\Lambda}_e + \frac{1}{i\omega}\hat{\mathcal{S}}^T\tilde{\Lambda}_p \right) + a\hat{\mathbf{f}} = \rho\left[(i\omega)^2 a\hat{\mathbf{u}} + i\omega b\hat{\mathbf{u}} + c\hat{\mathbf{u}} \right], \tag{2.31a}$$

$$\hat{\mathcal{S}} = \mathcal{C} : \hat{\mathcal{E}}, \tag{2.31b}$$

$$\begin{aligned} & i\omega a\hat{\mathcal{E}} + b\hat{\mathcal{E}} + \frac{c}{i\omega}\hat{\mathcal{E}} \\ & \qquad = \frac{1}{2} i\omega \left[(\nabla\hat{\mathbf{u}})\tilde{\Lambda}_e + \tilde{\Lambda}_e(\nabla\hat{\mathbf{u}})^T \right] + \frac{1}{2}\left[(\nabla\hat{\mathbf{u}})\tilde{\Lambda}_p + \tilde{\Lambda}_p(\nabla\hat{\mathbf{u}})^T \right]. \end{aligned} \tag{2.31c}$$

We note that the operation in (2.29) is not unique; for example, one could pre- and post-multiply (2.28) by $i\omega\Lambda^{-T}$ and Λ^{-1} similarly to [19], respectively, to obtain

$$i\omega\Lambda^{-T}\hat{\mathcal{E}}\Lambda^{-1} = \frac{1}{2} i\omega \left[\Lambda^{-T}(\nabla\hat{\mathbf{u}}) + (\nabla\hat{\mathbf{u}})^T\Lambda^{-1} \right], \tag{2.32}$$

where

$$\Lambda^{-1} = \begin{bmatrix} \varepsilon_x & 0 \\ 0 & \varepsilon_y \end{bmatrix} = \begin{bmatrix} \alpha_x & 0 \\ 0 & \alpha_y \end{bmatrix} + \frac{1}{i\omega}\begin{bmatrix} \beta_x & 0 \\ 0 & \beta_y \end{bmatrix} = \Lambda_e + \frac{1}{i\omega}\Lambda_p. \tag{2.33}$$

Using the latter definition results in

$$\begin{aligned} & i\omega\Lambda_e^T\hat{\mathcal{E}}\Lambda_e + \Lambda_e^T\hat{\mathcal{E}}\Lambda_p + \Lambda_p^T\hat{\mathcal{E}}\Lambda_e + \frac{1}{i\omega}\Lambda_p^T\hat{\mathcal{E}}\Lambda_p \\ & \qquad = \frac{1}{2}\left[\Lambda_p^T(\nabla\hat{\mathbf{u}}) + (\nabla\hat{\mathbf{u}})^T\Lambda_p \right] + \frac{1}{2} i\omega \left[\Lambda_e^T(\nabla\hat{\mathbf{u}}) + (\nabla\hat{\mathbf{u}})^T\Lambda_e \right], \end{aligned} \tag{2.34}$$

which differs considerably from (2.30). Use of (2.30) instead of (2.34) as the stretched kinematic condition entails advantages: specifically, the consistent stretching of the equilibrium and kinematic equations (both multiplied by $\varepsilon_x \varepsilon_y$), yields symmetric coefficients. Thus, the resulting semi-discrete form becomes fully-symmetric, by contrast to the non-symmetric form resulting from (2.34).

2.2.2 In the time-domain

Next, we are interested in inverting the stretched frequency-domain equations back into the time-domain. To aid in the development, we make use of the following Fourier transform valid for any function $g(t)$ satisfying the usual requirements:

$$\mathcal{F}^{-1}\left[\frac{\hat{g}(\omega)}{i\omega}\right] = \int_0^t g(\tau)\, d\tau, \tag{2.35}$$

where $\mathcal{F}^{-1}$ denotes the inverse Fourier operator[1]. With the aid of (2.35), the inverse Fourier transform of (2.31), written for both the regular and PML

---

[1] In general, $\mathcal{F}^{-1}\left[\frac{\hat{g}(\omega)}{i\omega}\right] = \int_0^t g(\tau) d\tau - \pi \hat{g}(0)\delta(\omega)$, but, it can be shown that since, by construction, the overall development excludes $\omega = 0$, the inverse transform reduces to (2.35).

domains, become:

$$\mathbf{div}\left[\mathcal{S}^T\tilde{\Lambda}_e + \left(\int_0^t \mathcal{S}^T d\tau\right)\tilde{\Lambda}_p\right] + a\mathbf{f} = \rho\left(a\ddot{\mathbf{u}} + b\dot{\mathbf{u}} + c\mathbf{u}\right), \tag{2.36a}$$

$$\mathcal{S} = \mathcal{C} : \mathcal{E}, \tag{2.36b}$$

$$\begin{aligned} a\dot{\mathcal{E}} + b\mathcal{E} + c\left(\int_0^t \mathcal{E} d\tau\right) \\ = \frac{1}{2}\left[(\nabla\dot{\mathbf{u}})\tilde{\Lambda}_e + \tilde{\Lambda}_e(\nabla\dot{\mathbf{u}})^T + (\nabla\mathbf{u})\tilde{\Lambda}_p + \tilde{\Lambda}_p(\nabla\mathbf{u})^T\right]. \end{aligned} \tag{2.36c}$$

Next, we introduce auxiliary variables $\mathbf{S}(\mathbf{x},t)$ and $\mathbf{E}(\mathbf{x},t)$, similar to what we had done in earlier work, e.g. [90], which physically represent stress and strain memories or histories, defined as

$$\mathbf{S}(\mathbf{x},t) = \int_0^t \mathcal{S}(\mathbf{x},\tau)d\tau, \quad \mathbf{E}(\mathbf{x},t) = \int_0^t \mathcal{E}(\mathbf{x},\tau)d\tau. \tag{2.37}$$

Clearly,

$$\dot{\mathbf{S}}(\mathbf{x},t) = \mathcal{S}(\mathbf{x},t), \tag{2.38a}$$

$$\ddot{\mathbf{S}}(\mathbf{x},t) = \dot{\mathcal{S}}(\mathbf{x},t), \tag{2.38b}$$

$$\dot{\mathbf{E}}(\mathbf{x},t) = \mathcal{E}(\mathbf{x},t), \tag{2.38c}$$

$$\ddot{\mathbf{E}}(\mathbf{x},t) = \dot{\mathcal{E}}(\mathbf{x},t). \tag{2.38d}$$

Thus, substituting (2.37) and (2.38) into (2.36) yields the time-domain equations of the unsplit-field PML formulation

$$\mathbf{div}\left(\dot{\mathbf{S}}^T\tilde{\Lambda}_e + \mathbf{S}^T\tilde{\Lambda}_p\right) + a\mathbf{f} = \rho\left(a\ddot{\mathbf{u}} + b\dot{\mathbf{u}} + c\mathbf{u}\right), \tag{2.39a}$$

$$\dot{\mathbf{S}} = \mathcal{C} : \dot{\mathbf{E}}, \tag{2.39b}$$

$$a\ddot{\mathbf{E}} + b\dot{\mathbf{E}} + c\mathbf{E} = \frac{1}{2}\left[(\nabla\dot{\mathbf{u}})\tilde{\Lambda}_e + \tilde{\Lambda}_e(\nabla\dot{\mathbf{u}})^T + (\nabla\mathbf{u})\tilde{\Lambda}_p + \tilde{\Lambda}_p(\nabla\mathbf{u})^T\right]. \tag{2.39c}$$

2.2.3 Mixed finite element implementation

Owing to the complexity of (2.39), one could not conceivably reduce the set (2.39) to a single unknown field, as it is routinely done in displacement-based interior elastodynamics problems where there is no PML involved. Here, we propose a fully-mixed method approach, whereby we retain both displacements and stresses (or, more appropriately, stress histories) as unknowns. To this end, we introduce the constitutive law (2.39b) into the kinematic condition (2.39c), to arrive at

$$\mathbf{div}\left(\dot{\mathbf{S}}^T\tilde{\Lambda}_e + \mathbf{S}^T\tilde{\Lambda}_p\right) + a\mathbf{f} = \rho\left(a\ddot{\mathbf{u}} + b\dot{\mathbf{u}} + c\mathbf{u}\right), \tag{2.40a}$$

$$\begin{aligned}\mathcal{D}:\Big(a\ddot{\mathbf{S}} + b\dot{\mathbf{S}} + c\mathbf{S}\Big) \\ = \frac{1}{2}\left[(\nabla\dot{\mathbf{u}})\tilde{\Lambda}_e + \tilde{\Lambda}_e(\nabla\dot{\mathbf{u}})^T + (\nabla\mathbf{u})\tilde{\Lambda}_p + \tilde{\Lambda}_p(\nabla\mathbf{u})^T\right],\end{aligned} \tag{2.40b}$$

where $\mathcal{D}$ denotes the compliance tensor ($\mathbf{E} = \mathcal{D}:\mathbf{S}$).

Consider next the half-plane problem depicted in Fig. 2.3(d). Let $\Omega^{\mathrm{RD}} \cup \Omega^{\mathrm{PML}} = \Omega \subset \mathbb{R}^2$ denote the region occupied by the elastic body (Ω^{RD})[2], surrounded on three of its sides by the PML buffer zone (Ω^{PML}). Ω is bounded by $\Gamma = \Gamma_D \cup \Gamma_N$, where $\Gamma_D \cap \Gamma_N = \emptyset$, and $\Gamma_D \equiv \Gamma_D^{\mathrm{PML}}$, $\Gamma_N = \Gamma_N^{\mathrm{RD}} \cup \Gamma_N^{\mathrm{PML}}$. Moreover, let $\mathsf{J} = (0, T)$ denote the time interval of interest.

Then, we require that (2.40) hold in $\Omega \times \mathsf{J}$, subject to the following

---

[2] RD stands for Regular Domain.

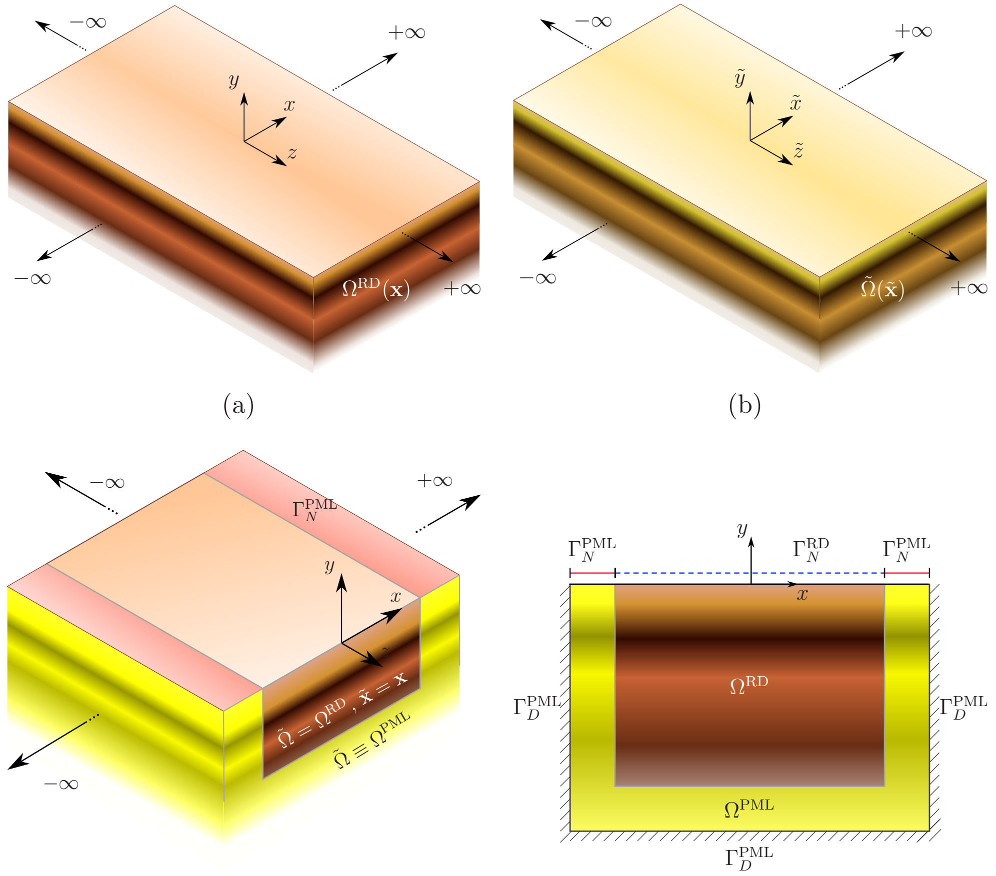

(a)

(b)

(c)

(d)

Figure 2.3: Two-dimensional prototype: (a) physical model; (b) model after the application of complex coordinate-stretching; (c) model after truncation; (d) computational model

boundary and initial conditions:

$$\mathbf{u}(\mathbf{x},t) = \mathbf{0} \qquad \text{on } \Gamma_D^{\mathrm{PML}} \times \mathsf{J}, \tag{2.41a}$$

$$(\dot{\mathbf{S}}^T\tilde{\Lambda}_e + \mathbf{S}^T\tilde{\Lambda}_p)\mathbf{n} = \mathbf{0} \qquad \text{on } \Gamma_N^{\mathrm{PML}} \times \mathsf{J}, \tag{2.41b}$$

$$\dot{\mathbf{S}}(\mathbf{x},t)^T\mathbf{n} = \boldsymbol{g}_n(\mathbf{x},t) \qquad \text{on } \Gamma_N^{\mathrm{RD}} \times \mathsf{J}, \tag{2.41c}$$

$$\mathbf{u}(\mathbf{x},0) = \mathbf{0}, \quad \dot{\mathbf{u}}(\mathbf{x},0) = \mathbf{0} \qquad \text{in } \Omega, \tag{2.41d}$$

$$\mathbf{S}(\mathbf{x},0) = \mathbf{0}, \quad \dot{\mathbf{S}}(\mathbf{x},0) = \mathbf{0} \qquad \text{in } \Omega, \tag{2.41e}$$

where $\boldsymbol{g}_n$ denotes prescribed tractions on Γ_N^{RD}. Equations (2.40-2.41) represent the initial-boundary-value-problem (IBVP) in the PML-truncated semi-infinite domain for the plane-strain case.

We seek next the weak form, in the Galerkin sense, corresponding to the strong form (2.40-2.41). To this end, and for notational clarity, we introduce the symbols representing functional spaces we intend to use for scalar- (v), vector- ($\mathbf{v}$), and tensor-valued ($\mathcal{A}$) functions:

$$L^2(\Omega) = \left\{ v : \int_\Omega |v|^2 d\mathbf{x} < \infty \right\}, \tag{2.42a}$$

$$\mathcal{L}^2(\Omega) = \left\{ \mathcal{A} : \mathcal{A} \in (L^2(\Omega))^{2\times 2} \right\}, \tag{2.42b}$$

$$H^1(\Omega) = \left\{ v : \int_\Omega \left(|v|^2 + |\nabla v|^2 \right) d\mathbf{x} < \infty \right\}, \tag{2.42c}$$

$$\mathbf{H}^1(\Omega) = \left\{ \mathbf{v} : \mathbf{v} \in (H^1(\Omega))^2 \right\}. \tag{2.42d}$$

As discussed in the introduction, there are two possible variational forms one could derive for the mixed problem at hand. The only difference between the two possible formulations arises from the judicious application of integration by parts, which results in distinctly different regularity requirements for the test and trial functions between the two formulations [32]. We take inner products of the equations (2.40) with test functions $\mathbf{w}(\mathbf{x})$ and $\mathbf{T}(\mathbf{x})$, respectively, residing in appropriate spaces, and then integrate over the entire computational domain Ω. In a first variational form, the equilibrium equation (2.40a) is not operated on by integration by parts, whereas (2.40b) is. By contrast, in a second variational form, integration by parts is applied to the equilibrium equation (2.40a). Here, we prefer the latter approach since it requires less regularity on the stresses. Thus, the weak form of (2.40) can be stated as: find $\mathbf{u} \in \mathbf{H}^1(\Omega) \times \mathsf{J}$ satisfying $\mathbf{u}|_{\Gamma_D^{\text{PML}}} = \mathbf{0}$, and $\mathbf{S} \in \mathcal{L}^2(\Omega) \times \mathsf{J}$, such that the following equations are satisfied for all $\mathbf{w} \in \mathbf{H}^1(\Omega)$ satisfying $\mathbf{w}|_{\Gamma_D} = \mathbf{0}$ and $\mathbf{T} \in \mathcal{L}^2(\Omega)$:

$$\begin{aligned}\int_\Omega \nabla\mathbf{w} : \left(\dot{\mathbf{S}}^T\tilde{\Lambda}_e + \mathbf{S}^T\tilde{\Lambda}_p\right)\,\mathrm{d}\Omega &+ \int_\Omega \mathbf{w}\cdot\rho\left(a\ddot{\mathbf{u}} + b\dot{\mathbf{u}} + c\mathbf{u}\right)\,\mathrm{d}\Omega \\ &= \int_{\Gamma_N} \mathbf{w}\cdot\left(\dot{\mathbf{S}}^T\tilde{\Lambda}_e + \mathbf{S}^T\tilde{\Lambda}_p\right)\mathbf{n}\,\mathrm{d}\Gamma + \int_\Omega \mathbf{w}\cdot a\mathbf{f}\,\mathrm{d}\Omega,\end{aligned} \tag{2.43a}$$

$$\begin{aligned}\int_\Omega \mathbf{T} : &\left[\mathcal{D} : \left(a\ddot{\mathbf{S}} + b\dot{\mathbf{S}} + c\mathbf{S}\right)\right]\,\mathrm{d}\Omega \\ &= \frac{1}{2}\int_\Omega \mathbf{T} : \left[(\nabla\dot{\mathbf{u}})\tilde{\Lambda}_e + \tilde{\Lambda}_e(\nabla\dot{\mathbf{u}})^T + (\nabla\mathbf{u})\tilde{\Lambda}_p + \tilde{\Lambda}_p(\nabla\mathbf{u})^T\right]\,\mathrm{d}\Omega.\end{aligned} \tag{2.43b}$$

For the mixed finite element implementation of the variational form (2.43), both $\mathbf{u}(\mathbf{x}, t)$ and $\mathbf{S}(\mathbf{x}, t)$ are treated as independent variables that need to be approximated separately. We introduce

$$\boldsymbol{\Xi}_r^h = \left\{\mathbf{q} \in \mathbf{H}^1(\Omega),\ \mathbf{q}|_K \in (Q_r(K))^2,\ \forall K \in \mathcal{K}_h\right\}, \tag{2.44a}$$

$$\boldsymbol{\Upsilon}_r^h = \left\{\mathcal{A} \in \mathcal{L}^2(\Omega),\ \mathcal{A}|_K \in (Q_r(K))^{2\times 2},\ \forall K \in \mathcal{K}_h\right\}, \tag{2.44b}$$

where $Q_r(K)$ is a polynomial of degree at most r on K. $\mathcal{K}_h$ is a partition of Ω into non-overlapping *triangles* or *quadrilaterals*. Note that $\boldsymbol{\Xi}_r^h \subset \mathbf{H}^1(\Omega)$ and $\boldsymbol{\Upsilon}_r^h \subset \mathcal{L}^2(\Omega)$. Let the basis functions in $\boldsymbol{\Xi}_r^h$ and $\boldsymbol{\Upsilon}_r^h$ be denoted by $\boldsymbol{\Phi}$ and $\boldsymbol{\Psi}$, respectively. The trial functions $\mathbf{u}_h \in \boldsymbol{\Xi}_r^h \times \mathsf{J}$ and $\mathbf{S}_h \in \boldsymbol{\Upsilon}_r^h \times \mathsf{J}$ are spatially discretized as

$$\mathbf{u}(\mathbf{x},t) \cong \mathbf{u}_h(\mathbf{x},t) = \begin{bmatrix} \boldsymbol{\Phi}^T(\mathbf{x})\mathbf{u}_x(t) \\ \boldsymbol{\Phi}^T(\mathbf{x})\mathbf{u}_y(t) \end{bmatrix}, \tag{2.45a}$$

$$\mathbf{S}(\mathbf{x},t) \cong \mathbf{S}_h(\mathbf{x},t) = \begin{bmatrix} \boldsymbol{\Psi}^T(\mathbf{x})\mathbf{S}_{xx}(t) & \boldsymbol{\Psi}^T(\mathbf{x})\mathbf{S}_{xy}(t) \\ \boldsymbol{\Psi}^T(\mathbf{x})\mathbf{S}_{yx}(t) & \boldsymbol{\Psi}^T(\mathbf{x})\mathbf{S}_{yy}(t) \end{bmatrix}. \tag{2.45b}$$

Similarly, the test functions $\mathbf{w} \in \boldsymbol{\Xi}_r^h$ and $\mathbf{T} \in \boldsymbol{\Upsilon}_r^h$ are expressed as

$$\mathbf{w}(\mathbf{x}) \cong \mathbf{w}_h(\mathbf{x}) = \begin{bmatrix} \mathbf{w}_x^T\boldsymbol{\Phi}(\mathbf{x}) \\ \mathbf{w}_y^T\boldsymbol{\Phi}(\mathbf{x}) \end{bmatrix}, \tag{2.46a}$$

$$\mathbf{T}(\mathbf{x}) \cong \mathbf{T}_h(\mathbf{x}) = \begin{bmatrix} \mathbf{T}_{xx}^T\boldsymbol{\Psi}(\mathbf{x}) & \mathbf{T}_{xy}^T\boldsymbol{\Psi}(\mathbf{x}) \\ \mathbf{T}_{yx}^T\boldsymbol{\Psi}(\mathbf{x}) & \mathbf{T}_{yy}^T\boldsymbol{\Psi}(\mathbf{x}) \end{bmatrix}. \tag{2.46b}$$

To reduce notational congestion, we henceforth drop the time and space dependencies. By introducing the symmetry of the stress tensor ($\mathcal{S} = \mathcal{S}^T$), we obtain the following *semi-discrete form*

$$\mathbf{M}\ddot{\mathbf{d}} + \mathbf{C}\dot{\mathbf{d}} + \mathbf{K}\mathbf{d} = \mathbf{F}, \tag{2.47}$$

where the system matrices $\mathbf{M}$, $\mathbf{C}$, $\mathbf{K}$, and the system vectors $\mathbf{d}$ and $\mathbf{F}$ are defined as

$$\mathbf{M} = \begin{bmatrix} \mathbf{M}_a & \mathbf{0} & \mathbf{0} & \mathbf{0} & \mathbf{0} \\ & \mathbf{M}_a & \mathbf{0} & \mathbf{0} & \mathbf{0} \\ & & -\mathbf{N}_a & \mathbf{Z}_a & \mathbf{0} \\ & sym & & -\mathbf{N}_a & \mathbf{0} \\ & & & & -\mathbf{G}_a \end{bmatrix}, \tag{2.48a}$$

$$\mathbf{C} = \begin{bmatrix} \mathbf{M}_b & \mathbf{0} & \mathbf{A}_{yx} & \mathbf{0} & \mathbf{A}_{xy} \\ & \mathbf{M}_b & \mathbf{0} & \mathbf{A}_{xy} & \mathbf{A}_{yx} \\ & & -\mathbf{N}_b & \mathbf{Z}_b & \mathbf{0} \\ & sym & & -\mathbf{N}_b & \mathbf{0} \\ & & & & -\mathbf{G}_b \end{bmatrix}, \tag{2.48b}$$

$$\mathbf{K} = \begin{bmatrix} \mathbf{M}_c & \mathbf{0} & \mathbf{B}_{yx} & \mathbf{0} & \mathbf{B}_{xy} \\ & \mathbf{M}_c & \mathbf{0} & \mathbf{B}_{xy} & \mathbf{B}_{yx} \\ & & -\mathbf{N}_c & \mathbf{Z}_c & \mathbf{0} \\ & sym & & -\mathbf{N}_c & \mathbf{0} \\ & & & & -\mathbf{G}_c \end{bmatrix}, \tag{2.48c}$$

$$\mathbf{d} = [\mathbf{u}_x \; \mathbf{u}_y \; \mathbf{S}_{xx} \; \mathbf{S}_{yy} \; \mathbf{S}_{xy}]^T, \tag{2.48d}$$

$$\mathbf{F} = [\mathbf{f^e}_x \; \mathbf{f^e}_y \; \mathbf{0} \; \mathbf{0} \; \mathbf{0}]^T, \tag{2.48e}$$

where

$$\mathbf{f^e}_x = \int_{\Gamma_N^{\mathrm{RD}}} \mathbf{\Phi} \; g_x(\mathbf{x}, t) \, \mathrm{d}\Gamma + \int_{\Omega} \mathbf{\Phi} a f_x \, \mathrm{d}\Omega, \tag{2.49a}$$

$$\mathbf{f^e}_y = \int_{\Gamma_N^{\mathrm{RD}}} \mathbf{\Phi} \; g_y(\mathbf{x}, t) \, \mathrm{d}\Gamma + \int_{\Omega} \mathbf{\Phi} a f_y \, \mathrm{d}\Omega, \tag{2.49b}$$

and

$$\mathbf{A}_{ij} = \int_\Omega \alpha_i \, \frac{\partial \mathbf{\Phi}}{\partial j} \mathbf{\Psi}^T \, \mathrm{d}\Omega, \qquad i,j = x,y \tag{2.50a}$$

$$\mathbf{B}_{ij} = \int_\Omega \beta_i \, \frac{\partial \mathbf{\Phi}}{\partial j} \mathbf{\Psi}^T \, \mathrm{d}\Omega, \qquad i,j = x,y \tag{2.50b}$$

$$\mathbf{M}_k = \int_\Omega k \, \rho \mathbf{\Phi} \mathbf{\Phi}^T \, \mathrm{d}\Omega, \qquad k = a,b,c \tag{2.50c}$$

$$\mathbf{N}_k = \int_\Omega k \, \frac{\lambda + 2\mu}{4\mu(\lambda + \mu)} \mathbf{\Psi} \mathbf{\Psi}^T \, \mathrm{d}\Omega, \qquad k = a,b,c \tag{2.50d}$$

$$\mathbf{Z}_k = \int_\Omega k \, \frac{\lambda}{4\mu(\lambda + \mu)} \mathbf{\Psi} \mathbf{\Psi}^T \, \mathrm{d}\Omega, \qquad k = a,b,c \tag{2.50e}$$

$$\mathbf{G}_k = \int_\Omega k \, \frac{1}{\mu} \mathbf{\Psi} \mathbf{\Psi}^T \, \mathrm{d}\Omega, \qquad k = a,b,c \tag{2.50f}$$

where a, b and c are defined in (2.26).

We remark that the symmetry of the mass-like, stiffness-like, and damping-like matrices in (2.48) has been preserved owing to the consistent way of stretching; displacements in the equilibrium equation and strains in the kinematic equation were multiplied by the same factor $\varepsilon_x \varepsilon_y$. Though the additional unknowns seem to increase the computational cost, the fully-mixed unsplit-field formulation requires less unknowns when compared to most mixed split-field formulations. Moreover, retaining the symmetry of the system matrices is computationally beneficial.

2.2.4 Time integration

The obtained semi-discrete form (2.47) is second-order in time. To resolve the time integration, we employ the classical Newmark-β scheme [87] (Algorithm 2.1), by, first, making use of the following finite difference formula describing the evolution of the corresponding quantities

$$\mathbf{d}_{n+1} = \mathbf{d}_n + \Delta\mathrm{t}\ \dot{\mathbf{d}}_n + \left(\frac{1}{2} - \beta\right) \Delta\mathrm{t}^2 \ddot{\mathbf{d}}_n + \beta\ \Delta\mathrm{t}^2 \ddot{\mathbf{d}}_{n+1}, \tag{2.51a}$$

$$\dot{\mathbf{d}}_{n+1} = \dot{\mathbf{d}}_n + (1-\gamma)\,\Delta\mathrm{t}\ \ddot{\mathbf{d}}_n + \gamma\ \Delta\mathrm{t}\ \ddot{\mathbf{d}}_{n+1}, \tag{2.51b}$$

where Δt denotes the time step, and subscripts (n) and $(n+1)$ denote current and next time step, respectively (β and γ are the usual Newmark-β parameters). For linear acceleration method, (β, γ) reduce to $(\frac{1}{6}, \frac{1}{2})$, whereas in the case of the constant (average) acceleration method, (β, γ) reduce to $(\frac{1}{4}, \frac{1}{2})$.

Next, after rewriting (2.47) for the $(n+1)$-th time step, and, subsequently, introducing (2.51), there results the following effective system matrix $\{\mathbf{K}^{\mathbf{eff}}\}$, and effective load vector $\{\mathbf{R}^{\mathbf{eff}}\}_{n+1}$

$$\{\mathbf{K}^{\mathbf{eff}}\}\ \ddot{\mathbf{d}}_{n+1} = \{\mathbf{R}^{\mathbf{eff}}\}_{n+1}, \tag{2.52}$$

where

$$\{\mathbf{K}^{\mathbf{eff}}\} = \mathbf{M} + \mathbf{C}\ \gamma\Delta\mathrm{t} + \mathbf{K}\ \beta\Delta\mathrm{t}^2, \tag{2.53a}$$

$$\begin{aligned}\{\mathbf{R}^{\mathbf{eff}}\}_{n+1} = \mathbf{F}_{n+1} - \mathbf{C}\left[\dot{\mathbf{d}}_n + (1-\gamma)\,\Delta\mathrm{t}\ \ddot{\mathbf{d}}_n\right] \\ - \mathbf{K}\left[\mathbf{d}_n + \Delta\mathrm{t}\ \dot{\mathbf{d}}_n + \left(\frac{1}{2} - \beta\right)\Delta\mathrm{t}^2 \ddot{\mathbf{d}}_n\right].\end{aligned} \tag{2.53b}$$

Equation (2.52) allows for the computation of the second-order terms at every $(n+1)$ time step; lower-order terms for the same time step are then recoverable via (2.51). In the numerical experiments that follow we used the average acceleration scheme.

Algorithm 2.1 Direct integration by classical Newmark-β method

```
procedure NEWMARK($nts$)                                ▷ nts: number of time steps
    Assemble $\mathbf{M}$, $\mathbf{C}$ and $\mathbf{K}$
    Set $\mathbf{d}_0$ and $\dot{\mathbf{d}}_0$                                   ▷ initial conditions
    Compute $\ddot{\mathbf{d}}_0$                                           ▷ eq. (2.47)
        $\ddot{\mathbf{d}}_0 = \mathbf{M}^{-1}\left[\mathbf{F}_0 - \mathbf{C}\dot{\mathbf{d}}_0 - \mathbf{K}\mathbf{d}_0\right]; n = -1$
    Set $\beta$ and $\gamma$                                  ▷ integration parameters
    Assemble $\{\mathbf{K}^{\mathbf{eff}}\}$                                     ▷ eq. (2.53a)
    $n \leftarrow 0$
    while $n < nts$ do                   ▷ integration is complete if $n$ is $nts$
        Assemble $\{\mathbf{R}^{\mathbf{eff}}\}_{n+1}$                            ▷ eq. (2.53b)
        Compute $\ddot{\mathbf{d}}_{n+1}$                                    ▷ eq. (2.52)
        Update $\mathbf{d}_{n+1}$ and $\dot{\mathbf{d}}_{n+1}$                         ▷ eq. (2.51)
        Output $\mathbf{d}_{n+1}$                                       ▷ if desired
        $n \leftarrow n + 1$
    end while
end procedure
```

2.2.5 Numerical experiments

To test the accuracy and efficiency of the mixed unsplit-field PML formulation, we discuss next five numerical experiments, involving both homogeneous and arbitrarily heterogeneous hosts. The first example is the simplest: it involves an explosive P-wave source within a homogeneous semi-infinite domain. Examples 2 and 3 involve elongated domains with near-bottom-PML and near-surface wave sources, respectively, that give rise to waves incident at grazing angles, and often result in degrading PML performance [57, 58, 100]. The final two examples, Examples 4 and 5 pertain to heterogeneous domains, one involving a horizontally-layered medium, and the last one implicating an arbitrarily heterogeneous profile.

Beyond comparisons of time histories at select target locations, as a measure of PML performance, we also provide plots of relative time-dependent errors. To obtain these relative errors, we create reference solutions by embedding the computational domain of interest Ω^{RD} within an enlarged domain Ω^{ED} with fixed exterior boundaries. The numerical solution within Ω^{ED} is obtained using a displacement-based formulation, in order to create a solution that is completely independent from the mixed approach discussed herein. We retain the enlarged domain's solution up to times that are prior to the arrival of any waves to Ω^{RD} from the part of the domain that is exterior to Ω^{RD}. We compare the reference and the mixed method solutions only within the regular domain Ω^{RD} ($\subset \Omega^{\mathrm{ED}}$). To define the error metrics, we introduce first the time-dependent L^2 norm of the displacement field over an arbitrary domain Ω as

$$D(t;\Omega) = \left[\int_{\Omega} \mathbf{u}^T(\mathbf{x},t)\mathbf{u}(\mathbf{x},t)\,\mathrm{d}\Omega\right]^{\frac{1}{2}}. \tag{2.54}$$

We define the time-dependent relative error metric $e(t)$ in terms of L^2 norm, normalized with respect to the aforementioned displacement field norm D, as

$$e(t) = \frac{\left\{\int_{\Omega^{\mathrm{RD}}} \left[\mathbf{u}(\mathbf{x},t) - \mathbf{u}_{\mathrm{ED}}(\mathbf{x},t)\right]^T \left[\mathbf{u}(\mathbf{x},t) - \mathbf{u}_{\mathrm{ED}}(\mathbf{x},t)\right]\,\mathrm{d}\Omega\right\}^{\frac{1}{2}}}{\max D(t;\Omega^{\mathrm{ED}})} \times 100. \tag{2.55}$$

As an additional performance metric, we also study the decay of the total energy within the regular domain, along lines similar to the ones discussed by Komatitsch and Martin in [100]. In short, the energy, injected to the domain via the loading, is carried by waves that are absorbed and attenuated within the PML, and, thus, a rapid decay should be expected if the PML is working correctly. The total energy of the system as a function of time is expressed as

$$E_t(t) = \frac{1}{2}\int_{\Omega} \rho(\mathbf{x},t)\left[\dot{\mathbf{u}}^T(\mathbf{x},t)\dot{\mathbf{u}}(\mathbf{x},t)\right] d\Omega + \frac{1}{2}\int_{\Omega}\left[\boldsymbol{\sigma}^T(\mathbf{x},t)\boldsymbol{\epsilon}(\mathbf{x},t)\right] d\Omega, \quad (2.56)$$

where $\dot{\mathbf{u}}$, $\boldsymbol{\sigma}$, and $\boldsymbol{\epsilon}$ are velocity, stress, and strain vectors, respectively. Similarly to $e(t)$, the total energy too is computed only within the regular domain Ω^{RD}.

We note that the loading in two-dimensional media corresponds to infinite-line or strip loads in three dimensions. Therefore, the motion at any given point within the two-dimensional domain is continuosly fed from waves arriving from ever more distant sources. This creates the appearance that the waves never leave the two-dimensional domain. In reality, the amplitudes from distant sources contributing to a point's motion are decreasing, and, at the limit, as time goes to infinity, the motion vanishes everywhere within the two-dimensional domain.

2.2.5.1 Homogeneous media

We consider first a homogeneous half-plane with density $\rho = 2200$ kg/m^3, shear-wave velocity $c_s \simeq 5.81$ m/s, and Poisson ratio $\nu = 0.2$[3]. We use an explosive P-wave source defined as

$$\mathbf{f}(\mathbf{x},t) = \mathrm{T_p}(t)\mathbf{S}_\mathrm{p}(r), \quad (2.57)$$

---

[3] We have used, by design and without loss of generality, low velocities to allow for clearer visual separation of the propagating waves and their reflections.

where $\mathrm{T_p}$ and $\mathbf{S}_\mathrm{p}$ denote the temporal and spatial parts of the loading, respectively. The spatial part is a radial function defined as

$$\mathbf{S}_\mathrm{p}(r) = \begin{cases} \left(1 - \dfrac{r^2}{r_d^2}\right)^3 \left(\dfrac{x - x_c}{r}, \dfrac{y - y_c}{r}\right), & (x, y) \in D_0, \\ 0, & (x, y) \notin D_0, \end{cases} \tag{2.58}$$

where $r = \sqrt{(x - x_c)^2 + (y - y_c)^2}$, and D_0 denotes the source disk of center (x_c, y_c) and radius r_d. For the temporal variation of the load we use a modified Ricker pulse defined as

$$\mathrm{T_p}(t) = \frac{(0.25u^2 - 0.5)e^{-0.25u^2} - 13e^{-13.5}}{0.5 + 13e^{-13.5}} \qquad \text{with } 0 \leq t \leq \frac{6\sqrt{6}}{\omega_r}, \tag{2.59}$$

where

$$u = \omega_r t - 3\sqrt{6}, \tag{2.60}$$

and ω_r denotes the characteristic central circular frequency ($= 2\pi f_r$) of the pulse.

In the simulations, we used a Ricker wavelet with a central frequency $f_r = 4$ Hz, and a peak amplitude of 10 Pa, as depicted in Fig. 2.4. The explosive source radius r_d was set to 0.4m.

Example 1 We reduced, through truncation, a semi-infinite domain to a 10m × 10m computational domain, surrounded on its sides and bottom by a 1m-thick PML, as shown in Fig. 2.5. The explosive source disk's center was placed at 5m below the surface, at the center of the domain. The PML and regular domains were discretized by quadratic elements with an element size

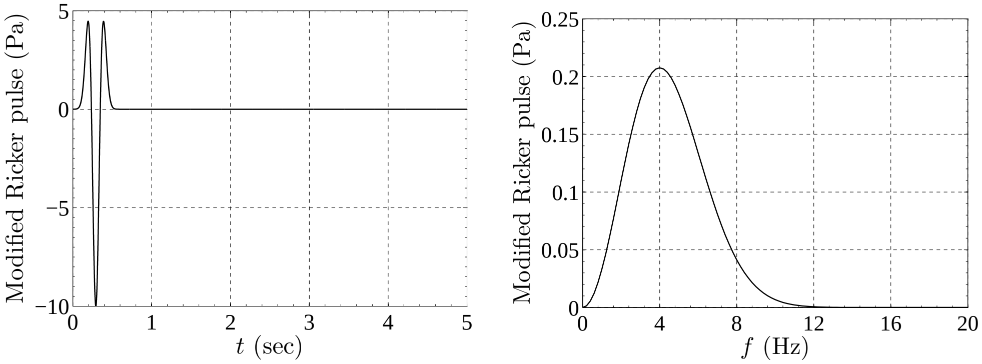

Figure 2.4: Excitation time signal and its Fourier spectrum

of 0.1m, whereas the disk was meshed with 0.05m quadratic elements. The discretization resulted in a 10-cell-thick PML. The reflection coefficient R was set to 10^{-8}. Using a time step of 0.0002s, we let the simulation run for 10s. The time histories of the displacements and stress components are sampled at five locations $sp_i, i = 1 \ldots 5$.

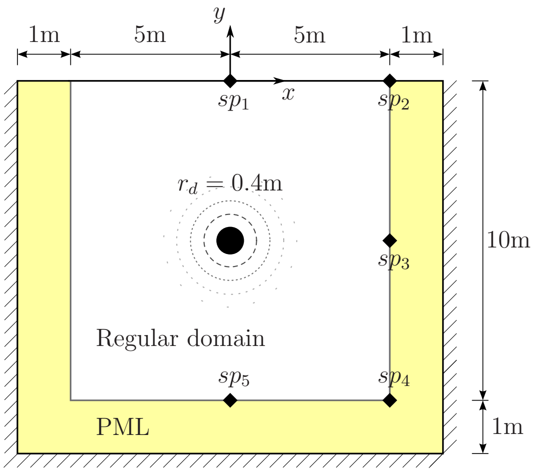

Figure 2.5: A PML-truncated semi-infinite domain in two dimensions subjected to an explosive load at the domain center

In order to assess the validity of the fully-mixed PML formulation, the displacement time histories at the sampling points were compared against the response obtained using an enlarged domain with fixed boundaries and a classical displacement-based plane-strain formulation. The enlarged domain's size (110m × 60m) was defined such that, during the specified time interval of interest, reflections from its fixed exterior boundaries do not travel back and interfere with the wave motion in the computational domain of interest. Figure 2.6 depicts the comparison of the response time histories for u_x and u_y at the various sp_i points. As it can be seen, the agreement is excellent: the PML has effectively absorbed the waves without any reflections. It is apparent from the figures that causality holds (sometimes an issue with PML implementations), and that the response is free of spurious reflections. No numerical instabilities were observed during the total simulation time of 10 seconds (only half the record is shown here), i.e., for $50,000$ time steps.

Figures 2.7 and 2.8 show snapshots of the displacements and stresses taken at two different times: the left column corresponds to, approximately, 0.2s after the wave has impinged upon the free surface, and has also entered the side and bottom PML zones, shown in the figure with solid black lines that are indented with respect to the outer boundary. Notice that there are reflections from the free surface as expected (e.g. local doubling of the displacement amplitudes), and contrast them against the reflection-less side and bottom PML interfaces. The right column corresponds to a later time and clearly shows two wave trains traveling towards the bottom: each wave train

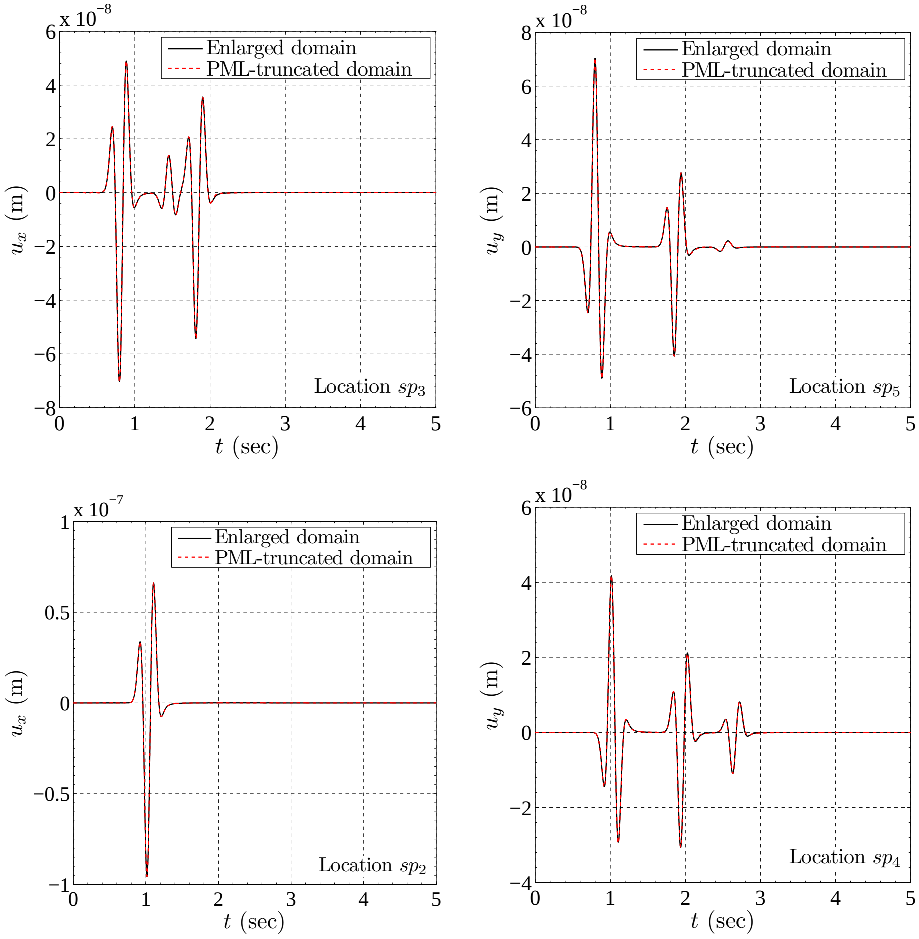

Figure 2.6: Comparison of u_x and u_y time histories between the enlarged and PML-truncated domain solutions at sampling points

features three zones, with each zone corresponding to the amplitude peaks of the Ricker wavelet. Both wave trains (one P and one S) are reflections from the free surface. Again, notice that there are no discernible reflections from the PML interfaces, nor any residual reflections from the fixed external boundaries that could have polluted the interior wave solution.

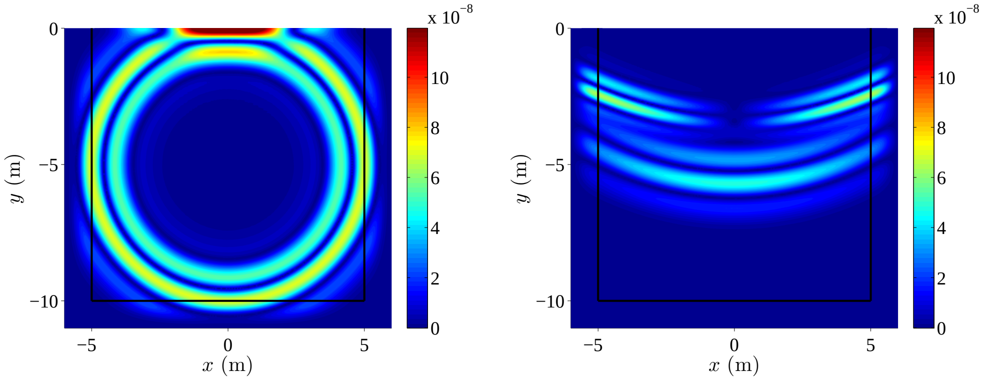

(a) u at $t = 0.8$s (b) u at $t = 1.4$s

Figure 2.7: Snapshots of u using an explosive Ricker pulse source at the center of the domain

Figure 2.9 depicts three different error metrics: Fig. 2.9(a) shows a visual comparison, displaying excellent agreement, between the reference solution and the PML-based solution for the displacement norm defined in (2.54); Fig. 2.9(b) shows the error norm defined in (2.55), which, at all times, is below 0.22%. Figures 2.9(c) and 2.9(d) show the absolute value of the error at two distinct locations, normalized with respect to the absolute value of the peak record value; the error remains below 0.43% at all times.

Next, we study the effect the reflection coefficient R has on the quality

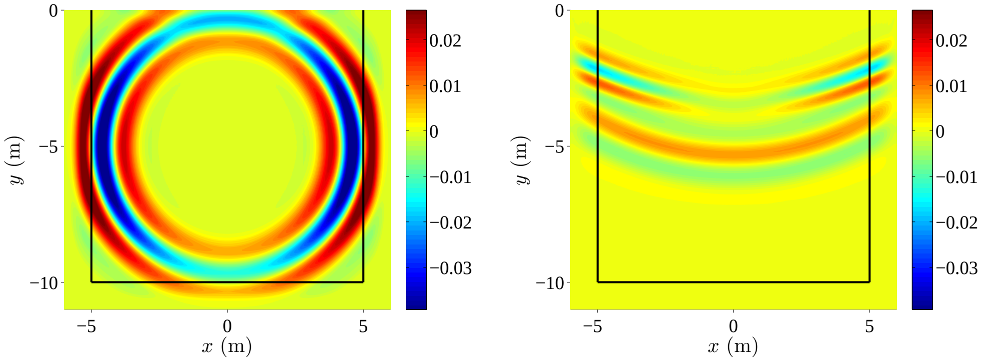

(a) σ_{xx} at $t = 0.8$s (b) σ_{xx} at $t = 1.4$s

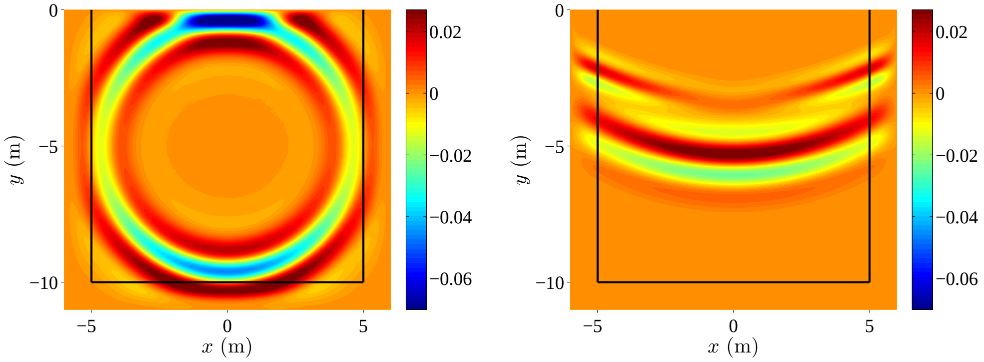

(c) σ_{yy} at $t = 0.8$s (d) σ_{yy} at $t = 1.4$s

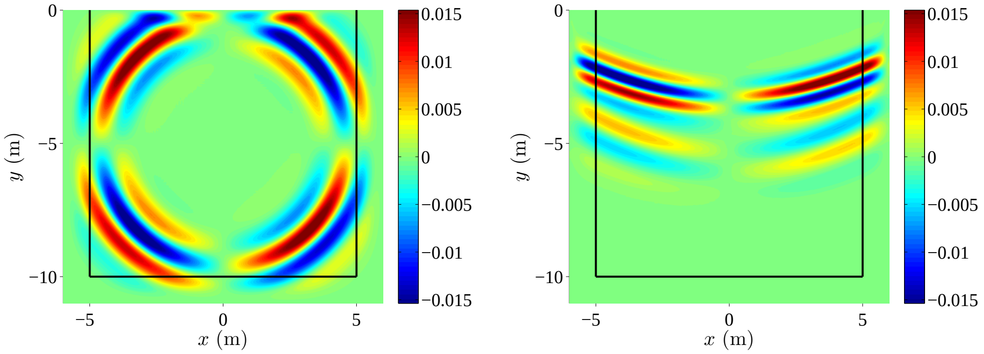

(e) σ_{xy} at $t = 0.8$s (f) σ_{xy} at $t = 1.4$s

Figure 2.8: Snapshots of σ_{xx}, σ_{yy}, and σ_{xy} using an explosive Ricker pulse source at the center of the domain

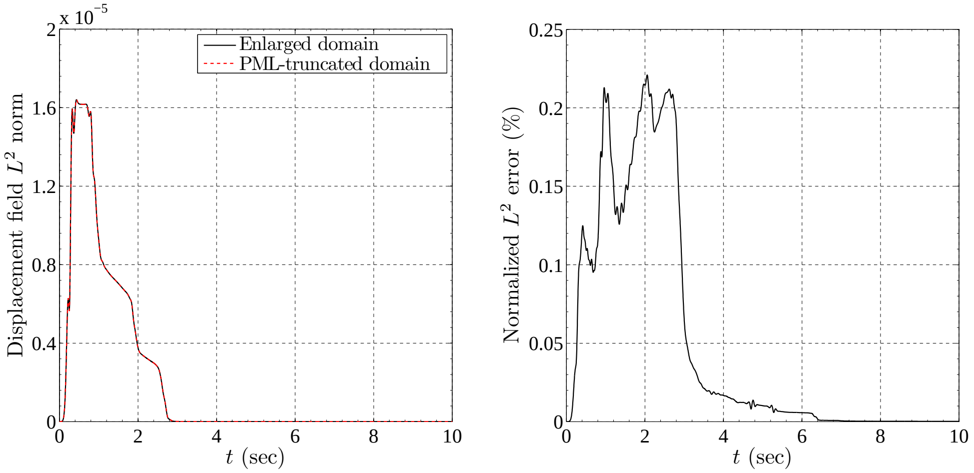

(a) Displacement field norm $D(t; \Omega^{\mathrm{RD}})$ (b) Relative error $e(t)$

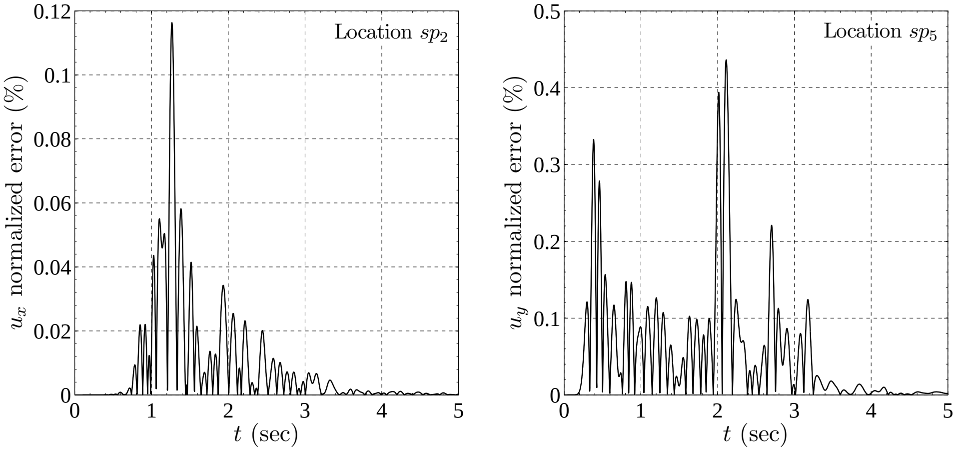

(c) Relative error for u_x at sp_2 (d) Relative error for u_y at sp_5

Figure 2.9: Error metrics for the homogeneous domain excited by an explosive Ricker pulse ($f_r = 4$ Hz) at the center of the domain (Example 1)

of the obtained solutions. To this end, R was varied from 10^{-1} to 10^{-8}, in multiples of 10, and the total energy decay (2.56) was computed for each one of the R values, as a function of time. Figure 2.10 shows the energy decay plotted in standard (left), and semi-log scale (right), the former terminated at 5s, the latter terminated at 10s. Shown on the same figure is the energy decay for all tested R values, as well as the reference decay corresponding to the enlarged domain (recall that this has been obtained using an independent displacement-based formulation). The figure is quite revealing in several ways. First, almost all R values (except for $R = 10^{-1}$) result in similarly sharp decay: after about 2.8 seconds, there is hardly any discernible residual energy left in the domain, since all the waves have traveled out of the domain and have been absorbed by the PML. A closer look, using the semi-log scale, reveals though that R plays a key role in determining the rate the energy decays, with lower R values enforcing more rapid decay. As R increases, the fixed exterior PML boundaries reflect back waves of higher amplitude than those that would have resulted from lower R reflection coefficients, first within the PML and later within the regular domain. Though still of small amplitude, when compared to the peak amplitudes observed in the regular domain, the reflections become amplified as they travel back into the regular domain (this is so by construction), and stand to pollute the solution and slow the energy decay. Thus, lower R values effectively decrease the absorptive capacity of the PML layer.

Secondly, it is worth noting a few characteristic points on the energy

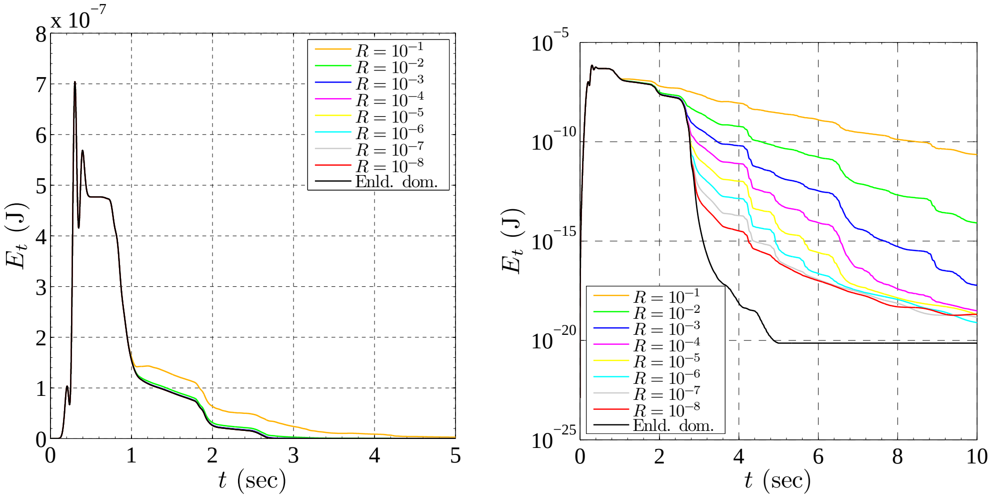

Figure 2.10: Total energy decay inside the regular domain (Example 1)

plots: first, notice on the left plot that the energy, initially, follows closely the maxima and minima of the Ricker wavelet. At about $t = 0.5$s, the P-wave fronts have reached the free surface and the side and bottom PMLs; the first peak of the Ricker wavelet enters the PMLs at about $t = 0.7$s, and the second and largest peak at about $t = 0.8$s, where there is a clear change in the slope of the energy decay curve (left plot). At about $t = 1$s, the last Ricker wavelet peak has been absorbed within the 3 PML zones, and the only remaining energy within the domain is associated with the surface reflections of the original waves (both P and S). Between $t = 1.7$s and $t = 1.9$s the reflections' P-train peaks arrive at the bottom PML and get absorbed, whereas between, approximately, $t = 2.3$s and $t = 2.5$s the reflections' S-train peaks arrive at the bottom PML. The above result in slope changes in the energy decay curve, which can be seen in Fig. 2.10; by about $t = 2.8$s all waves have left the domain.

The energy plot seems to suggest that it is always beneficial to reduce the R coefficient to as small a value as the machine accuracy may permit. However, lower R values introduce sharper PML decay profiles, as it can also be deduced from (2.14). That is, in sharper profiles, most of the wave absorption takes place within a small fraction of the PML length, right next to the PML-regular domain interface. For the absorption to be effective, it is critical that the mesh density within the PML adequately captures the sharp profile, to avoid the accumulation of numerical errors (the situation is similar to the difficulties arising when one attempts to approximate stress singularities with regular and inadequately sized isoparametric elements). In fact, sharper profiles are not only introduced by lower R coefficients, but arise also when *lower* polynomial degrees (m in (2.8)) are chosen, or when *higher* reference velocities are prescribed within the PML (c_p^{ref} in (2.14)). Though a detailed discussion and the necessary parametric study escapes the scope of this dissertation, we remark that we have found linear profiles to be very sharp and should, in general, be avoided, in favor of, at least, quadratic, or preferably, quartic profiles (see also Fig. 2.2).

Notice, lastly, that for R values lower than about 10^{-6} the remaining domain energy is lower than 10^{-12}, or roughly more than 5 orders of magnitude less than the peak domain energy, asserting effective wave absorption.

Example 2 Since, by construction, the PML enforces attenuation only in the direction normal to the PML-regular domain interface, difficulties may arise in simulations of wave motion within elongated domains, where waves may impinge at grazing angles upon the PML interface. The PML will not attenuate waves traveling parallel to the interface, and depending on the ability of the PML mesh to adequately resolve the non-attenuated propagating waves within the PML, the solution in the regular domain stands to be polluted. Such difficulties were reported for the regularly-stretched split-field PML in [57, 58], and resulted in the authors' favoring of an unsplit convolutional CFS-PML. Concurrently, in [100], the authors verified the same findings when they utilized the regularly-stretched split-field PML formulation of Collino and Tsogka [48]. However, in the simulations obtained with the unsplit-field mixed PML, we have not observed such difficulties; while the mixed formulation does have an advantage, we do not believe that the mixed formulation alone is responsible for the lack of spurious reflections. Rather, we iterate that the PML's mesh density is critical in the generation of spurious wave motion, especially in the presence of sharp decay profiles. Again, a careful examination of the relations between attenuation function parameters (degree of polynomial m, parameter β_o) resolves the contradiction. Since β_o is generally defined to be a function of a reference P-wave velocity c_p^{ref}, the reflection coefficient R, and the degree of polynomial m, these parameters cannot be arbitrarily chosen, if a gradual imposition of attenuation is to be attained. Increasing the P-wave velocity c_p^{ref}, lowering the polynomial order m, or decreasing the reflection coefficient R results in sharper attenuation profiles (Fig. 2.2). The faster decay necessitates more elements within the PML to properly sample the sharply-imposed attenuation profile. By contrast, lower velocities, higher polynomial orders, or larger R values, tend to broaden the support of the attenuation profile within the PML, thereby reducing the absorption, and, by and large, the accuracy.

To introduce near grazing-angle waves, we modeled a 30m × 5m computational domain, surrounded on three of its sides by a 2m-thick PML, as shown in Fig. 2.11(a). The explosive source disk was positioned at 4m below the surface and 5m to the right of the left PML interface. The PML and regular domain were discretized similarly to Example 1, and resulted in a 20-cell-thick PML. We used $R = 10^{-8}$, a time step of 0.0002 seconds, and, again, let the simulation run for 10 seconds.

Snapshots of the displacements (u) are shown in Fig. 2.12. As discussed above, and contrary to findings reported by others, there is no evidence of spurious energy leaking back into the regular domain: the PMLs have quite efficiently absorbed the waves[4]. Figure 2.13(a) displays the comparison of displacement field L^2 norms, while, Fig. 2.13(b) shows the normalized relative error $e(t)$ in percent. The peak relative error value is about 0.4% and occurs

---

[4] It has been reported often that spurious energy appears at the tail of the transient phase, and is only observable when the response is capped at a very small fraction ($\sim 0.001\%$) of the peak response amplitude. Modifying the PML parameters has been reported to have an effect on the spurious energy, but parameterization guidelines remain elusive. The CPML and the more recent M-PML both improve the behavior, but the issue is still open.

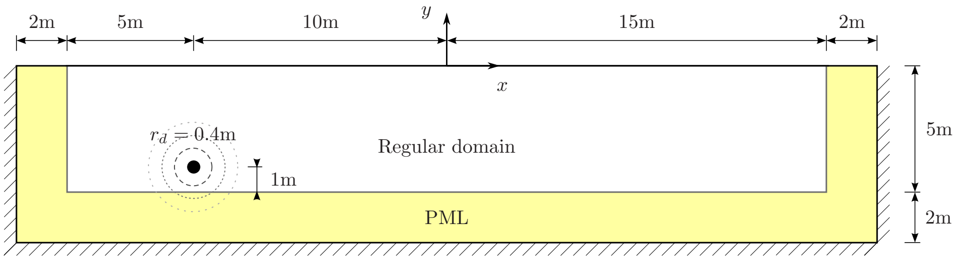

(a) Geometry of Example 2

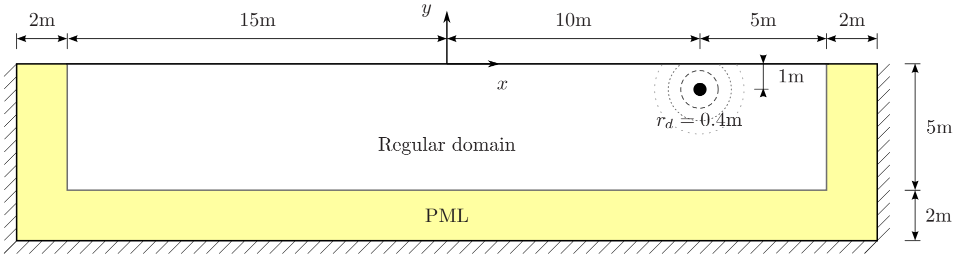

(b) Geometry of Example 3

Figure 2.11: Elongated PML-truncated semi-infinite domains in two dimension subjected to an explosive load

when the P-front reaches the right-side PML interface, causing small reflections (the continuous PML form is reflection-less, but the discrete PML is not). Figures 2.13(c) and 2.13(d) show that the energy decay is more gradual in this case than in Example 1, though the overall behavior is qualitatively similar to the one reported in Example 1. As a consequence of the direction of the propagation, which is mostly parallel to the bottom interface, initially it is only the bottom PML that imposes attenuation. Once the waves reach the right-side PML, the absorption is complete.

Example 3 Prior studies [63, 101] have noted the efficacy of the PML in absorbing surface waves. Using the geometry and discretization of Exam-

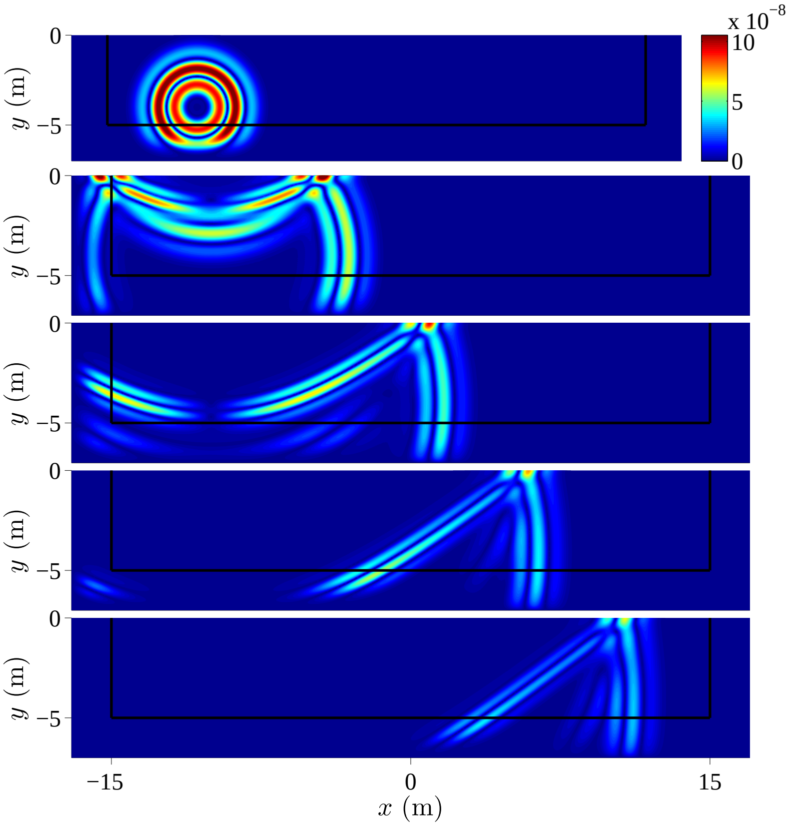

Figure 2.12: Snapshots of u taken at $t = 0.5\text{s}, 1.0\text{s}, 1.5\text{s}, 2.0\text{s}, 2.5\text{s}$ in Example 2, driven by an explosive Ricker wavelet source positioned close to the bottom PML

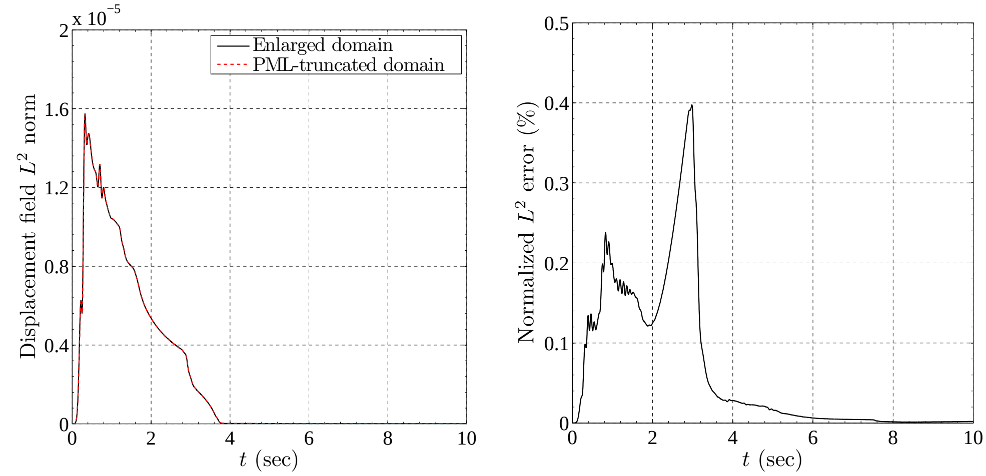

(a) Displacement field norm $D(t;\Omega^{\mathrm{RD}})$ (b) Relative error $e(t)$

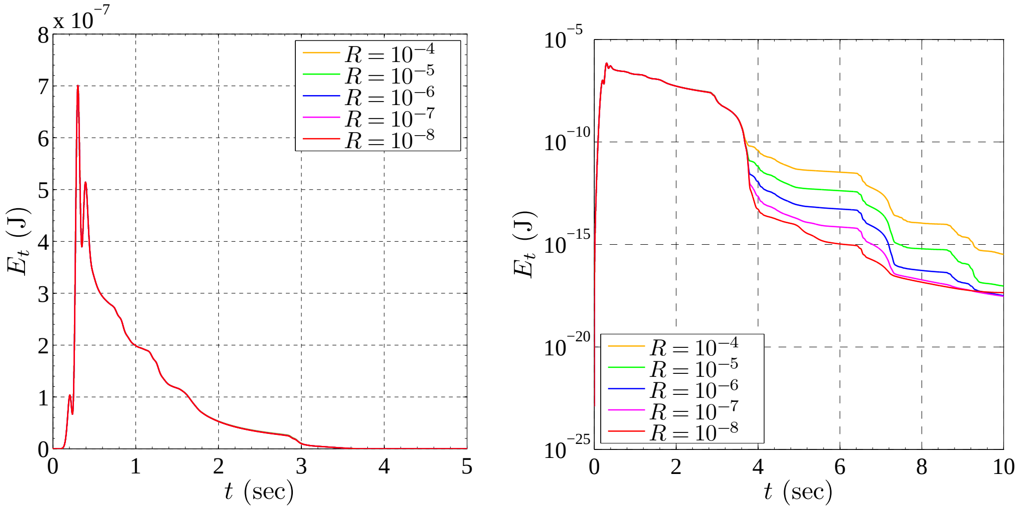

(c) Energy decay - standard scale (d) Energy decay - logarithmic scale

Figure 2.13: Error metrics for the homogeneous elongated domain excited by an explosive Ricker pulse ($f_r = 4$ Hz) located at (−10m, −4m) (Example 2)

ple 2, we relocated the source excitation 1m below the surface, as shown in Fig. 2.11(b) in order to corroborate the findings of previous works, and test the developed formulation with surface waves. Figure 2.14 shows snapshots of the displacement (u). These results are consistent with those of other studies and suggest that the proposed mixed, unsplit-field PML can effectively absorb and attenuate surface waves too. Similar to Example 2, the displacement field L^2 norm and the time-dependent relative error are shown in Fig. 2.15. Although not presented here, the energy decay is gradual for the same reasons as those previously described.

2.2.5.2 Heterogeneous media

To illustrate the performance of the PML in heterogeneous media, we consider next two simulations: first a layered profile, and then an arbitrarily heterogeneous profile with an inclusion. We apply a surface stress load over a region ($-1\text{m} \leq x \leq 1\text{m}$) in both cases. The time signal is a Ricker pulse with a central frequency of $f_r = 4$ Hz and amplitude of 10 Pa (Fig. 2.4). Using a time step of 0.0002 seconds, we let the simulations run for 7 and 10 seconds for the last two examples, respectively.

Example 4 As shown in Fig. 2.16(a), we consider a 20m × 20m layered medium surrounded by 2m-thick PML on its sides and bottom. We define

$$c_s(y) = \begin{cases} \sim 5.81 \text{ m/s}, & \text{for } -6\text{m} \leq y \leq 0\text{m}, \\ \sim 11.62 \text{ m/s}, & \text{for } -14\text{m} \leq y < -6\text{m}, \\ \sim 17.43 \text{ m/s}, & \text{for } -22\text{m} \leq y < -14\text{m}. \end{cases} \tag{2.61}$$

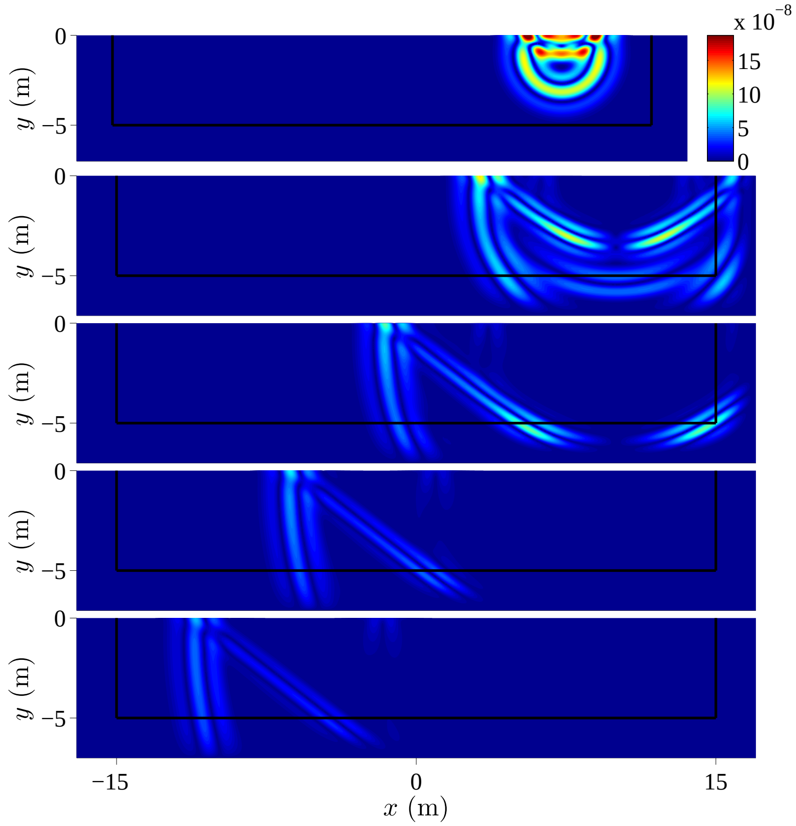

Figure 2.14: Snapshots of u taken at $t = 0.5\text{s}, 1.0\text{s}, 1.5\text{s}, 2.0\text{s}, 2.5\text{s}$ in Example 3 with an explosive near-surface Ricker wavelet source

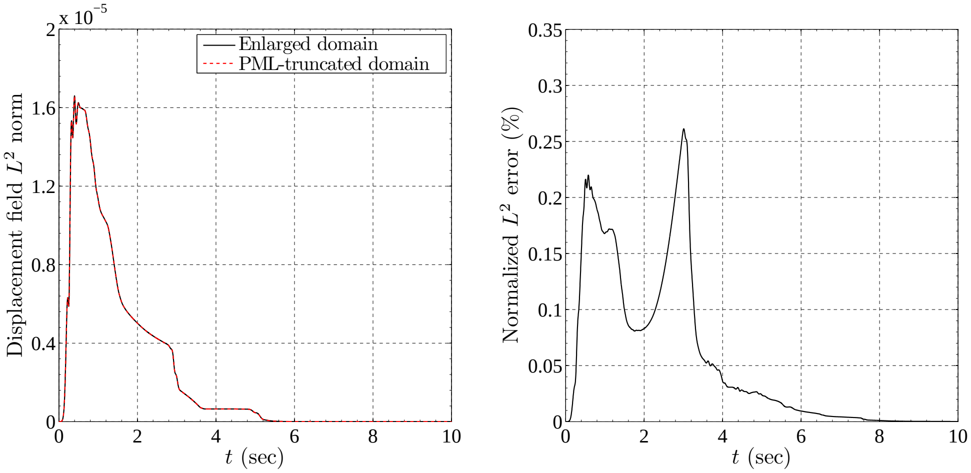

(a) Displacement field norm $D(t;\Omega^{\mathrm{RD}})$

(b) Relative error $e(t)$

Figure 2.15: Error metrics for the homogeneous elongated domain excited by an explosive Ricker pulse ($f_r = 4$ Hz) located at (10m, −1m) (Example 3)

The material interfaces were extended horizontally into the PML, thereby, avoiding sudden material changes at the interface between the PML and the regular domain. The PML and regular domains were discretized by quadratic elements with an element size of 0.1m, whereas in the vicinity of the surface load, the regular domain was meshed with 0.025m-elements. The reflection coefficient R was set to 10^{-8}.

Figure 2.17 shows the snapshots of displacement taken at two different times. The layer boundaries are clearly visible due to reflections at the material interface. However, the critical interface between the regular domain and PML is free of reflections, and the PML formulation handles the interface waves properly. Extending the layer boundaries into the PML preserved the transparency of the PML-regular domain interface to the outgoing waves.

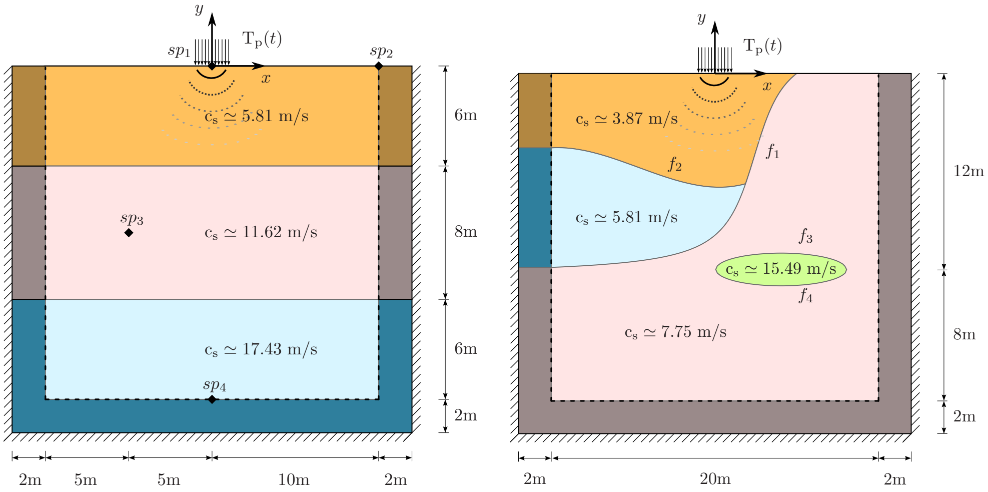

(a) Layered medium

(b) Arbitrarily heterogeneous medium

Figure 2.16: PML-truncated semi-infinite media in two dimensions subjected to surface loads

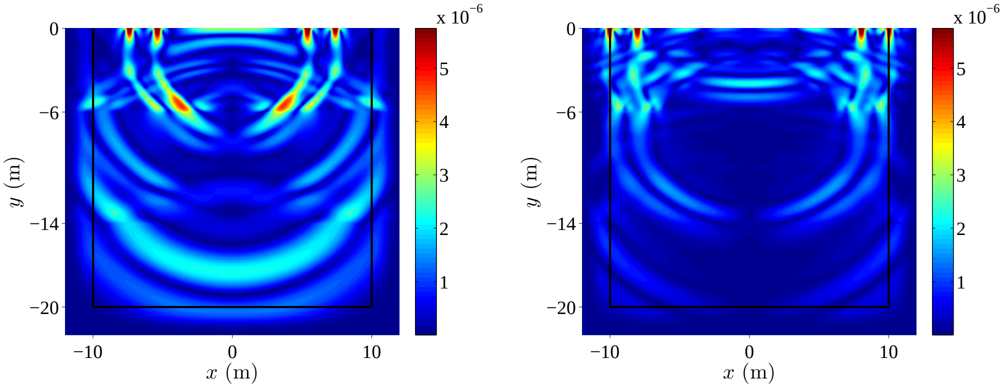

(a) u at $t = 1.5$s

(b) u at $t = 2.0$s

Figure 2.17: Snapshots of u for the layered domain

To further assess the performance of the mixed PML formulation, we compare the displacement time histories at the sampling points against a reference solution obtained using an enlarged domain (200m × 100m). Figure 2.18 depicts a visual comparison of the response time histories for u_x and u_y at the various sp_i points. As it can be seen, the agreement is quite satisfactory. Figure 2.19 is the counterpart of Fig. 2.9 for the heterogeneous case: the highest relative error in the L^2 norm is about 2.7%; though higher than the one we reported for the homogeneous case, we consider it satisfactory. The pointwise errors depicted in Figs. 2.19(c) and 2.19(d) are even better: under the load, the error does not exceed 0.63%, and at the PML-regular domain interface it is less than about 1.75% at all times. Figure 2.20 shows that the energy decay is more gradual in this case due to the layered profile (multiple reflections/transmissions) than in the homogeneous domain cases.

Example 5 As in the previous example, we consider a 20m × 20m computational domain surrounded by a 2m-thick PML on its sides and bottom. The profile functions f_1, f_2, f_3, and f_4 were used to define the various interfaces

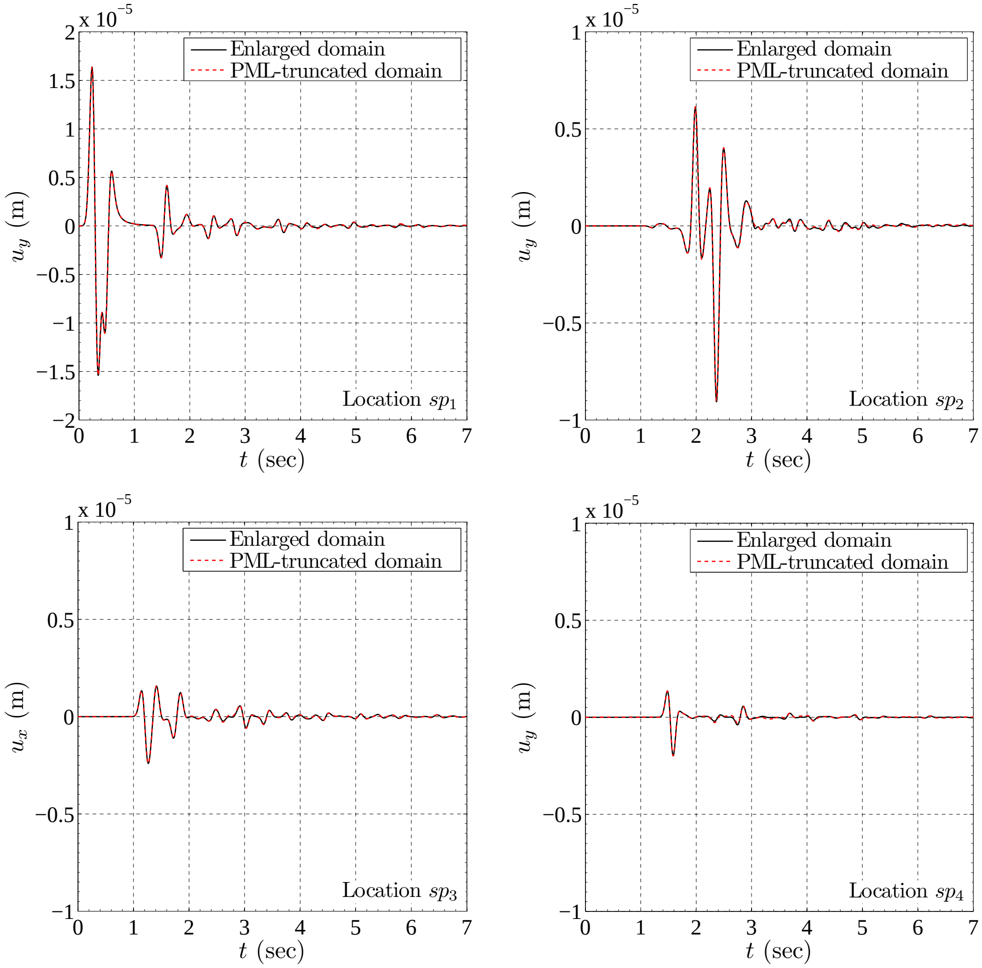

Figure 2.18: Comparison of u_x and u_y time histories between the enlarged and PML-truncated domains at sampling points (Example 4)

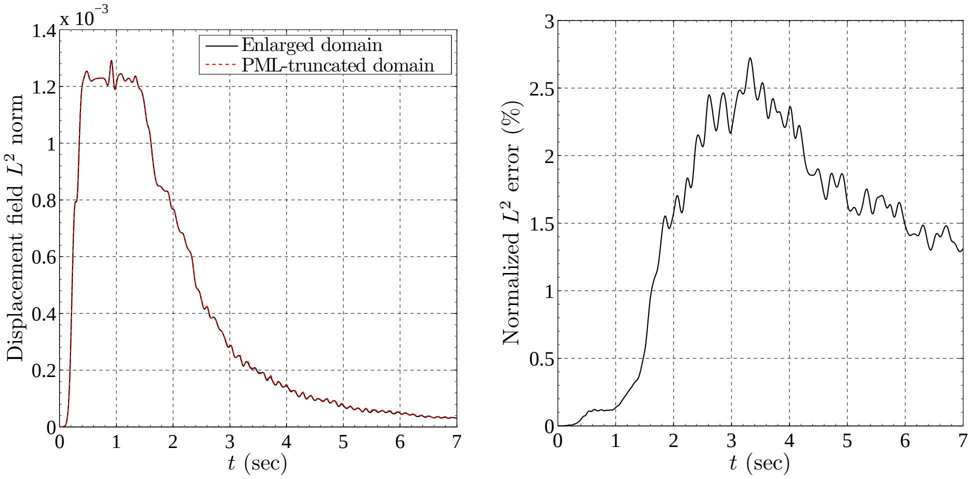

(a) Displacement field norm $D(t;\Omega^{\mathrm{RD}})$

(b) Relative error $e(t)$

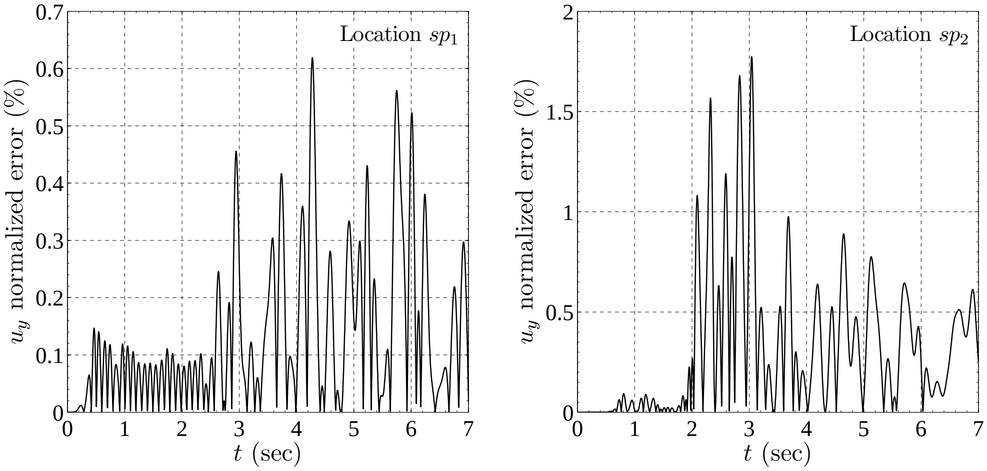

(c) Relative error for u_y at sp_1

(d) Relative error for u_y at sp_2

Figure 2.19: Error metrics for the layered medium excited by a surface Ricker pulse ($f_r = 4$ Hz) (Example 4)

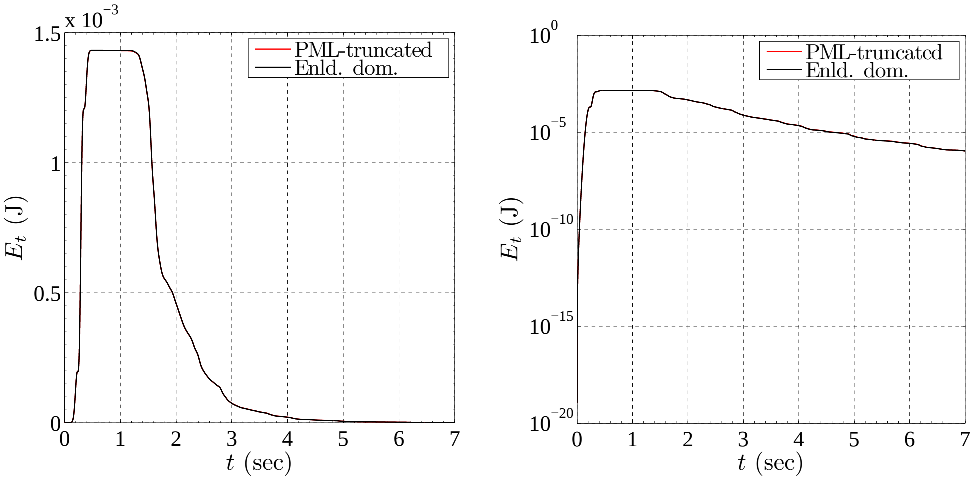

Figure 2.20: Total energy decay inside the regular domain (Example 4)

(Fig. 2.16(b)); they were defined as

$$f_1(x) = 4.7 \arctan(0.7x - 1.7) - 5, \tag{2.62a}$$

$$f_2(x) = -0.05(x+10)^2 + 0.005(x+8)^3 - 4.5, \tag{2.62b}$$

$$f_3(x) = \sqrt{1 - \left(\frac{x-4}{4}\right)^2} - 12, \tag{2.62c}$$

$$f_4(x) = -\sqrt{1 - \left(\frac{x-4}{4}\right)^2} - 12. \tag{2.62d}$$

As in Example 4, the material interfaces were extended horizontally into the PML. The reflection coefficient R was again set to 10^{-8}. Figure 2.21 shows the snapshots of the displacement taken at two different times. Although there are reflections introduced by the material interfaces, no spurious reflections are observed at the PML interface.

Figure 2.22 depicts the displacement field L^2 norm and the normalized relative error by comparing the response of the PML-truncated domain against

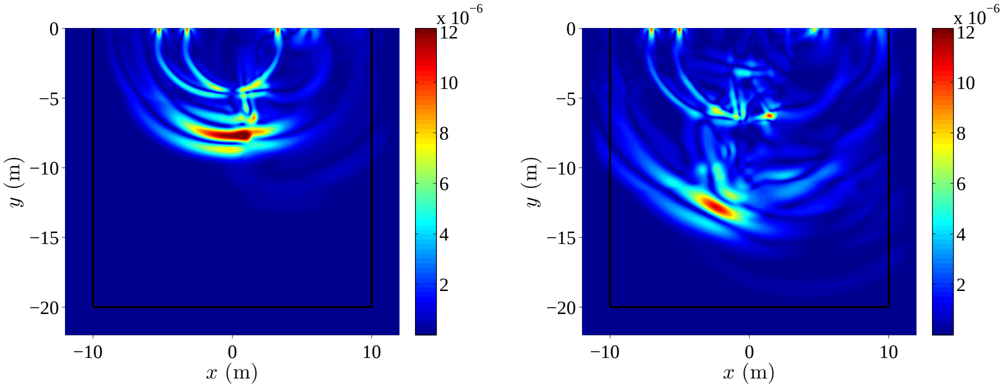

(a) u at $t = 1.5$s (b) u at $t = 2.0$s

Figure 2.21: Snapshots of u for the heterogeneous domain with an inclusion

the response obtained using an enlarged domain (150m × 80m). The agreement between displacement field norms is again fairly satisfactory. However, the normalized relative error is a few percentage points: until, approximately, $t = 4$s, the relative error is roughly around 2.6%, which is quite reasonable to expect considering the error metrics obtained for layered media (Example 4). Between about $t = 4$s and $t = 4.7$s, the displacement response amplitudes become so small that they interfere with small amplitude reflections from the fixed exterior boundary of the PML. Even the slightest disturbance in the propagation pattern triggers change; after about $t = 4.7$s, the normalized relative error decreases monotonically as the waves are steadily leaving the computational domain. The energy decay shown in Figs. 2.22(c) and 2.22(d) show good agreement between the reference and the PML solutions.

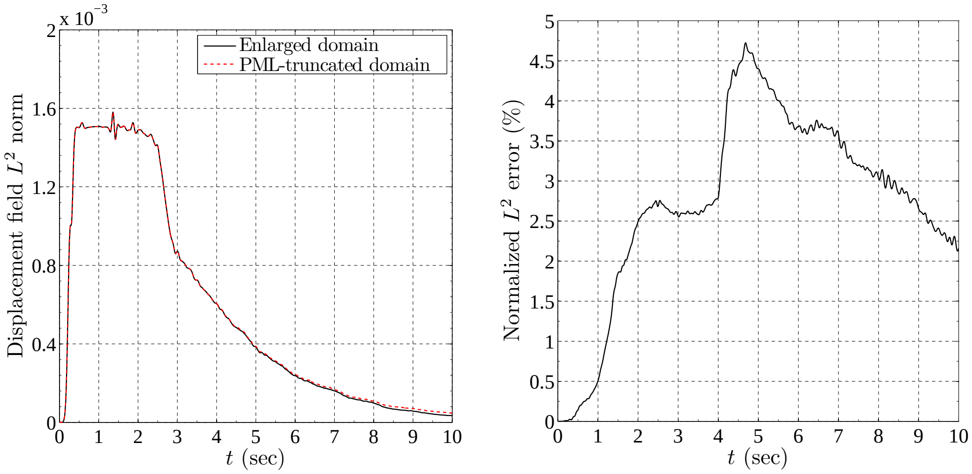

(a) Displacement field norm $D(t;\Omega^{\mathrm{RD}})$

(b) Relative error $e(t)$

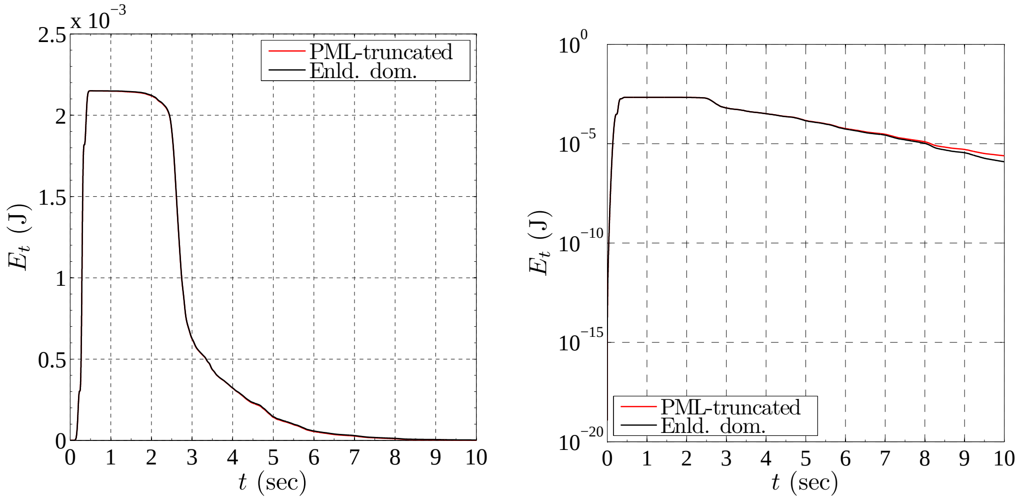

(c) Energy decay - standard scale

(d) Energy decay - logarithmic scale

Figure 2.22: Error metrics for the arbitrarily heterogeneous medium excited by a surface Ricker pulse ($f_r = 4$ Hz) (Example 5)

2.3 Fully-mixed axisymmetric elastic wave modeling

In section 2.2, we formulated a fully-mixed two-dimensional unsplit-field PML and validated its numerical accuracy and efficiency in homogeneous and arbitrarily heterogeneous media. In this section, we are concerned with elastic wave simulations arising in elastic, semi-infinite, horizontally-layered, but vertically heterogeneous media that are typically encountered in site characterization and pavement design problems. Specifically, we discuss the development of a new mixed displacement-stress formulation in PML-truncated axisymmetric media for transient wave simulations, following similar lines to the two-dimensional case. However, as it will be seen, differences arise due to the presence of a third spatial dimension, which affects the temporal complexity of the resulting equations, including the temporal order of the semi-discrete forms.

For the axisymmetric problem of interest herein, the equilibrium equations (2.17a), the constitutive law (2.17b), and the kinematic conditions (2.17c) must be recast in cylindrical coordinates (r, θ, z), where r denotes radial distance, θ is the polar angle, and z is vertical distance (along the domain's depth); to this end, we provide the definitions of the gradient of a vector $\mathbf{u}$, and the divergence of a tensor $\mathcal{S}$ as

$$\nabla \mathbf{u} = \frac{1}{h_i} \frac{\partial \mathbf{u}}{\partial i} \otimes \mathbf{e}_i, \qquad \mathbf{div}\, \mathcal{S} = \frac{1}{r} \frac{\partial}{\partial i} \left(r \frac{\mathcal{S}_{ji}}{h_i} \mathbf{e}_j \right), \qquad i, j = r, \theta, z, \tag{2.63}$$

where repeated indices imply summation, $\otimes$ denotes tensor product, $\mathbf{e}_i$ is the unit vector along the i-axis, and the scale factors in the case of cylindrical coordinates reduce to $h_r = h_z = 1$, and $h_\theta = r$.

2.3.1 In the frequency-domain

Application of the Fourier transform to the equilibrium, constitutive, and kinematic equations (2.17a-2.17c) results again in

$$\mathbf{div}\,\hat{\mathcal{S}}^T + \hat{\mathbf{f}} = -\omega^2 \rho \hat{\mathbf{u}}, \tag{2.64a}$$

$$\hat{\mathcal{S}} = \mathcal{C} : \hat{\mathcal{E}}, \tag{2.64b}$$

$$\hat{\mathcal{E}} = \frac{1}{2}\left[\nabla\hat{\mathbf{u}} + (\nabla\hat{\mathbf{u}})^T\right]. \tag{2.64c}$$

Next, we introduce the coordinate-stretched form for each coordinate,

$$\tilde{s} = \int_0^s \varepsilon_s(s')ds', \qquad \varepsilon_s(s,\omega) = \alpha_s(s) + \frac{\beta_s(s)}{i\omega}, \qquad s = r, z. \tag{2.65}$$

Then, we apply complex coordinate-stretching by making use of (2.65), (2.12), and the definitions (2.63). Since the problem of interest here is axisymmetric, we apply the stretching only in the r and z coordinates, i.e., in directions normal to the interface between the regular domain and PML, by replacing r and z with the stretched coordinates $\tilde{r}$ and $\tilde{z}$. In unabridged notation the equilibrium equations become

$$\frac{\partial\hat{\sigma}_{rr}}{\partial\tilde{r}} + \frac{\partial\hat{\sigma}_{zr}}{\partial\tilde{z}} + \frac{\hat{\sigma}_{rr}}{\tilde{r}} - \frac{\hat{\sigma}_{\theta\theta}}{\tilde{r}} + \hat{f}_r = -\omega^2\rho\hat{u}_r, \tag{2.66a}$$

$$\frac{\partial\hat{\sigma}_{rz}}{\partial\tilde{r}} + \frac{\partial\hat{\sigma}_{zz}}{\partial\tilde{z}} + \frac{\hat{\sigma}_{rz}}{\tilde{r}} + \hat{f}_z = -\omega^2\rho\hat{u}_z, \tag{2.66b}$$

where σ_{ij} denotes stress tensor components ($\sigma_{ij} = (\mathbb{S})_{ij}$). Using (2.7), the above equations can be expressed in terms of the unstretched coordinates as

$$\frac{1}{\varepsilon_r}\frac{\partial \hat{\sigma}_{rr}}{\partial r} + \frac{1}{\varepsilon_z}\frac{\partial \hat{\sigma}_{zr}}{\partial z} + \frac{\hat{\sigma}_{rr}}{\tilde{r}} - \frac{\hat{\sigma}_{\theta\theta}}{\tilde{r}} + \hat{f}_r = -\omega^2 \rho \hat{u}_r, \tag{2.67a}$$

$$\frac{1}{\varepsilon_r}\frac{\partial \hat{\sigma}_{rz}}{\partial r} + \frac{1}{\varepsilon_z}\frac{\partial \hat{\sigma}_{zz}}{\partial z} + \frac{\hat{\sigma}_{rz}}{\tilde{r}} + \hat{f}_z = -\omega^2 \rho \hat{u}_z. \tag{2.67b}$$

Next, we multiply both sides by $\varepsilon_r \varepsilon_z \frac{\tilde{r}}{r}$. Using again the definition of divergence (2.63), the equations of equilibrium can be compactly recast as

$$\mathbf{div}\left(\hat{\mathbb{S}}^T \tilde{\Lambda}\right) + \varepsilon_r \varepsilon_z \frac{\tilde{r}}{r}\hat{\mathbf{f}} = -\omega^2 \rho \varepsilon_r \varepsilon_z \frac{\tilde{r}}{r}\hat{\mathbf{u}}, \tag{2.68}$$

where $\tilde{\Lambda}$ is defined as follows by making use of (2.65) and (2.12)

$$\begin{aligned}
\tilde{\Lambda} = \begin{bmatrix} \varepsilon_z \frac{\tilde{r}}{r} & 0 & 0 \\ 0 & \varepsilon_r \varepsilon_z & 0 \\ 0 & 0 & \varepsilon_r \frac{\tilde{r}}{r} \end{bmatrix} &= \begin{bmatrix} \frac{\alpha_z \bar{\alpha}_r}{r} & 0 & 0 \\ 0 & \alpha_r \alpha_z & 0 \\ 0 & 0 & \frac{\alpha_r \bar{\alpha}_r}{r} \end{bmatrix} + \frac{1}{(i\omega)^2} \begin{bmatrix} \frac{\bar{\beta}_r \beta_z}{r} & 0 & 0 \\ 0 & \beta_r \beta_z & 0 \\ 0 & 0 & \frac{\beta_r \bar{\beta}_r}{r} \end{bmatrix} \\
&+ \frac{1}{i\omega} \begin{bmatrix} \frac{\alpha_z \bar{\beta}_r + \beta_z \bar{\alpha}_r}{r} & 0 & 0 \\ 0 & \alpha_r \beta_z + \beta_r \alpha_z & 0 \\ 0 & 0 & \frac{\alpha_r \bar{\beta}_r + \beta_r \bar{\alpha}_r}{r} \end{bmatrix} \\
&= \tilde{\Lambda}_e + \frac{1}{i\omega}\tilde{\Lambda}_p + \frac{1}{(i\omega)^2}\tilde{\Lambda}_w.
\end{aligned} \tag{2.69}$$

In the above, subscripts "*e*" and "*p*" refer again to attenuation functions associated with evanescent and propagating waves, respectively. We remark that in the regular domain, $\tilde{\Lambda}_e$ reduces to the identity tensor, whereas $\tilde{\Lambda}_p$ and $\tilde{\Lambda}_w$ vanish identically. After substituting (2.69) into (2.68), employing (2.65) and (2.12), multiplying both sides by $i\omega$, rearranging and grouping like-terms, there results

$$\begin{aligned}
\mathbf{div}\left(i\omega \hat{\mathbb{S}}^T \tilde{\Lambda}_e + \hat{\mathbb{S}}^T \tilde{\Lambda}_p + \frac{1}{i\omega}\hat{\mathbb{S}}^T \tilde{\Lambda}_w\right) + i\omega a \hat{\mathbf{f}} + b\hat{\mathbf{f}} + \frac{c}{i\omega}\hat{\mathbf{f}} + \frac{d}{(i\omega)^2}\hat{\mathbf{f}} \\
= \rho\left[(i\omega)^3 a \hat{\mathbf{u}} + (i\omega)^2 b \hat{\mathbf{u}} + i\omega c \hat{\mathbf{u}} + d\hat{\mathbf{u}}\right],
\end{aligned} \tag{2.70}$$

where

$$\begin{aligned} a &= \frac{\alpha_r \alpha_z \bar{\alpha}_r}{r}, & b &= \frac{\alpha_r \alpha_z \bar{\beta}_r + \bar{\alpha}_r \alpha_r \beta_z + \alpha_z \bar{\alpha}_r \beta_r}{r}, \\ c &= \frac{\alpha_r \bar{\beta}_r \beta_z + \bar{\alpha}_r \beta_z \beta_r + \alpha_z \beta_r \bar{\beta}_r}{r}, & d &= \frac{\beta_r \bar{\beta}_r \beta_z}{r}. \end{aligned} \tag{2.71}$$

We note that, within the regular domain, $a \equiv 1, b \equiv 0, c \equiv 0, d \equiv 0$, and since the body forces $\mathbf{f}$ are non-vanishing only within the regular domain ($\mathbf{f}$ vanishes within the PML), (2.70) reduces further to:

$$\begin{aligned} &\mathbf{div}\left(i\omega \hat{\mathcal{S}}^T \tilde{\Lambda}_e + \hat{\mathcal{S}}^T \tilde{\Lambda}_p + \frac{1}{i\omega} \hat{\mathcal{S}}^T \tilde{\Lambda}_w \right) + i\omega a \hat{\mathbf{f}} \\ &\qquad\qquad = \rho \left[(i\omega)^3 a \hat{\mathbf{u}} + (i\omega)^2 b \hat{\mathbf{u}} + i\omega c \hat{\mathbf{u}} + d \hat{\mathbf{u}} \right]. \end{aligned} \tag{2.72}$$

However, this reduction does not extend to the displacement terms on the right-hand-side of (2.72), since b, c, and d do not vanish within both the regular domain and the PML. Similarly, we apply complex coordinate-stretching to the kinematic equation (2.17c); there results

$$\hat{\mathcal{E}} = \frac{1}{2} \left\{ (\nabla \hat{\mathbf{u}}) \begin{bmatrix} \frac{1}{\varepsilon_r} & 0 & 0 \\ 0 & \frac{r}{\tilde{r}} & 0 \\ 0 & 0 & \frac{1}{\varepsilon_z} \end{bmatrix} + \begin{bmatrix} \frac{1}{\varepsilon_r} & 0 & 0 \\ 0 & \frac{r}{\tilde{r}} & 0 \\ 0 & 0 & \frac{1}{\varepsilon_z} \end{bmatrix} (\nabla \hat{\mathbf{u}})^T \right\}. \tag{2.73}$$

Next, we multiply both sides by $(i\omega)^2 \varepsilon_r \varepsilon_z \frac{\tilde{r}}{r}$ to obtain

$$(i\omega)^2 \varepsilon_r \varepsilon_z \frac{\tilde{r}}{r} \hat{\mathcal{E}} = \frac{1}{2} (i\omega)^2 \left[(\nabla \hat{\mathbf{u}}) \tilde{\Lambda} + \tilde{\Lambda} (\nabla \hat{\mathbf{u}})^T \right], \tag{2.74}$$

where the stretching tensor $\tilde{\Lambda}$ is defined in (2.69). Substituting (2.69) and (2.65) into (2.74), rearranging and grouping like-terms, yields

$$\begin{aligned} (i\omega)^2 a \hat{\mathcal{E}} + i\omega b \hat{\mathcal{E}} + c \hat{\mathcal{E}} + \frac{d}{i\omega} \hat{\mathcal{E}} &= \frac{1}{2} (i\omega)^2 \left[(\nabla \hat{\mathbf{u}}) \tilde{\Lambda}_e + \tilde{\Lambda}_e (\nabla \hat{\mathbf{u}})^T \right] \\ &+ \frac{1}{2} i\omega \left[(\nabla \hat{\mathbf{u}}) \tilde{\Lambda}_p + \tilde{\Lambda}_p (\nabla \hat{\mathbf{u}})^T \right] + \frac{1}{2} \left[(\nabla \hat{\mathbf{u}}) \tilde{\Lambda}_w + \tilde{\Lambda}_w (\nabla \hat{\mathbf{u}})^T \right], \end{aligned} \tag{2.75}$$

where a, b, c and d are defined in (2.71). Equations (2.72), (2.64b), and (2.75), constitute the stretched form of the governing frequency-domain equations, repeated below to ease their subsequent reference:

$$\begin{aligned}
&\mathbf{div}\left(i\omega\hat{\mathcal{S}}^T\tilde{\Lambda}_e + \hat{\mathcal{S}}^T\tilde{\Lambda}_p + \frac{1}{i\omega}\hat{\mathcal{S}}^T\tilde{\Lambda}_w\right) + i\omega a\hat{\mathbf{f}} \\
&\qquad\qquad = \rho\left[(i\omega)^3 a\hat{\mathbf{u}} + (i\omega)^2 b\hat{\mathbf{u}} + i\omega c\hat{\mathbf{u}} + d\hat{\mathbf{u}}\right], \qquad (2.76\text{a})
\end{aligned}$$

$$\hat{\mathcal{S}} = \mathcal{C} : \hat{\mathcal{E}}, \qquad (2.76\text{b})$$

$$\begin{aligned}
(i\omega)^2 a\hat{\mathcal{E}} + i\omega b\hat{\mathcal{E}} + c\hat{\mathcal{E}} + \frac{d}{i\omega}\hat{\mathcal{E}} &= \frac{1}{2}(i\omega)^2\left[(\nabla\hat{\mathbf{u}})\tilde{\Lambda}_e + \tilde{\Lambda}_e(\nabla\hat{\mathbf{u}})^T\right] \\
+ \frac{1}{2}i\omega\left[(\nabla\hat{\mathbf{u}})\tilde{\Lambda}_p + \tilde{\Lambda}_p(\nabla\hat{\mathbf{u}})^T\right] &+ \frac{1}{2}\left[(\nabla\hat{\mathbf{u}})\tilde{\Lambda}_w + \tilde{\Lambda}_w(\nabla\hat{\mathbf{u}})^T\right]. \qquad (2.76\text{c})
\end{aligned}$$

2.3.2 In the time-domain

By taking the inverse Fourier transform of (2.76), there results

$$\begin{aligned}
&\mathbf{div}\left[\dot{\mathcal{S}}^T\tilde{\Lambda}_e + \mathcal{S}^T\tilde{\Lambda}_p + \left(\int_0^t \mathcal{S}^T d\tau\right)\tilde{\Lambda}_w\right] + a\dot{\mathbf{f}} \\
&\qquad\qquad = \rho\left(a\dddot{\mathbf{u}} + b\ddot{\mathbf{u}} + c\dot{\mathbf{u}} + d\mathbf{u}\right), \qquad (2.77\text{a})
\end{aligned}$$

$$\mathcal{S} = \mathcal{C} : \mathcal{E}, \qquad (2.77\text{b})$$

$$\begin{aligned}
a\ddot{\mathcal{E}} + b\dot{\mathcal{E}} + c\mathcal{E} + d\left(\int_0^t \mathcal{E}d\tau\right) &= \frac{1}{2}\Big[(\nabla\ddot{\mathbf{u}})\tilde{\Lambda}_e + \tilde{\Lambda}_e(\nabla\ddot{\mathbf{u}})^T \\
&+ (\nabla\dot{\mathbf{u}})\tilde{\Lambda}_p + \tilde{\Lambda}_p(\nabla\dot{\mathbf{u}})^T + (\nabla\mathbf{u})\tilde{\Lambda}_w + \tilde{\Lambda}_w(\nabla\mathbf{u})^T\Big]. \qquad (2.77\text{c})
\end{aligned}$$

Notice that the equilibrium equation (2.77a) implicates a jerk term for the displacements. Having three consecutive derivative terms for the displacements in (2.77a) prevents a second-order temporal formulation. We define next the following stress and strain memory (or history) tensor terms:

$$\mathbf{S}(\mathbf{x},t) = \int_0^t \mathcal{S}(\mathbf{x},\tau)d\tau, \qquad \mathbf{E}(\mathbf{x},t) = \int_0^t \mathcal{E}(\mathbf{x},\tau)d\tau, \qquad (2.78)$$

which are such that

$$\dot{\mathbf{S}}(\mathbf{x},t) = \mathcal{S}(\mathbf{x},t), \qquad \ddot{\mathbf{S}}(\mathbf{x},t) = \dot{\mathcal{S}}(\mathbf{x},t), \tag{2.79a}$$

$$\dot{\mathbf{E}}(\mathbf{x},t) = \mathcal{E}(\mathbf{x},t), \qquad \ddot{\mathbf{E}}(\mathbf{x},t) = \dot{\mathcal{E}}(\mathbf{x},t). \tag{2.79b}$$

Substitution of (2.78) and (2.79) into (2.77a-2.77c) leads to the time-domain equations of the axisymmetric unsplit-field PML formulation

$$\mathbf{div}\left(\ddot{\mathbf{S}}^T\tilde{\Lambda}_e + \dot{\mathbf{S}}^T\tilde{\Lambda}_p + \mathbf{S}^T\tilde{\Lambda}_w\right) + a\dot{\mathbf{f}} = \rho\left(a\dddot{\mathbf{u}} + b\ddot{\mathbf{u}} + c\dot{\mathbf{u}} + d\mathbf{u}\right), \tag{2.80a}$$

$$\dot{\mathbf{S}} = \mathcal{C} : \dot{\mathbf{E}}, \tag{2.80b}$$

$$\begin{aligned} a\dddot{\mathbf{E}} + b\ddot{\mathbf{E}} + c\dot{\mathbf{E}} + d\mathbf{E} = \frac{1}{2}\Big[&(\nabla\ddot{\mathbf{u}})\tilde{\Lambda}_e + \tilde{\Lambda}_e(\nabla\ddot{\mathbf{u}})^T \\ &+ (\nabla\dot{\mathbf{u}})\tilde{\Lambda}_p + \tilde{\Lambda}_p(\nabla\dot{\mathbf{u}})^T + (\nabla\mathbf{u})\tilde{\Lambda}_w + \tilde{\Lambda}_w(\nabla\mathbf{u})^T\Big]. \end{aligned} \tag{2.80c}$$

2.3.3 Mixed finite element implementation

Following the same reduction approach as in section 2.2, we retain both displacements and stresses (or, more appropriately, stress histories) as unknowns. To this end, we introduce the constitutive law (2.80b) into the kinematic condition (2.80c), to arrive at

$$\mathbf{div}\left(\ddot{\mathbf{S}}^T\tilde{\Lambda}_e + \dot{\mathbf{S}}^T\tilde{\Lambda}_p + \mathbf{S}^T\tilde{\Lambda}_w\right) + a\dot{\mathbf{f}} = \rho\left(a\dddot{\mathbf{u}} + b\ddot{\mathbf{u}} + c\dot{\mathbf{u}} + d\mathbf{u}\right), \tag{2.81a}$$

$$\begin{aligned} \mathcal{D} : \left(a\dddot{\mathbf{S}} + b\ddot{\mathbf{S}} + c\dot{\mathbf{S}} + d\mathbf{S}\right) = \frac{1}{2}\Big[&(\nabla\ddot{\mathbf{u}})\tilde{\Lambda}_e + \tilde{\Lambda}_e(\nabla\ddot{\mathbf{u}})^T \\ &+ (\nabla\dot{\mathbf{u}})\tilde{\Lambda}_p + \tilde{\Lambda}_p(\nabla\dot{\mathbf{u}})^T + (\nabla\mathbf{u})\tilde{\Lambda}_w + \tilde{\Lambda}_w(\nabla\mathbf{u})^T\Big], \end{aligned} \tag{2.81b}$$

where $\mathcal{D}$ denotes again the compliance tensor ($\mathbf{E} = \mathcal{D} : \mathbf{S}$).

Consider next the half-space problem depicted in Fig. 2.23. Let $\Omega^{\mathrm{RD}} \cup \Omega^{\mathrm{PML}} = \Omega \subset \mathbb{R}^3$ denote the region occupied by the elastic body (Ω^{RD}), surrounded on its periphery and bottom by the PML buffer zone (Ω^{PML}). Ω is bounded by $\Gamma = \Gamma_D \cup \Gamma_N$, where $\Gamma_D \cap \Gamma_N = \emptyset$, and $\Gamma_D \equiv \Gamma_D^{\mathrm{PML}}$, $\Gamma_N = \Gamma_N^{\mathrm{RD}} \cup \Gamma_N^{\mathrm{PML}}$.

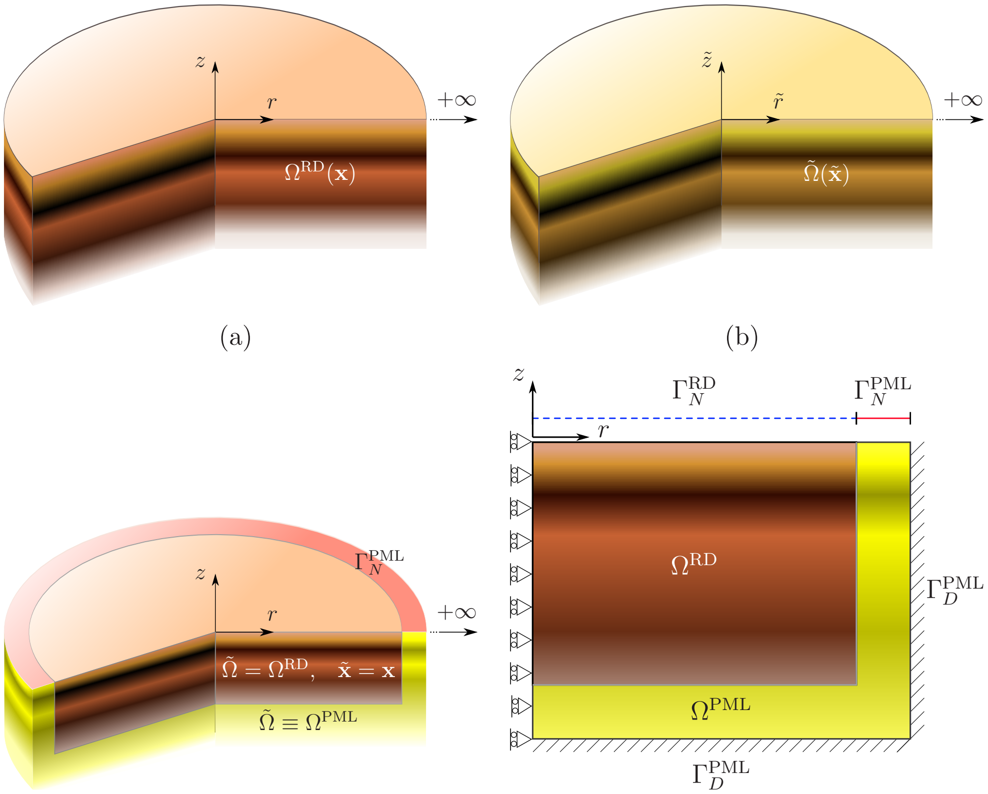

(a) (b)

(c) (d)

Figure 2.23: Axisymmetric prototype: (a) physical model; (b) model after the application of complex coordinate-stretching; (c) model after truncation; (d) computational model with symmetry conditions introduced on the axis

Then, we require that (2.81) hold in $\Omega \times \mathsf{J}$, subject to the following boundary and initial conditions:

$$\mathbf{u}(\mathbf{x},t) = \mathbf{0} \qquad \text{on } \Gamma_D^{\mathrm{PML}} \times \mathsf{J}, \tag{2.82a}$$

$$\left(\ddot{\mathbf{S}}^T \tilde{\Lambda}_e + \dot{\mathbf{S}}^T \tilde{\Lambda}_p + \mathbf{S}^T \tilde{\Lambda}_w\right) \mathbf{n} = \mathbf{0} \qquad \text{on } \Gamma_N^{\mathrm{PML}} \times \mathsf{J}, \tag{2.82b}$$

$$\dot{\mathbf{S}}(\mathbf{x},t)^T \mathbf{n} = \boldsymbol{g}_n(\mathbf{x},t) \qquad \text{on } \Gamma_N^{\mathrm{RD}} \times \mathsf{J}, \tag{2.82c}$$

$$\mathbf{u}(\mathbf{x},0) = \mathbf{0}, \quad \dot{\mathbf{u}}(\mathbf{x},0) = \mathbf{0}, \quad \ddot{\mathbf{u}}(\mathbf{x},0) = \mathbf{0} \qquad \text{in } \Omega, \tag{2.82d}$$

$$\mathbf{S}(\mathbf{x},0) = \mathbf{0}, \quad \dot{\mathbf{S}}(\mathbf{x},0) = \mathbf{0}, \quad \ddot{\mathbf{S}}(\mathbf{x},0) = \mathbf{0} \qquad \text{in } \Omega, \tag{2.82e}$$

where $\boldsymbol{g}_n$ denotes prescribed tractions on Γ_N^{RD}.

We seek next the weak form, in the Galerkin sense, corresponding to the strong form (2.81-2.82). Since both displacements and stresses are retained as independent unknowns, the resulting problem is again mixed. We take inner products of the equilibrium equation (2.81a), and the kinematic equation (2.81b) with arbitrary weight functions $\mathbf{w}(\mathbf{x})$ and $\mathbf{T}(\mathbf{x})$, respectively, residing in appropriate admissible spaces, and then integrate over the entire computational domain Ω. As with the two-dimensional case, here again we perform integration by parts to the (weighted form of the) equilibrium equation only. There results

$$\begin{aligned}\int_\Omega \nabla\mathbf{w} : \left(\ddot{\mathbf{S}}^T \tilde{\Lambda}_e + \dot{\mathbf{S}}^T \tilde{\Lambda}_p + \mathbf{S}^T \tilde{\Lambda}_w\right) \, \mathrm{d}\Omega + \int_\Omega \mathbf{w} \cdot \rho \, \left(a \dddot{\mathbf{u}} + b\ddot{\mathbf{u}} + c\dot{\mathbf{u}} + d\mathbf{u}\right) \, \mathrm{d}\Omega \\ = \int_{\Gamma_N} \mathbf{w} \cdot \left(\ddot{\mathbf{S}}^T \tilde{\Lambda}_e + \dot{\mathbf{S}}^T \tilde{\Lambda}_p + \mathbf{S}^T \tilde{\Lambda}_w\right) \mathbf{n} \, \mathrm{d}\Gamma + \int_\Omega \mathbf{w} \cdot a\dot{\mathbf{f}} \, \mathrm{d}\Omega,\end{aligned} \tag{2.83a}$$

$$\begin{aligned}\int_\Omega \mathbf{T} : \left[\mathcal{D} : \left(a\dddot{\mathbf{S}} + b\ddot{\mathbf{S}} + c\dot{\mathbf{S}} + d\mathbf{S}\right)\right] \, \mathrm{d}\Omega = \frac{1}{2} \int_\Omega \mathbf{T} : \Big[(\nabla\ddot{\mathbf{u}})\tilde{\Lambda}_e + \tilde{\Lambda}_e(\nabla\ddot{\mathbf{u}})^T \\ + (\nabla\dot{\mathbf{u}})\tilde{\Lambda}_p + \tilde{\Lambda}_p(\nabla\dot{\mathbf{u}})^T + (\nabla\mathbf{u})\tilde{\Lambda}_w + \tilde{\Lambda}_w(\nabla\mathbf{u})^T\Big] \, \mathrm{d}\Omega.\end{aligned} \tag{2.83b}$$

We seek $\mathbf{u} \in \mathbf{H}^1(\Omega) \times \mathsf{J}$ satisfying $\mathbf{u}|_{\Gamma_D^{\mathrm{PML}}} = \mathbf{0}$, and $\mathbf{S} \in \mathcal{L}^2(\Omega) \times \mathsf{J}$ such that equation (2.83) holds for all $\mathbf{w} \in \mathbf{H}^1(\Omega)$ satisfying $\mathbf{w}|_{\Gamma_D} = \mathbf{0}$ and $\mathbf{T} \in \mathcal{L}^2(\Omega)$. It is important to notice again that the regularity required for the stresses is *lower* than what is required of the displacements. Next, we seek approximate solutions for $\mathbf{u}(\mathbf{x}, t)$ and $\mathbf{S}(\mathbf{x}, t)$; to this end, we introduce the finite-dimensional spaces $\boldsymbol{\Xi}^h \subset \mathbf{H}^1(\Omega)$ and $\boldsymbol{\Upsilon}^h \subset \mathcal{L}^2(\Omega)$. Let the basis functions in $\boldsymbol{\Xi}^h$ and $\boldsymbol{\Upsilon}^h$ be denoted by $\boldsymbol{\Phi}$ and $\boldsymbol{\Psi}$, respectively. The trial functions $\mathbf{u}_h \in \boldsymbol{\Xi}^h \times \mathsf{J}$ and $\mathbf{S}_h \in \boldsymbol{\Upsilon}^h \times \mathsf{J}$ are spatially discretized as

$$\mathbf{u}(\mathbf{x}, t) \cong \mathbf{u}_h(\mathbf{x}, t) = \begin{bmatrix} \boldsymbol{\Phi}^T(\mathbf{x})\mathbf{u}_r(t) \\ \boldsymbol{\Phi}^T(\mathbf{x})\mathbf{u}_z(t) \end{bmatrix}, \tag{2.84a}$$

$$\mathbf{S}(\mathbf{x}, t) \cong \mathbf{S}_h(\mathbf{x}, t) = \begin{bmatrix} \boldsymbol{\Psi}^T(\mathbf{x})\mathbf{S}_{rr}(t) & 0 & \boldsymbol{\Psi}^T(\mathbf{x})\mathbf{S}_{rz}(t) \\ 0 & \boldsymbol{\Psi}^T(\mathbf{x})\mathbf{S}_{\theta\theta}(t) & 0 \\ \boldsymbol{\Psi}^T(\mathbf{x})\mathbf{S}_{zr}(t) & 0 & \boldsymbol{\Psi}^T(\mathbf{x})\mathbf{S}_{zz}(t) \end{bmatrix}. \tag{2.84b}$$

Similarly, the test functions $\mathbf{w} \in \boldsymbol{\Xi}^h$ and $\mathbf{T} \in \boldsymbol{\Upsilon}^h$ are expressed as

$$\mathbf{w}(\mathbf{x}) \cong \mathbf{w}_h(\mathbf{x}) = \begin{bmatrix} \mathbf{w}_r^T \boldsymbol{\Phi}(\mathbf{x}) \\ \mathbf{w}_z^T \boldsymbol{\Phi}(\mathbf{x}) \end{bmatrix}, \tag{2.85a}$$

$$\mathbf{T}(\mathbf{x}) \cong \mathbf{T}_h(\mathbf{x}) = \begin{bmatrix} \mathbf{T}_{rr}^T \boldsymbol{\Psi}(\mathbf{x}) & 0 & \mathbf{T}_{rz}^T \boldsymbol{\Psi}(\mathbf{x}) \\ 0 & \mathbf{T}_{\theta\theta}^T \boldsymbol{\Psi}(\mathbf{x}) & 0 \\ \mathbf{T}_{zr}^T \boldsymbol{\Psi}(\mathbf{x}) & 0 & \mathbf{T}_{zz}^T \boldsymbol{\Psi}(\mathbf{x}) \end{bmatrix}. \tag{2.85b}$$

By introducing the symmetry of the stress tensor ($\mathcal{S} = \mathcal{S}^T$), we obtain the *semi-discrete form*

$$\mathbf{M}\dddot{\mathbf{d}} + \mathbf{C}\ddot{\mathbf{d}} + \mathbf{K}\dot{\mathbf{d}} + \mathbf{G}\mathbf{d} = \mathbf{F}, \tag{2.86}$$

where

$$\mathbf{M} = \begin{bmatrix} \mathbf{M}_a & \mathbf{0} & \mathbf{0} & \mathbf{0} & \mathbf{0} & \mathbf{0} \\ & \mathbf{M}_a & \mathbf{0} & \mathbf{0} & \mathbf{0} & \mathbf{0} \\ & & -\mathbf{N}_a & \mathbf{Z}_a & \mathbf{Z}_a & \mathbf{0} \\ & & & -\mathbf{N}_a & \mathbf{Z}_a & \mathbf{0} \\ & sym & & & -\mathbf{N}_a & \mathbf{0} \\ & & & & & -\mathbf{G}_a \end{bmatrix}, \tag{2.87a}$$

$$\mathbf{C} = \begin{bmatrix} \mathbf{M}_b & \mathbf{0} & \mathbf{A}_{1r} & \mathbf{P}_{2e} & \mathbf{0} & \mathbf{A}_{3z} \\ & \mathbf{M}_b & \mathbf{0} & \mathbf{0} & \mathbf{A}_{3z} & \mathbf{A}_{1r} \\ & & -\mathbf{N}_b & \mathbf{Z}_b & \mathbf{Z}_b & \mathbf{0} \\ & & & -\mathbf{N}_b & \mathbf{Z}_b & \mathbf{0} \\ & sym & & & -\mathbf{N}_b & \mathbf{0} \\ & & & & & -\mathbf{G}_b \end{bmatrix}, \tag{2.87b}$$

$$\mathbf{K} = \begin{bmatrix} \mathbf{M}_c & \mathbf{0} & \mathbf{B}_{1r} & \mathbf{P}_{2p} & \mathbf{0} & \mathbf{B}_{3z} \\ & \mathbf{M}_c & \mathbf{0} & \mathbf{0} & \mathbf{B}_{3z} & \mathbf{B}_{1r} \\ & & -\mathbf{N}_c & \mathbf{Z}_c & \mathbf{Z}_c & \mathbf{0} \\ & & & -\mathbf{N}_c & \mathbf{Z}_c & \mathbf{0} \\ & sym & & & -\mathbf{N}_c & \mathbf{0} \\ & & & & & -\mathbf{G}_c \end{bmatrix}, \tag{2.87c}$$

$$\mathbf{G} = \begin{bmatrix} \mathbf{M}_d & \mathbf{0} & \mathbf{C}_{1r} & \mathbf{P}_{2w} & \mathbf{0} & \mathbf{C}_{3z} \\ & \mathbf{M}_d & \mathbf{0} & \mathbf{0} & \mathbf{C}_{3z} & \mathbf{C}_{1r} \\ & & -\mathbf{N}_d & \mathbf{Z}_d & \mathbf{Z}_d & \mathbf{0} \\ & & & -\mathbf{N}_d & \mathbf{Z}_d & \mathbf{0} \\ & sym & & & -\mathbf{N}_d & \mathbf{0} \\ & & & & & -\mathbf{G}_d \end{bmatrix}, \tag{2.87d}$$

$$\mathbf{d} = [\mathbf{u}_r \; \mathbf{u}_z \; \mathbf{S}_{rr} \; \mathbf{S}_{\theta\theta} \; \mathbf{S}_{zz} \; \mathbf{S}_{rz}]^T, \tag{2.87e}$$

$$\mathbf{F} = [{\mathbf{f}^{\mathbf{e}}}_r \; {\mathbf{f}^{\mathbf{e}}}_z \; \mathbf{0} \; \mathbf{0} \; \mathbf{0} \; \mathbf{0}]^T. \tag{2.87f}$$

The various matrix and vector blocks are defined as

$$\mathbf{f^e}_r = \int_{\Gamma_N^{\mathrm{RD}}} \mathbf{\Phi}\ \dot{g}_r(\mathbf{x},t)\ \mathrm{d}\Gamma + \int_\Omega \mathbf{\Phi} a \dot{f}_r\ \mathrm{d}\Omega, \tag{2.88a}$$

$$\mathbf{f^e}_z = \int_{\Gamma_N^{\mathrm{RD}}} \mathbf{\Phi}\ \dot{g}_z(\mathbf{x},t)\ \mathrm{d}\Gamma + \int_\Omega \mathbf{\Phi} a \dot{f}_z\ \mathrm{d}\Omega, \tag{2.88b}$$

and

$$\mathbf{A}_{ij} = \int_\Omega \tilde{\Lambda}_e^i\ \frac{\partial \mathbf{\Phi}}{\partial j} \mathbf{\Psi}^T\ \mathrm{d}\Omega, \qquad i = 1,2,3 \text{ and } j = r,z \tag{2.89a}$$

$$\mathbf{B}_{ij} = \int_\Omega \tilde{\Lambda}_p^i\ \frac{\partial \mathbf{\Phi}}{\partial j} \mathbf{\Psi}^T\ \mathrm{d}\Omega, \qquad i = 1,2,3 \text{ and } j = r,z \tag{2.89b}$$

$$\mathbf{C}_{ij} = \int_\Omega \tilde{\Lambda}_w^i\ \frac{\partial \mathbf{\Phi}}{\partial j} \mathbf{\Psi}^T\ \mathrm{d}\Omega, \qquad i = 1,2,3 \text{ and } j = r,z \tag{2.89c}$$

$$\mathbf{P}_{ij} = \int_\Omega \frac{1}{r} \tilde{\Lambda}_j^i\ \mathbf{\Phi}\mathbf{\Psi}^T\ \mathrm{d}\Omega, \qquad i = 1,2,3 \text{ and } j = e,p,w \tag{2.89d}$$

$$\mathbf{M}_k = \int_\Omega k\ \rho \mathbf{\Phi}\mathbf{\Phi}^T\ \mathrm{d}\Omega, \qquad k = a,b,c,d \tag{2.89e}$$

$$\mathbf{N}_k = \int_\Omega k\ \frac{\lambda + \mu}{\mu(3\lambda + 2\mu)} \mathbf{\Psi}\mathbf{\Psi}^T\ \mathrm{d}\Omega, \qquad k = a,b,c,d \tag{2.89f}$$

$$\mathbf{Z}_k = \int_\Omega k\ \frac{\lambda}{2\mu(3\lambda + 2\mu)} \mathbf{\Psi}\mathbf{\Psi}^T\ \mathrm{d}\Omega, \qquad k = a,b,c,d \tag{2.89g}$$

$$\mathbf{G}_k = \int_\Omega k\ \frac{1}{\mu} \mathbf{\Psi}\mathbf{\Psi}^T\ \mathrm{d}\Omega, \qquad k = a,b,c,d. \tag{2.89h}$$

Notice that $\tilde{\Lambda}^n$ denote the n^{th} component of the diagonal matrix $\tilde{\Lambda}$.

We remark that the symmetry of the mass-like, stiffness-like, and damping-like matrices in (2.87) has been retained owing to the consistent way of stretching; displacements in the equilibrium equation and strains in the kinematic equation are multiplied by the same factor $\varepsilon_r \varepsilon_z \frac{\tilde{r}}{r}$. However, the second-order temporal character has been sacrificed and thus, the semi-discrete form of the resulting formulation differs from that obtained in the two-dimensional case or in standard finite element analysis of dynamics problems limited to interior domains.

2.3.4 Time integration

The lowest-order time derivatives implicated in the semi-discrete form (2.86) are associated with **d**, which, in turn, involves displacements, and time-integrals of the stress history terms. Thus, clearly, the form (2.86) is unconventional and calls for a specialized time-integration scheme. To this end, we develop an extension (Algorithm 2.2) to the classical Newmark-β scheme, by, first, making use of the following finite difference formulas describing the evolution of the corresponding quantities

$$\mathbf{d}_{n+1} = \mathbf{d}_n + \Delta\mathrm{t}\ \dot{\mathbf{d}}_n + \frac{\Delta\mathrm{t}^2}{2}\ddot{\mathbf{d}}_n + \left(\frac{1}{6} - \alpha\right)\Delta\mathrm{t}^3\dddot{\mathbf{d}}_n + \alpha\ \Delta\mathrm{t}^3\dddot{\mathbf{d}}_{n+1}, \tag{2.90a}$$

$$\dot{\mathbf{d}}_{n+1} = \dot{\mathbf{d}}_n + \Delta\mathrm{t}\ \ddot{\mathbf{d}}_n + \left(\frac{1}{2} - \beta\right)\Delta\mathrm{t}^2\dddot{\mathbf{d}}_n + \beta\ \Delta\mathrm{t}^2\dddot{\mathbf{d}}_{n+1}, \tag{2.90b}$$

$$\ddot{\mathbf{d}}_{n+1} = \ddot{\mathbf{d}}_n + (1-\gamma)\,\Delta\mathrm{t}\ \dddot{\mathbf{d}}_n + \gamma\ \Delta\mathrm{t}\ \dddot{\mathbf{d}}_{n+1}, \tag{2.90c}$$

where $\Delta\mathrm{t}$ denotes the time step, and subscripts (n) and $(n+1)$ denote current and next time step, respectively (β and γ are the usual Newmark-β parameters, and α is a new Newmark-like parameter). For the linear jerk (quadratic acceleration) method, (α, β, γ) reduce to $(\frac{1}{24}, \frac{1}{6}, \frac{1}{2})$, whereas in the case of the constant (average) jerk (linear acceleration) method, (α, β, γ) reduce to $(\frac{1}{12}, \frac{1}{4}, \frac{1}{2})$.

Next, after rewriting (2.86) for the $(n+1)$-th time step, and, subsequently, introducing (2.90), there result the following effective system matrix

$\{\mathbf{K}^{\mathbf{eff}}\}$, and effective load vector $\{\mathbf{R}^{\mathbf{eff}}\}_{n+1}$

$$\{\mathbf{K}^{\mathbf{eff}}\}\ \dddot{\mathbf{d}}_{n+1} = \{\mathbf{R}^{\mathbf{eff}}\}_{n+1}, \tag{2.91}$$

where

$$\{\mathbf{K}^{\mathbf{eff}}\} = \mathbf{M} + \mathbf{C}\ \gamma\Delta\mathrm{t} + \mathbf{K}\ \beta\Delta\mathrm{t}^2 + \mathbf{G}\ \alpha\Delta\mathrm{t}^3, \tag{2.92a}$$

$$\begin{aligned} \{\mathbf{R}^{\mathbf{eff}}\}_{n+1} = \mathbf{F}_{n+1} &- \mathbf{C}\left[\ddot{\mathbf{d}}_n + (1-\gamma)\,\Delta\mathrm{t}\ \dddot{\mathbf{d}}_n\right] \\ &- \mathbf{K}\left[\dot{\mathbf{d}}_n + \Delta\mathrm{t}\ \ddot{\mathbf{d}}_n + \left(\frac{1}{2}-\beta\right)\Delta\mathrm{t}^2\dddot{\mathbf{d}}_n\right] \\ &- \mathbf{G}\left[\mathbf{d}_n + \Delta\mathrm{t}\ \dot{\mathbf{d}}_n + \frac{\Delta\mathrm{t}^2}{2}\ddot{\mathbf{d}}_n + \left(\frac{1}{6}-\alpha\right)\Delta\mathrm{t}^3\dddot{\mathbf{d}}_n\right]. \end{aligned} \tag{2.92b}$$

Equation (2.91) allows for the computation of the third-order terms at every $(n+1)$ time step; lower-order terms for the same time step are then recoverable via (2.90). In the applications that follow we used the average jerk (linear acceleration) scheme.

2.3.5 Numerical experiments

To test the accuracy of the mixed axisymmetric unsplit-field PML formulation, we discuss next two numerical experiments. The first pertains to a homogeneous half-space, whereas the second focuses on the effects of heterogeneity and involves a horizontally-layered system. For graphical presentation reasons, and without loss of generality, we have used low wave velocities to allow for clear wave front separation. In both simulations, we apply a distributed stress load on the surface, with a Ricker pulse time signature. The

Algorithm 2.2 Direct integration by *extended* Newmark-β method

```
procedure ExtendedNewmark($nts$)                          ▷ nts: number of time steps
    Assemble $\mathbf{M}$, $\mathbf{C}$, $\mathbf{K}$ and $\mathbf{G}$
    Set $\mathbf{d}_0$, $\dot{\mathbf{d}}_0$ and $\ddot{\mathbf{d}}_0$                        ▷ initial conditions
    Compute $\dddot{\mathbf{d}}_0$                                          ▷ eq. (2.86)
        $\dddot{\mathbf{d}}_0 = \mathbf{M}^{-1}\left[\mathbf{F}_0 - \mathbf{C}\ddot{\mathbf{d}}_0 - \mathbf{K}\dot{\mathbf{d}}_0 - \mathbf{G}\mathbf{d}_0\right]; n = -1$
    Set $\alpha$, $\beta$ and $\gamma$                               ▷ integration parameters
    Assemble $\{\mathbf{K}^{\mathbf{eff}}\}$                                   ▷ eq. (2.92a)
    $n \leftarrow 0$
    while $n < nts$ do                    ▷ integration is complete if $n$ is $nts$
        Assemble $\{\mathbf{R}^{\mathbf{eff}}\}_{n+1}$                         ▷ eq. (2.92b)
        Compute $\dddot{\mathbf{d}}_{n+1}$                                  ▷ eq. (2.91)
        Update $\mathbf{d}_{n+1}$, $\dot{\mathbf{d}}_{n+1}$ and $\ddot{\mathbf{d}}_{n+1}$                  ▷ eq. (2.90)
        Output $\mathbf{d}_{n+1}$                                      ▷ if desired
        $n \leftarrow n + 1$
    end while
end procedure
```

pulse is defined as

$$\mathrm{T_p}(t) = \frac{(0.25u^2 - 0.5)e^{-0.25u^2} - 13e^{-13.5}}{0.5 + 13e^{-13.5}} \qquad \text{with } 0 \leq t \leq \frac{6\sqrt{6}}{\omega_r}, \tag{2.93}$$

where

$$u = \omega_r t - 3\sqrt{6}, \tag{2.94}$$

and ω_r is the characteristic Ricker central circular frequency ($= 2\pi f_r$) of the pulse. Here, we used $f_r = 4$ Hz, and an amplitude of 10 Pa as depicted in Fig. 2.4.

Beyond comparisons of time histories at select target locations, as a measure of PML performance, we also provide plots of time-dependent errors relative to a reference solution. We use the same error metrics we used in section 2.2.5 for the two-dimensional case (2.54,2.55,2.56).

2.3.5.1 Homogeneous medium

We considered first a homogeneous half-space with density $\rho = 2200$ kg/m^3, shear wave velocity $c_s \simeq 5.81$ m/s, and Poisson ratio $\nu = 0.2$. We truncated the semi-infinite extent of the original domain arriving at a 10m × 10m two-dimensional computational domain, through the introduction of a finite height (10m) cylindrical surface of 10m radius. Surrounding the truncation surface is a 1m-thick PML, as shown in Fig. 2.24; the PML wraps around the cylindrical truncation surface and extends also to the bottom of the computational domain. Symmetry boundary conditions were imposed along the axis of symmetry. Both the PML and the regular domain were discretized by quadratic quadrilateral elements with an element size of 0.1m. The mesh in the vicinity of the loading was refined by using 0.025m quadratic quadrilateral elements to properly resolve the local load effects. The discretization resulted in a 10-cell-thick PML. The reflection coefficient R was set to 10^{-8}. We used a time step of 0.002 seconds, and let the simulation run for 5 seconds. The time histories of the displacements (u_r, u_z), and stresses $(\sigma_{rr}, \sigma_{\theta\theta}, \sigma_{zz}, \sigma_{rz})$ are sampled at seven locations $(sp_i, i = 1 \ldots 7)$, as shown in Fig. 2.24.

The displacement time histories at the various sampling points were compared against the response obtained using an enlarged domain with fixed boundaries in lieu of the PMLs, and a classical displacement-based axisymmetric formulation. The enlarged domain's size (40m × 40m) was defined such that, during the specified time interval of interest (5 seconds), reflections from its fixed exterior boundaries do not travel back and interfere with the

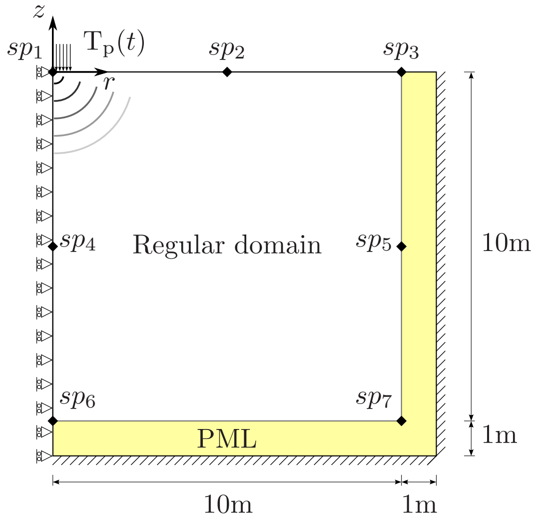

Figure 2.24: A PML-truncated axisymmetric domain subjected to a stress disk load on its surface over the region (0m $\leq r \leq$ 1m)

wave motion in the computational domain of interest. Figure 2.25 depicts the comparison of the response time histories for u_z at various sp_i points. As it can be seen, the agreement is excellent.

Figure 2.26 depicts snapshots of u_z taken at two different times ($t =$ 1.35s, 1.65s) for both the PML-truncated and the enlarged domain. The solid black lines in all the figures on the left column delineate the regular domain-PML interface. The right column figures depict snapshots taken of the enlarged domain simulations. Therein the dashed lines denote where the PML interface would have been (there is no PML in this case), in order to ease the comparison between the two sets of figures. Notice the excellent agreement (in the visual norm) of the two snapshot sets. Notice also the smoothness of the displacement contours along the regular domain-PML interface, betraying

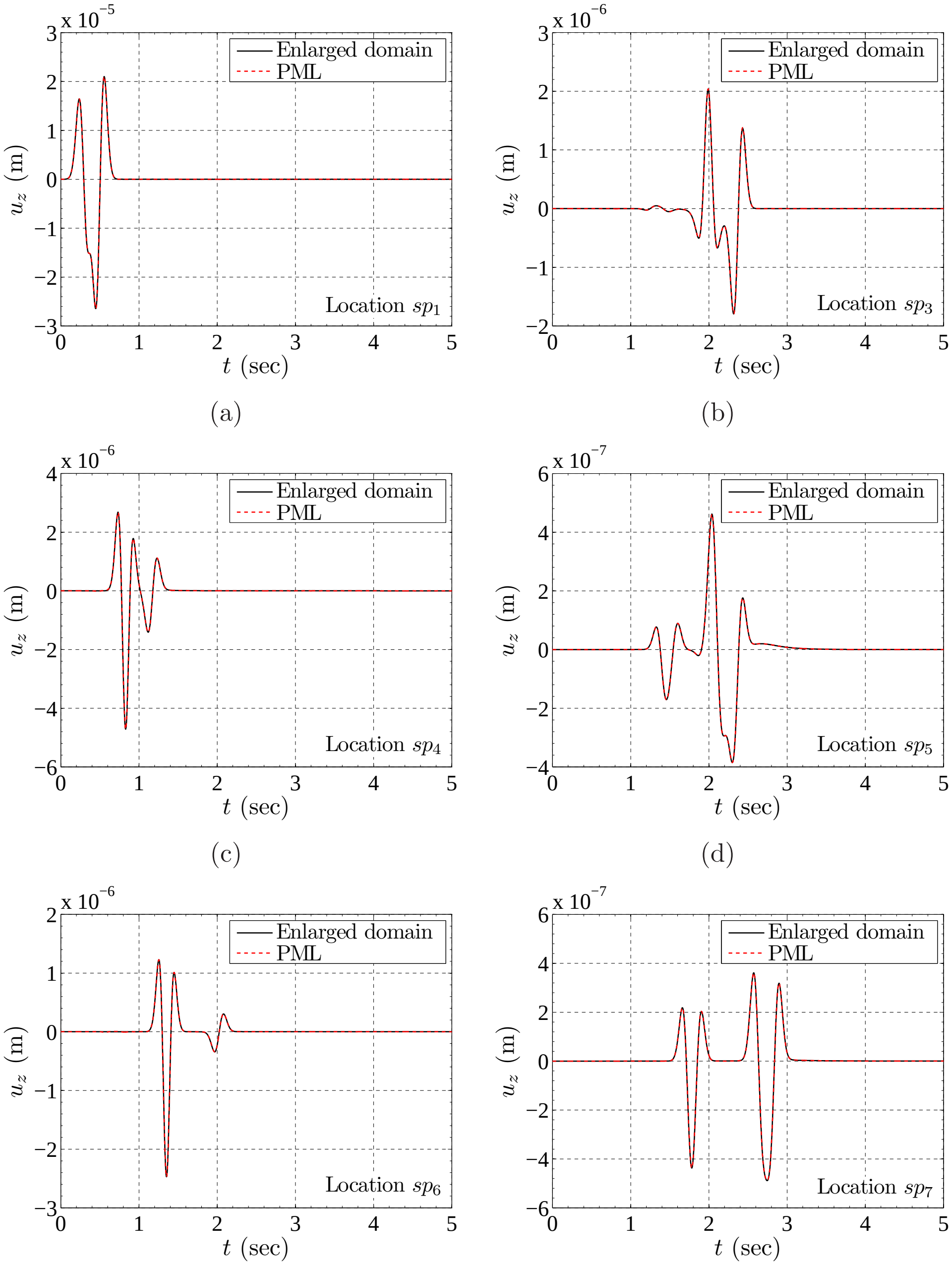

(a) (b) (c) (d) (e) (f)

Figure 2.25: Time histories of u_z sampled within the regular domain and on the regular domain-PML interface

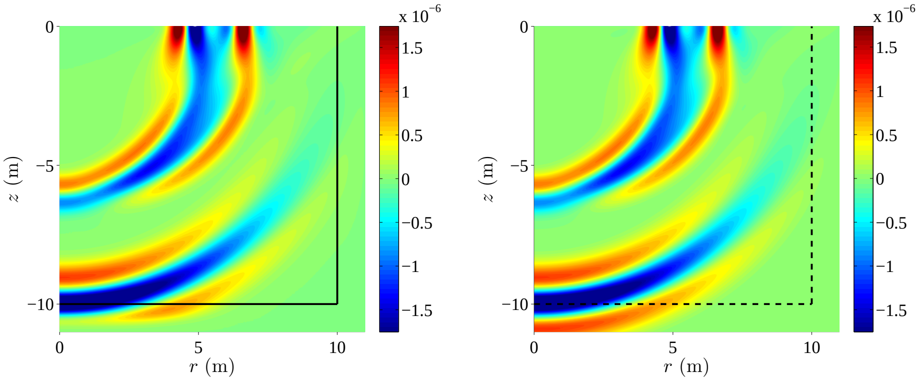

(a) u_z at $t = 1.35$s (PML) (b) u_z at $t = 1.35$s (ED)

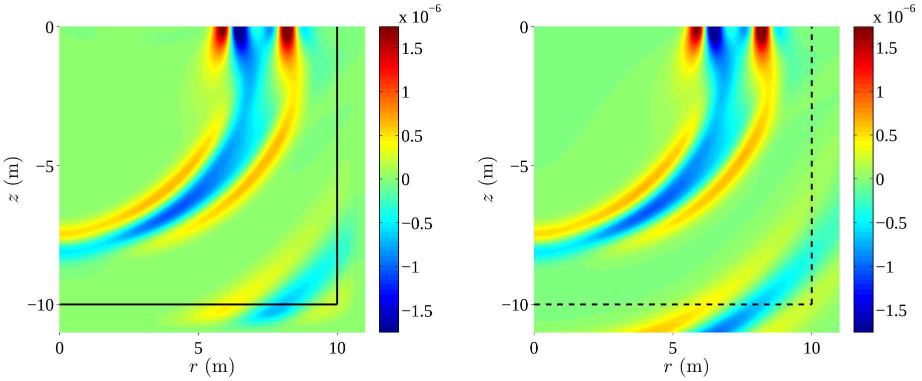

(c) u_z at $t = 1.65$s (PML) (d) u_z at $t = 1.65$s (ED)

Figure 2.26: Comparison of u_z snapshots between the PML-truncated (left column) and enlarged (right column) domains - homogeneous medium

reflection-less PML behavior. Within the domain notice also the two distinct P- and S-wave trains: each wave train is marked by a tri-band, corresponding to the maxima and minima of the Ricker pulse. Figure 2.27 depicts snapshots (taken at two distinct times) of σ_{zz} for the PML-truncated domain; notice that there are no reflections from the interface.

Figure 2.28 shows the response time histories of u_z and σ_{zz} at a few

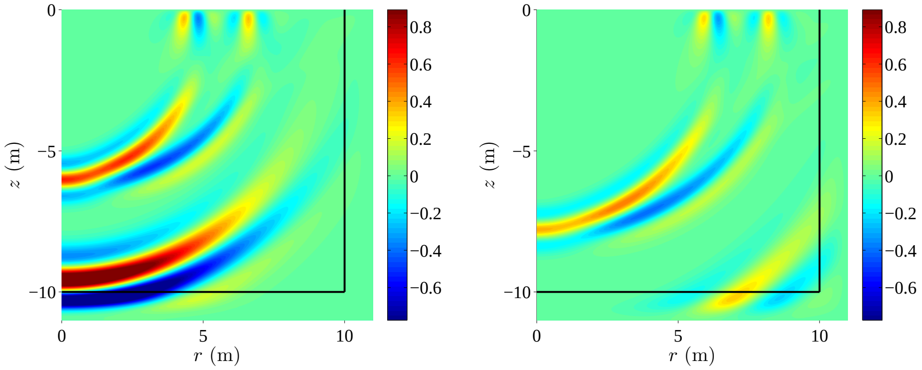

(a) σ_{zz} at $t = 1.35$s (b) σ_{zz} at $t = 1.65$s

Figure 2.27: Snapshots of σ_{zz} for the PML-truncated domain - homogeneous medium

sampling points. It is apparent from the figure that causality holds (sometimes a concern with PML implementations), and the response is free of spurious reflections. No numerical instabilities are observed.

Next, we illustrate the performance of the PML via the error metrics defined earlier. Figure 2.29 depicts the time-dependent displacement norm comparison and the normalized time-dependent relative error $e(t)$ in percent. The efficacy and quality of the PML is nicely corroborated by Fig. 2.29(b) with a relative error that stays below 0.18% at all times.

To further test the quality of the obtained solutions, we record the energy within the regular domain as a function of time for different values of the reflection coefficient R, between $R = 10^{-1}$ and 10^{-8}. Figure 2.30 shows the energy decay plotted in standard (left), and semi-log scale (right). Shown on the same figure is a reference energy decay corresponding to the enlarged domain (recall that this has been obtained using an independent displacement-

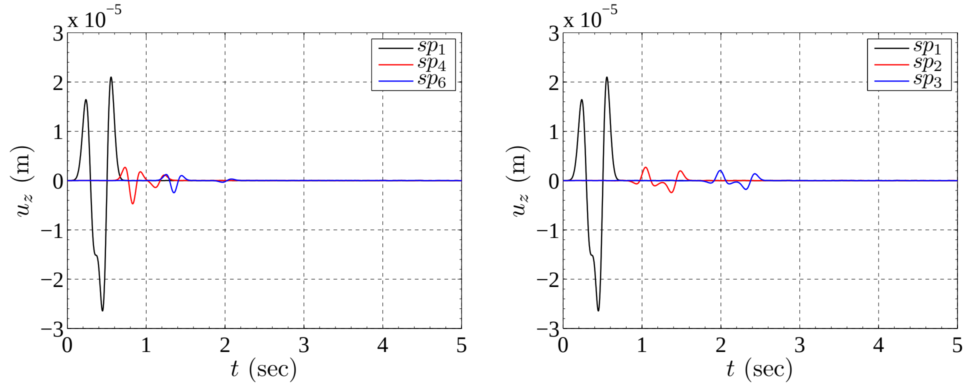

(a) u_z sampled at sp_1, sp_4, sp_6 (b) u_z sampled at sp_1, sp_2, sp_3

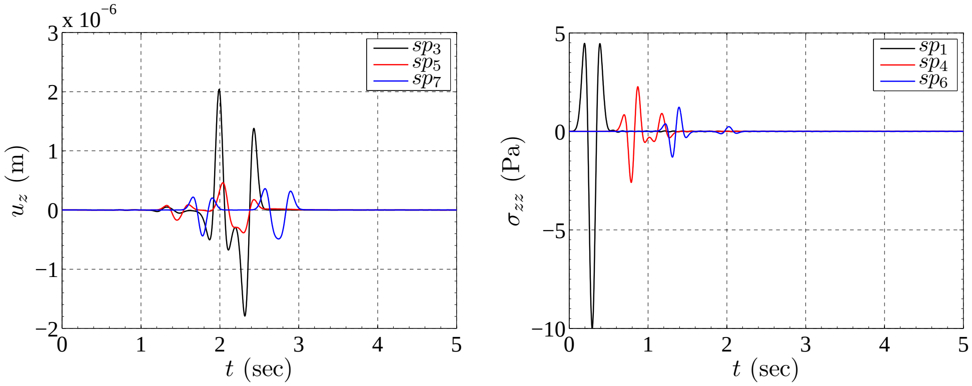

(c) u_z sampled at sp_3, sp_5, sp_7 (d) σ_{zz} sampled at sp_1, sp_4, sp_6

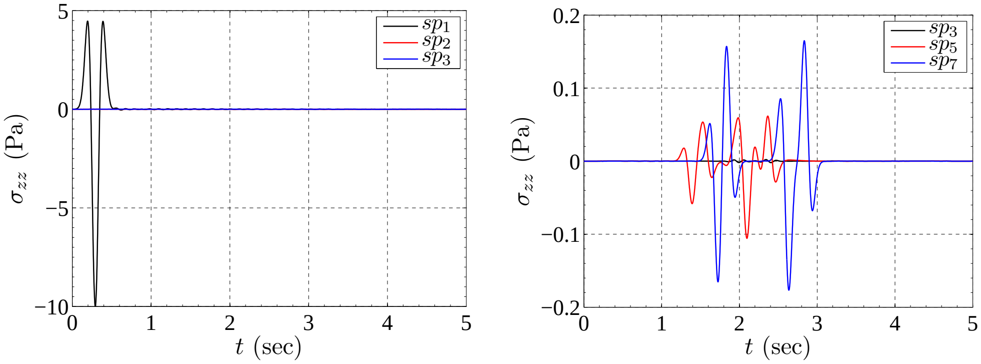

(e) σ_{zz} sampled at sp_1, sp_2, sp_3 (f) σ_{zz} sampled at sp_3, sp_5, sp_7

Figure 2.28: Time histories of u_z and σ_{zz} at sampling points

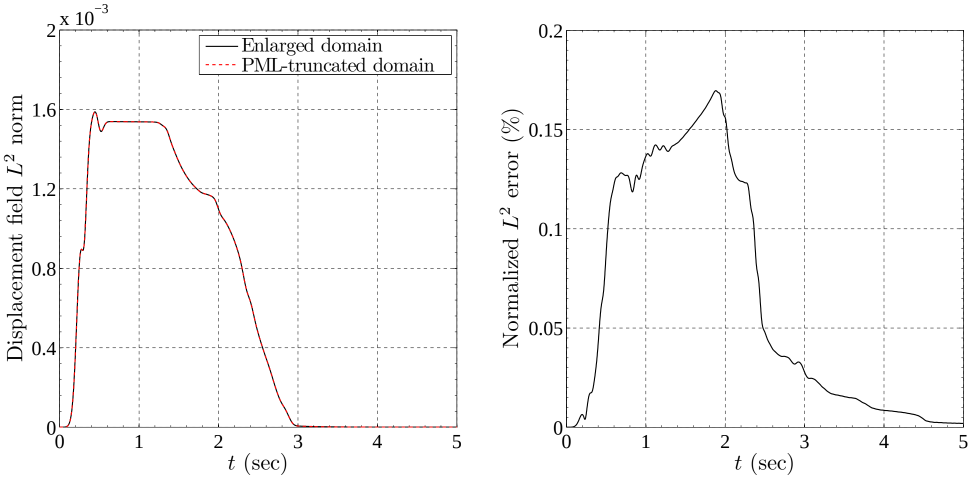

(a) Displacement field norm $D(t;\Omega^{\mathrm{RD}})$

(b) Relative error $e(t)$

Figure 2.29: Error metrics for the homogeneous domain

based formulation). There is a sharp ascent of the energy until about 0.4s, which corresponds to the highest peak of the Ricker pulse. By about $t = 1.05$s, the P-wave train has reached the bottom PML, with the first peak arriving at about $t = 1.25$s, and the major P-wave peak at about $t = 1.35$s. This is the point in time when the highest P-wave peaks reach the cylindrical truncation surface as well, and it is marked on the energy decay plot by the beginning of a sharp decline in the energy, as one would expect since the strongest wave motion has left the domain. By about $t = 2.02$s, the highest peak of the S-wave train has also reached the side and bottom PMLs (but not yet the domain corner), and also contributes to another sharp decline, as evidenced in the figure by a change in the slope. At, approximately, $t = 2.83$s the last S-wave peak has left the domain in the vicinity of the domain corner, and by about $t = 3$s all motion has seized within the domain –all of which are evident in the energy decay plot. Notice further that for almost all R values (except for $R = 10^{-1}$) the performance of the new fully-mixed PML formulation matches the enlarged domain's quite satisfactorily. A closer look, using the semi-log scale, reveals that lower R values enforce more rapid, and more accurate, decay, with R values less than about 10^{-6} driving the residual domain energy to about 10^{-8} or more than 5 orders of magnitude less than the peak domain energy.

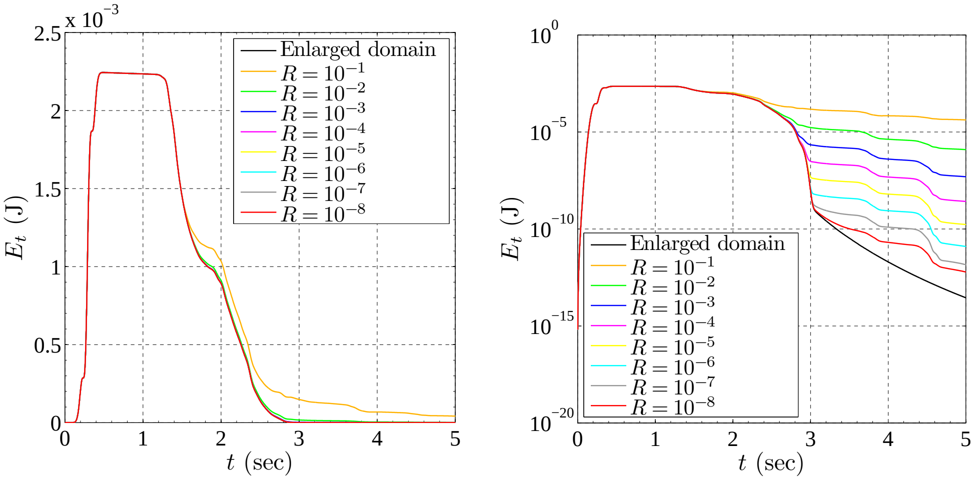

Figure 2.30: Total energy decay inside the regular domain - homogeneous medium

Moreover, we let the simulation run for 40 seconds with a time step of 0.0002 seconds. As evident from Fig. 2.31, no numerical instabilities were observed during the total simulation time that consisted of 200,000 time steps.

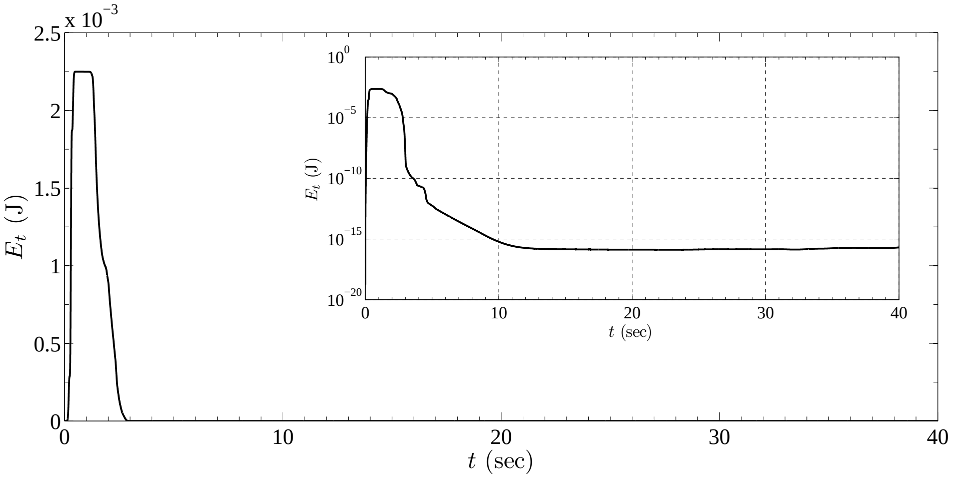

Figure 2.31: Long-time total energy decay inside the regular domain - homogeneous medium

2.3.5.2 Heterogeneous medium

To illustrate the performance of the PML in heterogeneous media, we consider a layered profile. Using a time step of 0.002 seconds, we let the simulations run for 8 seconds. As shown in Fig. 2.32, we considered a 5m × 5m layered medium, surrounded by 1m-thick PML on its cylindrical surface and bottom. We define

$$c_s(z) = \begin{cases} \sim 2.90 \text{ m/s}, & \text{for } -2\text{m} \le z \le 0\text{m}, \\ \sim 5.81 \text{ m/s}, & \text{for } -6\text{m} \le z < -2\text{m}, \end{cases} \tag{2.95}$$

and the Poisson's ratio is again $\nu = 0.2$. The material interfaces were extended horizontally into the PML, thereby avoiding sudden material changes at the interface between the PML and the regular domain. The PML and the regular domain were discretized by quadratic quadrilateral elements with an element size of 0.1m, whereas in the vicinity of the surface load we used

0.025m-elements. The reflection coefficient R was set to 10^{-8}, and we again simulated the wave motion using the PML formulation, as well as a displacement-based formulation for an enlarged domain with fixed exterior boundaries.

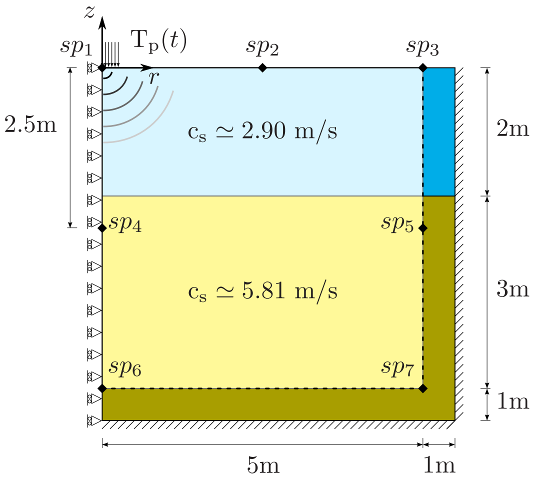

Figure 2.32: A PML-truncated axisymmetric domain subjected to a stress disk load on its surface over the region (0m $\leq r \leq$ 0.5m)

The displacement time histories at the various sampling points were compared against the response obtained using an enlarged domain (40m × 40m). The enlarged domain's size was defined such that, during the specified time interval of interest (8 seconds), reflections from its fixed exterior boundaries do not travel back and interfere with the wave motion in the computational domain of interest. Figure 2.33 depicts the comparison of the response time histories for u_z at various sp_i points. As it can be seen, the agreement is impressive.

Figure 2.34 shows the snapshots of the displacement u_z taken at two

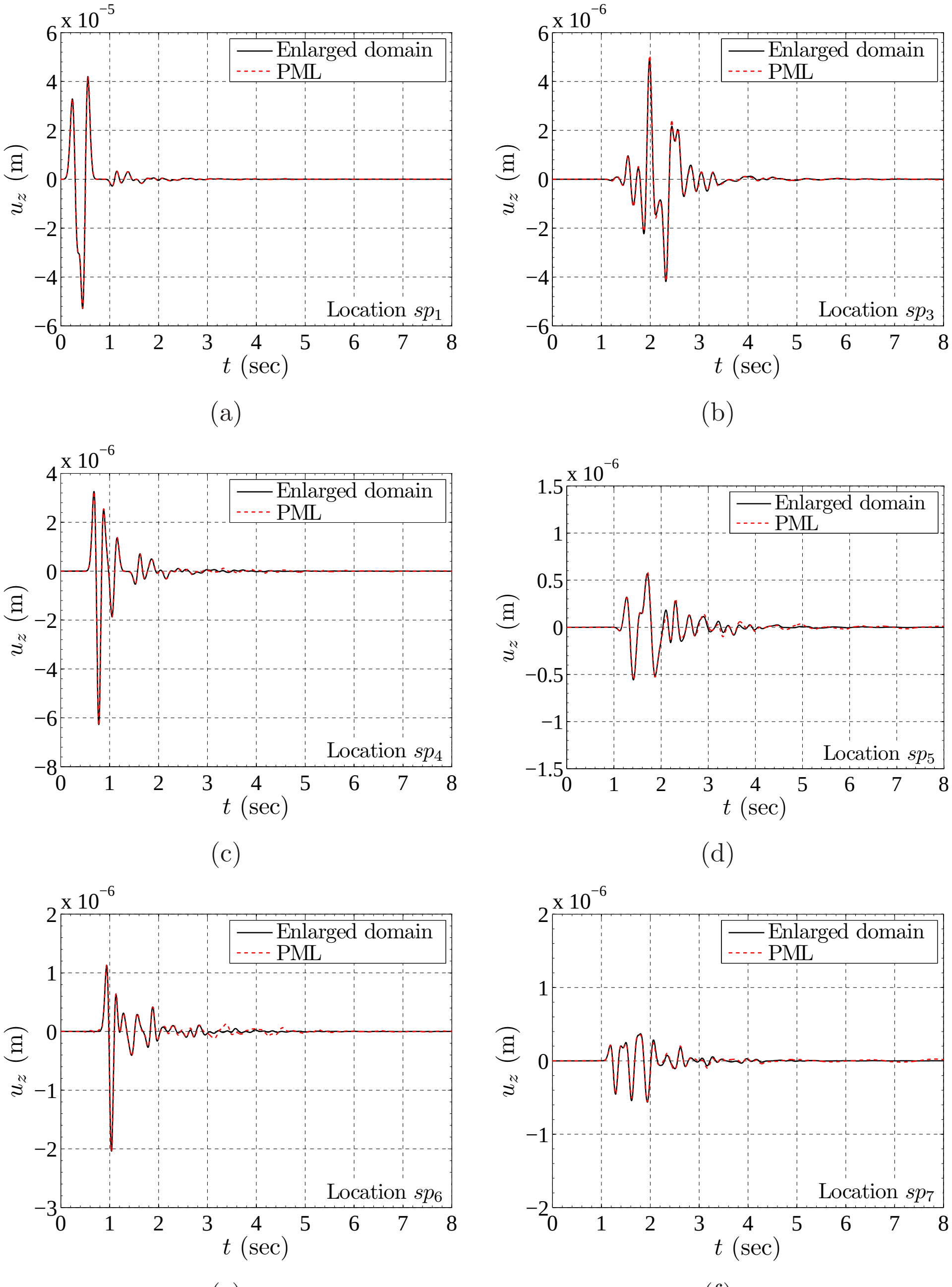

(a) (b)

(c) (d)

(e) (f)

Figure 2.33: Time histories of u_z sampled within the regular domain and on the regular domain-PML interface

different times ($t = 0.96$s and 1.16s) for both the PML-truncated domain and the enlarged domain. As before, we mark the PML-interface with dashed lines in the case of the enlarged domain to ease the visual comparison. The agreement is remarkable with no signs of instability or artificial reflections from the interface between the PML and regular domain. It is interesting to note that the waves are trapped inside the top layer due to the high-contrast $(1:2)$ of the material properties of the two layers. The effect of the layer interface is clearly visible in the snapshots at $z = -2$m.

Next, we quantify the performance of the PML via the error metrics defined earlier. Figure 2.35 depicts the time-dependent displacement norm comparison and the normalized time-dependent relative error $e(t)$ in percent. The quality of the PML manifests itself with a nicely decaying relative error shown in Fig. 2.35(b).

Lastly, Fig. 2.36 depicts the energy decay within the layered medium: in this case the decay is considerably more gradual than in the homogeneous case, since there are multiple reflections off of the layer interface that travel back to the free surface, reflect at the free surface, travel downwards to the layer interface, partially reflect there, travel back to the free surface, and so on and so forth. We explored four different reflection coefficient values ($R = 10^{-2}$, $R = 10^{-4}$, $R = 10^{-6}$, and $R = 10^{-8}$). The observed behavior is similar to the one discussed in the case of the homogeneous host: overall, the PML performance is excellent, with no discernible reflections or instabilities, even in the presence of heterogeneity.

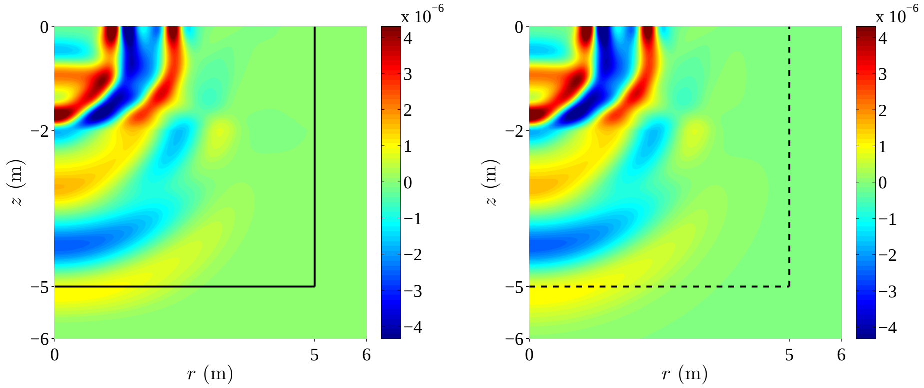

(a) u_z at $t = 0.96$s (PML) (b) u_z at $t = 0.96$s (ED)

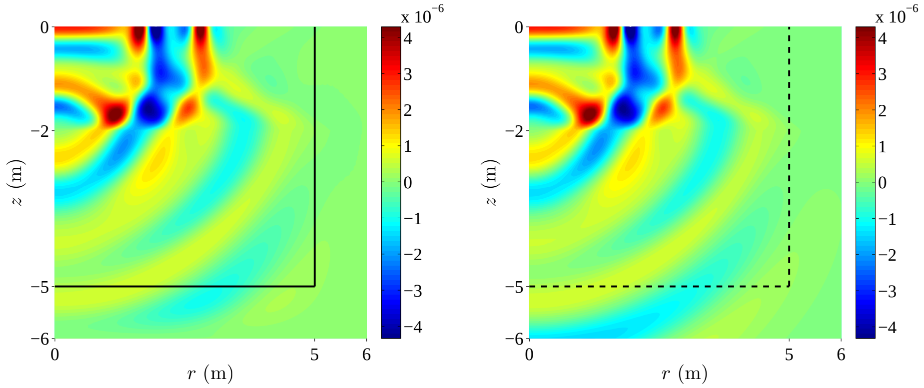

(c) u_z at $t = 1.16$s (PML) (d) u_z at $t = 1.16$s (ED)

Figure 2.34: Comparison of u_z snapshots between the PML-truncated (left column) and enlarged (right column) domains - heterogeneous medium

Finally, we remark that growth of spurious reflections has been reported by others when waves impinge at grazing incidence at the PML-regular domain interface. It has also been often reported that the grazing incidence difficulty is associated with the choice of the classical stretching function, which, by construction, is singular at zero frequency (this has been the choice herein as well). To overcome the singularity, and possibly the perceived difficulty

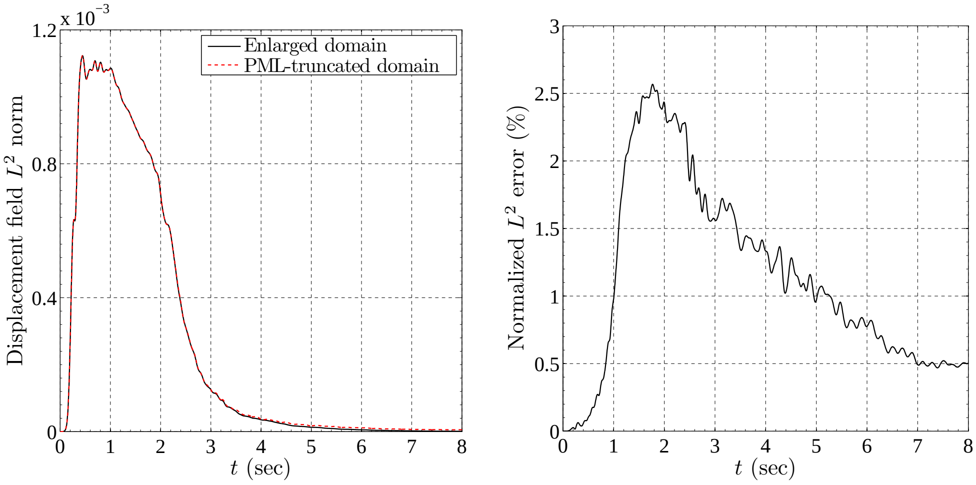

(a) Displacement field norm $D(t; \Omega^{\text{RD}})$ (b) Relative error $e(t)$

Figure 2.35: Error metrics for the heterogeneous domain

with the grazing angle incidence that has been attributed to the frequency singularity, modified stretching functions have been proposed that are not singular at zero frequency (as discussed in the introduction, the CPML is the most notable example of such a development: see, for example, [118]). The CPML has been reported to alleviate, but not eliminate the growth of spurious reflections (see, for example, the comparisons reported in [120]). To date, all reported studies are purely numerical, and a theoretical proof of the origin of the difficulty remains elusive. It is not clear whether indeed the origin of the spurious growth at grazing incidence is due to the choice of the stretching function; moreover, careful parameterization of the PML is also capable of alleviating the growth. Herein, we too are not addressing the grazing angle incidence issue, pending detailed studies that escape the scope of this dissertation.

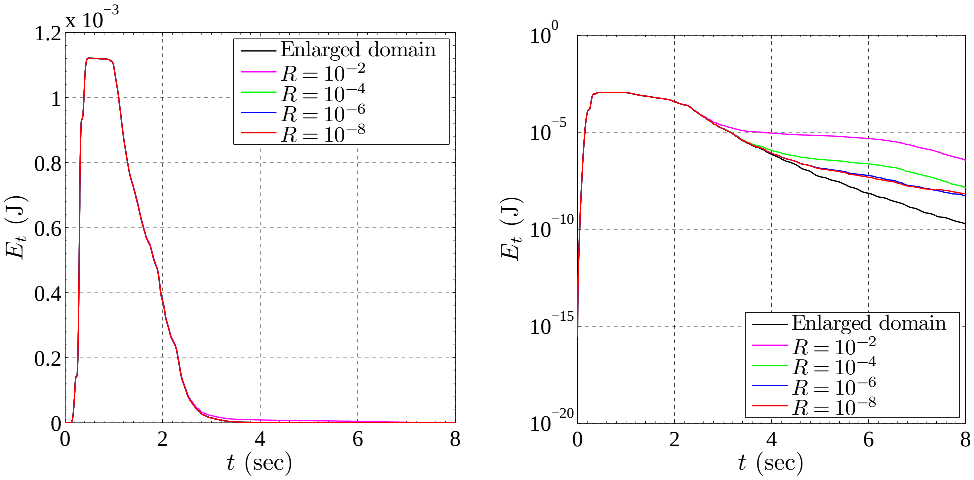

Figure 2.36: Total energy decay inside the regular domain - heterogeneous medium

2.4 Fully-mixed 3D elastic wave modeling

In this section, we extend the development reported in sections 2.2 and 2.3 to the three-dimensional case. The resulting forms differ from the two-dimensional case, but are similar to the axisymmetric case, and, thus, the semi-discrete forms include again a jerk term requiring the extended Newmark-β scheme for time integration as described earlier in section 2.3.4.

2.4.1 In the frequency-domain

Application of the Fourier transform to the equilibrium, constitutive, and kinematic equations (2.17a-2.17c) results in

$$\mathbf{div}\,\hat{\mathcal{S}}^T + \hat{\mathbf{f}} = -\omega^2 \rho \hat{\mathbf{u}}, \tag{2.96a}$$

$$\hat{\mathcal{S}} = \mathcal{C} : \hat{\mathcal{E}}, \tag{2.96b}$$

$$\hat{\mathcal{E}} = \frac{1}{2}\left[\nabla\hat{\mathbf{u}} + (\nabla\hat{\mathbf{u}})^T\right], \tag{2.96c}$$

Next, we introduce the coordinate-stretched form for each coordinate,

$$\tilde{s} = \int_0^s \varepsilon_s(s')ds', \qquad \varepsilon_s(s,\omega) = \alpha_s(s) + \frac{\beta_s(s)}{i\omega}, \qquad s = x, y, z. \tag{2.97}$$

Then, we apply complex coordinate-stretching by making use of (2.97) and the definitions (2.18). The stretching is applied first to the equations of motion (2.96a) by replacing (x, y, z) with the stretched coordinates $(\tilde{x}, \tilde{y}, \tilde{z})$; to clarify, we make use of unabridged notation:

$$\frac{\partial\hat{\sigma}_{xx}}{\partial\tilde{x}} + \frac{\partial\hat{\sigma}_{yx}}{\partial\tilde{y}} + \frac{\partial\hat{\sigma}_{zx}}{\partial\tilde{z}} + \hat{f}_x = -\omega^2\rho\hat{u}_x, \tag{2.98a}$$

$$\frac{\partial\hat{\sigma}_{xy}}{\partial\tilde{x}} + \frac{\partial\hat{\sigma}_{yy}}{\partial\tilde{y}} + \frac{\partial\hat{\sigma}_{zy}}{\partial\tilde{z}} + \hat{f}_y = -\omega^2\rho\hat{u}_y, \tag{2.98b}$$

$$\frac{\partial\hat{\sigma}_{xz}}{\partial\tilde{x}} + \frac{\partial\hat{\sigma}_{yz}}{\partial\tilde{y}} + \frac{\partial\hat{\sigma}_{zz}}{\partial\tilde{z}} + \hat{f}_z = -\omega^2\rho\hat{u}_z. \tag{2.98c}$$

Using (2.7), the above equations can be expressed in terms of the unstretched coordinates as

$$\frac{1}{\varepsilon_x}\frac{\partial \hat{\sigma}_{xx}}{\partial x} + \frac{1}{\varepsilon_y}\frac{\partial \hat{\sigma}_{yx}}{\partial y} + \frac{1}{\varepsilon_z}\frac{\partial \hat{\sigma}_{zx}}{\partial z} + \hat{f}_x = -\omega^2 \rho \hat{u}_x, \tag{2.99a}$$

$$\frac{1}{\varepsilon_x}\frac{\partial \hat{\sigma}_{xy}}{\partial x} + \frac{1}{\varepsilon_y}\frac{\partial \hat{\sigma}_{yy}}{\partial y} + \frac{1}{\varepsilon_z}\frac{\partial \hat{\sigma}_{zy}}{\partial z} + \hat{f}_y = -\omega^2 \rho \hat{u}_y, \tag{2.99b}$$

$$\frac{1}{\varepsilon_x}\frac{\partial \hat{\sigma}_{xz}}{\partial x} + \frac{1}{\varepsilon_y}\frac{\partial \hat{\sigma}_{yz}}{\partial y} + \frac{1}{\varepsilon_z}\frac{\partial \hat{\sigma}_{zz}}{\partial z} + \hat{f}_z = -\omega^2 \rho \hat{u}_z. \tag{2.99c}$$

Next, we multiply both sides by $\varepsilon_x\varepsilon_y\varepsilon_z$. Using again the definition of divergence (2.18), the equations of equilibrium can be compactly recast as

$$\mathbf{div}\left(\hat{\mathbb{S}}^T\tilde{\Lambda}\right) + \varepsilon_x\varepsilon_y\varepsilon_z\hat{\mathbf{f}} = -\omega^2\rho\varepsilon_x\varepsilon_y\varepsilon_z\hat{\mathbf{u}}, \tag{2.100}$$

where $\tilde{\Lambda}$ is defined as follows by making use of (2.97)

$$\begin{aligned}\tilde{\Lambda} = \begin{bmatrix}\varepsilon_y\varepsilon_z & 0 & 0\\ 0 & \varepsilon_x\varepsilon_z & 0\\ 0 & 0 & \varepsilon_x\varepsilon_y\end{bmatrix} &= \begin{bmatrix}\alpha_y\alpha_z & 0 & 0\\ 0 & \alpha_x\alpha_z & 0\\ 0 & 0 & \alpha_x\alpha_y\end{bmatrix} + \frac{1}{(i\omega)^2}\begin{bmatrix}\beta_y\beta_z & 0 & 0\\ 0 & \beta_x\beta_z & 0\\ 0 & 0 & \beta_x\beta_y\end{bmatrix}\\ &+ \frac{1}{i\omega}\begin{bmatrix}\alpha_z\beta_y + \beta_z\alpha_y & 0 & 0\\ 0 & \alpha_x\beta_z + \beta_x\alpha_z & 0\\ 0 & 0 & \alpha_x\beta_y + \beta_x\alpha_y\end{bmatrix}\\ &= \tilde{\Lambda}_e + \frac{1}{i\omega}\tilde{\Lambda}_p + \frac{1}{(i\omega)^2}\tilde{\Lambda}_w.\end{aligned} \tag{2.101}$$

We remark again that in the regular domain, $\tilde{\Lambda}_e$ reduces to the identity tensor, whereas $\tilde{\Lambda}_p$ and $\tilde{\Lambda}_w$ vanish identically. After substituting (2.101) into (2.100), employing (2.97), multiplying both sides by $i\omega$, rearranging and grouping like-terms, there results

$$\begin{aligned}\mathbf{div}\left(i\omega\hat{\mathbb{S}}^T\tilde{\Lambda}_e + \hat{\mathbb{S}}^T\tilde{\Lambda}_p + \frac{1}{i\omega}\hat{\mathbb{S}}^T\tilde{\Lambda}_w\right) + i\omega a\hat{\mathbf{f}} + b\hat{\mathbf{f}} + \frac{c}{i\omega}\hat{\mathbf{f}} + \frac{d}{(i\omega)^2}\hat{\mathbf{f}}\\ = \rho\left[(i\omega)^3 a\hat{\mathbf{u}} + (i\omega)^2 b\hat{\mathbf{u}} + i\omega c\hat{\mathbf{u}} + d\hat{\mathbf{u}}\right],\end{aligned} \tag{2.102}$$

where

$$
\begin{aligned}
&a = \alpha_x \alpha_y \alpha_z, && b = \alpha_x \alpha_y \beta_z + \alpha_z \alpha_x \beta_y + \alpha_y \alpha_z \beta_x, \\
&c = \alpha_x \beta_z \beta_y + \alpha_z \beta_y \beta_x + \alpha_y \beta_x \beta_z, && d = \beta_x \beta_y \beta_z.
\end{aligned}
\tag{2.103}
$$

We note that, within the regular domain, $a \equiv 1, b \equiv 0, c \equiv 0, d \equiv 0$, and since the body forces $\mathbf{f}$ are non-vanishing only within the regular domain ($\mathbf{f}$ vanishes within the PML), (2.102) reduces further to:

$$
\begin{aligned}
&\mathbf{div}\left(i\omega \hat{\mathbb{S}}^T \tilde{\Lambda}_e + \hat{\mathbb{S}}^T \tilde{\Lambda}_p + \frac{1}{i\omega} \hat{\mathbb{S}}^T \tilde{\Lambda}_w \right) + i\omega a \hat{\mathbf{f}} \\
&\qquad = \rho \left[(i\omega)^3 a \hat{\mathbf{u}} + (i\omega)^2 b \hat{\mathbf{u}} + i\omega c \hat{\mathbf{u}} + d \hat{\mathbf{u}} \right].
\end{aligned}
\tag{2.104}
$$

Similarly, we apply complex coordinate-stretching to the kinematic equation (2.17c); there results

$$
\hat{\mathcal{E}} = \frac{1}{2} \left\{ (\nabla \hat{\mathbf{u}}) \begin{bmatrix} \frac{1}{\varepsilon_x} & 0 & 0 \\ 0 & \frac{1}{\varepsilon_y} & 0 \\ 0 & 0 & \frac{1}{\varepsilon_z} \end{bmatrix} + \begin{bmatrix} \frac{1}{\varepsilon_x} & 0 & 0 \\ 0 & \frac{1}{\varepsilon_y} & 0 \\ 0 & 0 & \frac{1}{\varepsilon_z} \end{bmatrix} (\nabla \hat{\mathbf{u}})^T \right\}. \tag{2.105}
$$

Next, we multiply both sides by $(i\omega)^2 \varepsilon_x \varepsilon_y \varepsilon_z$ to obtain

$$
(i\omega)^2 \varepsilon_x \varepsilon_y \varepsilon_z \hat{\mathcal{E}} = \frac{1}{2} (i\omega)^2 \left[(\nabla \hat{\mathbf{u}}) \tilde{\Lambda} + \tilde{\Lambda} (\nabla \hat{\mathbf{u}})^T \right], \tag{2.106}
$$

where the stretching tensor $\tilde{\Lambda}$ is defined in (2.101). Substituting (2.101) and (2.97) into (2.106), rearranging and grouping like-terms, yields

$$
\begin{aligned}
&(i\omega)^2 a \hat{\mathcal{E}} + i\omega b \hat{\mathcal{E}} + c \hat{\mathcal{E}} + \frac{d}{i\omega} \hat{\mathcal{E}} = \frac{1}{2} (i\omega)^2 \left[(\nabla \hat{\mathbf{u}}) \tilde{\Lambda}_e + \tilde{\Lambda}_e (\nabla \hat{\mathbf{u}})^T \right] \\
&\qquad + \frac{1}{2} i\omega \left[(\nabla \hat{\mathbf{u}}) \tilde{\Lambda}_p + \tilde{\Lambda}_p (\nabla \hat{\mathbf{u}})^T \right] + \frac{1}{2} \left[(\nabla \hat{\mathbf{u}}) \tilde{\Lambda}_w + \tilde{\Lambda}_w (\nabla \hat{\mathbf{u}})^T \right],
\end{aligned}
\tag{2.107}
$$

where a, b, c and d are defined in (2.103). Equations (2.104), (2.96b), and (2.107), constitute the stretched form of the governing frequency-domain equations, repeated below to ease their subsequent reference:

$$\begin{aligned}\mathbf{div}\left(i\omega\hat{\mathcal{S}}^T\tilde{\Lambda}_e + \hat{\mathcal{S}}^T\tilde{\Lambda}_p + \frac{1}{i\omega}\hat{\mathcal{S}}^T\tilde{\Lambda}_w\right) + i\omega a\hat{\mathbf{f}} \\ = \rho\left[(i\omega)^3 a\hat{\mathbf{u}} + (i\omega)^2 b\hat{\mathbf{u}} + i\omega c\hat{\mathbf{u}} + d\hat{\mathbf{u}}\right],\end{aligned} \tag{2.108a}$$

$$\hat{\mathcal{S}} = \mathcal{C} : \hat{\mathcal{E}}, \tag{2.108b}$$

$$\begin{aligned}(i\omega)^2 a\hat{\mathcal{E}} + i\omega b\hat{\mathcal{E}} + c\hat{\mathcal{E}} + \frac{d}{i\omega}\hat{\mathcal{E}} = \frac{1}{2}(i\omega)^2\left[(\nabla\hat{\mathbf{u}})\tilde{\Lambda}_e + \tilde{\Lambda}_e(\nabla\hat{\mathbf{u}})^T\right] \\ + \frac{1}{2}i\omega\left[(\nabla\hat{\mathbf{u}})\tilde{\Lambda}_p + \tilde{\Lambda}_p(\nabla\hat{\mathbf{u}})^T\right] + \frac{1}{2}\left[(\nabla\hat{\mathbf{u}})\tilde{\Lambda}_w + \tilde{\Lambda}_w(\nabla\hat{\mathbf{u}})^T\right].\end{aligned} \tag{2.108c}$$

2.4.2 In the time-domain

By taking the inverse Fourier transform of (2.108), there results

$$\begin{aligned}\mathbf{div}\left[\dot{\mathcal{S}}^T\tilde{\Lambda}_e + \mathcal{S}^T\tilde{\Lambda}_p + \left(\int_0^t \mathcal{S}^T d\tau\right)\tilde{\Lambda}_w\right] + a\dot{\mathbf{f}} \\ = \rho\left(a\dddot{\mathbf{u}} + b\ddot{\mathbf{u}} + c\dot{\mathbf{u}} + d\mathbf{u}\right),\end{aligned} \tag{2.109a}$$

$$\mathcal{S} = \mathcal{C} : \mathcal{E}, \tag{2.109b}$$

$$\begin{aligned}a\ddot{\mathcal{E}} + b\dot{\mathcal{E}} + c\mathcal{E} + d\left(\int_0^t \mathcal{E}d\tau\right) = \frac{1}{2}\Big[(\nabla\ddot{\mathbf{u}})\tilde{\Lambda}_e + \tilde{\Lambda}_e(\nabla\ddot{\mathbf{u}})^T \\ + (\nabla\dot{\mathbf{u}})\tilde{\Lambda}_p + \tilde{\Lambda}_p(\nabla\dot{\mathbf{u}})^T + (\nabla\mathbf{u})\tilde{\Lambda}_w + \tilde{\Lambda}_w(\nabla\mathbf{u})^T\Big].\end{aligned} \tag{2.109c}$$

Next, we define again the following stress and strain memory (or history) tensor terms:

$$\mathbf{S}(\mathbf{x},t) = \int_0^t \mathcal{S}(\mathbf{x},\tau)d\tau, \qquad \mathbf{E}(\mathbf{x},t) = \int_0^t \mathcal{E}(\mathbf{x},\tau)d\tau, \tag{2.110}$$

which are such that

$$\dot{\mathbf{S}}(\mathbf{x},t) = \mathcal{S}(\mathbf{x},t), \qquad \ddot{\mathbf{S}}(\mathbf{x},t) = \dot{\mathcal{S}}(\mathbf{x},t), \tag{2.111a}$$

$$\dot{\mathbf{E}}(\mathbf{x},t) = \mathcal{E}(\mathbf{x},t), \qquad \ddot{\mathbf{E}}(\mathbf{x},t) = \dot{\mathcal{E}}(\mathbf{x},t). \tag{2.111b}$$

Substitution of (2.110) and (2.111) into (2.109a-2.109c) leads to the time-domain equations of the unsplit-field PML formulation in three dimensions.

$$\mathbf{div}\left(\ddot{\mathbf{S}}^T\tilde{\Lambda}_e + \dot{\mathbf{S}}^T\tilde{\Lambda}_p + \mathbf{S}^T\tilde{\Lambda}_w\right) + a\dot{\mathbf{f}} = \rho\left(a\dddot{\mathbf{u}} + b\ddot{\mathbf{u}} + c\dot{\mathbf{u}} + d\mathbf{u}\right), \tag{2.112a}$$

$$\dot{\mathbf{S}} = \mathcal{C} : \dot{\mathbf{E}}, \tag{2.112b}$$

$$\begin{aligned} a\dddot{\mathbf{E}} + b\ddot{\mathbf{E}} + c\dot{\mathbf{E}} + d\mathbf{E} = \frac{1}{2}\Big[&(\nabla\ddot{\mathbf{u}})\tilde{\Lambda}_e + \tilde{\Lambda}_e(\nabla\ddot{\mathbf{u}})^T \\ &+ (\nabla\dot{\mathbf{u}})\tilde{\Lambda}_p + \tilde{\Lambda}_p(\nabla\dot{\mathbf{u}})^T + (\nabla\mathbf{u})\tilde{\Lambda}_w + \tilde{\Lambda}_w(\nabla\mathbf{u})^T\Big]. \end{aligned} \tag{2.112c}$$

2.4.3 Mixed finite element implementation

We introduce the constitutive law (2.112b) into the kinematic condition (2.112c), to arrive at

$$\mathbf{div}\left(\ddot{\mathbf{S}}^T\tilde{\Lambda}_e + \dot{\mathbf{S}}^T\tilde{\Lambda}_p + \mathbf{S}^T\tilde{\Lambda}_w\right) + a\dot{\mathbf{f}} = \rho\left(a\dddot{\mathbf{u}} + b\ddot{\mathbf{u}} + c\dot{\mathbf{u}} + d\mathbf{u}\right), \tag{2.113a}$$

$$\begin{aligned} \mathcal{D} : \left(a\dddot{\mathbf{S}} + b\ddot{\mathbf{S}} + c\dot{\mathbf{S}} + d\mathbf{S}\right) = \frac{1}{2}\Big[&(\nabla\ddot{\mathbf{u}})\tilde{\Lambda}_e + \tilde{\Lambda}_e(\nabla\ddot{\mathbf{u}})^T \\ &+ (\nabla\dot{\mathbf{u}})\tilde{\Lambda}_p + \tilde{\Lambda}_p(\nabla\dot{\mathbf{u}})^T + (\nabla\mathbf{u})\tilde{\Lambda}_w + \tilde{\Lambda}_w(\nabla\mathbf{u})^T\Big], \end{aligned} \tag{2.113b}$$

where $\mathcal{D}$ denotes the compliance tensor ($\mathbf{E} = \mathcal{D} : \mathbf{S}$).

Consider next the half-space problem depicted in Fig. 2.37. Let again $\Omega^{\mathrm{RD}} \cup \Omega^{\mathrm{PML}} = \Omega \subset \mathbb{R}^3$ denote the region occupied by the elastic body (Ω^{RD}), surrounded on its periphery and bottom by the PML buffer zone (Ω^{PML}). Ω is bounded by $\Gamma = \Gamma_D \cup \Gamma_N$, where $\Gamma_D \cap \Gamma_N = \emptyset$, and $\Gamma_D \equiv \Gamma_D^{\text{PML}}$, $\Gamma_N = \Gamma_N^{\text{RD}} \cup \Gamma_N^{\text{PML}}$. Then, we require that (2.113) hold in $\Omega \times \mathsf{J}$, subject to the following boundary and initial conditions:

$$\mathbf{u}(\mathbf{x}, t) = \mathbf{0} \qquad \text{on } \Gamma_D^{\text{PML}} \times \mathsf{J}, \tag{2.114a}$$

$$\left(\ddot{\mathbf{S}}^T \tilde{\Lambda}_e + \dot{\mathbf{S}}^T \tilde{\Lambda}_p + \mathbf{S}^T \tilde{\Lambda}_w\right) \mathbf{n} = \mathbf{0} \qquad \text{on } \Gamma_N^{\text{PML}} \times \mathsf{J}, \tag{2.114b}$$

$$\dot{\mathbf{S}}(\mathbf{x}, t)^T \mathbf{n} = \boldsymbol{g}_n(\mathbf{x}, t) \qquad \text{on } \Gamma_N^{\text{RD}} \times \mathsf{J}, \tag{2.114c}$$

$$\mathbf{u}(\mathbf{x}, 0) = \mathbf{0}, \quad \dot{\mathbf{u}}(\mathbf{x}, 0) = \mathbf{0}, \quad \ddot{\mathbf{u}}(\mathbf{x}, 0) = \mathbf{0} \qquad \text{in } \Omega, \tag{2.114d}$$

$$\mathbf{S}(\mathbf{x}, 0) = \mathbf{0}, \quad \dot{\mathbf{S}}(\mathbf{x}, 0) = \mathbf{0}, \quad \ddot{\mathbf{S}}(\mathbf{x}, 0) = \mathbf{0} \qquad \text{in } \Omega, \tag{2.114e}$$

where $\boldsymbol{g}_n$ denotes prescribed tractions on Γ_N^{RD}.

We seek next the weak form, in the Galerkin sense, corresponding to the strong form (2.113-2.114). We take inner products of the equilibrium equation (2.113a), and the kinematic equation (2.113b) with arbitrary weight functions $\mathbf{w}(\mathbf{x})$ and $\mathbf{T}(\mathbf{x})$, respectively, residing in appropriate admissible spaces, and then integrate over the entire computational domain Ω. There results

$$\int_\Omega \nabla \mathbf{w} : \left(\ddot{\mathbf{S}}^T \tilde{\Lambda}_e + \dot{\mathbf{S}}^T \tilde{\Lambda}_p + \mathbf{S}^T \tilde{\Lambda}_w\right) \, \mathrm{d}\Omega + \int_\Omega \mathbf{w} \cdot \rho \, \left(a \dddot{\mathbf{u}} + b \ddot{\mathbf{u}} + c \dot{\mathbf{u}} + d \mathbf{u}\right) \, \mathrm{d}\Omega$$
$$= \int_{\Gamma_N} \mathbf{w} \cdot \left(\ddot{\mathbf{S}}^T \tilde{\Lambda}_e + \dot{\mathbf{S}}^T \tilde{\Lambda}_p + \mathbf{S}^T \tilde{\Lambda}_w\right) \mathbf{n} \, \mathrm{d}\Gamma + \int_\Omega \mathbf{w} \cdot a \dot{\mathbf{f}} \, \mathrm{d}\Omega, \tag{2.115a}$$

$$\int_\Omega \mathbf{T} : \left[\mathcal{D} : \left(a \dddot{\mathbf{S}} + b \ddot{\mathbf{S}} + c \dot{\mathbf{S}} + d \mathbf{S}\right)\right] \, \mathrm{d}\Omega = \frac{1}{2} \int_\Omega \mathbf{T} : \Big[(\nabla \ddot{\mathbf{u}}) \tilde{\Lambda}_e + \tilde{\Lambda}_e (\nabla \ddot{\mathbf{u}})^T$$
$$+ (\nabla \dot{\mathbf{u}}) \tilde{\Lambda}_p + \tilde{\Lambda}_p (\nabla \dot{\mathbf{u}})^T + (\nabla \mathbf{u}) \tilde{\Lambda}_w + \tilde{\Lambda}_w (\nabla \mathbf{u})^T\Big] \, \mathrm{d}\Omega. \tag{2.115b}$$

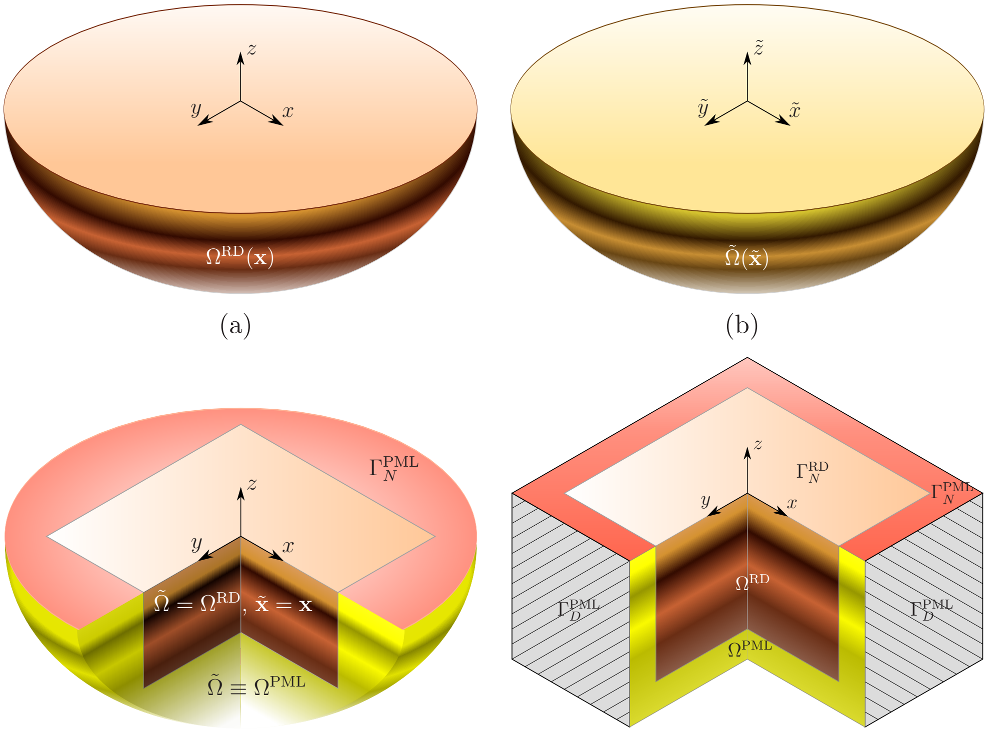

(a) (b)

(c) (d)

Figure 2.37: Three-dimensional prototype: (a) physical model; (b) model after the application of complex coordinate-stretching; (c) model after truncation; (d) computational model

We seek $\mathbf{u} \in \mathbf{H}^1(\Omega) \times \mathsf{J}$ satisfying $\mathbf{u}|_{\Gamma_D^{\text{PML}}} = \mathbf{0}$, and $\mathbf{S} \in \mathcal{L}^2(\Omega) \times \mathsf{J}$ such that equation (2.115) holds for all $\mathbf{w} \in \mathbf{H}^1(\Omega)$ satisfying $\mathbf{w}|_{\Gamma_D} = \mathbf{0}$ and $\mathbf{T} \in \mathcal{L}^2(\Omega)$. Next, we seek approximate solutions for $\mathbf{u}(\mathbf{x}, t)$ and $\mathbf{S}(\mathbf{x}, t)$; to this end, we introduce the finite-dimensional spaces $\boldsymbol{\Xi}^h \subset \mathbf{H}^1(\Omega)$ and $\boldsymbol{\Upsilon}^h \subset \mathcal{L}^2(\Omega)$:

$$\boldsymbol{\Xi}_r^h = \left\{\mathbf{q} \in \mathbf{H}^1(\Omega),\ \mathbf{q}|_K \in (Q_r(K))^3,\ \forall K \in \mathcal{K}_h\right\}, \tag{2.116a}$$

$$\boldsymbol{\Upsilon}_r^h = \left\{\mathcal{A} \in \mathcal{L}^2(\Omega),\ \mathcal{A}|_K \in (Q_r(K))^{3\times 3},\ \forall K \in \mathcal{K}_h\right\}, \tag{2.116b}$$

where $Q_r(K)$ is a polynomial of degree at most r on K. $\mathcal{K}_h$ is a partition of Ω. Let the basis functions in $\boldsymbol{\Xi}^h$ and $\boldsymbol{\Upsilon}^h$ be denoted by $\boldsymbol{\Phi}$ and $\boldsymbol{\Psi}$, respectively. The trial functions $\mathbf{u}_h \in \boldsymbol{\Xi}^h \times \mathsf{J}$ and $\mathbf{S}_h \in \boldsymbol{\Upsilon}^h \times \mathsf{J}$ are spatially discretized as

$$\mathbf{u}(\mathbf{x}, t) \cong \mathbf{u}_h(\mathbf{x}, t) = \begin{bmatrix} \boldsymbol{\Phi}^T(\mathbf{x})\mathbf{u}_x(t) \\ \boldsymbol{\Phi}^T(\mathbf{x})\mathbf{u}_y(t) \\ \boldsymbol{\Phi}^T(\mathbf{x})\mathbf{u}_z(t) \end{bmatrix}, \tag{2.117a}$$

$$\mathbf{S}(\mathbf{x}, t) \cong \mathbf{S}_h(\mathbf{x}, t) = \begin{bmatrix} \boldsymbol{\Psi}^T(\mathbf{x})\mathbf{S}_{xx}(t) & \boldsymbol{\Psi}^T(\mathbf{x})\mathbf{S}_{xy}(t) & \boldsymbol{\Psi}^T(\mathbf{x})\mathbf{S}_{xz}(t) \\ \boldsymbol{\Psi}^T(\mathbf{x})\mathbf{S}_{yx}(t) & \boldsymbol{\Psi}^T(\mathbf{x})\mathbf{S}_{yy}(t) & \boldsymbol{\Psi}^T(\mathbf{x})\mathbf{S}_{yz}(t) \\ \boldsymbol{\Psi}^T(\mathbf{x})\mathbf{S}_{zx}(t) & \boldsymbol{\Psi}^T(\mathbf{x})\mathbf{S}_{zy}(t) & \boldsymbol{\Psi}^T(\mathbf{x})\mathbf{S}_{zz}(t) \end{bmatrix}. \tag{2.117b}$$

Similarly, the test functions $\mathbf{w} \in \boldsymbol{\Xi}^h$ and $\mathbf{T} \in \boldsymbol{\Upsilon}^h$ are expressed as

$$\mathbf{w}(\mathbf{x}) \cong \mathbf{w}_h(\mathbf{x}) = \begin{bmatrix} \mathbf{w}_x^T\boldsymbol{\Phi}(\mathbf{x}) \\ \mathbf{w}_y^T\boldsymbol{\Phi}(\mathbf{x}) \\ \mathbf{w}_z^T\boldsymbol{\Phi}(\mathbf{x}) \end{bmatrix}, \tag{2.118a}$$

$$\mathbf{T}(\mathbf{x}) \cong \mathbf{T}_h(\mathbf{x}) = \begin{bmatrix} \mathbf{T}_{xx}^T\boldsymbol{\Psi}(\mathbf{x}) & \mathbf{T}_{xy}^T\boldsymbol{\Psi}(\mathbf{x}) & \mathbf{T}_{xz}^T\boldsymbol{\Psi}(\mathbf{x}) \\ \mathbf{T}_{yx}^T\boldsymbol{\Psi}(\mathbf{x}) & \mathbf{T}_{yy}^T\boldsymbol{\Psi}(\mathbf{x}) & \mathbf{T}_{yz}^T\boldsymbol{\Psi}(\mathbf{x}) \\ \mathbf{T}_{zx}^T\boldsymbol{\Psi}(\mathbf{x}) & \mathbf{T}_{zy}^T\boldsymbol{\Psi}(\mathbf{x}) & \mathbf{T}_{zz}^T\boldsymbol{\Psi}(\mathbf{x}) \end{bmatrix}. \tag{2.118b}$$

By introducing the symmetry of the stress tensor ($\mathcal{S} = \mathcal{S}^T$), we obtain the *semi-discrete form*

$$\mathbf{M}\dddot{\mathbf{d}} + \mathbf{C}\ddot{\mathbf{d}} + \mathbf{K}\dot{\mathbf{d}} + \mathbf{G}\mathbf{d} = \mathbf{F}, \tag{2.119}$$

where

$$\mathbf{M} = \begin{bmatrix} \mathbf{M}_a & \mathbf{0} & \mathbf{0} & \mathbf{0} & \mathbf{0} & \mathbf{0} & \mathbf{0} & \mathbf{0} & \mathbf{0} \\ & \mathbf{M}_a & \mathbf{0} & \mathbf{0} & \mathbf{0} & \mathbf{0} & \mathbf{0} & \mathbf{0} & \mathbf{0} \\ & & \mathbf{M}_a & \mathbf{0} & \mathbf{0} & \mathbf{0} & \mathbf{0} & \mathbf{0} & \mathbf{0} \\ & & & -\mathbf{N}_a & \mathbf{Z}_a & \mathbf{Z}_a & \mathbf{0} & \mathbf{0} & \mathbf{0} \\ & & & & -\mathbf{N}_a & \mathbf{Z}_a & \mathbf{0} & \mathbf{0} & \mathbf{0} \\ & & & & & -\mathbf{N}_a & \mathbf{0} & \mathbf{0} & \mathbf{0} \\ & & sym & & & & -\mathbf{G}_a & \mathbf{0} & \mathbf{0} \\ & & & & & & & -\mathbf{G}_a & \mathbf{0} \\ & & & & & & & & -\mathbf{G}_a \end{bmatrix}, \tag{2.120a}$$

$$\mathbf{C} = \begin{bmatrix} \mathbf{M}_b & \mathbf{0} & \mathbf{0} & \mathbf{A}_{1x} & \mathbf{0} & \mathbf{0} & \mathbf{A}_{2y} & \mathbf{A}_{3z} & \mathbf{0} \\ & \mathbf{M}_b & \mathbf{0} & \mathbf{0} & \mathbf{A}_{2y} & \mathbf{0} & \mathbf{A}_{1x} & \mathbf{0} & \mathbf{A}_{3z} \\ & & \mathbf{M}_b & \mathbf{0} & \mathbf{0} & \mathbf{A}_{3z} & \mathbf{0} & \mathbf{A}_{1x} & \mathbf{A}_{2y} \\ & & & -\mathbf{N}_b & \mathbf{Z}_b & \mathbf{Z}_b & \mathbf{0} & \mathbf{0} & \mathbf{0} \\ & & & & -\mathbf{N}_b & \mathbf{Z}_b & \mathbf{0} & \mathbf{0} & \mathbf{0} \\ & & & & & -\mathbf{N}_b & \mathbf{0} & \mathbf{0} & \mathbf{0} \\ & & sym & & & & -\mathbf{G}_b & \mathbf{0} & \mathbf{0} \\ & & & & & & & -\mathbf{G}_b & \mathbf{0} \\ & & & & & & & & -\mathbf{G}_b \end{bmatrix}, \tag{2.120b}$$

$$\mathbf{K} = \begin{bmatrix} \mathbf{M}_c & \mathbf{0} & \mathbf{0} & \mathbf{B}_{1x} & \mathbf{0} & \mathbf{0} & \mathbf{B}_{2y} & \mathbf{B}_{3z} & \mathbf{0} \\ & \mathbf{M}_c & \mathbf{0} & \mathbf{0} & \mathbf{B}_{2y} & \mathbf{0} & \mathbf{B}_{1x} & \mathbf{0} & \mathbf{B}_{3z} \\ & & \mathbf{M}_c & \mathbf{0} & \mathbf{0} & \mathbf{B}_{3z} & \mathbf{0} & \mathbf{B}_{1x} & \mathbf{B}_{2y} \\ & & & -\mathbf{N}_c & \mathbf{Z}_c & \mathbf{Z}_c & \mathbf{0} & \mathbf{0} & \mathbf{0} \\ & & & & -\mathbf{N}_c & \mathbf{Z}_c & \mathbf{0} & \mathbf{0} & \mathbf{0} \\ & & & & & -\mathbf{N}_c & \mathbf{0} & \mathbf{0} & \mathbf{0} \\ & & sym & & & & -\mathbf{G}_c & \mathbf{0} & \mathbf{0} \\ & & & & & & & -\mathbf{G}_c & \mathbf{0} \\ & & & & & & & & -\mathbf{G}_c \end{bmatrix}, \tag{2.120c}$$

$$\mathbf{G} = \begin{bmatrix} \mathbf{M}_d & \mathbf{0} & \mathbf{0} & \mathbf{C}_{1x} & \mathbf{0} & \mathbf{0} & \mathbf{C}_{2y} & \mathbf{C}_{3z} & \mathbf{0} \\ & \mathbf{M}_d & \mathbf{0} & \mathbf{0} & \mathbf{C}_{2y} & \mathbf{0} & \mathbf{C}_{1x} & \mathbf{0} & \mathbf{C}_{3z} \\ & & \mathbf{M}_d & \mathbf{0} & \mathbf{0} & \mathbf{C}_{3z} & \mathbf{0} & \mathbf{C}_{1x} & \mathbf{C}_{2y} \\ & & & -\mathbf{N}_d & \mathbf{Z}_d & \mathbf{Z}_d & \mathbf{0} & \mathbf{0} & \mathbf{0} \\ & & & & -\mathbf{N}_d & \mathbf{Z}_d & \mathbf{0} & \mathbf{0} & \mathbf{0} \\ & & & & & -\mathbf{N}_d & \mathbf{0} & \mathbf{0} & \mathbf{0} \\ & & sym & & & & -\mathbf{G}_d & \mathbf{0} & \mathbf{0} \\ & & & & & & & -\mathbf{G}_d & \mathbf{0} \\ & & & & & & & & -\mathbf{G}_d \end{bmatrix}, \tag{2.120d}$$

$$\mathbf{d} = [\mathbf{u}_x \; \mathbf{u}_y \; \mathbf{u}_z \; \mathbf{S}_{xx} \; \mathbf{S}_{yy} \; \mathbf{S}_{zz} \; \mathbf{S}_{xy} \; \mathbf{S}_{xz} \; \mathbf{S}_{yz}]^T, \tag{2.120e}$$

$$\mathbf{F} = [\mathbf{f^e}_x \; \mathbf{f^e}_y \; \mathbf{f^e}_z \; \mathbf{0} \; \mathbf{0} \; \mathbf{0} \; \mathbf{0} \; \mathbf{0} \; \mathbf{0}]^T. \tag{2.120f}$$

The various matrix and vector blocks are defined as

$$\mathbf{f^e}_x = \int_{\Gamma_N^{\mathrm{RD}}} \mathbf{\Phi}\ \dot{g}_x(\mathbf{x}, t)\ \mathrm{d}\Gamma + \int_\Omega \mathbf{\Phi} \dot{f}_x\ \mathrm{d}\Omega, \tag{2.121a}$$

$$\mathbf{f^e}_y = \int_{\Gamma_N^{\mathrm{RD}}} \mathbf{\Phi}\ \dot{g}_y(\mathbf{x}, t)\ \mathrm{d}\Gamma + \int_\Omega \mathbf{\Phi} \dot{f}_y\ \mathrm{d}\Omega, \tag{2.121b}$$

$$\mathbf{f^e}_z = \int_{\Gamma_N^{\mathrm{RD}}} \mathbf{\Phi}\ \dot{g}_z(\mathbf{x}, t)\ \mathrm{d}\Gamma + \int_\Omega \mathbf{\Phi} \dot{f}_z\ \mathrm{d}\Omega, \tag{2.121c}$$

and

$$\mathbf{A}_{ij} = \int_\Omega \tilde{\Lambda}_e^i\ \frac{\partial \mathbf{\Phi}}{\partial j} \mathbf{\Psi}^T\ \mathrm{d}\Omega, \qquad i = 1, 2, 3 \text{ and } j = x, y, z \tag{2.122a}$$

$$\mathbf{B}_{ij} = \int_\Omega \tilde{\Lambda}_p^i\ \frac{\partial \mathbf{\Phi}}{\partial j} \mathbf{\Psi}^T\ \mathrm{d}\Omega, \qquad i = 1, 2, 3 \text{ and } j = x, y, z \tag{2.122b}$$

$$\mathbf{C}_{ij} = \int_\Omega \tilde{\Lambda}_w^i\ \frac{\partial \mathbf{\Phi}}{\partial j} \mathbf{\Psi}^T\ \mathrm{d}\Omega, \qquad i = 1, 2, 3 \text{ and } j = x, y, z \tag{2.122c}$$

$$\mathbf{M}_k = \int_\Omega k\ \rho \mathbf{\Phi} \mathbf{\Phi}^T\ \mathrm{d}\Omega, \qquad k = a, b, c, d \tag{2.122d}$$

$$\mathbf{N}_k = \int_\Omega k\ \frac{\lambda + \mu}{\mu(3\lambda + 2\mu)} \mathbf{\Psi} \mathbf{\Psi}^T\ \mathrm{d}\Omega, \qquad k = a, b, c, d \tag{2.122e}$$

$$\mathbf{Z}_k = \int_\Omega k\ \frac{\lambda}{2\mu(3\lambda + 2\mu)} \mathbf{\Psi} \mathbf{\Psi}^T\ \mathrm{d}\Omega, \qquad k = a, b, c, d \tag{2.122f}$$

$$\mathbf{G}_k = \int_\Omega k\ \frac{1}{\mu} \mathbf{\Psi} \mathbf{\Psi}^T\ \mathrm{d}\Omega, \qquad k = a, b, c, d. \tag{2.122g}$$

Notice that $\tilde{\Lambda}^n$ denote the n-th component of the diagonal matrix $\tilde{\Lambda}$.

2.4.4 Time integration

The lowest-order time derivatives implicated in the semi-discrete form (2.119) are associated with **d**, which, in turn, involve displacements, and time-integrals of the stress history terms. Thus, clearly, the form (2.119) is the same as the semi-discrete form of the axisymmetric PML and calls for the *extended* Newmark-β scheme (Algorithm 2.2).

2.5 Hybrid 2D elastic wave modeling

In section 2.2, we introduced a new mixed non-convolutional unsplit-field PML for transient wave simulations in two-dimensional heterogeneous domains, and, in subsequent sections, we extended the approach to both axisymmetric and three-dimensional domains. However, the resulting formulations treat identically both the interior domain and the PML buffer zone, as it is the case with most PML formulations to date. This unified treatment resulted in displacements and stresses (or stress histories) that were retained as unknowns throughout the entire computational domain, thereby resulting in considerable computational cost (even though the method is still economical when compared against split-field schemes).

In this section, we discuss an alternative formulation that proved to be far more economical than the preceding development. The formulation evolved during the progress of the research reported in this dissertation from the fully-mixed approach, and it is now our preferred methodology for wave simulations in PML-truncated domains. In fact, this is the approach we adopted for resolving the inverse medium problem as well. In this section, we describe the development and provide implementation details and numerical results. We describe only the two-dimensional case, but the axisymmetric and three-dimensional cases follow directly from the development in this section.

The formulation we describe is hybrid in nature, coupling a mixed with a non-mixed or single-field approach, in a variational setting, resulting in symmetric semi-discrete forms, and exhibiting optimal computational cost in terms of the number of degrees-of-freedom implicated in the formulation. We show also that existing displacement-based codes for interior domains can be easily modified to accommodate PMLs as a means of domain truncation.

2.5.1 Hybrid formulation

Equations (2.40) could only be reduced to a single (vector) equation implicating a single field (displacements) at the expense of the temporal complexity, which would, in that case, involve convolutory terms. In the hybrid approach[5] we describe next, we retain the single-field formulation (displacements only) for the interior problem, and couple it with the mixed formulation for the unsplit-field PML. Thus, the wave motion in the two-dimensional PML-truncated domain (Fig. 2.38) is governed by the following system of equations:

---

[5] We use *hybrid* to imply the coupling of a non-mixed with a mixed formulation.

$$\mathbf{div}\left\{\mu\left[\nabla\mathbf{u}+(\nabla\mathbf{u})^T\right]+\lambda(\operatorname{div}\mathbf{u})\mathcal{I}\right\}+\mathbf{f}=\rho\ddot{\mathbf{u}} \qquad \text{in } \Omega^{\mathrm{RD}}\times \mathsf{J}, \tag{2.123a}$$

$$\mathbf{div}\left(\dot{\mathbf{S}}^T\tilde{\Lambda}_e+\mathbf{S}^T\tilde{\Lambda}_p\right)=\rho\left(a\ddot{\mathbf{u}}+b\dot{\mathbf{u}}+c\mathbf{u}\right) \qquad \text{in } \Omega^{\mathrm{PML}}\times \mathsf{J}, \tag{2.123b}$$

$$\begin{aligned}\mathcal{D}:&\left(a\ddot{\mathbf{S}}+b\dot{\mathbf{S}}+c\mathbf{S}\right)\\ &=\frac{1}{2}\left[(\nabla\dot{\mathbf{u}})\tilde{\Lambda}_e+\tilde{\Lambda}_e(\nabla\dot{\mathbf{u}})^T+(\nabla\mathbf{u})\tilde{\Lambda}_p+\tilde{\Lambda}_p(\nabla\mathbf{u})^T\right] \qquad \text{in } \Omega^{\mathrm{PML}}\times \mathsf{J},\end{aligned} \tag{2.123c}$$

subject to silent initial conditions, and the following boundary and interface conditions:

$$\left\{\mu\left[\nabla\mathbf{u}+(\nabla\mathbf{u})^T\right]+\lambda(\operatorname{div}\mathbf{u})\mathcal{I}\right\}\mathbf{n}=\boldsymbol{g}_n \qquad \text{on } \Gamma_N^{\mathrm{RD}}\times \mathsf{J}, \tag{2.124a}$$

$$(\dot{\mathbf{S}}^T\tilde{\Lambda}_e+\mathbf{S}^T\tilde{\Lambda}_p)\mathbf{n}=\mathbf{0} \qquad \text{on } \Gamma_N^{\mathrm{PML}}\times \mathsf{J}, \tag{2.124b}$$

$$\mathbf{u}=\mathbf{0} \qquad \text{on } \Gamma_D^{\mathrm{PML}}\times \mathsf{J}, \tag{2.124c}$$

$$\mathbf{u}^+=\mathbf{u}^- \qquad \text{on } \Gamma^{\mathrm{I}}\times \mathsf{J}, \tag{2.124d}$$

$$\left\{\mu\left[\nabla\mathbf{u}+(\nabla\mathbf{u})^T\right]+\lambda(\operatorname{div}\mathbf{u})\mathcal{I}\right\}\mathbf{n}=-(\dot{\mathbf{S}}^T\tilde{\Lambda}_e+\mathbf{S}^T\tilde{\Lambda}_p)\mathbf{n} \qquad \text{on } \Gamma^{\mathrm{I}}\times \mathsf{J}, \tag{2.124e}$$

where the domain and associated boundaries notation is shown in Fig. 2.38, and $\mathcal{I}$ denotes the identity tensor.

We seek next the weak form, in the Galerkin sense, corresponding to the strong form (2.123-2.124). We take inner products of (2.123) with test functions $\mathbf{w}_1(\mathbf{x})$, $\mathbf{w}_2(\mathbf{x})$ and $\mathbf{T}(\mathbf{x})$, and then integrate over Ω^{RD}, Ω^{PML} and Ω^{PML}, respectively, where the integration by parts is applied only to the equi-

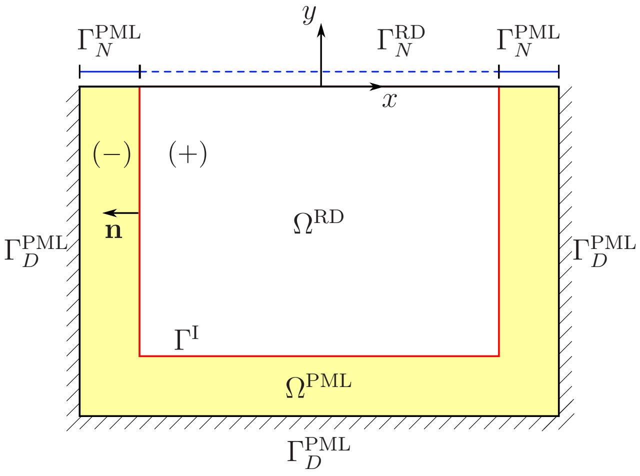

Figure 2.38: PML-truncated semi-infinite domain in two dimensions

librium equations (2.123a) and (2.123b). By adding the equilibrium equations, the weak form of (2.123) can be cast as:

$$
\begin{aligned}
&\int_{\Omega^{\mathrm{RD}}} \nabla\mathbf{w}_1 : \left\{\mu\left[\nabla\mathbf{u} + (\nabla\mathbf{u})^T\right] + \lambda(\operatorname{div}\mathbf{u})\mathcal{I}\right\}\, \mathrm{d}\Omega \\
&+ \int\limits_{\Omega^{\mathrm{PML}}} \nabla\mathbf{w}_2 : \left(\dot{\mathbf{S}}^T\tilde{\Lambda}_e + \mathbf{S}^T\tilde{\Lambda}_p\right)\, \mathrm{d}\Omega + \int_{\Omega^{\mathrm{RD}}} \mathbf{w}_1\cdot\rho\ddot{\mathbf{u}}\,\mathrm{d}\Omega \\
&+ \int\limits_{\Omega^{\mathrm{PML}}} \mathbf{w}_2\cdot\rho\left(a\ddot{\mathbf{u}} + b\dot{\mathbf{u}} + c\mathbf{u}\right)\, \mathrm{d}\Omega = \int_{\Gamma_N^{\mathrm{RD}}} \mathbf{w}_1\cdot\boldsymbol{g}_n\,\mathrm{d}\Gamma + \int_{\Omega^{\mathrm{RD}}} \mathbf{w}_1\cdot\mathbf{f}\,\mathrm{d}\Omega,
\end{aligned}
\tag{2.125a}
$$

$$
\begin{aligned}
&\int\limits_{\Omega^{\mathrm{PML}}} \mathbf{T} : \left[\mathcal{D} : \left(a\ddot{\mathbf{S}} + b\dot{\mathbf{S}} + c\mathbf{S}\right)\right]\, \mathrm{d}\Omega \\
&\qquad = \frac{1}{2}\int\limits_{\Omega^{\mathrm{PML}}} \mathbf{T} : \left[(\nabla\dot{\mathbf{u}})\tilde{\Lambda}_e + \tilde{\Lambda}_e(\nabla\dot{\mathbf{u}})^T + (\nabla\mathbf{u})\tilde{\Lambda}_p + \tilde{\Lambda}_p(\nabla\mathbf{u})^T\right]\, \mathrm{d}\Omega.
\end{aligned}
\tag{2.125b}
$$

We note that the hybrid approach couples two initially-uncoupled sets of governing equations via the continuity of displacements (2.124d) and tractions

(2.124e) at the interface. To satisfy both conditions, the displacement test functions must match, i.e. $\mathbf{w}_1 = \mathbf{w}_2$, along the interface.

We seek $\mathbf{u} \in \mathbf{H}^1(\Omega) \times \mathsf{J}$ satisfying $\mathbf{u}|_{\Gamma_D^{\mathrm{PML}}} = \mathbf{0}$, and $\mathbf{S} \in \mathcal{L}^2(\Omega) \times \mathsf{J}$, such that equation (2.125) holds for all $\mathbf{w}_1 \in \mathbf{H}^1(\Omega)$, $\mathbf{w}_2 \in \mathbf{H}^1(\Omega)$ satisfying $\mathbf{w}_2|_{\Gamma_D^{\mathrm{PML}}} = \mathbf{0}$ and $\mathbf{T} \in \mathcal{L}^2(\Omega)$.

For the mixed finite element implementation of the variational form (2.125), both $\mathbf{u}(\mathbf{x}, t)$ and $\mathbf{S}(\mathbf{x}, t)$ are treated as independent variables that need to be approximated separately now only within the PML domain. Let the basis functions residing in $\boldsymbol{\Xi}_h \subset \mathbf{H}^1(\Omega)$ and $\boldsymbol{\Upsilon}_h \subset \mathcal{L}^2(\Omega)$ be denoted by $\boldsymbol{\Phi}$ and $\boldsymbol{\Psi}$, respectively. The trial functions $\mathbf{u}_h \in \boldsymbol{\Xi}_h \times \mathsf{J}$ and $\mathbf{S}_h \in \boldsymbol{\Upsilon}_h \times \mathsf{J}$ are spatially discretized as

$$\mathbf{u}(\mathbf{x}, t) \cong \mathbf{u}_h(\mathbf{x}, t) = \begin{bmatrix} \boldsymbol{\Phi}^T(\mathbf{x})\mathbf{u}_x(t) \\ \boldsymbol{\Phi}^T(\mathbf{x})\mathbf{u}_y(t) \end{bmatrix}, \tag{2.126a}$$

$$\mathbf{S}(\mathbf{x}, t) \cong \mathbf{S}_h(\mathbf{x}, t) = \begin{bmatrix} \boldsymbol{\Psi}^T(\mathbf{x})\mathbf{S}_{xx}(t) & \boldsymbol{\Psi}^T(\mathbf{x})\mathbf{S}_{xy}(t) \\ \boldsymbol{\Psi}^T(\mathbf{x})\mathbf{S}_{yx}(t) & \boldsymbol{\Psi}^T(\mathbf{x})\mathbf{S}_{yy}(t) \end{bmatrix}. \tag{2.126b}$$

Similarly, the test functions $\mathbf{w}_1 \in \boldsymbol{\Xi}_h$, $\mathbf{w}_2 \in \boldsymbol{\Xi}_h$ and $\mathbf{T} \in \boldsymbol{\Upsilon}_h$ are expressed as

$$\mathbf{w}_1(\mathbf{x}) \cong \mathbf{w}_{1h}(\mathbf{x}) = \begin{bmatrix} \mathbf{w}_{1x}^T\boldsymbol{\Phi}(\mathbf{x}) \\ \mathbf{w}_{1y}^T\boldsymbol{\Phi}(\mathbf{x}) \end{bmatrix}, \tag{2.127a}$$

$$\mathbf{w}_2(\mathbf{x}) \cong \mathbf{w}_{2h}(\mathbf{x}) = \begin{bmatrix} \mathbf{w}_{2x}^T\boldsymbol{\Phi}(\mathbf{x}) \\ \mathbf{w}_{2y}^T\boldsymbol{\Phi}(\mathbf{x}) \end{bmatrix}, \tag{2.127b}$$

$$\mathbf{T}(\mathbf{x}) \cong \mathbf{T}_h(\mathbf{x}) = \begin{bmatrix} \mathbf{T}_{xx}^T\boldsymbol{\Psi}(\mathbf{x}) & \mathbf{T}_{xy}^T\boldsymbol{\Psi}(\mathbf{x}) \\ \mathbf{T}_{yx}^T\boldsymbol{\Psi}(\mathbf{x}) & \mathbf{T}_{yy}^T\boldsymbol{\Psi}(\mathbf{x}) \end{bmatrix}. \tag{2.127c}$$

We, subsequently, obtain the following *semi-discrete form*[6]

$$\mathbf{M}^{\mathrm{st}}\ddot{\mathbf{d}}^{\mathrm{st}} + \mathbf{C}^{\mathrm{st}}\dot{\mathbf{d}}^{\mathrm{st}} + \mathbf{K}^{\mathrm{st}}\mathbf{d}^{\mathrm{st}} = \mathbf{F}^{\mathrm{st}}, \tag{2.128}$$

---

[6] The superscript "st" stands for the *state* problem.

where the system matrices $\mathbf{M}^{\mathrm{st}}$, $\mathbf{C}^{\mathrm{st}}$, $\mathbf{K}^{\mathrm{st}}$, and the system vectors $\mathbf{d}^{\mathrm{st}}$ and $\mathbf{F}^{\mathrm{st}}$ are defined as

$$\mathbf{M}^{\mathrm{st}} = \begin{bmatrix} \mathbf{M}^{rr} & \mathbf{M}^{ri} & \mathbf{0} & \mathbf{0} & \mathbf{0} \\ & \mathbf{M}_a^{ii} & \mathbf{M}_a^{ip} & \mathbf{0} & \mathbf{0} \\ & & \mathbf{M}_a^{pp} & \mathbf{0} & \mathbf{0} \\ & sym & & \mathbf{N}_a^{ii} & \mathbf{N}_a^{ip} \\ & & & & \mathbf{N}_a^{pp} \end{bmatrix}, \quad \mathbf{C}^{\mathrm{st}} = \begin{bmatrix} \mathbf{0} & \mathbf{0} & \mathbf{0} & \mathbf{0} & \mathbf{0} \\ & \mathbf{M}_b^{ii} & \mathbf{M}_b^{ip} & \mathbf{A}^{ii} & \mathbf{A}^{ip} \\ & & \mathbf{M}_b^{pp} & \mathbf{A}^{pi} & \mathbf{A}^{pp} \\ & sym & & \mathbf{N}_b^{ii} & \mathbf{N}_b^{ip} \\ & & & & \mathbf{N}_b^{pp} \end{bmatrix}, \tag{2.129a}$$

$$\mathbf{K}^{\mathrm{st}} = \begin{bmatrix} \mathbf{Q}^{rr} & \mathbf{Q}^{ri} & \mathbf{0} & \mathbf{0} & \mathbf{0} \\ & \mathbf{M}_c^{ii} & \mathbf{M}_c^{ip} & \mathbf{B}^{ii} & \mathbf{B}^{ip} \\ & & \mathbf{M}_c^{pp} & \mathbf{B}^{pi} & \mathbf{B}^{pp} \\ & sym & & \mathbf{N}_c^{ii} & \mathbf{N}_c^{ip} \\ & & & & \mathbf{N}_c^{pp} \end{bmatrix}, \tag{2.129b}$$

$$\mathbf{d}^{\mathrm{st}} = \begin{bmatrix} \mathbf{u}^r & \mathbf{u}^i & \mathbf{u}^p & \mathbf{S}^i & \mathbf{S}^p \end{bmatrix}^T, \qquad \mathbf{F}^{\mathrm{st}} = \begin{bmatrix} \mathbf{f}^r & \mathbf{f}^i & \mathbf{0} & \mathbf{0} & \mathbf{0} \end{bmatrix}^T, \tag{2.129c}$$

with r, i, and p representing *regular* (interior) domain, *interface*, and *PML* domain, respectively. The various submatrices in the above expression are constructible by using standard Lagrange polynomial approximations (see Appendix A), and account for the imposed wave amplitude attenuation within the PML domain. Note that the upper-left corner blocks consist of the standard submatrices resulting from a displacement-based plane-strain formulation. This clearly suggests that to incorporate the effect of the PML into existing codes, one need only account for the submatrices in the lower parts of (2.129).

We note the resulting matrices are symmetric, and that their size is substantially smaller than that required by the fully-mixed formulations (split- or unsplit-field) since the interior elastodynamics problem remains displacement-based.

2.5.2 Time integration

The obtained semi-discrete form (2.128) is second-order in time. The lowest-order time derivatives implicated in (2.128) are associated with $\mathbf{d}^{\mathrm{st}}$, which, in turn, involve displacements and stress history terms. To resolve the time integration we employ the classical Newmark-β scheme (Algorithm 2.1).

2.5.3 Numerical experiments

To test the accuracy and efficiency of the hybrid formulation, we discuss next two numerical experiments: a homogeneous semi-infinite domain, and a horizontally-layered medium with an elliptic inclusion. In both simulations, we apply a stress load, with a Ricker pulse time signature defined in (2.59-2.60). Here, we used $f_r = 15$ Hz, and an amplitude of 10 kPa as depicted in Fig. 2.39.

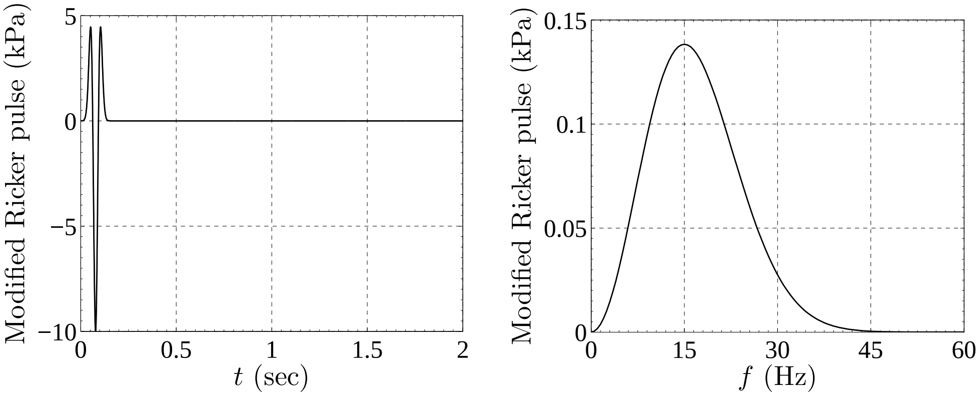

Figure 2.39: Excitation time signal and its Fourier spectrum

We provide three measures to quantify the PML's performance: (a) time history comparisons at select target locations; (b) decay of total energy inside the interior domain; and (c) time-dependent errors relative to a reference solution. To be able to compare the solutions of the PML-truncated domains, we create again reference solutions by embedding the computational domain of interest Ω^{RD} within an enlarged domain Ω^{ED} with fixed exterior boundaries. The numerical solution within Ω^{ED} is obtained using a displacement-based formulation, in order to create a solution that is completely independent from the hybrid approach discussed herein. We retain the enlarged domain's solution up to times that are prior to the arrival of any waves to Ω^{RD} from the part of the domain that is exterior to Ω^{RD}. We then compare the reference and the hybrid method solutions only within the regular domain Ω^{RD} ($\subset \Omega^{\mathrm{ED}}$).

2.5.3.1 Homogeneous medium

We consider first a homogeneous half-plane with density $\rho = 2000$ kg/m^3, shear-wave velocity $c_s = 500$ m/s, and $\nu = 0.25$, that is reduced, through truncation, to a 250m × 250m computational domain, surrounded on its sides and bottom by a 12.5m-thick PML, as shown in Fig. 2.40. We use an explosive P-wave source defined in (2.57) with the modified Ricker pulse time signature depicted in Fig. 2.39. The explosive source disk's center was placed at 125m below the surface, at the center of the domain. The PML and interior domains were discretized by quadratic quadrilateral elements with an element size of 1.25m, whereas the disk was meshed with 0.625m quadratic elements. The discretization resulted in a 10-cell-thick PML with a quadratic attenuation profile $m = 2$. The parameters β_o and α_o were set to 100 m/s and 0.75[7]. Using a time step of 0.001 seconds, we let the simulation run for 2 seconds and sample the time histories of the displacements at five locations $sp_i, i = 1 \dots 5$.

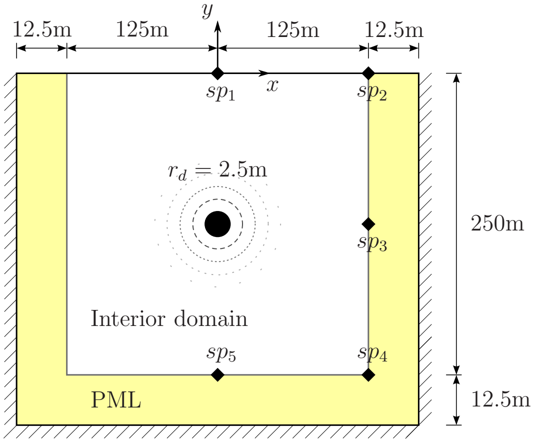

Figure 2.40: A PML-truncated semi-infinite homogeneous medium in two dimensions subjected to an explosive P-wave source at the domain center

To assess the validity of the hybrid PML-formulation, the displacement time histories at the sampling points were compared against the response obtained using the enlarged domain with fixed boundaries and a classic displacement-based plane-strain formulation. The enlarged domain's size was set to (1130m × 565m), and the observation time is limited so that reflections from its fixed exterior boundaries do not travel back and interfere with the wave motion solution in the computational domain of interest. Figure 2.41 de-

---

[7] Though an estimator for β_o has been provided in [48], α_o lacks such explicit form. Here, we favor a small stretch since evanescent waves are not dominant.

picts the comparison of the response time histories for u_x and u_y at the various sp_i points. As it can be seen, the agreement is excellent: the PML has effectively absorbed the waves without any reflections. It is also apparent from the figures that causality holds (sometimes an issue with PML implementations), and that the response is free of spurious reflections.

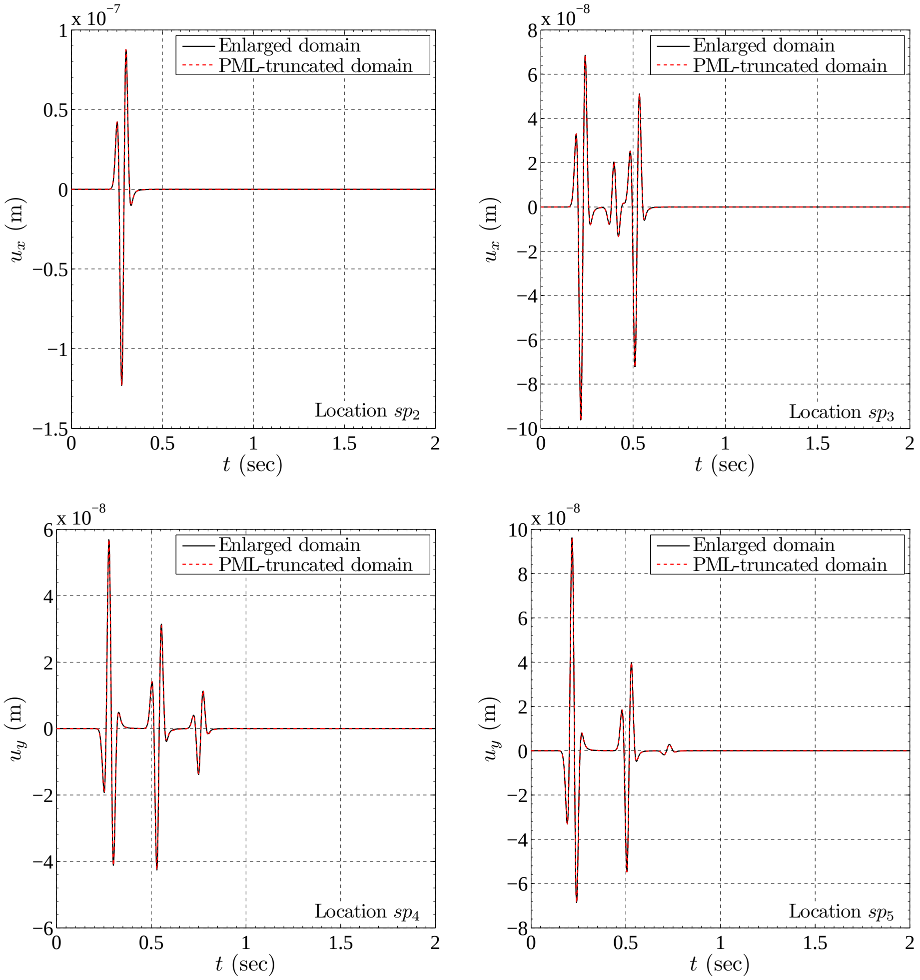

Figure 2.41: Comparison of u_x and u_y time histories between the enlarged and PML-truncated domain solutions at sampling points (homogeneous case)

Figure 2.42 shows snapshots of the displacements taken at two different times. In the figure on the left, the wave has impinged upon the free surface, and has also entered the side and bottom PML zones, which are shown in the figure with solid black lines that are indented with respect to the outer boundary. Notice that there are reflections from the free surface as expected (e.g. local doubling of the displacement amplitudes), and contrast them against the reflection-less side and bottom PML interfaces. The figure on the right corresponds to a later time, and clearly shows two wave trains traveling towards the bottom: each wave train features three zones, with each zone corresponding to the amplitude peaks of the Ricker wavelet. Both wave trains (one P and one S) are reflections from the free surface. Again, notice that there are no discernible reflections from the PML interfaces, nor any residual reflections from the fixed external boundaries that could have polluted the interior wave solution.

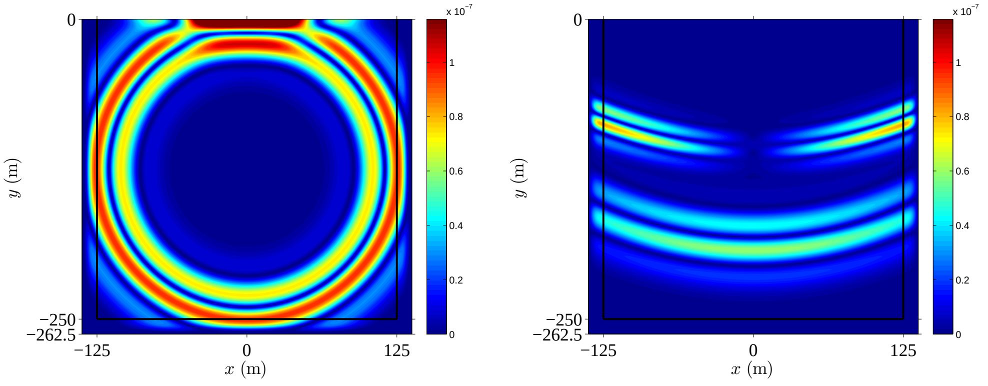

(a) u at $t = 0.218$s

(b) u at $t = 0.44$s

Figure 2.42: Snapshots of u using an explosive Ricker pulse source at the center of the domain

Figure 2.43 depicts three different error metrics: Fig. 2.43(a) shows a visual comparison, displaying excellent agreement, between the reference solution and the PML-based solution for the displacement norm defined in (2.54); Fig. 2.43(b) shows the error norm defined in (2.55), which, at all times, is below 0.143%. Figures 2.43(c) and 2.43(d) show the absolute value of the error at two distinct locations, normalized with respect to the absolute value of the peak record value; the error remains below 0.07% at all times.

Next, we study the effect the parameter β_o (see equation (2.9) for a definition) has on the quality of the obtained solutions. To this end, β_o was allowed to vary between 20 and 100, in multiples of 20, and the total energy decay (2.56) was computed for each one of the β_o values, as a function of time. Figure 2.44 shows the energy decay plotted in standard (left), and semi-log scale (right), both terminated at 2s. Shown on the same figure is the energy decay for all tested β_o values, as well as the reference decay corresponding to the enlarged domain (recall that this has been obtained using an independent displacement-based formulation).

Figure 2.44 is quite revealing in several ways. First, almost all β_o values (except for $\beta_o = 20$) result in similarly sharp decay: after about 0.75 seconds, there is hardly any discernible residual energy left in the domain, since all the waves have traveled out of the domain and have been absorbed by the PML. Secondly, a closer look, using the semi-log scale, reveals though that β_o plays a key role in determining the rate the energy decays, with lower β_o values enforcing slower decay. As β_o decreases, the fixed exterior PML boundaries re-

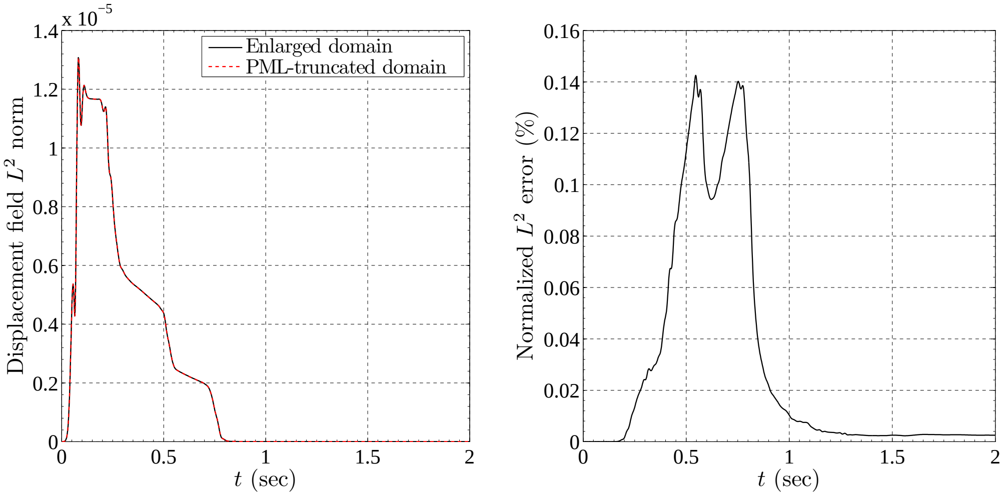

(a) Displacement norm $D(t; \Omega^{\mathrm{RD}})$ (b) Relative error $e(t)$

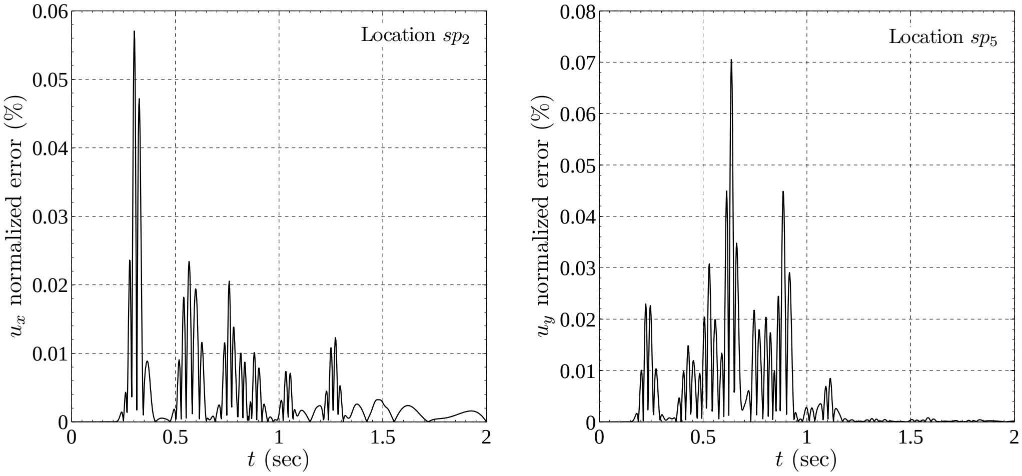

(c) Relative error for u_x at sp_2 (d) Relative error for u_y at sp_5

Figure 2.43: Error metrics for the homogeneous domain case excited by an explosive Ricker pulse ($f_r = 15$ Hz) at the center of the domain

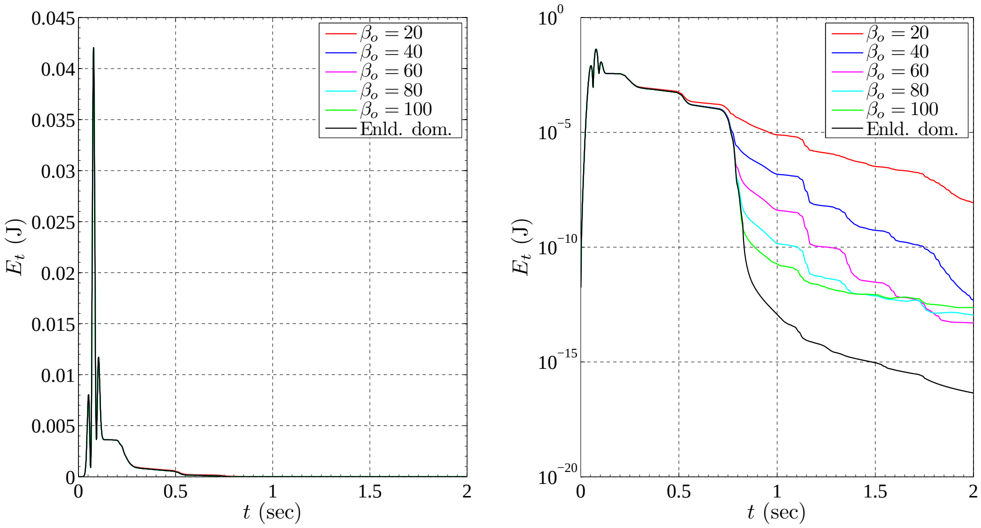

(a) standard scale (b) logarithmic scale

Figure 2.44: Total energy decay inside the regular domain (homogeneous case)

flect back waves of higher amplitude than those that would have resulted from higher β_o, first within the PML and later within the regular domain. Though still of small amplitude, when compared to the peak amplitudes observed in the regular domain, the reflections become amplified as they travel back into the regular domain (this is so by construction), and stand to pollute the solution and slow the energy decay. Thus, lower β_o values effectively decrease the absorptive capacity of the PML layer. Notice, lastly, that for $\beta_o = 100$ the remaining domain energy is lower than 10^{-12}, or roughly more than 10 orders of magnitude less than the peak domain energy, betraying effective wave absorption.

While the polynomial degree m specifies the sharpness of the attenuation profile, the strength of decay inside the PML is determined by the parameter β_o. The energy plot seems to suggest that it is always beneficial to increase β_o to as large a value as possible. However, higher β_o values also introduce sharper PML decay profiles, as it can also be deduced from (2.8). That is, in sharper profiles, most of the wave absorption takes place within a small fraction of the PML length, right next to the PML-regular domain interface. For the absorption to be effective, it is critical that the mesh density within the PML adequately captures the sharp profile, to avoid the accumulation of numerical errors (the situation is similar to the difficulties arising when one attempts to approximate stress singularities with regular and inadequately sized isoparametric elements). In fact, sharper profiles are not only introduced by larger β_o, but arise also when lower polynomial degrees (m in (2.8)) are chosen. Though a detailed discussion and the necessary parametric study escapes the scope of this dissertation, we remark that we have found linear profiles to be very sharp and should, in general, be avoided, in favor of, at least, quadratic, or preferably, quartic profiles.

To illustrate the long-term stability of the proposed formulation, we let the simulation run for 50 seconds. As depicted in Fig. 2.45, no numerical instabilities were observed during the total simulation time of 50 seconds, i.e., for $50,000$ time steps.

2.5.3.2 Heterogeneous medium

To illustrate the performance of the PML in heterogeneous media, we consider a 200m × 200m layered medium with an elliptic inclusion as depicted

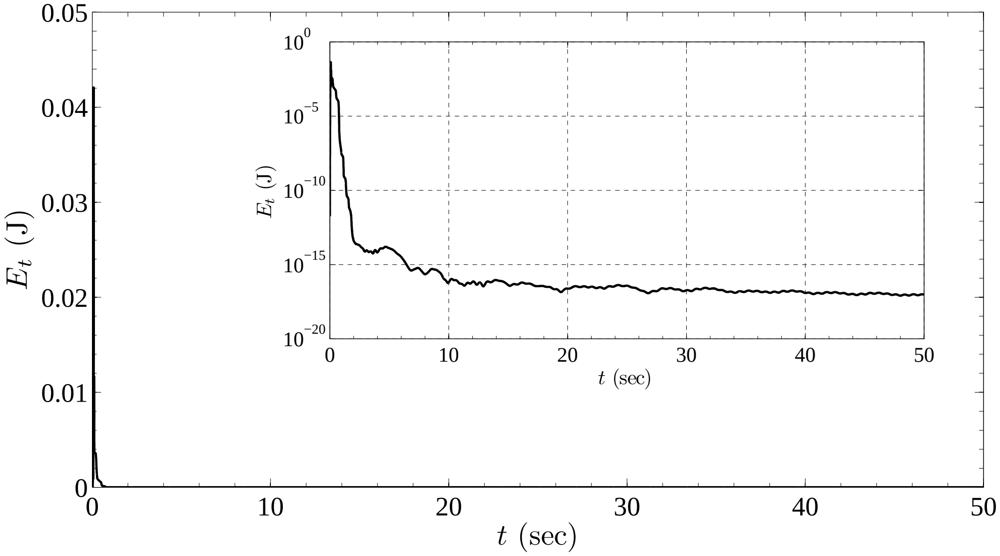

Figure 2.45: Total energy decay inside the regular domain: standard scale, insert: logarithmic scale (homogeneous case)

in Fig. 2.46, which we truncate on its sides and bottom by 10m-thick PML. A surface stress load with a Ricker pulse time signal ($f_r = 15$ Hz, amplitude of 10 kPa) is applied over a region ($-1\text{m} \leq x \leq 1\text{m}$). We define

$$c_s(y) = \begin{cases} 300 \text{ m/s}, & \text{for } -70\text{m} \leq y \leq 0\text{m}, \\ 400 \text{ m/s}, & \text{for } -130\text{m} \leq y < -70\text{m}, \\ 500 \text{ m/s}, & \text{for } -210\text{m} \leq y < -130\text{m}, \\ 700 \text{ m/s}, & \text{for elliptic inclusion}, \end{cases} \tag{2.130}$$

with density $\rho = 2000$ kg/m^3 and $\nu = 0.25$. The material interfaces were extended horizontally into the PML, thereby, avoiding sudden material changes at the interface Γ^{I}. The PML and interior domains were discretized by quadratic quadrilateral elements with an element size of 1.0m, whereas in the vicinity of the surface load, the interior domain was meshed with 0.25m-elements.

The parameter β_o was set to 80 m/s (as in the homogeneous case, we set $m = 2$ and $\alpha_o = 0.75$). Using a time step of 0.0005 seconds, we again simulated the wave motion for 2 seconds using the PML formulation, as well as a displacement-based formulation for an enlarged domain with fixed exterior boundaries.

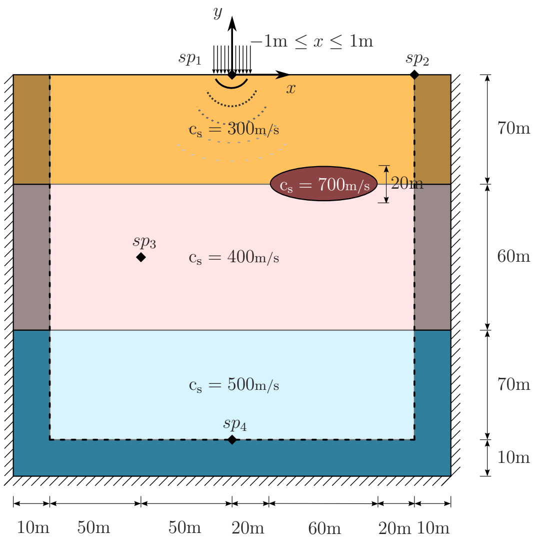

Figure 2.46: A PML-truncated heterogeneous domain subjected to a surface load

To assess the performance of the hybrid PML formulation, we compare the displacement time histories at the sampling points against the reference solution obtained using the enlarged domain (900m × 550m). Figure 2.47 depicts a visual comparison of the response time histories for u_x and u_y at various sp_i points. As it can be seen, the agreement among the response time histories is quite satisfactory.

Figure 2.48 shows the snapshots of the displacements taken at two

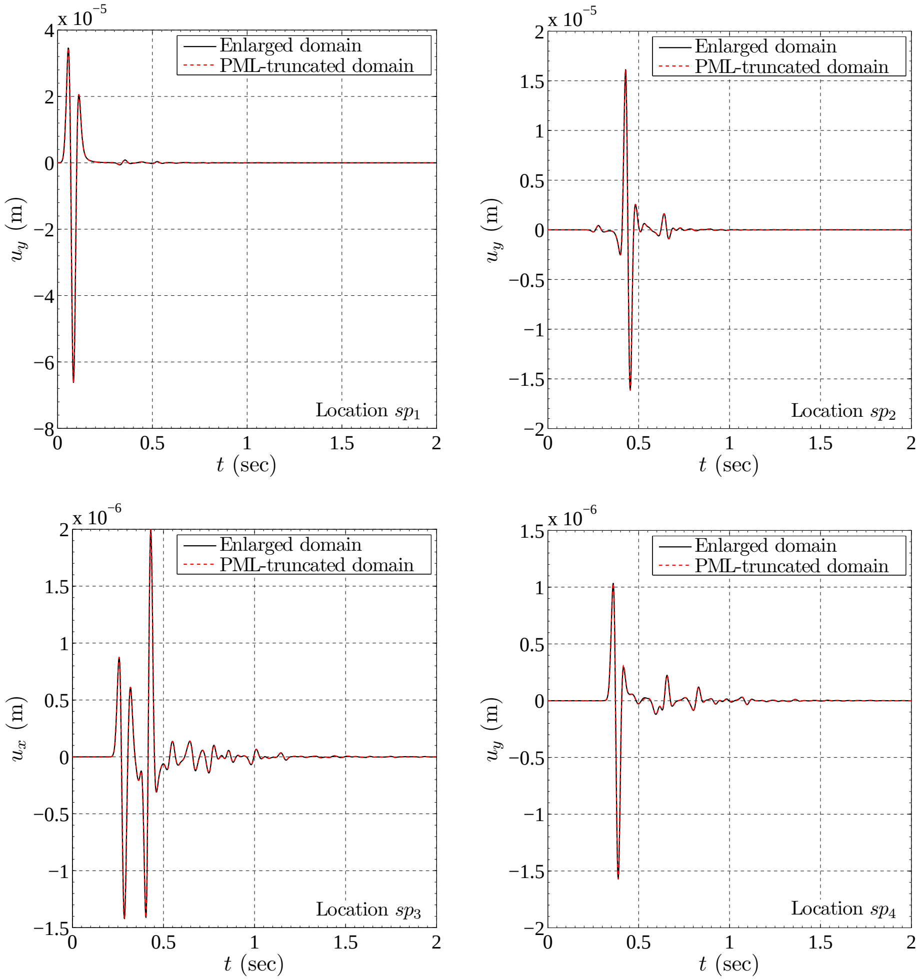

Figure 2.47: Comparison of u_x and u_y time histories between the enlarged and PML-truncated domain solutions at sampling points (heterogeneous case)

different times ($t = 0.34$s and 0.45s). We mark the layer and inclusion material interfaces with thin lines to ease visual examination. The layer boundaries are clearly visible due to reflections at the material interfaces. However, the critical interface Γ^{I} is free of reflections, and the hybrid PML formulation handles the interface waves properly. Extending the layer boundaries into the PML preserved the transparency of the PML-interior domain interface to the outgoing waves.

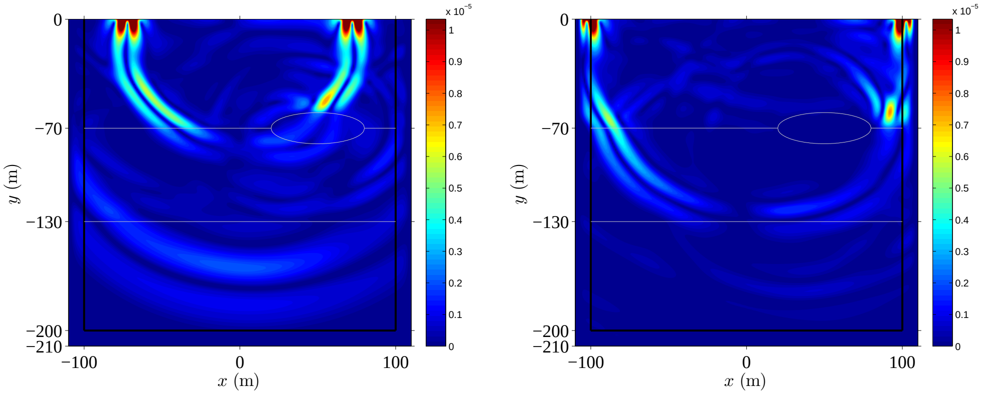

(a) u at $t = 0.34$s (b) u at $t = 0.45$s

Figure 2.48: Snapshots of u for the layered domain with an inclusion

Next, we quantify the performance of the PML via the same error metrics defined earlier. Figure 2.49 is the counterpart of Fig. 2.43 for the heterogeneous case: the highest relative error in the L^2 norm is about 0.5%; though higher than the one we reported for the homogeneous case, we consider it satisfactory. The pointwise errors depicted in Figs. 2.49(c) and 2.49(d) are also quite pleasing: the error is less than about 1.0% at all times.

Lastly, Fig. 2.50 depicts the energy decay within the layered medium:

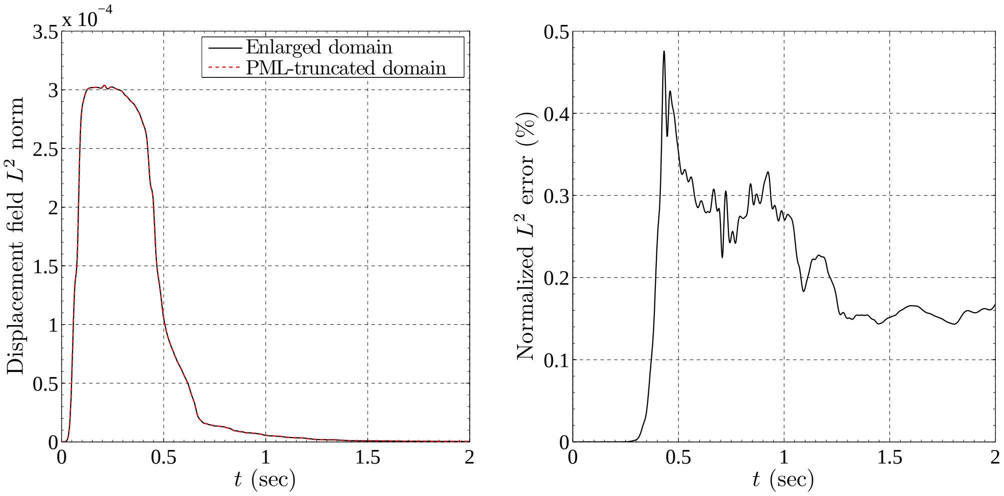

(a) Displacement norm $D(t; \Omega^{\mathrm{RD}})$

(b) Relative error $e(t)$

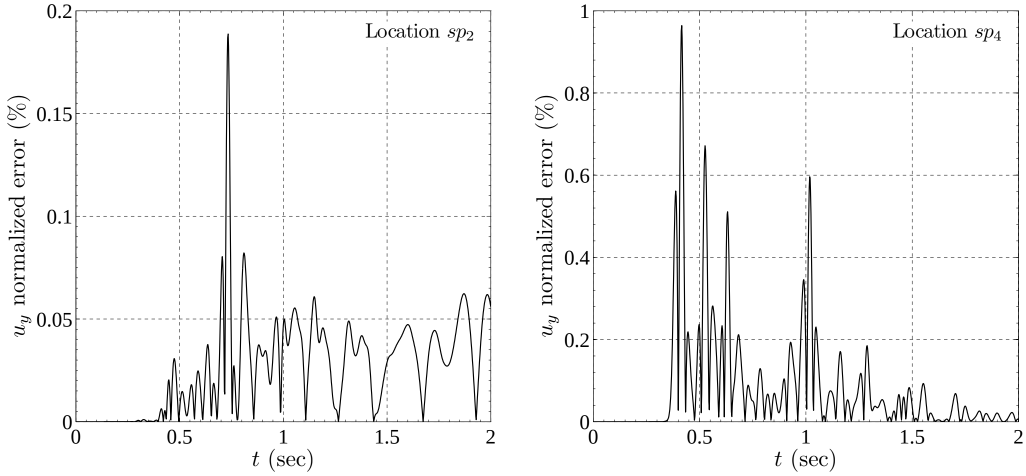

(c) Relative error for u_y at sp_2

(d) Relative error for u_y at sp_4

Figure 2.49: Error metrics for the layered medium excited by a surface Ricker pulse ($f_r = 15$ Hz) over a region ($-1\text{m} \leq x \leq 1\text{m}$)

in this case the decay is considerably more gradual than in the homogeneous case, since there are multiple reflections off of the layer interfaces that travel back to the free surface, reflect at the free surface, travel downwards to the first layer interface, partially reflect there, travel back to the free surface, and so on and so forth. We explored four different β_o values (β_0 = 20 m/s, 40 m/s, 60 m/s, and 80 m/s). The observed behavior is similar to the one discussed in the case of the homogeneous host: overall, the PML performance is excellent, with no discernible reflections or instabilities, even in the presence of heterogeneity.

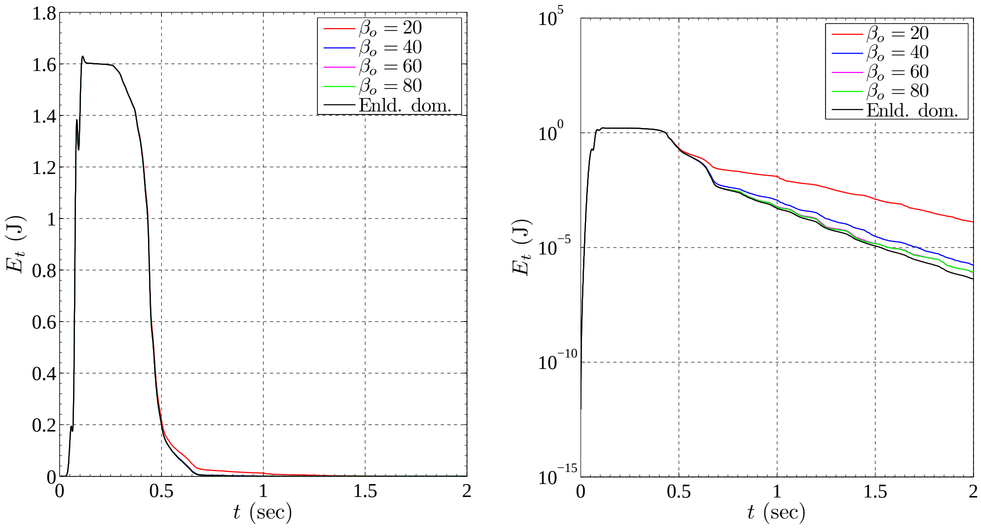

(a) standard scale

(b) logarithmic scale

Figure 2.50: Total energy decay inside the regular domain (heterogeneous case)

All simulations were conducted by adhering to the usual rules of thumb for wave simulations, whereby a minimum of 12 points per wavelength are necessary to adequately resolve the wave motion. The minimum expected wavelength was used to drive the mesh density, while simultaneously satisfying the Courant condition. However, we have found and reported that the sharpness of the decay profile within the PML may impose more onerous requirements on the PML's mesh density than those imposed from a wave propagation perspective. Detailed parametric studies are necessary for providing proper guidance on the choice of the PML parameters.

2.5.4 Computational cost

Table 2.1 shows the computational savings realized for a specific problem, as well as the maximum theoretical savings, when the hybrid method is used over the fully-mixed. In summary, the hybrid formulation is preferred, since it results in symmetric matrices whose size is only slightly larger than the size of matrices resulting from purely interior problems.

Table 2.1: Computational cost comparison between fully-mixed (FM) and hybrid (H) formulations

	Homogeneous	**Heterogeneous**	**Generic**
elements	46414	46458	e
nodes	140101	140247	n
r **nodes**	120240	120386	r
i **nodes**	1201	1201	i
p **nodes**	18660	18660	p
# of unknowns (FM)	700505	701235	$5r+5(i+p)$
# of unknowns (H)	339785	340077	$2r+5(i+p)$
savings	51.5%	51.5%	$60\frac{r}{n}\%$

Chapter 3

The inverse medium problem

In the preceding chapter, we discussed the development of two new formulations for transient elastic wave simulations in PML-truncated heterogeneous media. We showed that both approaches result in fairly accurate numerical simulations of the wave motion within the originally semi-infinite domain; of the two, we favor the hybrid approach, for it is the most computationally economical of the two. In this chapter, we discuss the incorporation of the forward hybrid approach in the inverse medium problem, with applications to the near-surface material profile reconstruction problem arising in geotechnical site characterization investigations. Specifically, we are concerned with the identification of the spatially-distributed material properties $\lambda(\mathbf{x})$ and $\mu(\mathbf{x})$ within a near-surface region of interest, using as drivers the surface measurements of the response to known dynamic excitations situated on the ground surface.

We discuss a systematic methodology, implemented directly in the time-domain: we formulate the inverse medium problem as a PDE-constrained least-squares misfit optimization problem (à la [60, 96]), and discuss implementational details. Lastly, we report on numerical experiments.

3.1 Key components

Schematically, Fig. 3.1(a) depicts the probes and receivers on the originally semi-infinite domain, while Fig. 3.1(b) depicts the PML-truncated domain over which the inverse medium problem is defined. As discussed earlier, there are two key elements to the inverse problem: a) the treatment of the forward problem, and b) the algorithmic framework for the resolution of the inverse problem. To allow for this chapter to be self-contained, we repeat first the hybrid forward initial-and-boundary-value problem. We, then, outline the steps to the resolution of the inverse problem.

3.1.1 The forward problem

Consider an arbitrarily heterogeneous semi-infinite medium as shown in Fig. 3.1(b).

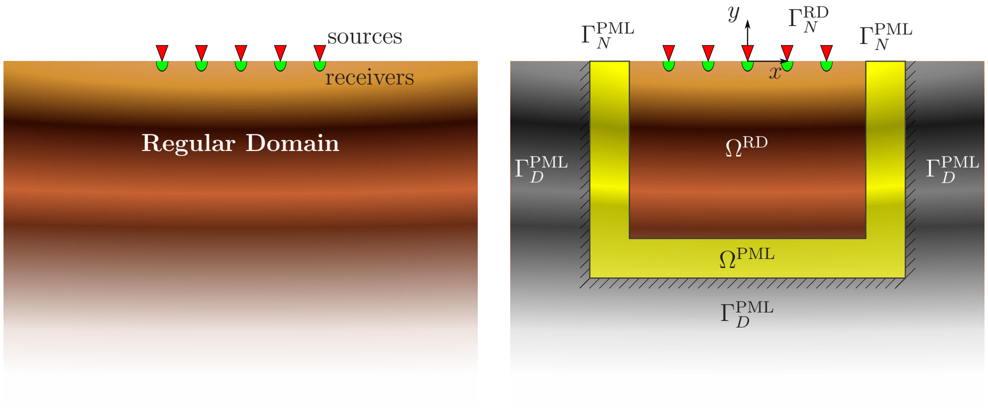

(a) (b)

Figure 3.1: (a) A heterogeneous semi-infinite domain probed by surface sources; (b) conceptual configuration of a PML-truncated semi-infinite domain in two dimensions.

In the forward problem setting, the sources and the spatial distribution of the material parameters $\lambda(\mathbf{x})$ and $\mu(\mathbf{x})$ are known. Then, the wave motion in the PML-truncated domain is governed by the system of PDEs (hybrid formulation) and associated conditions shown below; the *forward problem* can be cast as: *Find* $\mathbf{u} \equiv \mathbf{u}(\mathbf{x}, t)$ *and* $\mathbf{S} \equiv \mathbf{S}(\mathbf{x}, t)$ *such that*

$$\mathbf{div} \left\{ \mu \left[\nabla \mathbf{u} + (\nabla \mathbf{u})^T \right] + \lambda (\operatorname{div} \mathbf{u}) \mathcal{I} \right\} + \mathbf{f} = \rho \ddot{\mathbf{u}} \qquad \text{in } \Omega^{\text{RD}} \times \mathsf{J}, \quad (3.1\text{a})$$

$$\mathbf{div} \left(\dot{\mathbf{S}}^T \tilde{\Lambda}_e + \mathbf{S}^T \tilde{\Lambda}_p \right) = \rho \left(a \ddot{\mathbf{u}} + b \dot{\mathbf{u}} + c \mathbf{u} \right) \qquad \text{in } \Omega^{\text{PML}} \times \mathsf{J}, \quad (3.1\text{b})$$

$$\begin{aligned} &\mathcal{D} : \left(a \ddot{\mathbf{S}} + b \dot{\mathbf{S}} + c \mathbf{S} \right) \\ &\qquad = \frac{1}{2} \left[(\nabla \dot{\mathbf{u}}) \tilde{\Lambda}_e + \tilde{\Lambda}_e (\nabla \dot{\mathbf{u}})^T + (\nabla \mathbf{u}) \tilde{\Lambda}_p + \tilde{\Lambda}_p (\nabla \mathbf{u})^T \right] \quad \text{in } \Omega^{\text{PML}} \times \mathsf{J}, \quad (3.1\text{c}) \end{aligned}$$

subject to silent initial, and the following boundary and interface conditions:

$$\left\{ \mu \left[\nabla \mathbf{u} + (\nabla \mathbf{u})^T \right] + \lambda (\operatorname{div} \mathbf{u}) \mathcal{I} \right\} \mathbf{n} = \boldsymbol{g}_n \qquad \text{on } \Gamma_N^{\text{RD}} \times \mathsf{J}, \quad (3.2\text{a})$$

$$(\dot{\mathbf{S}}^T \tilde{\Lambda}_e + \mathbf{S}^T \tilde{\Lambda}_p) \mathbf{n} = \mathbf{0} \qquad \text{on } \Gamma_N^{\text{PML}} \times \mathsf{J}, \quad (3.2\text{b})$$

$$\mathbf{u} = \mathbf{0} \qquad \text{on } \Gamma_D^{\text{PML}} \times \mathsf{J}, \quad (3.2\text{c})$$

$$\mathbf{u}^{\text{RD}} = \mathbf{u}^{\text{PML}} \qquad \text{on } \Gamma^{\text{I}} \times \mathsf{J}, \quad (3.2\text{d})$$

$$\left\{ \mu \left[\nabla \mathbf{u} + (\nabla \mathbf{u})^T \right] + \lambda (\operatorname{div} \mathbf{u}) \mathcal{I} \right\} \mathbf{n} = -(\dot{\mathbf{S}}^T \tilde{\Lambda}_e + \mathbf{S}^T \tilde{\Lambda}_p) \mathbf{n} \quad \text{on } \Gamma^{\text{I}} \times \mathsf{J}, \quad (3.2\text{e})$$

where $\Omega \subset \mathbb{R}^2$ denotes the region occupied by the elastic body (Ω^{RD}), surrounded on three of its sides by the PML buffer zone (Ω^{PML}). Γ^{I} is the interface boundary between regular and PML domains. Ω is bounded by $\Gamma = \Gamma_D \cup \Gamma_N$, where $\Gamma_D \cap \Gamma_N = \emptyset$, and $\Gamma_D \equiv \Gamma_D^{\text{PML}}$, $\Gamma_N = \Gamma_N^{\text{RD}} \cup \Gamma_N^{\text{PML}}$. Moreover, $\boldsymbol{g}_n$ denotes prescribed tractions, and $\mathsf{J} = (0, T)$ denotes the time interval of interest.

3.1.2 The inverse problem

We consider the sources and the response collected at the ground surface receivers as known. We formulate the inverse problem initially as a misfit minimization problem, where the misfit is defined as the difference between the measured response at the receivers and a computed response, where the latter is obtained using trial distributions of the material parameters $\lambda(\mathbf{x})$ and $\mu(\mathbf{x})$. The misfit minimization is subject to the physics of the problem, as the latter are expressed by the forward problem statement shown in the preceding section. Thus, in short, the inverse medium problem is cast as a PDE-constrained least-squares misfit optimization problem, whose treatment is discussed next.

3.2 The PDE-constrained optimization problem

Referring to Fig. 3.1(b), let Γ_m denote the part of the surface Γ_N^{RD} occupied by measuring stations (receivers), and let $\mathbf{u}_m(\mathbf{x}, t)$ denote the measured displacement response to a known excitation. Let also N_r denote the total number of receivers on the surface, and let $\mathbf{u}(\mathbf{x}, t)$ be the computed response corresponding to a trial material profile. Then, the misfit least-squares minimization problem can be cast as: *minimize*

$$\mathcal{F} := \frac{1}{2} \sum_{j=1}^{N_r} \int_0^T \int_{\Gamma_m} (\mathbf{u} - \mathbf{u}_m) \cdot (\mathbf{u} - \mathbf{u}_m) \; \delta(\mathbf{x} - \mathbf{x}_j) \, \mathrm{d}\Gamma_m dt + \mathcal{R}(\lambda, \mu), \tag{3.3}$$

subject to (3.1) and (3.2).

In the above, $\mathcal{F}$ denotes the objective functional, comprising the misfit functional augmented by an additional term –the regularization functional. In

(3.3), $\mathcal{R}$ has been introduced to alleviate the solution multiplicity, inherent in this as is in all inverse problems. We discuss next two candidate regularization choices for $\mathcal{R}$.

3.3 Regularization functionals

Solution multiplicity in inverse problems is, in general, due to the presence of insufficient data, which, in turn, lead to an ill-posed problem in the Hadamard sense. Common strategies used to alleviate solution multiplicity include Tikhonov (TN) [156], and Total Variation (TV) [139] regularization schemes. We discuss and use both.

3.3.1 Tikhonov (TN) regularization

Tikhonov regularization [156] is a widely-adopted scheme; it is defined in terms of the L^2 norm of the gradient of the control parameter (λ and μ, in this case). Accordingly, the $\mathcal{R}$ term in (3.3) becomes

$$\mathcal{R}(\lambda, \mu) = \frac{R_\lambda}{2} \int_\Omega \nabla\lambda \cdot \nabla\lambda \ \mathrm{d}\Omega + \frac{R_\mu}{2} \int_\Omega \nabla\mu \cdot \nabla\mu \ \mathrm{d}\Omega \tag{3.4}$$

where R_λ and R_μ are user-defined regularization factors for λ and μ, respectively. These factors control the amount of penalty imposed via (3.4) on the gradients of λ and μ. Typically, the TN scheme penalizes sharp and highly oscillatory gradients and, thus, precludes spatially rapid material variations from becoming solutions to the inverse medium problem. Consequently, sharp material interfaces may not be well reconstructed when using the TN scheme, which tends to smoothen discontinuities.

3.3.2 Total Variation (TV) regularization

The Total Variation regularization [139] is defined in terms of the semi-norm of the control parameters. Specifically, in this case, the $\mathcal{R}$ term in (3.3) becomes

$$\mathcal{R}(\lambda, \mu) = R_\lambda \int_\Omega (\nabla\lambda \cdot \nabla\lambda + \epsilon)^{\frac{1}{2}} \, \mathrm{d}\Omega + R_\mu \int_\Omega (\nabla\mu \cdot \nabla\mu + \epsilon)^{\frac{1}{2}} \, \mathrm{d}\Omega \tag{3.5}$$

where, again, R_λ and R_μ are user-defined regularization factors. The small parameter ϵ changes the overall behavior of the scheme by making $\mathcal{R}$ differentiable when the gradient of the control parameter vanishes. The TV scheme typically preserves sharp interfaces since, unlike TN, the first variation of TV is bounded. In addition, the TV will still penalize spatial material oscillations in smooth target regions. Overall, the TV's performance with sharply-varying profiles is expected to be better than that of the TN scheme.

3.4 The optimization problem

We cast the constrained optimization problem (3.3) with the aid of a Lagrangian $\mathcal{L}$, whereby the misfit functional $\mathcal{F}$ is augmented with the side-imposition of the governing PDEs and boundary conditions via Lagrange multipliers, per:

$$
\begin{aligned}
&\mathcal{L}(\mathbf{u}, \mathbf{S}, \boldsymbol{\theta}_{\boldsymbol{u1}}, \boldsymbol{\theta}_{\boldsymbol{u2}}, \boldsymbol{\theta}_{\boldsymbol{s}}, \boldsymbol{\theta}_{\boldsymbol{b1}}, \boldsymbol{\theta}_{\boldsymbol{b2}}, \lambda, \mu) \\
&\quad = \frac{1}{2} \sum_{j=1}^{N_r} \int_0^T \int_{\Gamma_m} (\mathbf{u} - \mathbf{u}_m) \cdot (\mathbf{u} - \mathbf{u}_m) \ \delta(\mathbf{x} - \mathbf{x}_j) \, \mathrm{d}\Gamma_m dt \ + \ \mathcal{R}(\lambda, \mu) \\
&\quad + \int_{\Omega^{\mathrm{RD}}} \int_0^T \boldsymbol{\theta}_{\boldsymbol{u1}} \cdot \left[\mathbf{div} \left\{ \mu \left[\nabla \mathbf{u} + (\nabla \mathbf{u})^T \right] + \lambda (\operatorname{div} \mathbf{u}) \mathcal{I} \right\} + \mathbf{f} - \rho \ddot{\mathbf{u}} \right] \, dt \mathrm{d}\Omega \\
&\quad + \int_{\Omega^{\mathrm{PML}}} \int_0^T \boldsymbol{\theta}_{\boldsymbol{u2}} \cdot \left[\mathbf{div} \left(\dot{\mathbf{S}}^T \tilde{\Lambda}_e + \mathbf{S}^T \tilde{\Lambda}_p \right) - \rho \left(a \ddot{\mathbf{u}} + b \dot{\mathbf{u}} + c \mathbf{u} \right) \right] \, dt \mathrm{d}\Omega \\
&\quad + \int_{\Omega^{\mathrm{PML}}} \int_0^T \boldsymbol{\theta}_{\boldsymbol{s}} : \Big\{ \mathcal{D} : \left(a \ddot{\mathbf{S}} + b \dot{\mathbf{S}} + c \mathbf{S} \right) \\
&\qquad\qquad\qquad - \frac{1}{2} \left[(\nabla \dot{\mathbf{u}}) \tilde{\Lambda}_e + \tilde{\Lambda}_e (\nabla \dot{\mathbf{u}})^T + (\nabla \mathbf{u}) \tilde{\Lambda}_p + \tilde{\Lambda}_p (\nabla \mathbf{u})^T \right] \Big\} \, dt \mathrm{d}\Omega \\
&\quad + \int_{\Gamma_N^{\mathrm{RD}}} \int_0^T \boldsymbol{\theta}_{\boldsymbol{b1}} \cdot \left\{ \left(\mu \left[\nabla \mathbf{u} + (\nabla \mathbf{u})^T \right] + \lambda (\operatorname{div} \mathbf{u}) \mathcal{I} \right) \mathbf{n} - \boldsymbol{g}_n \right\} \ dt \mathrm{d}\Gamma \\
&\quad + \int_{\Gamma_N^{\mathrm{PML}}} \int_0^T \boldsymbol{\theta}_{\boldsymbol{b2}} \cdot \left[\left(\dot{\mathbf{S}}^T \tilde{\Lambda}_e + \mathbf{S}^T \tilde{\Lambda}_p \right) \mathbf{n} \right] \ dt \mathrm{d}\Gamma
\end{aligned}
\tag{3.6}
$$

with

$$\mathbf{u} = \mathbf{0} \qquad \text{on } \Gamma_D^{\mathrm{PML}} \times \mathsf{J}, \tag{3.7a}$$

$$\mathbf{u}^+ = \mathbf{u}^- \qquad \text{on } \Gamma^{\mathrm{I}} \times \mathsf{J}, \tag{3.7b}$$

$$\left\{ \mu \left[\nabla \mathbf{u} + (\nabla \mathbf{u})^T \right] + \lambda (\operatorname{div} \mathbf{u}) \mathcal{I} \right\} \mathbf{n} = -(\dot{\mathbf{S}}^T \tilde{\Lambda}_e + \mathbf{S}^T \tilde{\Lambda}_p) \mathbf{n} \qquad \text{on } \Gamma^{\mathrm{I}} \times \mathsf{J}, \tag{3.7c}$$

$$\mathbf{u}(\mathbf{x}, 0) = \mathbf{0}, \qquad \dot{\mathbf{u}}(\mathbf{x}, 0) = \mathbf{0} \qquad \text{in } \Omega, \tag{3.7d}$$

$$\mathbf{S}(\mathbf{x}, 0) = \mathbf{0}, \qquad \dot{\mathbf{S}}(\mathbf{x}, 0) = \mathbf{0} \qquad \text{in } \Omega. \tag{3.7e}$$

In the above and in the parlance customarily used for such problems, $\{\mathbf{u}, \mathbf{S}\}$ are the *state variables* (s), $\{\boldsymbol{\theta}_{\boldsymbol{u1}}, \ \boldsymbol{\theta}_{\boldsymbol{u2}}, \ \boldsymbol{\theta}_{\boldsymbol{s}}, \ \boldsymbol{\theta}_{\boldsymbol{b1}}, \ \boldsymbol{\theta}_{\boldsymbol{b2}}\}$ are the Lagrange multipliers or *adjoint variables* (m), and $\{\lambda,\ \mu\}$ are the *control variables* (c). The Lagrangian functional can be summarily rewritten as

$$\mathcal{L}(\mathrm{s,m,c}) = \text{misfit} \ + \ \text{regularization} \ + \ \text{side-imposed PDEs and BCs}. \tag{3.8}$$

Next, we seek to satisfy the stationarity[1] of $\mathcal{L}$ by requiring that the first variations of $\mathcal{L}$ vanish, i.e.,

$$\nabla\mathcal{L} = \begin{bmatrix} \delta_{\mathrm{s}}\mathcal{L} \\ \delta_{\mathrm{m}}\mathcal{L} \\ \delta_{\mathrm{c}}\mathcal{L} \end{bmatrix} = \mathbf{0}. \tag{3.9}$$

We derive next the three first-order optimality conditions associated with $\delta_{\mathrm{m}}\mathcal{L}$, $\delta_{\mathrm{s}}\mathcal{L}$, and $\delta_{\mathrm{c}}\mathcal{L}$, respectively.

3.4.1 The 1st optimality condition (State problem)

The variation of $\mathcal{L}$ with respect to the Lagrange multipliers must vanish; accordingly

$$\delta_{\boldsymbol{\theta_{u1}}}\mathcal{L} + \delta_{\boldsymbol{\theta_{u2}}}\mathcal{L} + \delta_{\boldsymbol{\theta_{s}}}\mathcal{L} + \delta_{\boldsymbol{\theta_{b1}}}\mathcal{L} + \delta_{\boldsymbol{\theta_{b2}}}\mathcal{L} = 0, \tag{3.10}$$

---

[1] Stationarity does not imply attainment of a minimum, since the convexity of the Lagrangian is not guaranteed

or equivalently,

$$\begin{aligned}
0 = & \int_{\Omega^{\mathrm{RD}}} \int_0^T \delta \boldsymbol{\theta}_{\boldsymbol{u1}} \cdot \left[\mathbf{div}\left\{\mu\left[\nabla \mathbf{u} + (\nabla \mathbf{u})^T\right] + \lambda(\operatorname{div} \mathbf{u})\mathcal{I}\right\} + \mathbf{f} - \rho \ddot{\mathbf{u}}\right] \, dt \mathrm{d}\Omega \\
& + \int_{\Omega^{\mathrm{PML}}} \int_0^T \delta \boldsymbol{\theta}_{\boldsymbol{u2}} \cdot \left[\mathbf{div}\left(\dot{\mathbf{S}}^T \tilde{\Lambda}_e + \mathbf{S}^T \tilde{\Lambda}_p\right) - \rho\left(a\ddot{\mathbf{u}} + b\dot{\mathbf{u}} + c\mathbf{u}\right)\right] \, dt \mathrm{d}\Omega \\
& + \int_{\Omega^{\mathrm{PML}}} \int_0^T \delta \boldsymbol{\theta}_{\boldsymbol{s}} : \left\{\mathcal{D} : \left(a\ddot{\mathbf{S}} + b\dot{\mathbf{S}} + c\mathbf{S}\right)\right. \\
& \qquad \left. - \frac{1}{2}\left[(\nabla \dot{\mathbf{u}})\tilde{\Lambda}_e + \tilde{\Lambda}_e(\nabla \dot{\mathbf{u}})^T + (\nabla \mathbf{u})\tilde{\Lambda}_p + \tilde{\Lambda}_p(\nabla \mathbf{u})^T\right]\right\} \, dt \mathrm{d}\Omega \\
& + \int_{\Gamma_N^{\mathrm{RD}}} \int_0^T \delta \boldsymbol{\theta}_{\boldsymbol{b1}} \cdot \left\{\left(\mu\left[\nabla \mathbf{u} + (\nabla \mathbf{u})^T\right] + \lambda(\operatorname{div} \mathbf{u})\mathcal{I}\right)\mathbf{n} - \boldsymbol{g}_n\right\} \, dt \mathrm{d}\Gamma \\
& + \int_{\Gamma_N^{\mathrm{PML}}} \int_0^T \delta \boldsymbol{\theta}_{\boldsymbol{b2}} \cdot \left[\left(\dot{\mathbf{S}}^T \tilde{\Lambda}_e + \mathbf{S}^T \tilde{\Lambda}_p\right)\mathbf{n}\right] \, dt \mathrm{d}\Gamma. \qquad (3.11)
\end{aligned}$$

Since $\delta\boldsymbol{\theta}_{\boldsymbol{u1}}, \delta\boldsymbol{\theta}_{\boldsymbol{u2}}, \delta\boldsymbol{\theta}_{\boldsymbol{s}}, \delta\boldsymbol{\theta}_{\boldsymbol{b1}}$, and $\delta\boldsymbol{\theta}_{\boldsymbol{b2}}$ are arbitrary, the terms they multiply must vanish identically. There results the *state (or forward) problem*[2], identical to the IBVP given by (3.1-3.2).

3.4.2 The 2^{nd} optimality condition (Adjoint problem)

Similarly, we enforce the vanishing of the variation of $\mathcal{L}$ with respect to the state variables:

$$\delta_{\mathbf{u}}\mathcal{L} + \delta_{\mathbf{S}}\mathcal{L} = 0. \qquad (3.12)$$

---

[2] We use *state* and *forward* interchangeably throughout the dissertation.

The details of the derivation are shown in Appendix B. There results the following *adjoint problem*:

$$\mathbf{div}\left[\mu(\nabla\boldsymbol{\theta}_{\boldsymbol{u1}} + \nabla\boldsymbol{\theta}_{\boldsymbol{u1}}{}^{T}) + \lambda\ \mathrm{div}\,\boldsymbol{\theta}_{\boldsymbol{u1}}\,\mathcal{I}\right] = \rho\ddot{\boldsymbol{\theta}}_{\boldsymbol{u1}} \qquad \text{in } \Omega^{\mathrm{RD}} \times \mathsf{J}, \tag{3.13a}$$

$$\mathbf{div}\left(-\dot{\boldsymbol{\theta}}_{\boldsymbol{s}}\tilde{\Lambda}_{e} + \boldsymbol{\theta}_{\boldsymbol{s}}\tilde{\Lambda}_{p}\right) = \rho\left(a\ddot{\boldsymbol{\theta}}_{\boldsymbol{u2}} - b\dot{\boldsymbol{\theta}}_{\boldsymbol{u2}} + c\boldsymbol{\theta}_{\boldsymbol{u2}}\right) \qquad \text{in } \Omega^{\mathrm{PML}} \times \mathsf{J}, \tag{3.13b}$$

$$\mathcal{D} : \left(a\ddot{\boldsymbol{\theta}}_{\boldsymbol{s}} - b\dot{\boldsymbol{\theta}}_{\boldsymbol{s}} + c\boldsymbol{\theta}_{\boldsymbol{s}}\right) = -\tilde{\Lambda}_{e}\left(\nabla\dot{\boldsymbol{\theta}}_{\boldsymbol{u2}}\right)^{T} + \tilde{\Lambda}_{p}\left(\nabla\boldsymbol{\theta}_{\boldsymbol{u2}}\right)^{T} \qquad \text{in } \Omega^{\mathrm{PML}} \times \mathsf{J}, \tag{3.13c}$$

subject to

$$\left\{\mu(\nabla\boldsymbol{\theta}_{\boldsymbol{u1}} + \nabla\boldsymbol{\theta}_{\boldsymbol{u1}}{}^{T}) + \lambda\ \mathrm{div}\,\boldsymbol{\theta}_{\boldsymbol{u1}}\,\mathcal{I}\right\}\mathbf{n} = \sum_{j=1}^{N_r}(\mathbf{u} - \mathbf{u}_m)\,\delta(\mathbf{x} - \mathbf{x}_j) \qquad \text{on } \Gamma_m \times \mathsf{J}, \tag{3.14a}$$

$$\left(-\dot{\boldsymbol{\theta}}_{\boldsymbol{s}}\tilde{\Lambda}_{e} + \boldsymbol{\theta}_{\boldsymbol{s}}\tilde{\Lambda}_{p}\right)\mathbf{n} = \mathbf{0} \qquad \text{on } \Gamma_{N}^{\mathrm{PML}} \times \mathsf{J}, \tag{3.14b}$$

$$\boldsymbol{\theta}_{\boldsymbol{u2}} = \mathbf{0} \qquad \text{on } \Gamma_{D}^{\mathrm{PML}} \times \mathsf{J}, \tag{3.14c}$$

$$\boldsymbol{\theta}_{\boldsymbol{u1}} = \boldsymbol{\theta}_{\boldsymbol{u2}} \qquad \text{on } \Gamma^{\mathrm{I}} \times \mathsf{J}, \tag{3.14d}$$

$$\left\{\mu(\nabla\boldsymbol{\theta}_{\boldsymbol{u1}} + \nabla\boldsymbol{\theta}_{\boldsymbol{u1}}{}^{T}) + \lambda\ \mathrm{div}\,\boldsymbol{\theta}_{\boldsymbol{u1}}\,\mathcal{I}\right\}\mathbf{n} = -\left(-\dot{\boldsymbol{\theta}}_{\boldsymbol{s}}\tilde{\Lambda}_{e} + \boldsymbol{\theta}_{\boldsymbol{s}}\tilde{\Lambda}_{p}\right)\mathbf{n} \qquad \text{on } \Gamma^{\mathrm{I}} \times \mathsf{J}, \tag{3.14e}$$

$$\boldsymbol{\theta}_{\boldsymbol{u1}}(\mathbf{x}, T) = \mathbf{0}, \qquad \dot{\boldsymbol{\theta}}_{\boldsymbol{u1}}(\mathbf{x}, T) = \mathbf{0} \qquad \text{in } \Omega^{\mathrm{RD}}, \tag{3.14f}$$

$$\boldsymbol{\theta}_{\boldsymbol{u2}}(\mathbf{x}, T) = \mathbf{0}, \qquad \dot{\boldsymbol{\theta}}_{\boldsymbol{u2}}(\mathbf{x}, T) = \mathbf{0} \qquad \text{in } \Omega^{\mathrm{PML}}, \tag{3.14g}$$

$$\boldsymbol{\theta}_{\boldsymbol{s}}(\mathbf{x}, T) = \mathbf{0}, \qquad \dot{\boldsymbol{\theta}}_{\boldsymbol{s}}(\mathbf{x}, T) = \mathbf{0} \qquad \text{in } \Omega^{\mathrm{PML}}. \tag{3.14h}$$

We note that the adjoint problem is a *final-value* problem as opposed to the initial-value state problem. Moreover, it is driven by the misfit between the computed and observed responses at measuring stations. We note that the operators implicated in the adjoint PDEs are identical to the state operators, modulo the sign reversal for those terms implicating first-order time derivatives. By construction, the adjoint equations are also hybrid and PML-endowed, with $(\boldsymbol{\theta_{u1}}, \boldsymbol{\theta_{u2}})$ and $\boldsymbol{\theta_s}$ playing a role analogous to $\mathbf{u}$ and $\mathbf{S}$ of the state problem, respectively.

3.4.3 The 3^{rd} optimality condition (Control problem)

Lastly, we impose the vanishing of the variation of $\mathcal{L}$ with respect to the Lamé parameters:

$$\delta_\lambda \mathcal{L} = 0, \tag{3.15}$$

$$\delta_\mu \mathcal{L} = 0. \tag{3.16}$$

As shown in Appendix C, the above variations result in the following two boundary-value control problems:

λ-control problem:

$$-R_\lambda \Delta\lambda - \int_0^T (\operatorname{div} \boldsymbol{\theta_{u1}})(\operatorname{div} \mathbf{u})\, dt = 0 \qquad \text{in } \Omega^{\text{RD}}, \tag{3.17a}$$

subject to

$$\int_{\Gamma_N^{\text{RD}}} \nabla\lambda \cdot \mathbf{n}\, \mathrm{d}\Gamma = 0 \qquad \text{on } \Gamma_N^{\text{RD}}, \tag{3.17b}$$

$$R_\lambda \nabla\lambda \cdot \mathbf{n} = -\int_0^T \boldsymbol{\theta_{u1}} \cdot (\operatorname{div} \mathbf{u})\mathbf{n}\, dt \qquad \text{on } \Gamma^{\text{I}}. \tag{3.17c}$$

μ-control problem:

$$-R_{\mu}\Delta\mu - \int_0^T \nabla\boldsymbol{\theta}_{\boldsymbol{u1}} : \left(\nabla\mathbf{u} + \nabla\mathbf{u}^T\right)\, dt = 0 \qquad \text{in } \Omega^{\mathrm{RD}}, \tag{3.18a}$$

subject to

$$\int_{\Gamma_N^{\mathrm{RD}}} \nabla\mu \cdot \mathbf{n}\,\mathrm{d}\Gamma = 0 \qquad \text{on } \Gamma_N^{\mathrm{RD}}, \tag{3.18b}$$

$$R_{\mu}\nabla\mu \cdot \mathbf{n} = -\int_0^T \boldsymbol{\theta}_{\boldsymbol{u1}} \cdot \left(\nabla\mathbf{u} + \nabla\mathbf{u}^T\right)\mathbf{n}\, dt \qquad \text{on } \Gamma^{\mathrm{I}}. \tag{3.18c}$$

In writing (3.17) and (3.18), we adopted the TN scheme for regularizing the solutions. If the TV regularization were to be used instead, the first terms in (3.17a) and (3.18a) are modified[3], and the control problems now read

$$-R_{\lambda}\,\nabla\cdot\left[(\nabla\lambda\cdot\nabla\lambda+\epsilon)^{-\frac{1}{2}}\,\nabla\lambda\right] - \int_0^T (\operatorname{div}\boldsymbol{\theta}_{\boldsymbol{u1}})(\operatorname{div}\mathbf{u})\, dt = 0 \qquad \text{in } \Omega^{\mathrm{RD}}, \tag{3.19}$$

$$-R_{\mu}\,\nabla\cdot\left[(\nabla\mu\cdot\nabla\mu+\epsilon)^{-\frac{1}{2}}\,\nabla\mu\right] - \int_0^T \nabla\boldsymbol{\theta}_{\boldsymbol{u1}} : \left(\nabla\mathbf{u} + \nabla\mathbf{u}^T\right)\, dt = 0 \qquad \text{in } \Omega^{\mathrm{RD}}. \tag{3.20}$$

We remark that the TV scheme leads to a nonlinear operator in the control equations, as opposed to the Laplacian operator that results when TN regularization is used.

3.5 The inversion process

As implied by (3.9), to satisfy the stationarity of $\mathcal{L}$, all three problems (*state*, *adjoint*, and *control*) must be solved. There are two possible solution

---

[3] See the details in Appendix C.

strategies one could proceed with. The first strategy is a *full-space method*, where one attempts to solve the coupled system simultaneously for all of the state ($\mathbf{u}$, $\mathbf{S}$), adjoint ($\boldsymbol{\theta}_{\boldsymbol{u}}$, $\boldsymbol{\theta}_{\boldsymbol{s}}$), and control ($\lambda$, μ) variables. However, the solution of the resulting KKT[4] system is computationally expensive. Alternatively, and similarly to what was done in [60, 96], a *reduced-space method*, in which the coupled system of PDEs are solved in the reduced space of the control variables, is preferable. The procedure is iterative: we start with an assumed initial spatial distribution of the control parameters (λ and μ) and solve the state problem (3.1-3.2) for the state variables $\mathbf{u}$ and $\mathbf{S}$. Then, we solve the adjoint problem (3.13-3.14) to obtain the adjoint variables $\boldsymbol{\theta}_{\boldsymbol{u}}$ and $\boldsymbol{\theta}_{\boldsymbol{s}}$ based on the state solutions (the adjoint problem is driven by the misfit, and requires the state solutions to form the misfit). By doing so, we satisfy the first and second optimality conditions, that is, the gradient of the Lagrangian becomes

$$\nabla\mathcal{L} = \begin{bmatrix} 0 \\ 0 \\ \delta_{\mathrm{c}}\mathcal{L} \end{bmatrix} \qquad \Rightarrow \qquad \nabla_c\mathcal{L} = \delta_{\mathrm{c}}\mathcal{L}, \tag{3.21}$$

where the vanishing of the last term in the bracket leads to, as discussed earlier, the control problem. Owing to (3.21), the term ($\delta_{\mathrm{c}}\mathcal{L}$) can be seen as the *reduced gradient* ($\nabla_c\mathcal{L}$), and can be incorporated into a gradient-based scheme to update the control/material parameters. Specifically, a second-order expansion of the Lagrangian $\mathcal{L}$ can be expressed, in general, as

$$\mathcal{L}(\mathbf{c}_{k+1}) \cong \mathcal{L}(\mathbf{c}_k) + \nabla_c\mathcal{L}(\mathbf{c}_k)\cdot\Delta\mathbf{c}_k + \frac{1}{2}(\Delta\mathbf{c}_k)^T\mathbf{H}\Delta\mathbf{c}_k, \tag{3.22}$$

---

[4] Upon discretization, the state, adjoint, and control problems lead to a system, commonly known as Karush-Kuhn-Tucker (KKT) system.

with $\Delta \mathbf{c}_k = \mathbf{c}_{k+1} - \mathbf{c}_k$. Here k denotes the k-th inversion iteration of the material parameters. Thus, by ignoring the higher-order term implicating the Hessian $\mathbf{H}$, a gradient scheme can be used to compute the parameters $\mathbf{c}_{k+1}$ at the next iteration $k+1$, using the parameters at the previous iteration $\mathbf{c}_k$ and the reduced gradient. We note that, owing to the satisfaction of the state problem, the Lagrangian in (3.22) reduces to the objective functional (3.3). This statement, however, is not rigorous: the state problem is satisfied in a *weak* sense, whereas in the Lagrangian we have side-imposed the *strong* form of the state problem. Thus, the Lagrangian, once the state problem has been solved, reduces to the objective functional augmented by the *residual* of the state problem. In adequately discretized problems, we expect the objective functional to dominate over the state problem's residual, and, thus, we justify replacing the Lagrangian in (3.22) with the objective functional. Herein, to iteratively update the material parameters $\mathbf{c}_k = [\,\lambda \quad \mu\,]^T$ we use a conjugate gradient method with inexact line search. Schematically, the inversion process is captured in the flow chart shown in Fig. 3.2. We discuss next each chart component in detail.

3.5.1 The state problem solution

The state problem is solved using the hybrid approach described in section 2.5.

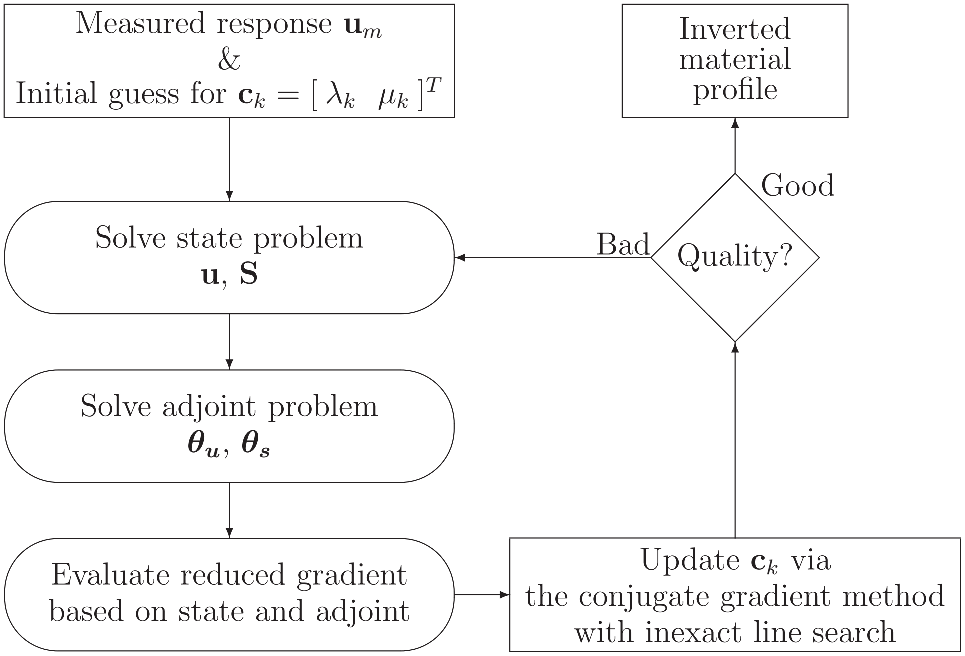

Figure 3.2: Flowchart of inversion process - reduced-space method

3.5.2 The adjoint problem solution

Owing to the similarity of the operators implicated in the state and adjoint problems, we use a hybrid formulation for the adjoint problem (3.13)-(3.14) too. To reduce notational congestion, we condense $\boldsymbol{\theta_{u1}}$ and $\boldsymbol{\theta_{u2}}$ in (3.13-3.14) into $\boldsymbol{\theta_u}$, since $\boldsymbol{\theta_{u1}}$ and $\boldsymbol{\theta_{u2}}$ represent the same Lagrange multiplier defined on different domains, that is,

$$\boldsymbol{\theta_u} = \begin{cases} \boldsymbol{\theta_{u1}} & \text{in } \Omega^{\mathrm{RD}} \\ \boldsymbol{\theta_{u1}} = \boldsymbol{\theta_{u2}} & \text{on } \Gamma^{\mathrm{I}} \\ \boldsymbol{\theta_{u2}} & \text{in } \Omega^{\mathrm{PML}} \end{cases} . \tag{3.23}$$

To obtain the variational form of the adjoint problem, we take inner products of (3.13) with arbitrary weight functions $\mathbf{w}_1(\mathbf{x})$, $\mathbf{w}_2(\mathbf{x})$, and $\mathbf{T}(\mathbf{x})$, residing in appropriate admissible spaces, and then integrate over the associated computational domains Ω^{RD}, Ω^{PML}, and Ω^{PML}, respectively. Along lines similar to the state problem, the integration by parts is applied to the equilibrium-like equations (3.13a) and (3.13b), and by adding the two, we arrive at the weak form of (3.13):

$$\begin{aligned}
&\int_{\Omega^{\mathrm{RD}}} \nabla \mathbf{w}_1 : \left[\mu(\nabla\boldsymbol{\theta_u} + \nabla\boldsymbol{\theta_u}^T) + \lambda \operatorname{div}\boldsymbol{\theta_u}\,\mathcal{I}\right]\,\mathrm{d}\Omega \\
&\qquad + \int_{\Omega^{\mathrm{PML}}} \nabla\mathbf{w}_2 : \left(-\dot{\boldsymbol{\theta}}_{\boldsymbol{s}}\tilde{\Lambda}_e + \boldsymbol{\theta_s}\tilde{\Lambda}_p\right)\,\mathrm{d}\Omega + \int_{\Omega^{\mathrm{RD}}} \mathbf{w}_1\cdot\rho\ddot{\boldsymbol{\theta}}_{\boldsymbol{u}}\,\mathrm{d}\Omega \\
&\qquad\qquad + \int_{\Omega^{\mathrm{PML}}} \mathbf{w}_2\cdot\rho\left(a\ddot{\boldsymbol{\theta}}_{\boldsymbol{u}} - b\dot{\boldsymbol{\theta}}_{\boldsymbol{u}} + c\boldsymbol{\theta_u}\right)\,\mathrm{d}\Omega \\
&\qquad\qquad\qquad = \int_{\Gamma_m} \mathbf{w}_1\cdot\left[\sum_{j=1}^{N_r}(\mathbf{u}-\mathbf{u}_m)\,\delta(\mathbf{x}-\mathbf{x}_j)\right]\,\mathrm{d}\Gamma_m, \qquad (3.24a)
\end{aligned}$$

$$\begin{aligned}
&\int_{\Omega^{\mathrm{PML}}} \mathbf{T} : \left[\mathcal{D} : \left(a\ddot{\boldsymbol{\theta}}_{\boldsymbol{s}} - b\dot{\boldsymbol{\theta}}_{\boldsymbol{s}} + c\boldsymbol{\theta_s}\right)\right]\,\mathrm{d}\Omega \\
&\qquad\qquad = \int_{\Omega^{\mathrm{PML}}} \mathbf{T} : \left[-\tilde{\Lambda}_e\left(\nabla\dot{\boldsymbol{\theta}}_{\boldsymbol{u}}\right)^T + \tilde{\Lambda}_p\left(\nabla\boldsymbol{\theta_u}\right)^T\right]\,\mathrm{d}\Omega. \qquad (3.24b)
\end{aligned}$$

Next, we seek $\boldsymbol{\theta_u} \in \mathbf{H}^1(\Omega)\times\mathsf{J}$ satisfying $\boldsymbol{\theta_u}|_{\Gamma_D^{\mathrm{PML}}} = \mathbf{0}$, and $\boldsymbol{\theta_s} \in \mathcal{L}^2(\Omega)\times\mathsf{J}$, such that equation (3.24) holds for all $\mathbf{w}_1 \in \mathbf{H}^1(\Omega)$, $\mathbf{w}_2 \in \mathbf{H}^1(\Omega)$ satisfying $\mathbf{w}_2|_{\Gamma_D^{\mathrm{PML}}} = \mathbf{0}$, and $\mathbf{T} \in \mathcal{L}^2(\Omega)$. Recall that within the PML we use a mixed method, where both $\boldsymbol{\theta_u}(\mathbf{x},t)$ and $\boldsymbol{\theta_s}(\mathbf{x},t)$ are treated as independent variables that need to be approximated separately. Let the basis functions in $\boldsymbol{\Xi}_h \subset \mathbf{H}^1(\Omega)$ and $\boldsymbol{\Upsilon}_h \subset \mathcal{L}^2(\Omega)$ be denoted by $\boldsymbol{\Phi}$ and $\boldsymbol{\Psi}$, respectively. The trial functions $\boldsymbol{\theta}^h_{\mathbf{u}} \in \boldsymbol{\Xi}_h\times\mathsf{J}$ and $\boldsymbol{\theta}^h_{\mathbf{s}} \in \boldsymbol{\Upsilon}_h\times\mathsf{J}$ are spatially discretized as

$$\boldsymbol{\theta_u}(\mathbf{x},t) \cong \boldsymbol{\theta}^h_{\mathbf{u}}(\mathbf{x},t) = \begin{bmatrix}\boldsymbol{\Phi}^T(\mathbf{x})\boldsymbol{\theta}^x_{\mathbf{u}}(t)\\ \boldsymbol{\Phi}^T(\mathbf{x})\boldsymbol{\theta}^y_{\mathbf{u}}(t)\end{bmatrix}, \qquad (3.25a)$$

$$\boldsymbol{\theta_s}(\mathbf{x},t) \cong \boldsymbol{\theta}^h_{\mathbf{s}}(\mathbf{x},t) = \begin{bmatrix}\boldsymbol{\Psi}^T(\mathbf{x})\boldsymbol{\theta}^{xx}_{\mathbf{s}}(t) & \boldsymbol{\Psi}^T(\mathbf{x})\boldsymbol{\theta}^{xy}_{\mathbf{s}}(t)\\ \boldsymbol{\Psi}^T(\mathbf{x})\boldsymbol{\theta}^{yx}_{\mathbf{s}}(t) & \boldsymbol{\Psi}^T(\mathbf{x})\boldsymbol{\theta}^{yy}_{\mathbf{s}}(t)\end{bmatrix}. \qquad (3.25b)$$

Similarly, the test functions $\mathbf{w}_1 \in \boldsymbol{\Xi}_h$, $\mathbf{w}_2 \in \boldsymbol{\Xi}_h$, and $\mathbf{T} \in \boldsymbol{\Upsilon}_h$ are expressed as

$$\mathbf{w}_1(\mathbf{x}) \cong \mathbf{w}_{1h}(\mathbf{x}) = \begin{bmatrix} \mathbf{w}_{1x}^T \boldsymbol{\Phi}(\mathbf{x}) \\ \mathbf{w}_{1y}^T \boldsymbol{\Phi}(\mathbf{x}) \end{bmatrix}, \tag{3.26a}$$

$$\mathbf{w}_2(\mathbf{x}) \cong \mathbf{w}_{2h}(\mathbf{x}) = \begin{bmatrix} \mathbf{w}_{2x}^T \boldsymbol{\Phi}(\mathbf{x}) \\ \mathbf{w}_{2y}^T \boldsymbol{\Phi}(\mathbf{x}) \end{bmatrix}, \tag{3.26b}$$

$$\mathbf{T}(\mathbf{x}) \cong \mathbf{T}_h(\mathbf{x}) = \begin{bmatrix} \mathbf{T}_{xx}^T \boldsymbol{\Psi}(\mathbf{x}) & \mathbf{T}_{xy}^T \boldsymbol{\Psi}(\mathbf{x}) \\ \mathbf{T}_{yx}^T \boldsymbol{\Psi}(\mathbf{x}) & \mathbf{T}_{yy}^T \boldsymbol{\Psi}(\mathbf{x}) \end{bmatrix}. \tag{3.26c}$$

Substituting the above approximants into (3.24) results in the following *semi-discrete form*[5]

$$\mathbf{M}^{\mathrm{ad}}\ddot{\mathbf{d}}^{\mathrm{ad}} + \mathbf{C}^{\mathrm{ad}}\dot{\mathbf{d}}^{\mathrm{ad}} + \mathbf{K}^{\mathrm{ad}}\mathbf{d}^{\mathrm{ad}} = \mathbf{F}^{\mathrm{ad}}, \tag{3.27}$$

where the mass-like, damping-like, stiffness-like matrices, the vector of nodal unknowns (comprising $\boldsymbol{\theta_u}$ and $\boldsymbol{\theta_s}$) and the load vector are defined in block-

---

[5] The superscript ‘ad’ stands for the *adjoint* problem.

matrix form as

$$\mathbf{M}^{\mathrm{ad}} = \begin{bmatrix} \mathbf{M}^{rr} & \mathbf{M}^{ri} & \mathbf{0} & \mathbf{0} & \mathbf{0} \\ & \mathbf{M}_a^{ii} & \mathbf{M}_a^{ip} & \mathbf{0} & \mathbf{0} \\ & & \mathbf{M}_a^{pp} & \mathbf{0} & \mathbf{0} \\ & sym & & \mathbf{N}_a^{ii} & \mathbf{N}_a^{ip} \\ & & & & \mathbf{N}_a^{pp} \end{bmatrix}, \tag{3.28a}$$

$$\mathbf{C}^{\mathrm{ad}} = \begin{bmatrix} \mathbf{0} & \mathbf{0} & \mathbf{0} & \mathbf{0} & \mathbf{0} \\ & -\mathbf{M}_b^{ii} & -\mathbf{M}_b^{ip} & -\mathbf{A}^{ii} & -\mathbf{A}^{ip} \\ & & -\mathbf{M}_b^{pp} & -\mathbf{A}^{pi} & -\mathbf{A}^{pp} \\ & sym & & -\mathbf{N}_b^{ii} & -\mathbf{N}_b^{ip} \\ & & & & -\mathbf{N}_b^{pp} \end{bmatrix}, \tag{3.28b}$$

$$\mathbf{K}^{\mathrm{ad}} = \begin{bmatrix} \mathbf{Q}^{rr} & \mathbf{Q}^{ri} & \mathbf{0} & \mathbf{0} & \mathbf{0} \\ & \mathbf{M}_c^{ii} & \mathbf{M}_c^{ip} & \mathbf{B}^{ii} & \mathbf{B}^{ip} \\ & & \mathbf{M}_c^{pp} & \mathbf{B}^{pi} & \mathbf{B}^{pp} \\ & sym & & \mathbf{N}_c^{ii} & \mathbf{N}_c^{ip} \\ & & & & \mathbf{N}_c^{pp} \end{bmatrix}, \tag{3.28c}$$

$$\mathbf{d}^{\mathrm{ad}} = \begin{bmatrix} \boldsymbol{\theta}_{\mathbf{u}}^r & \boldsymbol{\theta}_{\mathbf{u}}^i & \boldsymbol{\theta}_{\mathbf{u}}^p & \boldsymbol{\theta}_{\mathbf{s}}^i & \boldsymbol{\theta}_{\mathbf{s}}^p \end{bmatrix}^T, \tag{3.28d}$$

$$\mathbf{F}^{\mathrm{ad}} = \begin{bmatrix} \mathbf{f}^r & \mathbf{f}^i & \mathbf{0} & \mathbf{0} & \mathbf{0} \end{bmatrix}^T, \tag{3.28e}$$

with r, i, and p representing *regular* (interior) domain, *interface*, and *PML* domain, respectively. The various submatrices in the above expression are constructible by using standard Lagrange polynomial approximations (see Appendix D). We remark that the adjoint problem matrices are the *same* as those resulting from the state problem, modulo a sign reversal for the damping matrix; that is

$$\mathbf{M}^{\mathrm{ad}} = \mathbf{M}^{\mathrm{st}}, \tag{3.29a}$$

$$\mathbf{C}^{\mathrm{ad}} = -\mathbf{C}^{\mathrm{st}}, \tag{3.29b}$$

$$\mathbf{K}^{\mathrm{ad}} = \mathbf{K}^{\mathrm{st}}. \tag{3.29c}$$

The above identities lead to very cost-effective implementations since the assembly process for the adjoint problem is avoided. Thus, at every inversion iteration, one can perform the assembly corresponding to the state problem and the resulting global system matrices become readily available for the adjoint problem. Therefore, the computational cost of the entire inversion process is reduced, in addition to the savings gained by the symmetry of the system matrices.

The obtained semi-discrete form is second-order in time. However, it is a final-value problem that requires reverse marching along the time line. To resolve the time integration, we employ a Newmark-β-like scheme (Algorithm E.1) in which time marching is reversed[6].

3.5.3 Material parameter updates (Control problem)

The first and second optimality conditions are automatically satisfied once the state and adjoint problems are solved. However, the third optimality condition is satisfied exactly only for the true/target material profile. Other profiles result in non-vanishing control equations (3.17a) and (3.18a) (TN regularization case, or, equations (3.19) and (3.20), in the TV regularization case). We iteratively update the control parameters (λ and μ) so that the misfit between the measured and computed responses reduces to a preset tolerance, thereby allowing the third optimality condition to be satisfied. To this end, we use a conjugate gradient method with inexact line search and make use

---

[6] See Appendix E for details.

of the information stored in the reduced gradient ($\nabla_c \mathcal{L}$). Since there are two control/material parameters, the continuous forms of the associated reduced gradients can be expressed, in the TN case, as[7]

$$\nabla_\lambda \mathcal{L} = -R_\lambda \Delta\lambda - \int_0^T (\operatorname{div} \boldsymbol{\theta}_{\boldsymbol{u1}})(\operatorname{div} \mathbf{u})\, dt \qquad \text{in } \Omega^{\mathrm{RD}}, \tag{3.30}$$

$$\nabla_\mu \mathcal{L} = -R_\mu \Delta\mu - \int_0^T \nabla\boldsymbol{\theta}_{\boldsymbol{u1}} : \left(\nabla\mathbf{u} + \nabla\mathbf{u}^T\right)\, dt \qquad \text{in } \Omega^{\mathrm{RD}}, \tag{3.31}$$

whereas, in the case of TV regularization, they become

$$\nabla_\lambda \mathcal{L} = -R_\lambda\ \nabla \cdot \left[(\nabla\lambda \cdot \nabla\lambda + \epsilon)^{-\frac{1}{2}}\ \nabla\lambda\right] - \int_0^T (\operatorname{div} \boldsymbol{\theta}_{\boldsymbol{u1}})(\operatorname{div} \mathbf{u})\, dt, \tag{3.32}$$

$$\nabla_\mu \mathcal{L} = -R_\mu\ \nabla \cdot \left[(\nabla\mu \cdot \nabla\mu + \epsilon)^{-\frac{1}{2}}\ \nabla\mu\right] - \int_0^T \nabla\boldsymbol{\theta}_{\boldsymbol{u1}} : \left(\nabla\mathbf{u} + \nabla\mathbf{u}^T\right)\, dt. \tag{3.33}$$

In the above, the reduced gradients are restricted to Ω^{RD}. In the implementation, $\nabla_\lambda \mathcal{L}$ and $\nabla_\mu \mathcal{L}$ are evaluated at each nodal point. Specifically: using the discrete solutions of the state and adjoint problems, the time integral in the above expressions is trivially computed. On the other hand, the first terms (the Laplacian operator in the TN case, and the nonlinear operator in the TV case) of the reduced gradients are evaluated by second-order accurate finite-difference schemes. The resulting discrete reduced gradients are then used to iteratively update the nodal values of $\lambda(\mathbf{x})$ and $\mu(\mathbf{x})$, the details of which are discussed below.

---

[7] $\nabla_\lambda \mathcal{L}$ and $\nabla_\mu \mathcal{L}$ are the left-hand-sides of the control equations.

3.5.3.1 Conjugate gradient method

To fix ideas, we review first the basic steps of the conjugate gradient method. The method is widely used to solve unconstrained optimization problems of the form:

$$\min_{\mathbf{x}\in\mathbb{R}^n} f(\mathbf{x}), \tag{3.34}$$

where $\mathbb{R}^n$ denotes an n-dimensional Euclidean space and $f : \mathbb{R}^n \to \mathbb{R}$ is a continuously differentiable nonlinear function. The iterative evolution of $\mathbf{x}$ in the context of the conjugate gradient method can be cast as:

$$\mathbf{x}_{k+1} = \mathbf{x}_k + \alpha_k \mathbf{d}_k, \qquad k = 1, 2, \ldots \tag{3.35}$$

where k is an iteration counter, $\mathbf{x}_{k+1}$ is the updated iterate, α_k is a *step length* obtained by carrying out a line search, and $\mathbf{d}_k$ is a *search direction* defined by

$$\mathbf{d}_k = \begin{cases} -\mathbf{g}_k & k = 1, \\ -\mathbf{g}_k + \beta_k \mathbf{d}_{k-1} & k \geq 2. \end{cases} \tag{3.36}$$

Here, β_k is a scalar parameter and $\mathbf{g}_k = \nabla f(\mathbf{x}_k)^T$ is a column gradient vector[8] at $\mathbf{x}_k$. Various conjugate gradient methods are possible depending on the

---

[8] The gradient operation produces a row vector.

choice of the parameter β_k; a few well-known choices for β_k are

$$\beta_k^{HS} = \frac{\mathbf{g}_k^T(\mathbf{g}_k - \mathbf{g}_{k-1})}{\mathbf{d}_{k-1}^T(\mathbf{g}_k - \mathbf{g}_{k-1})}, \tag{3.37a}$$

$$\beta_k^{FR} = \frac{\|\mathbf{g}_k\|^2}{\|\mathbf{g}_{k-1}\|^2}, \tag{3.37b}$$

$$\beta_k^{PRP} = \frac{\mathbf{g}_k^T(\mathbf{g}_k - \mathbf{g}_{k-1})}{\|\mathbf{g}_{k-1}\|^2}, \tag{3.37c}$$

$$\beta_k^{CD} = -\frac{\|\mathbf{g}_k\|^2}{\mathbf{d}_{k-1}^T\mathbf{g}_{k-1}}, \tag{3.37d}$$

$$\beta_k^{LS} = -\frac{\mathbf{g}_k^T(\mathbf{g}_k - \mathbf{g}_{k-1})}{\mathbf{d}_{k-1}^T\mathbf{g}_{k-1}}, \tag{3.37e}$$

$$\beta_k^{DY} = \frac{\|\mathbf{g}_k\|^2}{\mathbf{d}_{k-1}^T(\mathbf{g}_k - \mathbf{g}_{k-1})}, \tag{3.37f}$$

$$\beta_k^{N} = \left[(\mathbf{g}_k - \mathbf{g}_{k-1}) - 2\mathbf{d}_{k-1}\frac{\|\mathbf{g}_k - \mathbf{g}_{k-1}\|^2}{\mathbf{d}_{k-1}^T(\mathbf{g}_k - \mathbf{g}_{k-1})}\right]^T \frac{\mathbf{g}_k}{\mathbf{d}_{k-1}^T(\mathbf{g}_k - \mathbf{g}_{k-1})}, \tag{3.37g}$$

where $\|\cdot\|$ denotes Euclidean norm. The corresponding methods in (3.37) are the Hestenes-Stiefel (HS) [83], Fletcher-Revees (FR) [66], Polak-Ribiére-Polyak (PRP) [130, 131], Conjugate Descent (CD) [65], Liu-Storey (LS) [113], Dai-Yuan (DS) [53] and Hager-Zhang (N) [77], respectively.

The search direction $\mathbf{d}_k$ is guaranteed to be a descent direction of $f(\mathbf{x})$ at $\mathbf{x}_k$ provided that $\mathbf{g}_k^T\mathbf{d}_k < 0$. For global convergence, $\mathbf{d}_k$ is required to satisfy the sufficient descent condition

$$\mathbf{g}_k^T\mathbf{d}_k \leq -c\|\mathbf{g}_k\|^2, \tag{3.38}$$

where $c > 0$ is a constant. The convergence behavior of conjugate gradient methods under several line searches (i.e., strong Wolfe, standard Wolfe, Goldstein, Armijo) has been extensively studied in the literature (e.g., [1, 51, 143, 161, 169–171, 174–176]). A few of these methods (FR, DY and CD) are shown to have good theoretical convergence properties, although, in practice, they suffer due to the progressive contamination of $\mathbf{d}_k$, whereas others (PRP, HS and LS) may not be guaranteed to always converge, but perform better in practice. To overcome these issues, several hybrid methods have been proposed that combine the desired features of each method [52, 71, 86, 157]. A restart strategy

$$\mathbf{d}_k = -\mathbf{g}_k \quad \text{if } k \bmod m = 0, \qquad \text{(in general; } m = 15\text{)}, \tag{3.39}$$

is used in most methods to avoid polluting the search direction by round-off errors and inaccurate step length determination. A comprehensive review of nonlinear conjugate gradient methods is available in [78].

Based on the above discussion, we discuss next a procedure for the material parameter updates. Starting with[9]

$$\min_{\boldsymbol{\lambda},\boldsymbol{\mu}\in\mathbb{R}^n} \mathcal{L}(\boldsymbol{\lambda},\boldsymbol{\mu}), \tag{3.40}$$

we cast the iterative evolution of $\boldsymbol{\lambda}$ and $\boldsymbol{\mu}$ in the context of the conjugate gradient method as

$$\boldsymbol{\lambda}_{k+1} = \boldsymbol{\lambda}_k + \alpha_k^{\lambda}\mathbf{d}_k^{\lambda}, \tag{3.41a}$$

$$\boldsymbol{\mu}_{k+1} = \boldsymbol{\mu}_k + \alpha_k^{\mu}\mathbf{d}_k^{\mu}, \tag{3.41b}$$

---

[9] $\boldsymbol{\lambda}$ and $\boldsymbol{\mu}$ are nodal material parameter vectors.

where $k = 1, 2, \ldots$, $(\alpha_k^\lambda, \alpha_k^\mu)$ are the step lengths for λ and μ, and $(\mathbf{d}_k^\lambda, \mathbf{d}_k^\mu)$ are the associated search directions defined by

$$\mathbf{d}_k^\lambda = \begin{cases} -\mathbf{g}_k^\lambda & k = 1, \\ -\mathbf{g}_k^\lambda + \beta_k^\lambda \mathbf{d}_{k-1}^\lambda & k \geq 2, \end{cases} \tag{3.42a}$$

$$\mathbf{d}_k^\mu = \begin{cases} -\mathbf{g}_k^\mu & k = 1, \\ -\mathbf{g}_k^\mu + \beta_k^\mu \mathbf{d}_{k-1}^\mu & k \geq 2. \end{cases} \tag{3.42b}$$

Here,

$$\mathbf{g}_k^\lambda = (\nabla_{\boldsymbol{\lambda}} \mathcal{L})_k, \tag{3.43a}$$

$$\mathbf{g}_k^\mu = (\nabla_{\boldsymbol{\mu}} \mathcal{L})_k, \tag{3.43b}$$

are the discrete reduced gradients[10] at $\boldsymbol{\lambda}_k$ and $\boldsymbol{\mu}_k$, respectively.

At each iteration step, we evaluate the discrete reduced gradients after solving sequentially the state and adjoint problems. Then, we compute the search directions, and determine reasonable step lengths (which we discuss in the next section in detail). Once we achieve adequate reductions in the objective functional (3.3), we update the material property vectors $\boldsymbol{\lambda}_k$ and $\boldsymbol{\mu}_k$, and progress to the next iteration.

3.5.3.2 Line search

In the following, we discuss the principles of line search by considering a generic function $f(\mathbf{x})$. Once a proper decent direction $\mathbf{d}_k$ is determined, the

---

[10] The discrete reduced gradients are computed at each node, and their values are stored as column vectors.

next step is to decide how far to move along that direction. One strategy is to seek an optimal step size α_k such that for a generic function $f(\mathbf{x})$

$$\min_{\alpha_k \in \mathbb{R}} f(\mathbf{x}_k + \alpha_k \mathbf{d}_k), \qquad \alpha_k > 0. \tag{3.44}$$

The *exact* line search optimizes the step length and, thus, guarantees sufficient descent. However, to find a local minimizer (let alone a global minimizer) requires multiple evaluations of the objective function and its gradient, which is computationally expensive. Even if α_k is a global minimizer of $f(\mathbf{x}_{k+1})$, it produces only an iterate $\mathbf{x}_{k+1}$ in the inversion process that may still be far from the target solution. A better practical strategy is to perform an *inexact* line search to compute a step length that achieves adequate reduction of the objective function f. A well-known inexact line search is the *Wolfe line search* [165, 166]. The *strong Wolfe conditions* are expressed as

$$f(\mathbf{x}_k + \alpha_k \mathbf{d}_k) - f(\mathbf{x}_k) \leq \delta \, \alpha_k \, \mathbf{g}_k^T \mathbf{d}_k, \tag{3.45a}$$

$$|\mathbf{g}\left(\mathbf{x}_k + \alpha_k \mathbf{d}_k\right)^T \mathbf{d}_k| \leq |\sigma \, \mathbf{g}_k^T \mathbf{d}_k|, \tag{3.45b}$$

with $0 < \delta < \sigma < 1$, and the *standard Wolfe conditions* are

$$f(\mathbf{x}_k + \alpha_k \mathbf{d}_k) - f(\mathbf{x}_k) \leq \delta \, \alpha_k \, \mathbf{g}_k^T \mathbf{d}_k, \tag{3.46a}$$

$$\mathbf{g}\left(\mathbf{x}_k + \alpha_k \mathbf{d}_k\right)^T \mathbf{d}_k \geq \sigma \, \mathbf{g}_k^T \mathbf{d}_k. \tag{3.46b}$$

The first inequality in both conditions ensures the sufficient decrease of f along $\mathbf{d}_k$ with a step size α_k. The second inequality, called the *curvature condition*, excludes unsuitably short steps by incorporating gradient information. Similarly to Wolfe conditions, there exists the *Goldstein conditions* [76], stated as

$$f(\mathbf{x}_k) + (1-\delta)\alpha_k \mathbf{g}_k^T \mathbf{d}_k \leq f(\mathbf{x}_k + \alpha_k \mathbf{d}_k) \leq f(\mathbf{x}_k) + \delta\, \alpha_k\, \mathbf{g}_k^T \mathbf{d}_k, \tag{3.47}$$

with $0 < \delta < 0.5$.

Another widely adopted and easy to implement inexact line search is the *Armijo line search* [3]

$$f(\mathbf{x}_k + \alpha_k \mathbf{d}_k) - f(\mathbf{x}_k) \leq \delta\, \alpha_k\, \mathbf{g}_k^T \mathbf{d}_k, \tag{3.48}$$

in which α_k is chosen to be the largest of $\{\alpha, \alpha\rho, \alpha\rho^2, \ldots\}$, where $\alpha > 0$ is an initial step length, $\rho \in (0, 1)$ is a contraction factor, and $\delta \in (0, 1)$ is a constant parameter (in practice, δ is chosen to be quite small). Notice that the Armijo line search is actually the first Wolfe condition. However, the second condition is rendered obsolete by creating a set of candidate step lengths, and choosing the largest one that satisfies the sufficient descent condition. The sequential contraction of the step size is referred to as the *backtracking* procedure. As depicted in Algorithm 3.1, the initial step length α is scaled down by ρ until the sufficient decrease condition is satisfied. After a finite number of trials the condition holds, and the line search is terminated by setting $\alpha_k = \alpha$.

Here, we too adopt an Armijo-like line search for both $\boldsymbol{\lambda}_k$ and $\boldsymbol{\mu}_k$. However, instead of enforcing sufficient decrease on the Lagrangian $\mathcal{L}$, we favor the use of the objective functional $\mathcal{F}$ instead, simply because the side-imposed PDEs vanish in a weak sense and minimizing $\mathcal{L}$ becomes nearly equivalent to minimizing $\mathcal{F}$ (we have found this to be a more robust choice than enforcing

Algorithm 3.1 Armijo line search with *backtracking* procedure

```
procedure ARMIJO-BACKTRACKING($\alpha$)                          ▷ $\alpha$: initial step length
    Choose $\rho, \delta \in (0,1)$                              ▷ e.g., $\rho = 0.5$, $\delta = 10^{-10}$
    while $\left\{ f(\mathbf{x}_k + \alpha \mathbf{d}_k) - f(\mathbf{x}_k) > \delta\, \alpha\, \mathbf{g}_k^T \mathbf{d}_k \right\}$ do   ▷ insufficient decrease
        $\alpha \leftarrow \rho\alpha$                           ▷ reduce step size
    end while
    $\alpha_k \leftarrow \alpha$
end procedure
```

the Armijo condition on the Lagrangian). Thus, we force sufficient decrease in the objective functional $\mathcal{F}$ by

$$\mathcal{F}\left(\boldsymbol{\lambda}_{k+1}, \boldsymbol{\mu}_{k+1}\right) - \mathcal{F}\left(\boldsymbol{\lambda}_k, \boldsymbol{\mu}_k\right) \leq \min\left\{\delta^\lambda \alpha_k^\lambda (\mathbf{g}_k^\lambda)^T \mathbf{d}_k^\lambda,\ \delta^\mu \alpha_k^\mu (\mathbf{g}_k^\mu)^T \mathbf{d}_k^\mu\right\}, \tag{3.49}$$

where $\delta^\lambda = \delta^\mu = 10^{-10}$. If the above inequality is not satisfied, a backtracking procedure (Algorithm 3.1) is followed by contracting the associated step size (α_k^λ and/or α_k^μ). Specifically, the step sizes for $\boldsymbol{\lambda}_k$ and $\boldsymbol{\mu}_k$ are determined independently since each has its own search direction. We summarize the entire inversion process (Fig. 3.2) discussed thus far in Algorithm 3.2. Though not included in Algorithm 3.2, we also use continuation schemes to further alleviate the solution multiplicity. The implementation details of these continuation schemes are discussed next.

3.5.4 Continuation schemes

Inverse problems suffer from solution multiplicity. Imposing regularization over the control parameters helps to alleviate the ill-posedness and associated solution multiplicity. However, one needs to bring in additional remedies to improve the solution quality. We discuss next two such remedies

Algorithm 3.2 Inversion process for material profile reconstruction

```
procedure MPR($\boldsymbol{\lambda}_o$, $\boldsymbol{\mu}_o$)    ▷ initial guesses
    Choose $\rho, \delta^\lambda, \delta^\mu$    ▷ e.g., $\rho = 0.5$, $\delta^\lambda = \delta^\mu = 10^{-10}$
    Set convergence tolerance $tol$    ▷ e.g., $tol = 10^{-12}$
    $k \leftarrow 0$    ▷ $k$: iteration counter
    Set $\mathcal{F}_k \leftarrow tol + 1$    ▷ $\mathcal{F}_k$ denotes $\mathcal{F}(\boldsymbol{\lambda}_k, \boldsymbol{\mu}_k)$
    while $\{\mathcal{F}_k > tol\}$ do
        Solve the state problem for $(\mathbf{u}, \mathbf{S})$    ▷ eq. (3.1-3.2)
        Solve the adjoint problem for $(\boldsymbol{\theta_u}, \boldsymbol{\theta_s})$    ▷ eq. (3.13-3.14)
        Evaluate the discrete reduced gradients
            $\mathbf{g}_k^\lambda \leftarrow (\nabla_\lambda \mathcal{L})_k$    ▷ eq. (3.30) for TN, eq. (3.32) for TV
            $\mathbf{g}_k^\mu \leftarrow (\nabla_\mu \mathcal{L})_k$    ▷ eq. (3.31) for TN, eq. (3.33) for TV
        Compute the search directions $\mathbf{d}_k^\lambda$ and $\mathbf{d}_k^\mu$    ▷ eq. (3.31)
        $\alpha^\lambda \leftarrow s^\lambda \, \text{mean}[\mathbf{d}_k^\lambda]^{-1}$    ▷ initial step size for $\lambda$
        $\alpha^\mu \leftarrow s^\mu \, \text{mean}[\mathbf{d}_k^\mu]^{-1}$    ▷ initial step size for $\mu$
        while $\left\{\mathcal{F}_{k+1} - \mathcal{F}_k > \min\left[\delta^\lambda \alpha^\lambda (\mathbf{g}_k^\lambda)^T \mathbf{d}_k^\lambda,\ \delta^\mu \alpha^\mu (\mathbf{g}_k^\mu)^T \mathbf{d}_k^\mu\right]\right\}$ do
            $\alpha^\lambda \leftarrow \rho \alpha^\lambda$ if $\left[\mathcal{F}_{k+1} - \mathcal{F}_k > \delta^\lambda \alpha^\lambda (\mathbf{g}_k^\lambda)^T \mathbf{d}_k^\lambda\right]$
            $\alpha^\mu \leftarrow \rho \alpha^\mu$ if $\left[\mathcal{F}_{k+1} - \mathcal{F}_k > \delta^\mu \alpha^\mu (\mathbf{g}_k^\mu)^T \mathbf{d}_k^\mu\right]$
        end while
        $\alpha_k^\lambda \leftarrow \alpha^\lambda$
        $\alpha_k^\mu \leftarrow \alpha^\mu$
        Update the material property vectors $\boldsymbol{\lambda}_k$ and $\boldsymbol{\mu}_k$    ▷ eq. (3.41)
        $k \leftarrow k + 1$
    end while
end procedure
```

that aid the inversion process in reconstructing high-quality material profiles.

3.5.4.1 Regularization factor continuation

The amount of penalty placed on the gradients via the regularization factors R_λ and R_μ is critical, since the inversion process depends on the reduced gradients. Though there are various developments for choosing the regularization factor intelligently (e.g., L-curve [79, 119]), a fixed value for R_λ and R_μ can also be used. Here, we favor adjusting the regularization factor dynamically so that it penalizes high-frequency material oscillations initially, but as iterates evolve, relaxes the imposed penalty in order to be able to refine target profiles. To address the manner by which the regularization factors are continuously updated, we first recast the continuous form of the reduced gradients (3.30 - 3.33) as

$$\nabla_i \mathcal{L} = -\, R_i \, \mathbb{K} \, - \, \mathbb{F}, \tag{3.50}$$

where the subscript i refers to either of the two control/material parameters λ or μ, $\mathbb{K}$ corresponds to the part of the reduced gradient stemming from the regularization, and $\mathbb{F}$ corresponds to the part that originates in the side-imposed PDEs. Once discretized, $\mathbb{K}$ and $\mathbb{F}$ denote n-dimensional vectors with n being the number of nodal unknowns in Ω^{RD}. Representing each vector as a product of its magnitude and associated unit vector yields[11]

$$(\nabla_i \mathcal{L})_k = -\|\mathbb{F}\| \left[\, R_i \, \frac{\|\mathbb{K}\|}{\|\mathbb{F}\|} \mathbf{n}_{\mathbb{K}} \, + \, \mathbf{n}_{\mathbb{F}} \right], \tag{3.51}$$

---

[11] We employ the definition of a unit vector: $\mathbf{n} = \frac{\mathbf{v}}{\|\mathbf{v}\|}$, $\forall \mathbf{v} \in \mathbb{R}^n$.

where $\|\cdot\|$ denotes the Euclidean norm, and $\mathbf{n}_j$ is the unit vector along j. Equation (3.51) shows explicitly that the discrete reduced gradient, which drives the conjugate gradient method, is the weighted average of the gradient information coming from the regularization term ($\mathbb{K}$), and the side-imposed PDEs ($\mathbb{F}$). Depending on the weight, i.e., the factor in front of $\mathbf{n}_{\mathbb{K}}$, we decide on what controls the search direction of the conjugate gradient method. Having a weight that is too small produces high-frequency fluctuations, and the inversion process suffers from solution multiplicity. By contrast, placing too much weight on the regularization smoothens the reconstructed material profile by over-penalizing the gradients. Therefore, $\mathbf{n}_{\mathbb{K}}$ needs to be scaled continuously so that it regularizes $\mathbf{n}_{\mathbb{F}}$ without hindering the overall search direction. This can be achieved by forcing $\mathbf{n}_{\mathbb{K}}$ to compete with $\mathbf{n}_{\mathbb{F}}$ throughout the entire inversion process, that is,

$$R_i \, \frac{\|\mathbb{K}\|}{\|\mathbb{F}\|} = \wp, \tag{3.52}$$

where $\wp$ ($0 \leq \wp \leq 1$) is a tuning parameter. The above can be recast to choose R_i as

$$R_i = \wp \, \frac{\|\mathbb{F}\|}{\|\mathbb{K}\|}, \qquad 0 \leq \wp \leq 1, \tag{3.53}$$

at each iteration. By this continuation scheme, the regularization factor can take a large value at the beginning of the inversion process (to narrow down the initial feasibility space of the solution), and it is continuously reduced as iterations progress so as to enable refinement of the target profiles.

3.5.4.2 Source-frequency continuation

In the source-frequency continuation scheme, we start the probing with a signal having a low-frequency content, and increase the content frequency in subsequent iterations, until convergence. The key idea is that a low-frequency excitation typically allows for a rough resolution of the material profile, whereas an excitation with higher-frequency components fine-tunes the profile. In practice, we need only a few probing signals to arrive at a converged profile. Starting with the lowest source frequency, the inversion process is let to converge to a profile that captures the overall spatial variability of the material parameters in a rather crude way. Next, we feed this coarse profile as an initial guess to the inversion process driven by the next higher frequency in the sequence, and let again the optimizer to arrive at a converged profile. The process is repeated for all the probing signals.

In practice, source-frequency and grid continuation schemes are jointly implemented since one complements the other. Typically, one starts the inversion process with a coarse grid probed by a low-frequency excitation. The converged profile is, then, projected onto a finer grid, and used as an initial guess in the inversion for the next higher source frequency in the sequence. In general, five distinct frequencies, each resolved by a different resolution mesh, are enough to reconstruct high quality material profiles. Consequently, the amount of computational time spent in early iterations is reduced dramatically, thereby resulting in substantial speed-ups of the entire inversion process.

3.6 Numerical experiments

To test the proposed inversion scheme, we discuss next numerical experiments, involving arbitrarily heterogeneous hosts and synthetic data. The first example is a fictitious medium that has material properties varying smoothly with depth. We use the first example to discuss various aspects of the inversion process. Example 2 involves a horizontally-layered medium, and we use it to discuss the effect of the regularization schemes in the presence of sharp layer interfaces. The last example focuses on a layered medium with an embedded inclusion in an effort to implicate arbitrary heterogeneity.

3.6.1 Example 1 - smoothly-varying heterogeneous medium

We consider first a heterogeneous half-plane with constant density $\rho = 2000$ kg/m^3 and constant Poisson's ratio $\nu = 0.25$ (both assumptions are physically consistent for near-surface deposits). We reduce the half-plane, through truncation, to a 45m × 45m computational domain, surrounded on its sides and bottom by a 5m-thick PML, as shown in Fig. 3.3(a). The soil profile varies smoothly with depth; specifically, we define the spatial variation of the Lamé parameters as

$$\lambda = 80 + 0.45|y| + 35 \exp\left[-\frac{(|y| - 22.5)^2}{150}\right] \text{ (MPa)}, \tag{3.54a}$$

$$\mu = 80 + 0.45|y| + 35 \exp\left[-\frac{(|y| - 22.5)^2}{150}\right] \text{ (MPa)}. \tag{3.54b}$$

The material interfaces were extended horizontally into the PML, thereby, avoiding sudden material changes at the interface between the PML and the regular domain. The PML and regular domains were discretized[12] by square elements with an element size of 0.5m. We used a quadratic-quadratic pair for the displacements and stresses, whereas the material properties λ and μ were approximated linearly. The discretization resulted in a 10-cell-thick PML with a quadratic attenuation profile ($m = 2$). The parameters β_o and α_o of the attenuation and scaling functions were set to 500 m/s and 0.75, respectively.

To recover the target material profiles depicted in Figs. 3.3(c) and 3.3(d), we apply a Gaussian pulse[13] point loads at every grid point (uniformly distributed with 0.25m spacing) on the surface of the regular domain, with a maximum frequency of $f_r = 40$ Hz and amplitude of 50 kPa (Fig. 3.4). The receivers that measure the displacement response $\mathbf{u}(\mathbf{x}, t)$ were also located at every grid point on the surface resulting in 179 receiver locations (excluding the PML-regular domain interface). Using a time step of 0.001 seconds, we let the forward problem run for 1.0 seconds under the target material profile, but using a different (refined) mesh, in order to obtain the synthetic data at the sensor locations.

Before attempting simultaneous inversion for both λ and μ, we start with two separate experiments of *single-parameter* inversion: the first is to invert for μ assuming λ is *a priori* known, and vice versa. To this end, the inversion procedure outlined in Algorithm 3.2 has been used by shutting down

---

[12] We used 0.5m × 0.5m 8-noded serendipity elements.

[13] $\mathrm{T_p}(t) = -50 \exp -\frac{(t-\bar{\mu})^2}{\bar{\sigma}^2}$, where $\bar{\mu}$ and $\bar{\sigma}$ denote the mean and deviation of the Gaussian pulse.

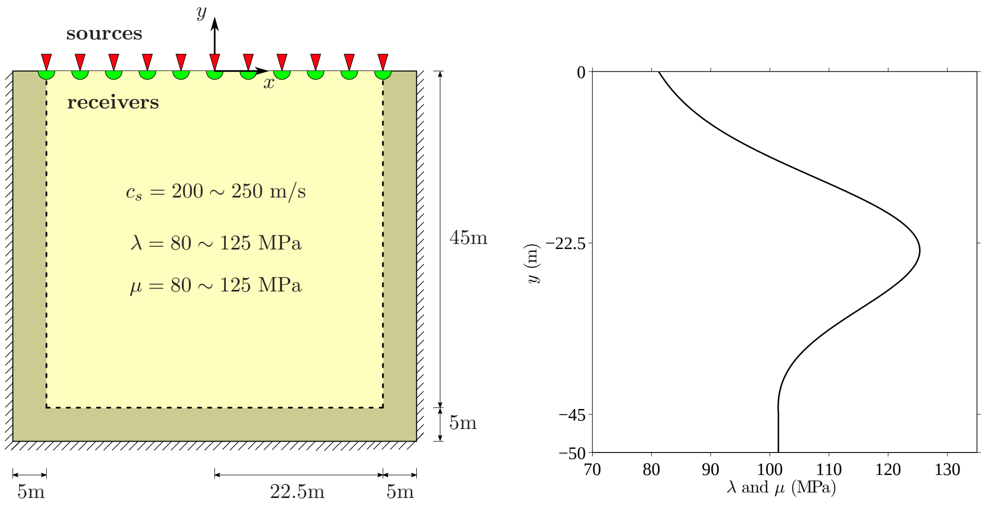

(a) Geometry (b) Cross-section profile at $x = 0$m

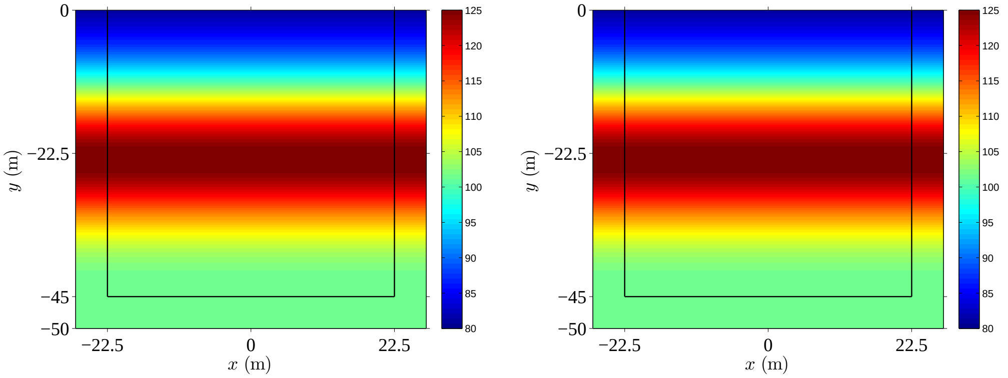

(c) Target λ (d) Target μ

Figure 3.3: A PML-truncated semi-infinite domain in two dimensions

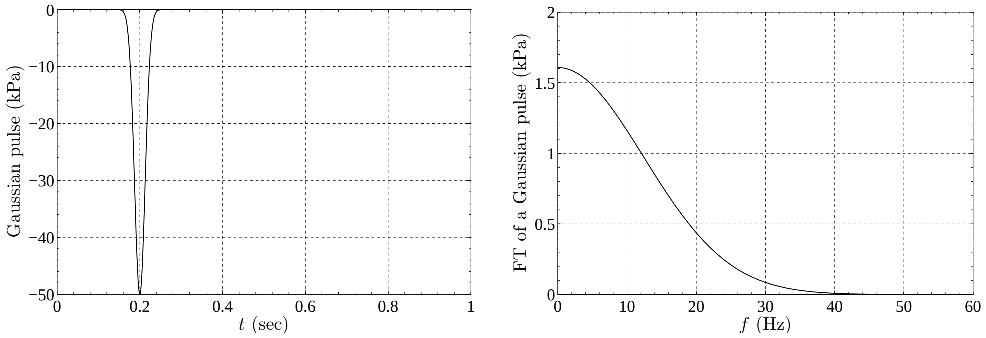

Figure 3.4: Excitation time signal and its Fourier spectrum

the evolution of either λ or μ, respectively. We favor TN regularization, and implemented the regularization factor continuation scheme described in section 3.5.4.1. For both experiments, we provide the variation of the response misfit with respect to the number of inversion iterations, however we remark that the total number of iterations cannot be a measure of convergence since the decay rate of the response misfit (i.e. convergence) depends highly on the step lengths (α_k^λ and α_k^μ) used in the conjugate gradient method.

In the first experiment, we assume λ to be *a priori* known and we fix it to the target profile; we start the inversion process for μ with a homogeneous initial guess of 80 MPa. The reconstructed μ is shown in Fig. 3.5(b) and is almost identical to the target μ. Figures 3.5(c), 3.5(d), and 3.5(e) compare target cross-sectional profiles of μ with the reconstructed ones at $x = 0$m, 7m, and 14m, respectively. The agreement is excellent. As shown in Fig. 3.5(f), the response misfit (i.e., difference between measured and computed responses at receiver locations) was reduced from its initial value of 0.398×10^{-4} down to 0.714×10^{-9}, that is, less than 0.0018% of the initial misfit. The inversion process achieved almost 5 orders of magnitude reduction in the response misfit.

In the second experiment, we fix μ to the target profile, and start the inversion process for λ only with, again, a homogeneous initial guess of 80 MPa. Figure 3.6 depicts the accurately reconstructed λ, which is practically indistinguishable from the target λ. Figures 3.6(c), 3.6(d), and 3.6(e) compare target cross-sectional profiles of λ with the reconstructed ones at $x = 0$m, 7m, and 14m, respectively; the agreement is again excellent. In Fig. 3.6(f), the response misfit is shown to have been reduced from its initial value of 0.136×10^{-5} to 0.428×10^{-10}, that is, less than 0.0032% of the initial misfit. As in the previous experiment, the inversion process achieved almost 5 orders of magnitude reduction in the response misfit. However, we remark that the initial value of the response misfit in the first experiment (inversion for μ) is, at least, one order of magnitude larger than the misfit's initial value in the second experiment (inversion for λ). The disparity clearly demonstrates that the objective functional is unequally sensitive to the material properties λ and μ, and accordingly, one should expect difficulties while inverting simultaneously for both λ and μ.

Encouraged by the single-parameter inversion results, we turn next to the simultaneous inversion for both Lamé parameters. We start the inversion process with a homogeneous profile that has both λ and μ set to 80 MPa. We use the regularization factor continuation scheme described earlier, and following the procedure described in Algorithm 3.2, we reconstruct the material profiles shown in Fig. 3.7. The top row in Fig. 3.7 depicts the target

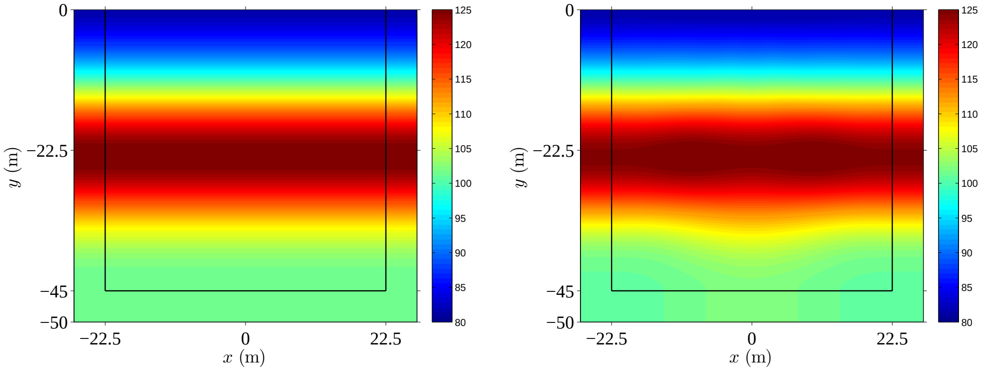

(a) λ (*a priori* known) (b) μ (TN)

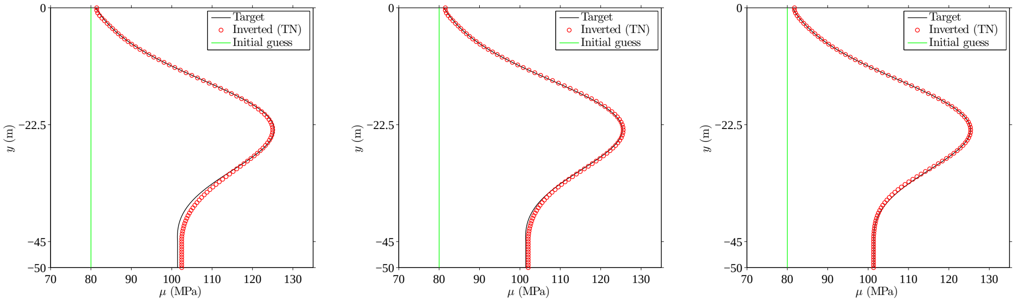

(c) μ profile at $x = 0$m (d) μ profile at $x = 7$m (e) μ profile at $x = 14$m

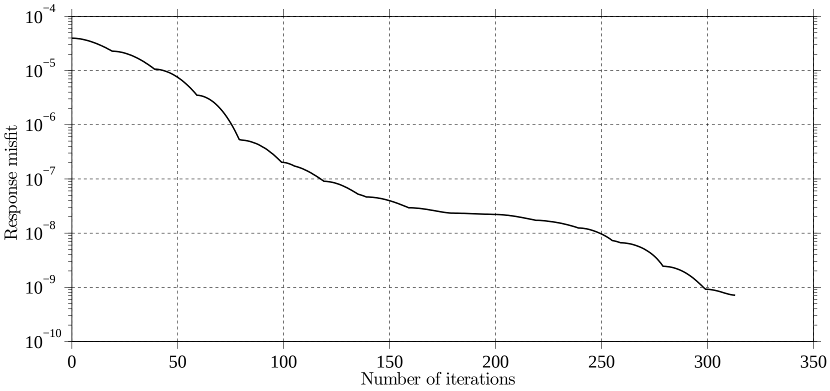

(f) Variation of response misfit during the inversion process

Figure 3.5: Single-parameter inversion for μ only, when λ is held to the target; inversion terminated after 313 iterations

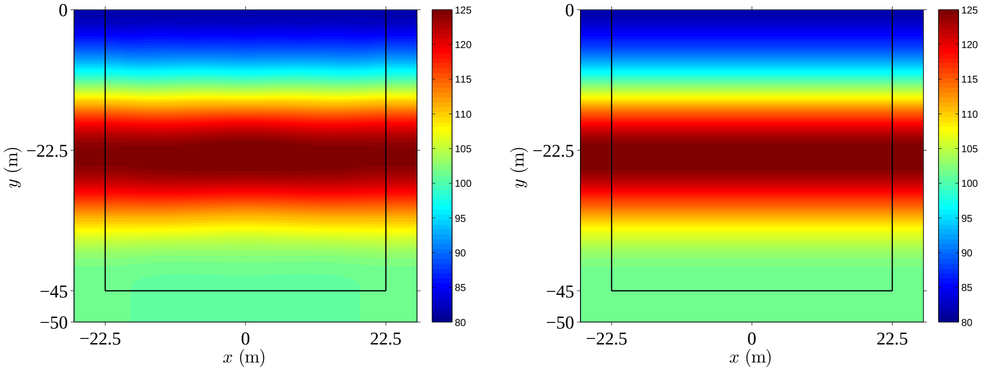

(a) λ (TN) (b) μ (*a priori* known)

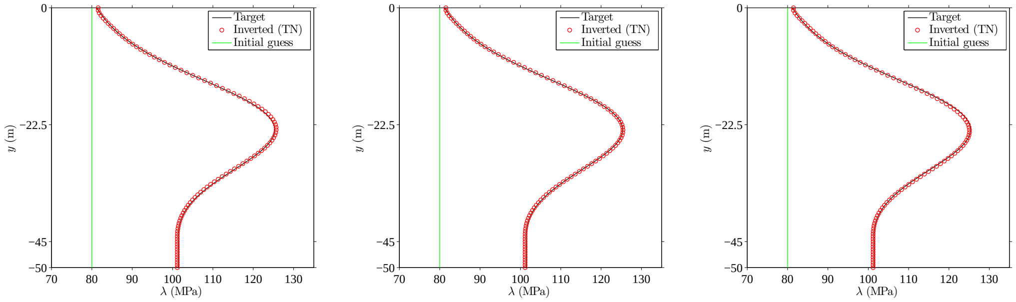

(c) λ profile at $x = 0$m (d) λ profile at $x = 7$m (e) λ profile at $x = 14$m

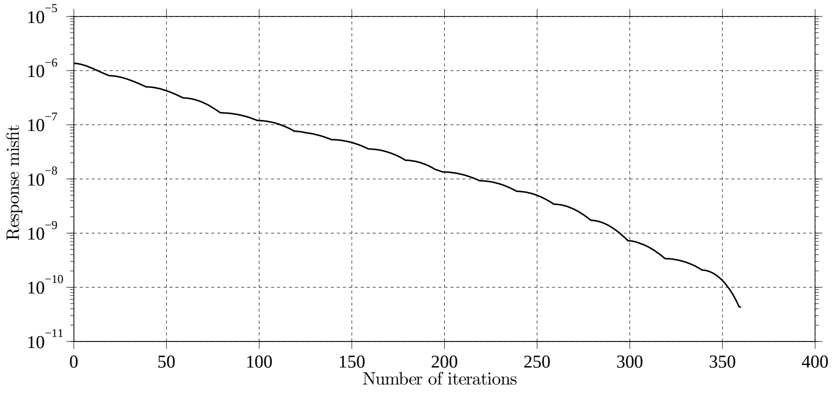

(f) Variation of response misfit during inversion process

Figure 3.6: Single-parameter inversion for λ only, when μ is held to the target; inversion terminated after 360 iterations

profiles, whereas the center and bottom rows correspond to *simultaneous* two-parameter inversion results obtained by using the TN and TV regularization schemes, respectively. As previously stated, both regularization schemes are expected to be successful in recovering the *smooth* target profiles, and indeed, this is the case for μ. However, we remark that the spatial variability of μ is captured much more accurately than the spatial variability of λ. This peculiarity has also been reported in [61]. One possible explanation is the sensitivity of the objective functional to the elastic parameters λ and μ: by construction, the updates for μ are driven by gradient operators in the μ-control problem (see time integral in either (3.31) or (3.33)), whereas, by contrast, the updates on λ are based on divergence operators in the λ-control problem ((3.30) or (3.32)). The gradient operator incorporates richer information on the spatial variability of $\mathbf{u}(\mathbf{x}, t)$ than the uncoupled smoothing divergence operator. As a result, μ evolves towards the target profile faster than λ: in all of the numerical experiments we conducted, it appears that the convergence of λ is always lagging behind μ.

Figure 3.8 compares the inverted profiles against the target profile at the $x = 0$m, 7m, and 14m cross-sections of the domain. In solutions of full waveform inversion problems in finite domains, it is common that the central part ($x = 0$m) of the domain is better illuminated by surface loads, as evident from Fig. 3.8(d). Since the reconstructed λ moves towards the target slowly, the quality reduces in the proximity of the truncation interfaces on both sides. To compensate, μ slightly increases on regions closer to the sides resulting in

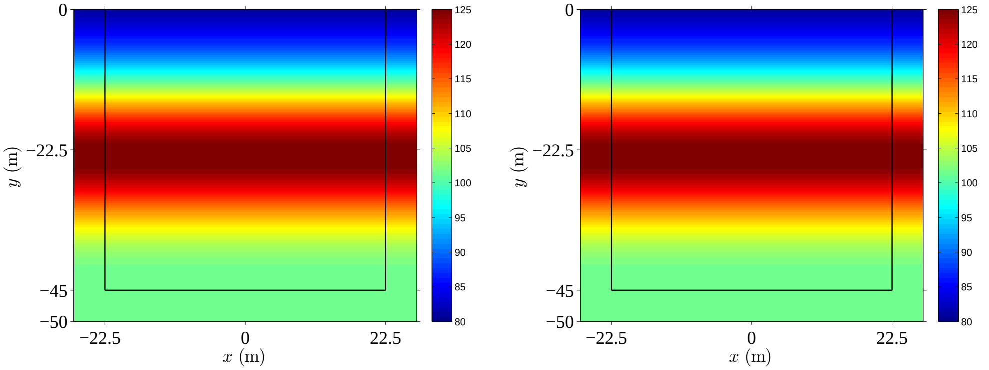

(a) Target λ (b) Target μ

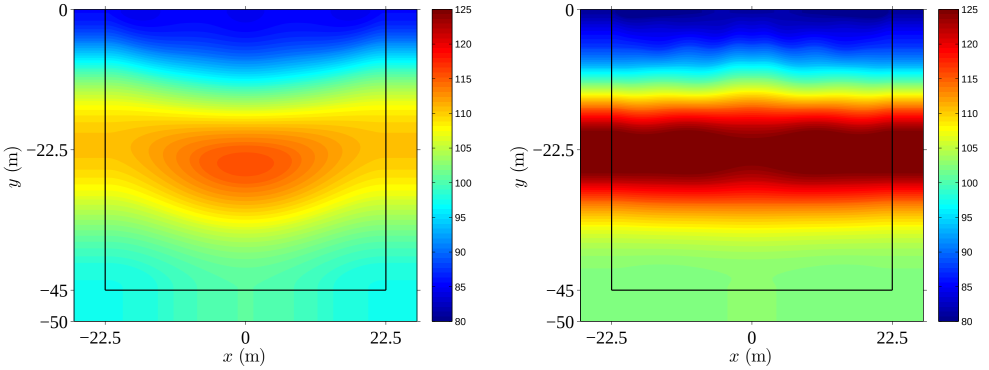

(c) λ (TN) (d) μ (TN)

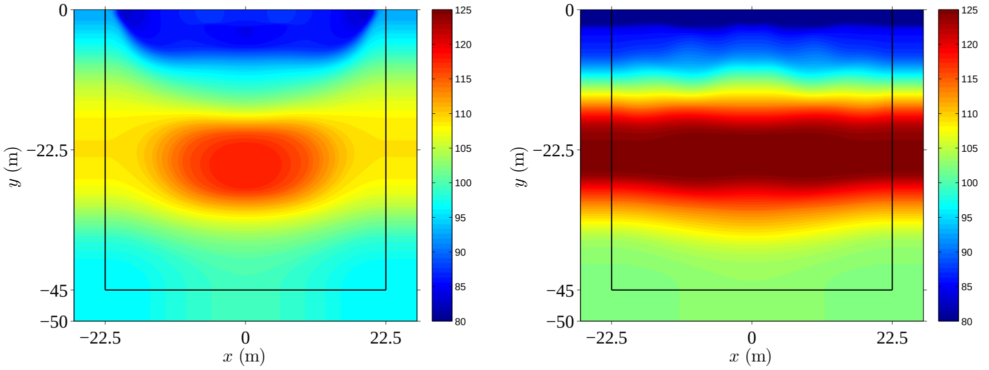

(e) λ (TV) (f) μ (TV)

Figure 3.7: Simultaneous inversion for the Lamé parameters using Algorithm 3.2; convergence after 278 iterations (TN), and 280 iterations (TV)

larger deviations from the target, as can be seen in Figs. 3.8(e) and 3.8(f). Lastly, Fig. 3.9 depicts the variation of the response misfit with number of iterations. Using the TN and TV regularization schemes, the response misfit is reduced from its initial value of 0.576×10^{-4} down to 0.121×10^{-7} and 0.129×10^{-7} respectively, that is, less than approximately 0.022% of the initial misfit. Despite the unequal sensitivity to Lamé parameters, the inversion process could still achieve 3 orders of magnitude reduction in the response misfit.

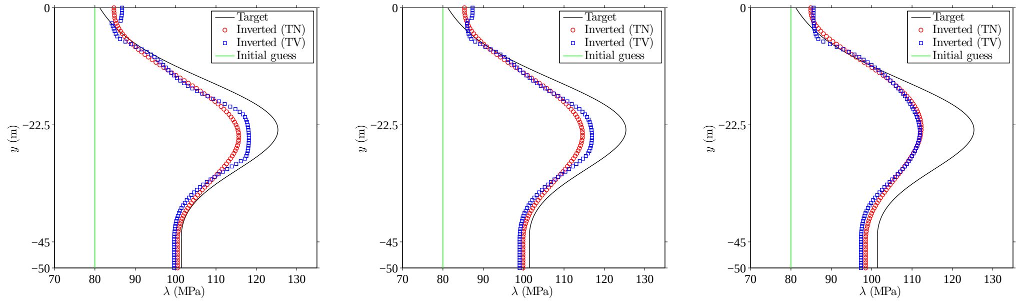

(a) λ profile at $x = 0$m (b) λ profile at $x = 7$m (c) λ profile at $x = 14$m

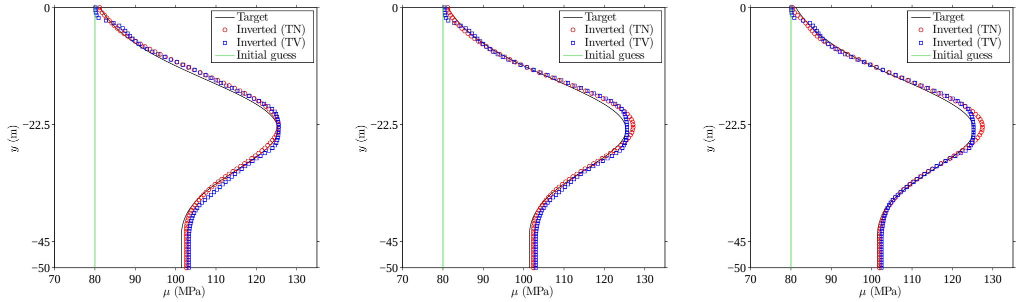

(d) μ profile at $x = 0$m (e) μ profile at $x = 7$m (f) μ profile at $x = 14$m

Figure 3.8: Cross-sectional profiles for simultaneously inverted Lamé parameters using Algorithm 3.2; convergence after 278 iterations (TN), and 280 iterations (TV)

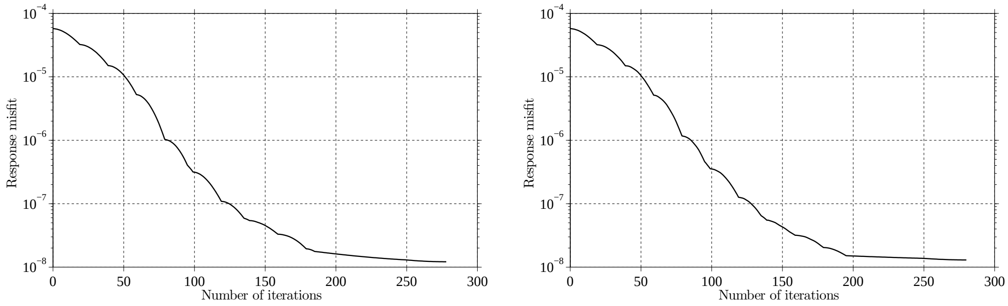

(a) TN regularization (b) TV regularization

Figure 3.9: Variation of response misfit during simultaneous inversion process

To better observe how λ lags behind μ during the inversion process, we present in Fig. 3.10 the snapshots of λ and μ at five different iterations (i.e., 30, 60, 90, 120, and 278 (the converged profile)) when TN regularization is used. There are two key observations that emerge from this figure: first, the convergence pattern of λ is strikingly different than that of μ. At the beginning of the inversion process, λ fails to detect a proper velocity-gradient, whereas μ almost instantly discloses the property-gradient of the target profile. As a result, λ converges very slowly and falls behind μ. Secondly, μ seems to converge towards the target profile without being hindered by a low quality λ, which implies that the objective functional is less sensitive to variations of λ. However, we note that when μ gets very close to the target, its profile may gradually deviate in an attempt to compensate for λ, while still reducing the misfit.

To tackle the apparent difficulty, we propose a scheme where the search directions of λ are biased by the search directions of μ during the early stages

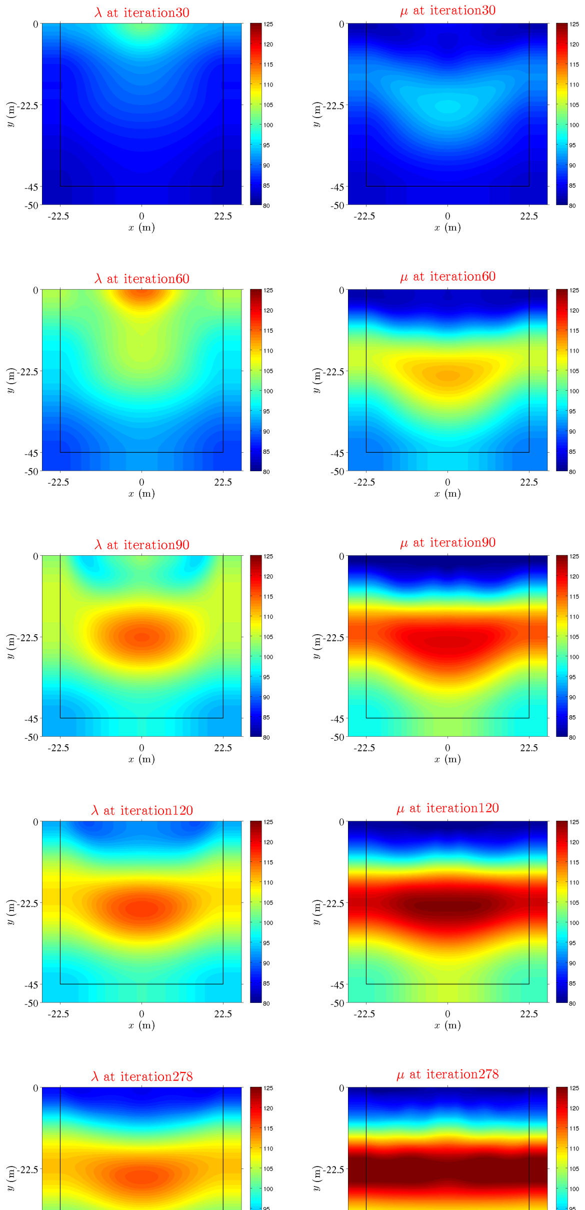

Figure 3.10: Evolution snapshots of λ (left column), and μ (right column) during simultaneous inversion using the TN regularization

of the inversion process. The key idea behind this is to let λ know about the spatial structure (contours) of μ and update itself with a similar pattern; after all, the physics dictate that both λ and μ profiles should look similar. Since the spatial update pattern of μ is embedded in the n-dimensional unit search direction vector, we use a weighted average of *unit* λ- and μ-search directions for the evolution of λ. To implement, Algorithm 3.2 needs an extra step after line 12. As depicted in Algorithm 3.3, the new biased search direction of λ is still scaled by the L^2-norm of the original λ-search direction. Initially, we assign full weight ($W = 1$) on μ, but as iterates evolve the weight is reduced down to zero ($W = 0$), thereby letting λ evolve on its own. Once the updates on μ numerically vanish (μ has converged), we stop the evolution of μ, and continue the inversion process with λ only.

Algorithm 3.3 A patch to bias the λ-search directions

```
    procedure MPR($\boldsymbol{\lambda}_o$, $\boldsymbol{\mu}_o$)                              ▷ initial guesses
        ...
        while {$\mathcal{F}_k > tol$} do
            ...
12:         Compute the search directions $\mathbf{d}_k^\lambda$ and $\mathbf{d}_k^\mu$                ▷ eq. (3.31)
13:         $\mathbf{d}_k^\lambda \leftarrow \|\mathbf{d}_k^\lambda\| \left[ W \frac{\mathbf{d}_k^\mu}{\|\mathbf{d}_k^\mu\|} + (1 - W) \frac{\mathbf{d}_k^\lambda}{\|\mathbf{d}_k^\lambda\|} \right]$    ▷ new biased $\mathbf{d}_k^\lambda$
14:         $\alpha^\lambda \leftarrow s^\lambda \text{ mean}[\mathbf{d}_k^\lambda]^{-1}$                       ▷ initial step size for $\lambda$
15:         $\alpha^\mu \leftarrow s^\mu \text{ mean}[\mathbf{d}_k^\mu]^{-1}$                       ▷ initial step size for $\mu$
            ...
        end while
    end procedure
```

The advantages of the proposed approach are multi-fold: first, we prevent λ from lagging behind μ at the early stages of inversion by biasing its search direction. Secondly, when the weight W goes to zero, λ starts its evolution from an inversion step that structurally matches μ. Therefore, the simultaneous inversion of λ and μ has now better chances of converging to the target. Thirdly, an up-to-date (i.e., not lagging behind) λ profile allows the reconstructed μ to further improve its quality. Once the updates on μ numerically vanish, we stop the evolution of μ and continue the inversion process with λ only. Hence, in this manner, we also provide a second chance for λ to keep up with μ and improve further on its profile.

Figure 3.11 shows the recovered Lamé parameters using the biased simultaneous inversion approach described in Algorithm 3.2 enhanced with the patch 3.3. By contrast to the results shown in Fig. 3.7, now both Lamé parameters are satisfactorily inverted. The proposed modification improved the quality of λ under both regularization schemes. As evident also from the cross-sectional profiles depicted in Figs. 3.12 and 3.13, the enhanced inversion scheme did an excellent job in capturing the smoothly-varying target μ profile and dramatically improved the reconstructed λ profile. In addition, the number of iterations was reduced, especially during the early stages of the inversion process.

3.6.2 Example 2 - layered medium

As shown in Fig. 3.14(a), we consider next a 45m × 45m layered medium surrounded by 5m-thick PML on its sides and bottom with constant density $\rho = 2000$ kg/m^3 and constant Poisson's ratio $\nu = 0.25$. We define the

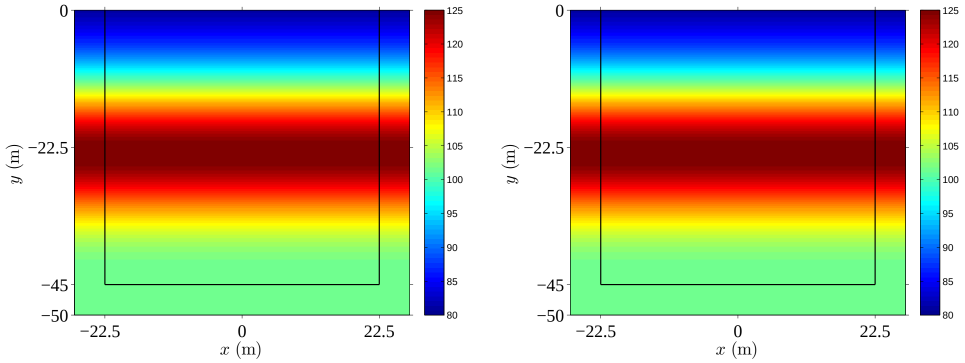

(a) Target λ (b) Target μ

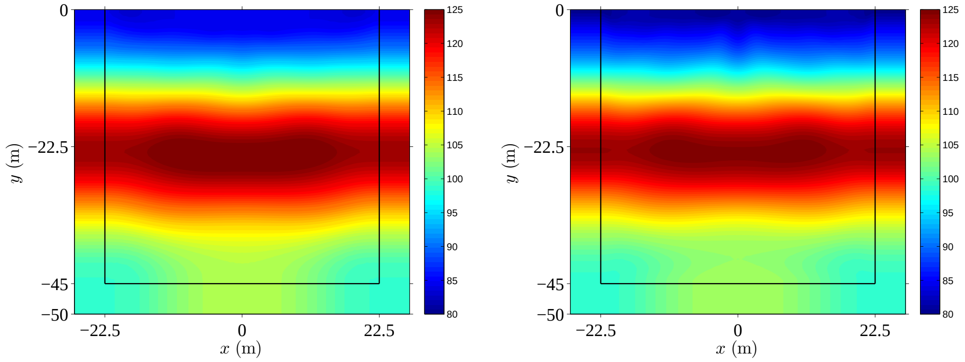

(c) λ (TN) (d) μ (TN)

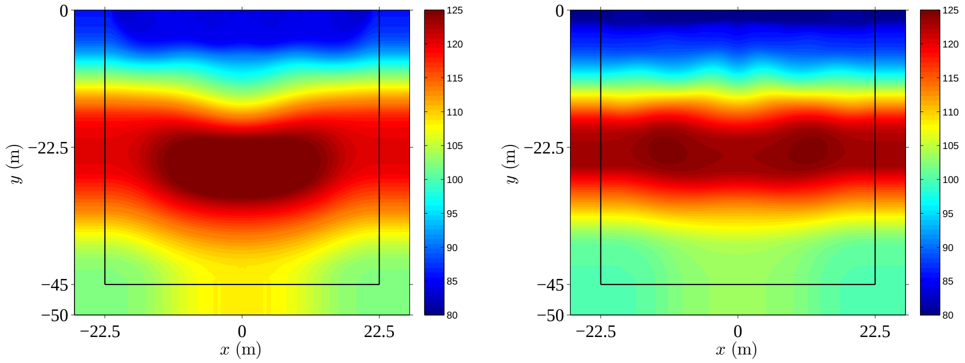

(e) λ (TV) (f) μ (TV)

Figure 3.11: Simultaneous inversion for the Lamé parameters using the *biased*-directions Algorithm 3.3; convergence after 70 iterations (TN), and 180 iterations (TV)

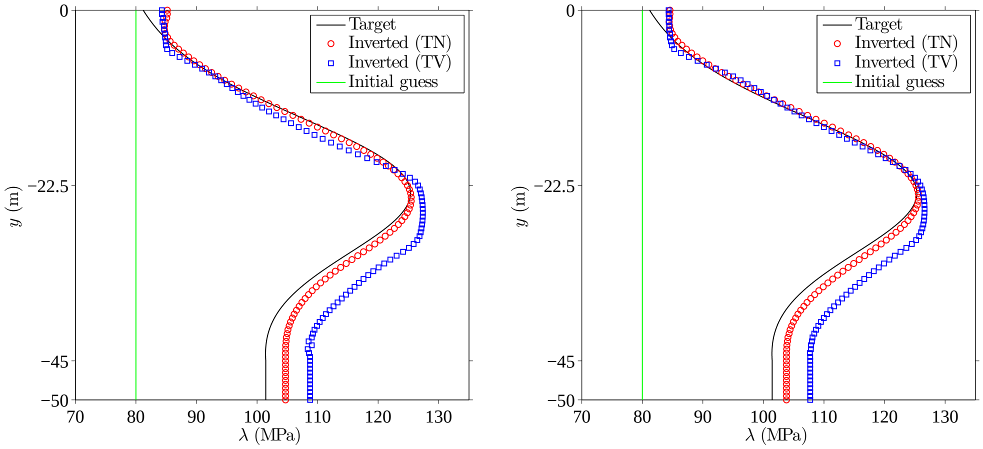

(a) λ profile at $x = 0$m (b) λ profile at $x = 7$m

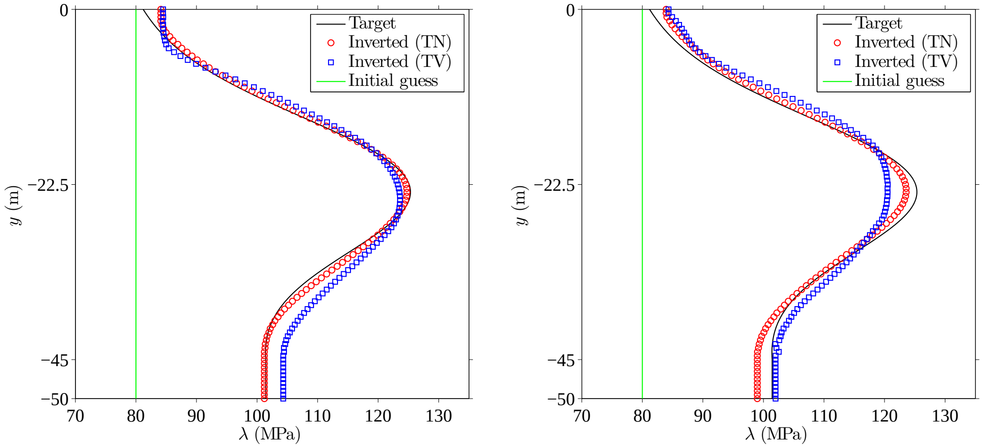

(c) λ profile at $x = 14$m (d) λ profile at $x = 21$m

Figure 3.12: λ cross-sectional profiles obtained with the *biased*-directions inversion Algorithm 3.3

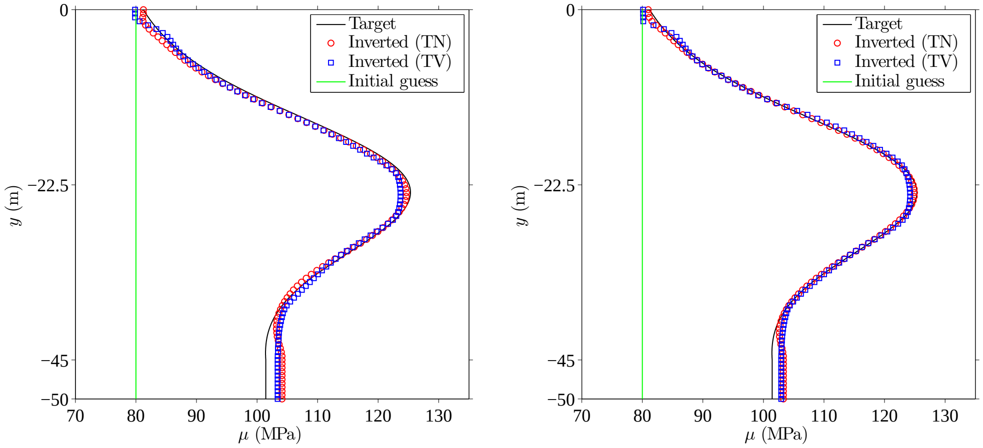

(a) μ profile at $x = 0$m (b) μ profile at $x = 7$m

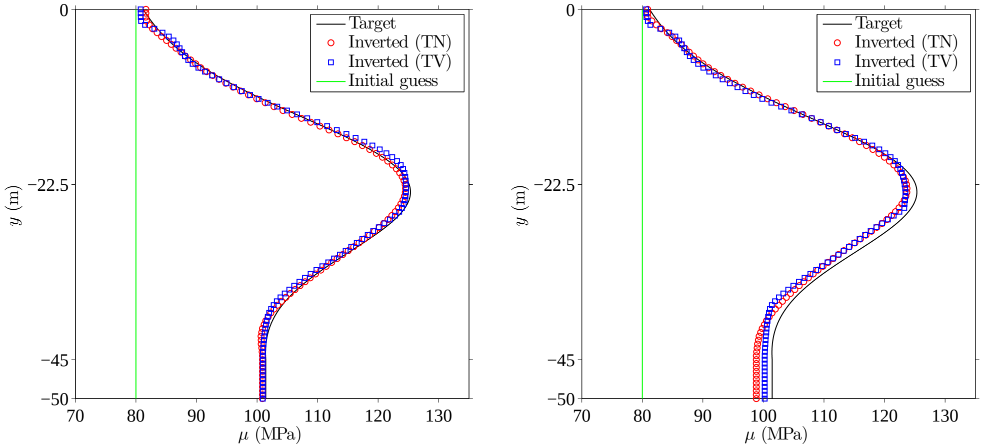

(c) μ profile at $x = 14$m (d) μ profile at $x = 21$m

Figure 3.13: μ cross-sectional profiles obtained with the *biased*-directions inversion Algorithm 3.3

spatial variation of the Lamé parameters as

$$\lambda(y) = \mu(y) = \begin{cases} 80 \text{ MPa}, & \text{for } -12\text{m} \leq y \leq 0\text{m}, \\ 101.25 \text{ MPa}, & \text{for } -27\text{m} \leq y < -12\text{m}, \\ 125 \text{ MPa}, & \text{for } -50\text{m} \leq y < -27\text{m}. \end{cases} \tag{3.55}$$

As in Example 1, the material interfaces were extended horizontally into the PML. The PML and regular domains were discretized by quadratic quadrilateral elements with an element size of 0.5m. We used a quadratic-quadratic pair for the displacements and stresses, whereas the material properties λ and μ were approximated linearly. The discretization resulted in a 10-cell-thick PML (as in Example 1, we set $m = 2$, $\beta_o = 500$ m/s, and $\alpha_o = 0.75$).

To illuminate the domain, we apply a Gaussian pulse point load at every grid point (uniformly distributed with 0.25m spacing) on the surface of the regular domain. The receivers that measure the displacement response $\mathbf{u}(\mathbf{x}, t)$ were also located at every grid point on the surface resulting in 179 receiver locations. Using a time step of 0.001 seconds, we let the forward problem run for 1.0 seconds under the target material profile, but using a different (refined) mesh to create the synthetic data that will drive the inversion. In this example, we use a source-frequency continuation scheme according to which a few time signals with different frequency content are used to probe the domain, thereby creating a set of, seemingly, uncoupled inversion problems. We start the inversion process with a low-frequency source and feed the converged reconstructed λ and μ profiles as initial guesses to the problem excited with a higher-frequency source. This procedure was repeated as many times as the number of independent sources probing the domain: here, we considered four

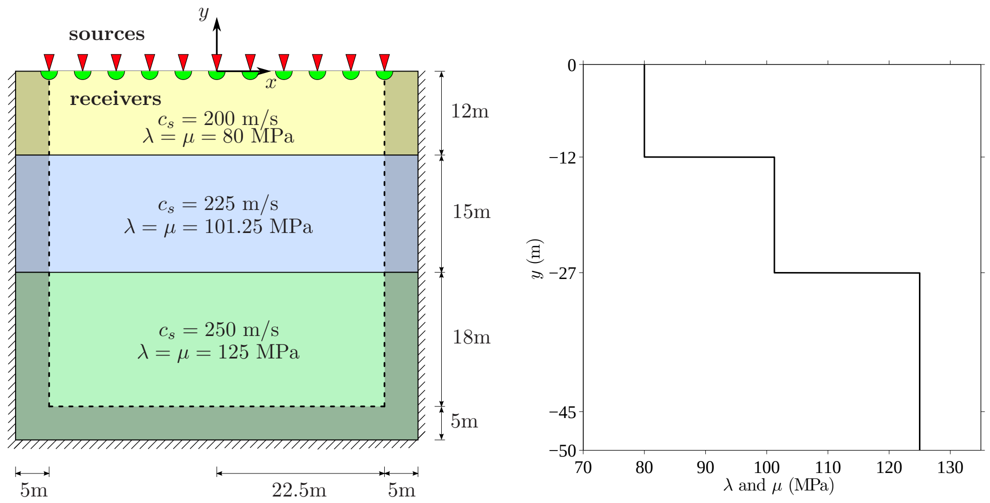

(a) Geometry (b) Cross-section profile at $x = 0$m

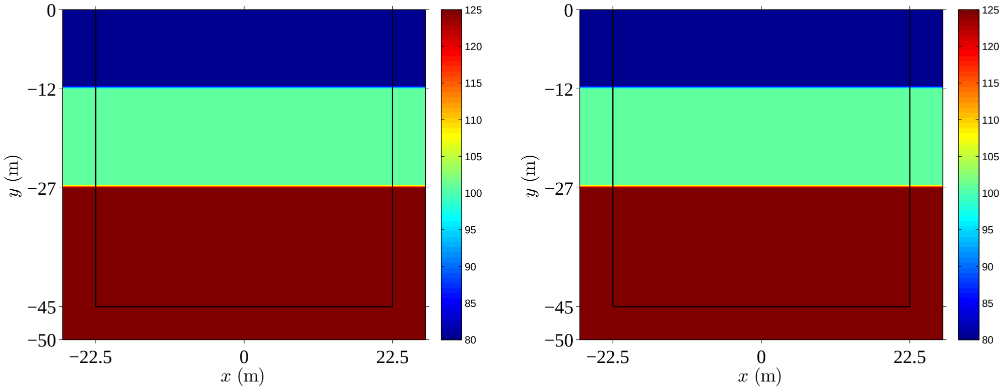

(c) Target λ (d) Target μ

Figure 3.14: A PML-truncated horizontally-layered semi-infinite domain in two dimensions

different Gaussian pulses with maximum frequencies ranging from 10 Hz to 40 Hz, as shown in Fig. 3.15.

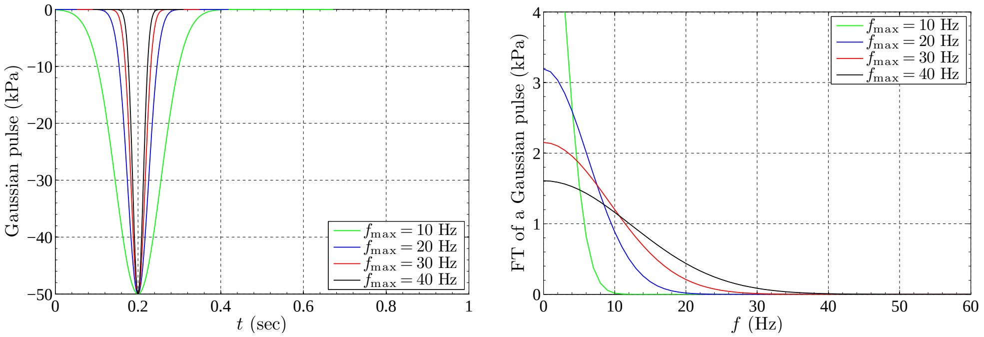

Figure 3.15: Gaussian pulses and their Fourier spectrum

Following the inversion procedure outlined in Algorithm 3.3 endowed with the regularization factor continuation, we reconstruct the material profiles shown in Figs. 3.16 and 3.17 using the TN and TV regularization schemes, respectively. In each figure, the first row displays the reconstructed profiles when the domain was probed by a source signal with $f_{\max} = 10$ Hz. These profiles were fed as an initial guess to the next problem in the sequence, where the probing source now increased to $f_{\max} = 20$ Hz. Upon inversion, we obtained the profiles presented in the second row. Continuing in this manner, we obtained the converged reconstructed profiles for λ and μ shown in the last row corresponding to a source with $f_{\max} = 40$ Hz. The effect of source-frequency continuation is clearly visible: increasing the source frequency results in refinement of the recovered profiles. Here, the refinement is in the form of localization and sharpening of the layer interfaces, which has been achieved quite satisfactorily under both regularization schemes.

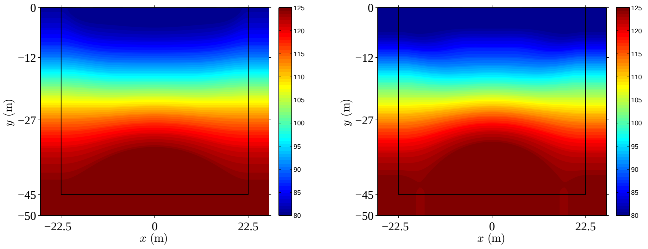

(a) λ ($f_{\max} = 10$ Hz) (b) μ ($f_{\max} = 10$ Hz)

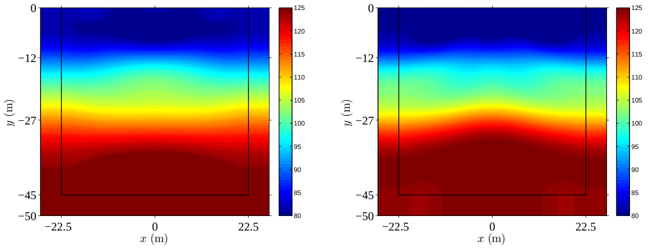

(c) λ ($f_{\max} = 20$ Hz) (d) μ ($f_{\max} = 20$ Hz)

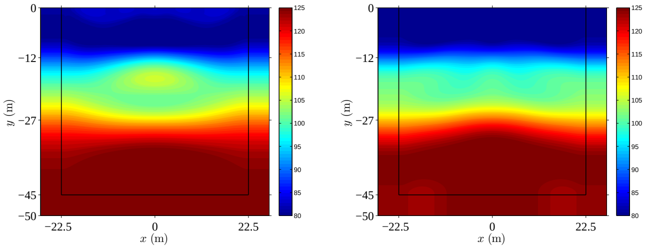

(e) λ ($f_{\max} = 30$ Hz) (f) μ ($f_{\max} = 30$ Hz)

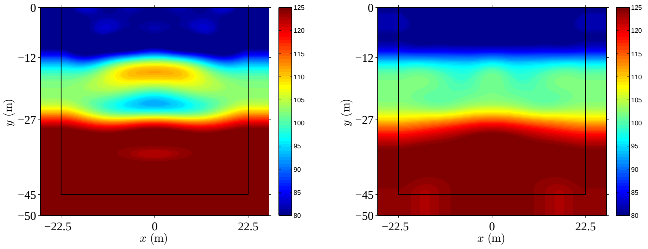

(g) λ ($f_{\max} = 40$ Hz) (h) μ ($f_{\max} = 40$ Hz)

Figure 3.16: Simultaneously inverted Lamé parameters using Algorithm 3.3 and TN regularization; 10 Hz source (105 iterations); 20 Hz source (124 iterations); 30 Hz source (145 iterations); and 40 Hz source (189 iterations)

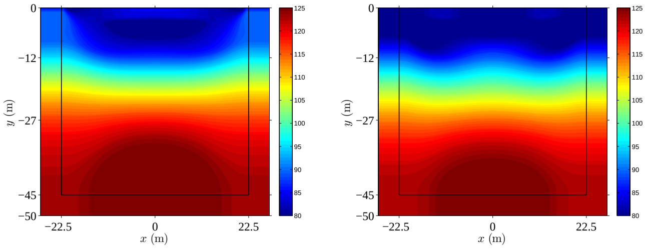

(a) λ ($f_{\max} = 10$ Hz) (b) μ ($f_{\max} = 10$ Hz)

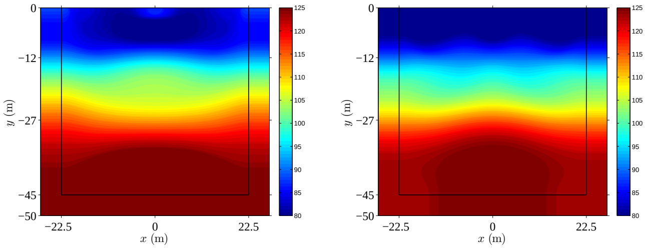

(c) λ ($f_{\max} = 20$ Hz) (d) μ ($f_{\max} = 20$ Hz)

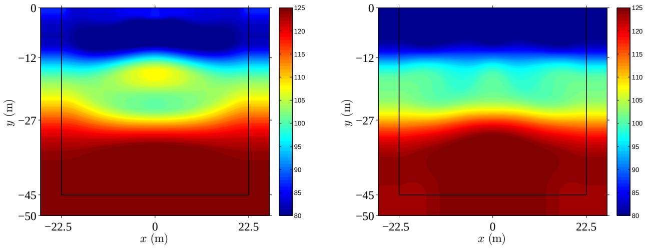

(e) λ ($f_{\max} = 30$ Hz) (f) μ ($f_{\max} = 30$ Hz)

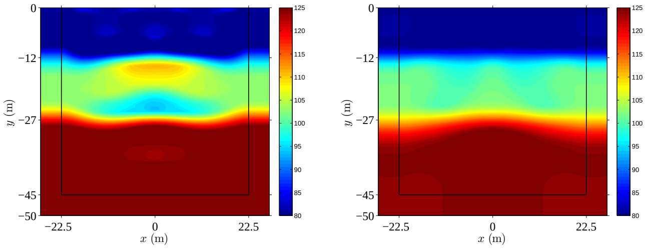

(g) λ ($f_{\max} = 40$ Hz) (h) μ ($f_{\max} = 40$ Hz)

Figure 3.17: Simultaneously inverted Lamé parameters using Algorithm 3.3 and TV regularization; 10 Hz source (145 iterations); 20 Hz source (180 iterations); 30 Hz source (205 iterations); and 40 Hz source (255 iterations)

Figure 3.18 compares the inverted profiles with the target profile at the $x = 0$m, 7m, and 14m cross-sectional lines of the domain. The agreement is excellent for the μ profiles, whereas the λ profiles seem to fluctuate around the target even with the proposed biased-directions inversion algorithm. We are inclined to blame the objective functional being less-sensitive to λ, since varying λ has a mild effect on the misfit provided that it captures, in an average sense, the target profile. As stated in the earlier discussions, the TV regularization scheme is expected to perform better than the TN regularization in recovering the *sharply*-varying target profiles, and indeed, this is the case here, especially with the reconstructed μ profiles. One may sharpen the layer interfaces further by increasing the source-frequency content.

In Fig. 3.19, the response misfit was reduced from its initial value of 0.134×10^{-2} down to 0.819×10^{-7} and 0.662×10^{-7} for the TN and TV regularizations, respectively; this corresponds to about 0.006% and 0.005% of the initial misfit, respectively. Similar to the reduction obtained in the single-parameter inversion experiments, the inversion process achieved almost 5 orders of magnitude reduction in the response misfit. Since the TV regularization captures the sharp layer interfaces better, the final value of the corresponding misfit is lower than the one attained by the TN regularization.

We are also interested in the quality of the compressional and shear wave velocity profiles one could obtain on the basis of the converged λ and μ profiles. The two velocities are the two most commonly used parameters in

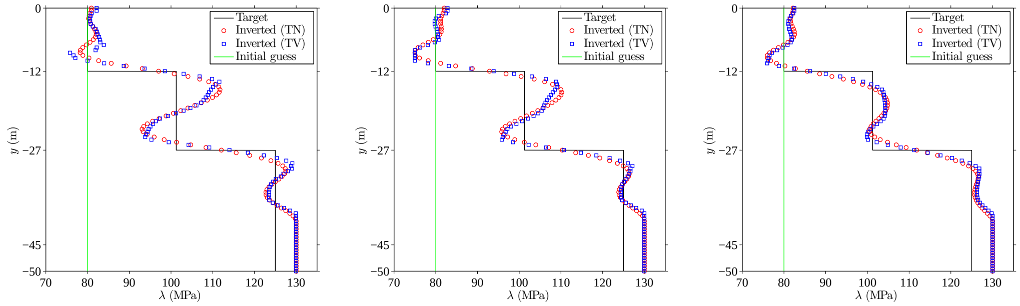

(a) λ profile at $x = 0$m (b) λ profile at $x = 7$m (c) λ profile at $x = 14$m

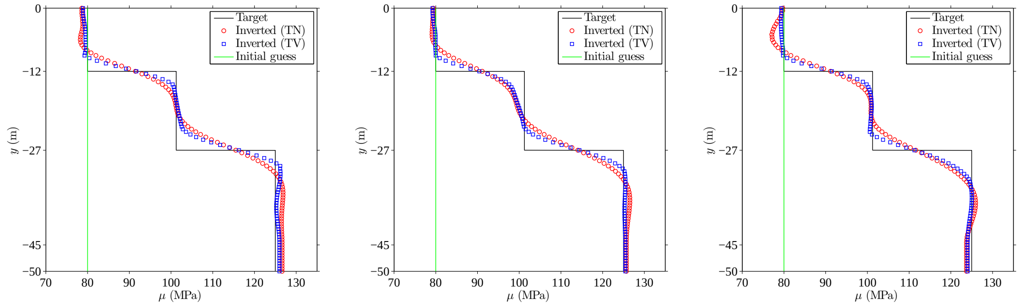

(d) μ profile at $x = 0$m (e) μ profile at $x = 7$m (f) μ profile at $x = 14$m

Figure 3.18: Cross-sectional profiles for simultaneously inverted Lamé parameters using Algorithm 3.3

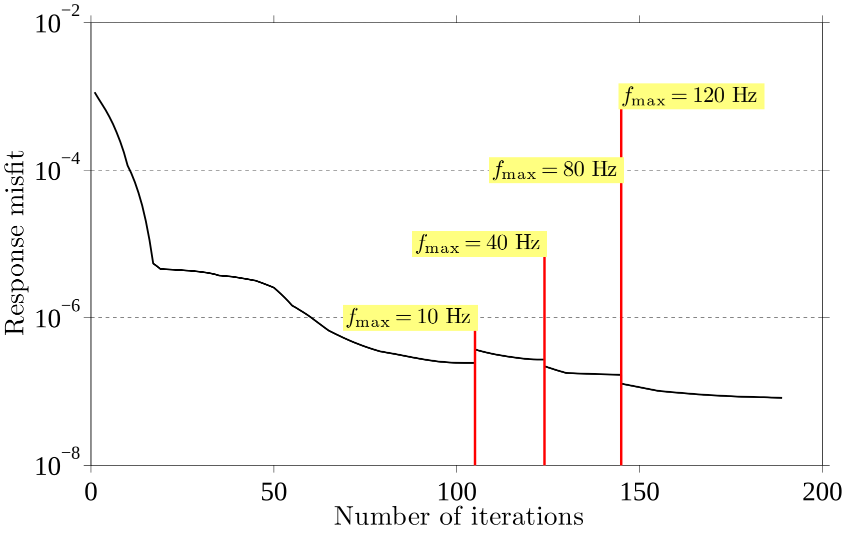

(a) TN regularization

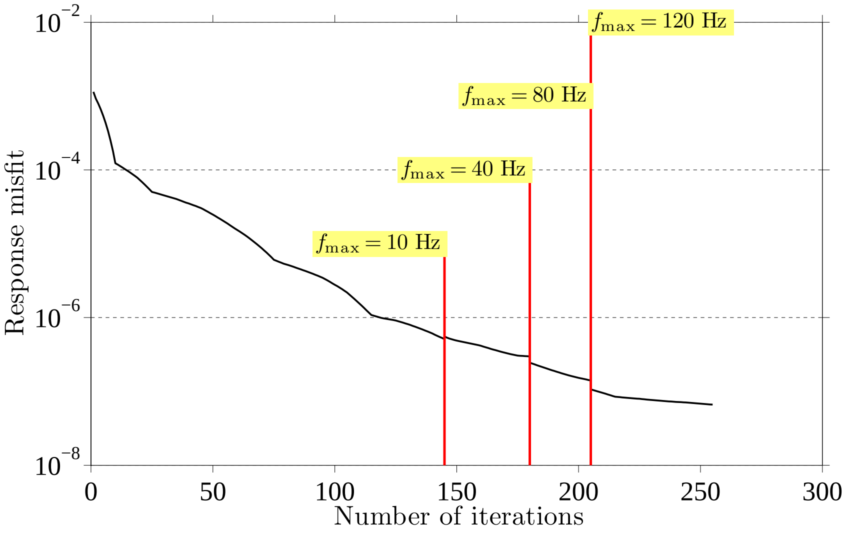

(b) TV regularization

Figure 3.19: Variation of response misfit during the simultaneous inversion endowed with the source-frequency continuation scheme

site characterization; they are expressed as

$$c_p = \sqrt{\frac{\lambda + 2\mu}{\rho}} \qquad \text{and} \qquad c_s = \sqrt{\frac{\mu}{\rho}}. \tag{3.56}$$

Figure 3.20 shows the velocity profiles computed via the above expressions from the converged Lamé parameter profiles. A clear benefit of plotting the velocities instead of the Lamé parameters is that c_p depends weakly on λ and is mostly dominated by μ (contrast the weight of μ to λ in the above expression). Therefore, not surprisingly, both velocity profiles seem to be recovered as well as μ. To further support this observation, we provide in Fig. 3.21 a side-by-side comparison of λ against c_p at two cross-sections (at $x = 0$m and at $x = 14$m). As expected, there is a difference between the two, with the c_p profile capturing the target better than what λ did. Overall, the fluctuations in the reconstructed λ do not seem to affect c_p discernibly.

3.6.3 Example 3 - layered medium with inclusion

We consider a layered semi-infinite domain with an elliptic inclusion located inside a 45m × 45m domain of interest truncated by a 5m-thick PML, as depicted in Fig. 3.22. The density and Poisson's ratio are assumed to be constant and taken as $\rho = 2000$ kg/m^3 and $\nu = 0.25$, respectively. We define the spatial variation of the Lamé parameters as

$$\lambda(y) = \mu(y) = \begin{cases} 320 \text{ MPa}, & \text{for } -15\text{m} \leq y \leq 0\text{m}, \\ 500 \text{ MPa}, & \text{for } -30\text{m} \leq y < -15\text{m}, \\ 720 \text{ MPa}, & \text{for } -50\text{m} \leq y < -30\text{m}, \\ 720 \text{ MPa}, & \text{for elliptic inclusion.} \end{cases} \tag{3.57}$$

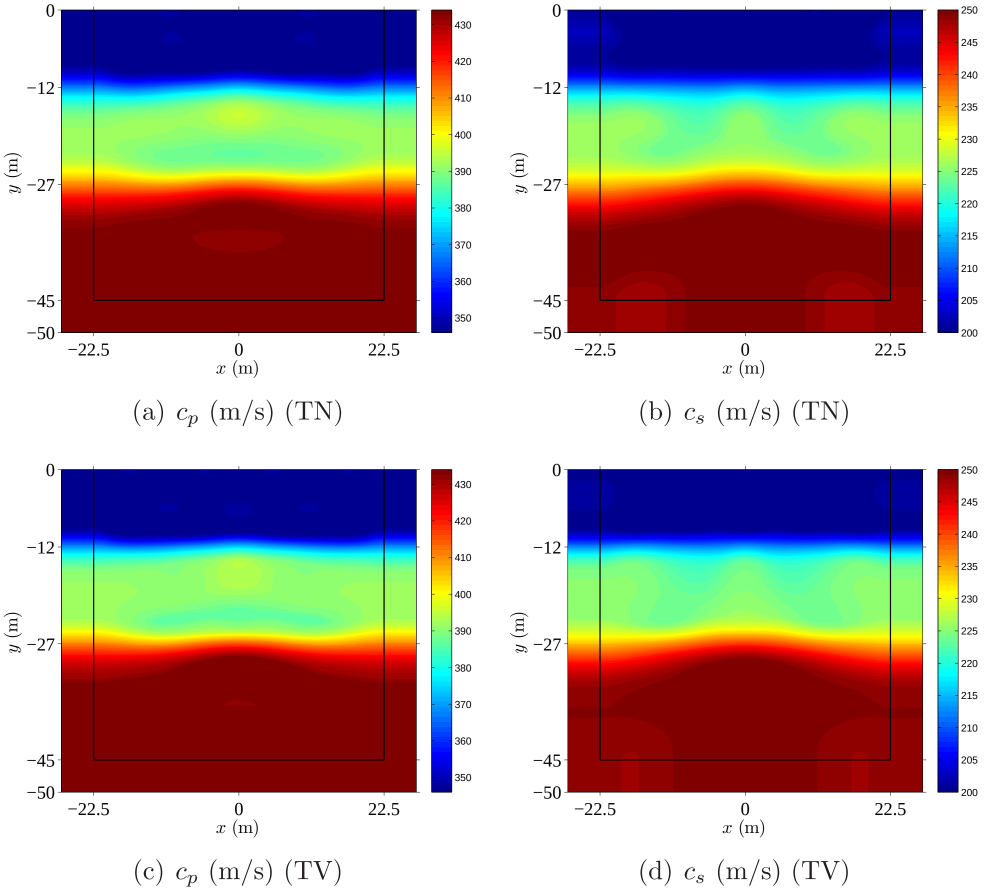

(a) c_p (m/s) (TN) (b) c_s (m/s) (TN)

(c) c_p (m/s) (TV) (d) c_s (m/s) (TV)

Figure 3.20: Velocities computed from the reconstructed Lamé parameters shown in the last rows of Figs. 3.16 and 3.17

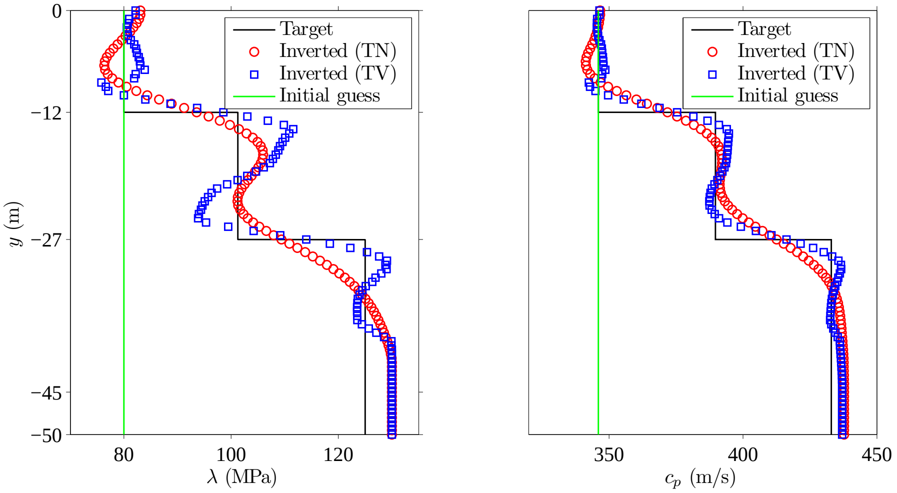

(a) λ vs. c_p profile at $x = 0$m

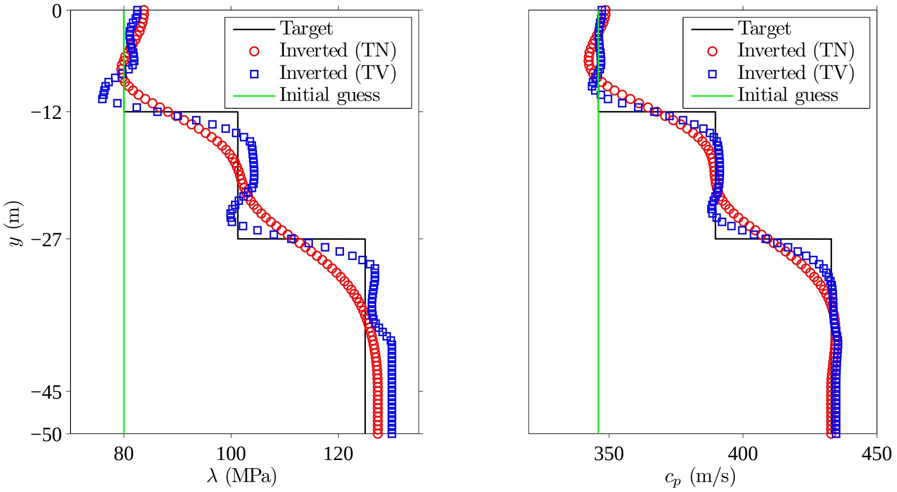

(b) λ vs. c_p profile at $x = 14$m

Figure 3.21: Comparison of cross-sectional profiles using λ (on the left), and c_p (on the right)

As in Examples 1 and 2, the material interfaces were extended horizontally into the PML. The PML and regular domains were discretized by linear quadrilateral elements with an element size of 0.5m. We used a linear-linear pair for the displacements and stresses, and linear approximations for the material properties λ and μ. The discretization resulted in a 10-cell-thick PML (as in previous examples, we set $m = 2$, $\beta_o = 500$ m/s, and $\alpha_o = 0.75$).

To recover the target material profiles shown in Figs. 3.22(b) and 3.22(c), we use a source-frequency continuation scheme as in Example 2. However, here we used four distinct Gaussian pulses with $f_{\max} = 10$, 40, 80, and 120 Hz, as shown in Fig. 3.23, to probe the domain. The receivers that measure the displacement response $\mathbf{u}(\mathbf{x}, t)$ were located at every grid point on the surface resulting in 89 receiver locations. Using a time step of 0.001 seconds, we let the forward problem run for 1.0 seconds under the target material profile, but using a different (refined) mesh to arrive at the synthetic data.

Guided by the earlier discussions on sharply-varying profiles (Example 2), here we opted for using the TV regularization only. We initiated the inversion process with a homogeneous medium that has $\lambda = \mu = 310$ MPa, and used the time signal associated with the lowest source frequency ($f_{\max} = 10$ Hz) to probe the domain. Accordingly, we reconstructed the material profiles shown in Figs. 3.24(a) and 3.24(b) corresponding to λ and μ, respectively. The reconstructed profiles adequately capture the layering of the domain and were able to localize the inclusion to some extent. Though the quality seems rather poor, we note that the minimum wavelength in this setting was 40m,

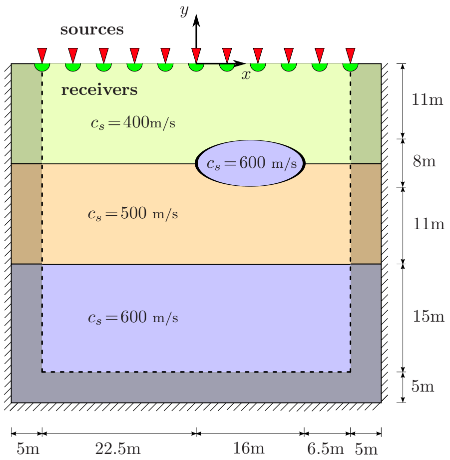

(a) Geometry

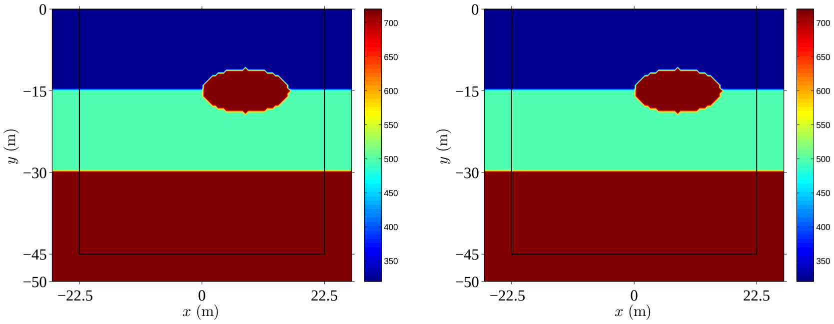

(b) Target λ (c) Target μ

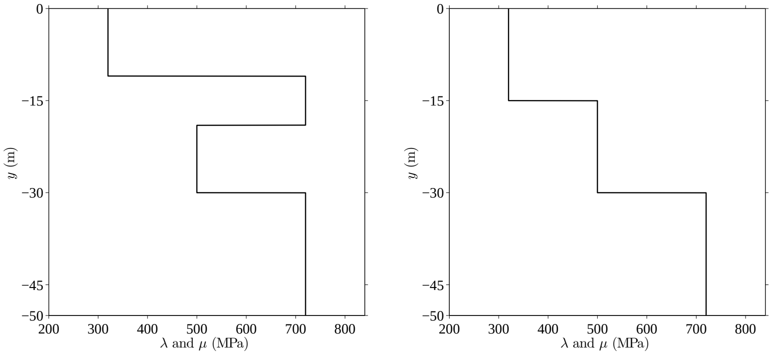

(d) Section profile at $x = 8$m (e) Section profile at $x = -12$m

Figure 3.22: A PML-truncated layered semi-infinite domain with an elliptic inclusion

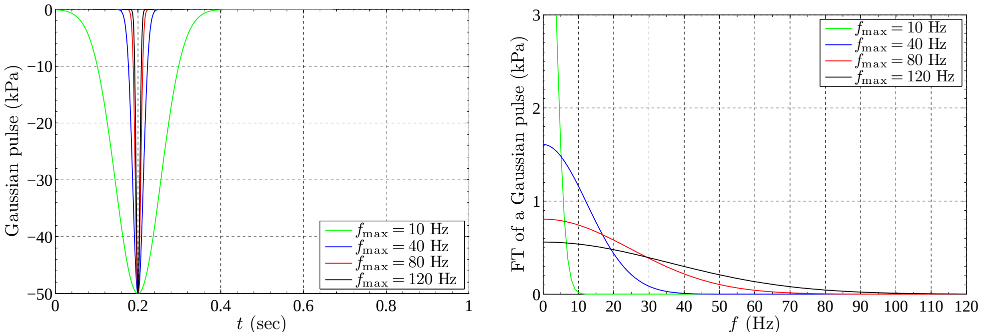

Figure 3.23: Excitation time signals and their Fourier spectrum

which is almost equal to the domain size. To improve the resolution, the source frequency should be increased so that the truncated domain can accommodate several wavelengths. To this end, we fed these profiles as an initial guess to the next problem, where the domain was excited by a Gaussian pulse with $f_{\max} =$ 40 Hz. The reconstructed λ and μ are shown in Figs. 3.24(c) and 3.24(d), respectively. Two key observations in these figures are: (1) the inclusion is localized and better delineated than before, and (2) the blurry layer interfaces of Figs. 3.24(a) and 3.24(b) are now sharper by comparison.

Continuing along the same lines with the source-frequency continuation scheme, we increased the source frequency to $f_{\max} = 80$ Hz, fed the previous reconstructed profiles as an initial guess, and obtained the inverted profiles shown in Figs. 3.24(e) and 3.24(f). Again, we observe that increasing the source frequency resolves the inclusion more clearly, and produces higher quality profiles of λ and μ by further sharpening the layer interfaces. Lastly, we probed the domain by a Gaussian pulse with $f_{\max} = 120$, and reconstructed the profiles depicted in Figs. 3.24(g) and 3.24(h), where further thinning of the material interfaces has been achieved.

Figures 3.25 and 3.26 compare the inverted profiles with the target profile at the $x = -21$m, -8m, 8m and 21m cross-sectional lines of the domain. It is apparent from these figures that both the layering and the inclusion are recovered satisfactorily. Further improvements around the material interfaces can be achieved either by using quadratic approximations for the displacement-stress pair and/or the material properties, or by increasing the source frequency. Lastly, Fig. 3.27 depicts the variation of the response misfit with the number of iterations.

Motivated by the discussion on the velocities in the preceding example, Fig. 3.28 provides the velocity profiles computed from the reconstructed λ and μ shown in Figs. 3.24(g) and 3.24(h). Once again, both velocity profiles seem to have been recovered as well as μ. We also provide a side-by-side comparison of two cross-sectional profiles (at $x = -8$m and $x = 8$m) associated with λ and c_p in Fig. 3.29.

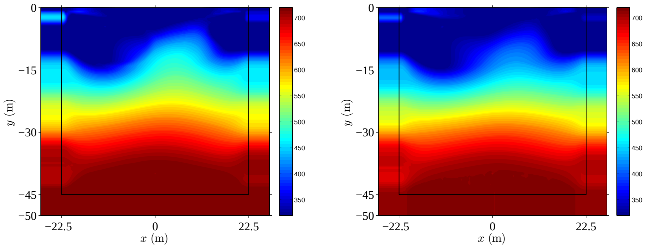

(a) λ ($f_{\max} = 10$ Hz) (b) μ ($f_{\max} = 10$ Hz)

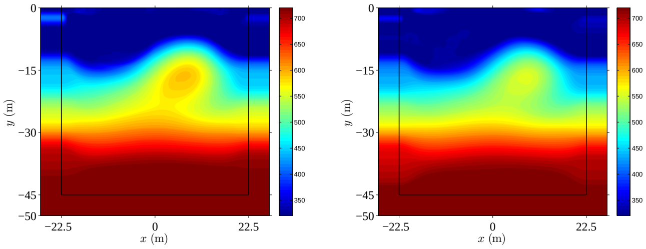

(c) λ ($f_{\max} = 40$ Hz) (d) μ ($f_{\max} = 40$ Hz)

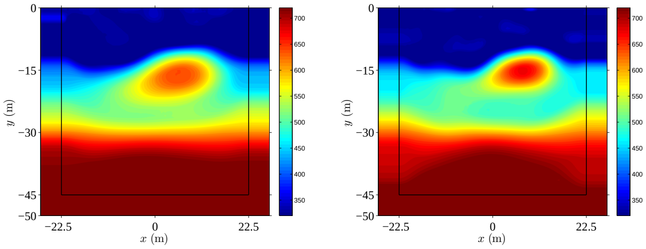

(e) λ ($f_{\max} = 80$ Hz) (f) μ ($f_{\max} = 80$ Hz)

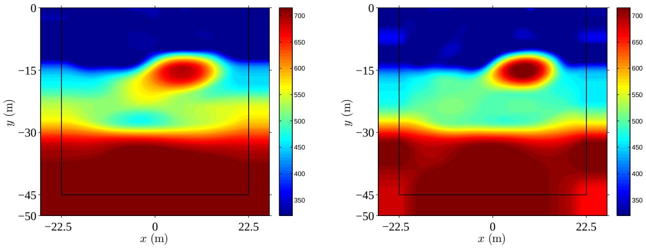

(g) λ ($f_{\max} = 120$ Hz) (h) μ ($f_{\max} = 120$ Hz)

Figure 3.24: Simultaneously inverted Lamé parameters using Algorithm 3.3 and TV regularization; 10 Hz source (225 iterations); 40 Hz source (275 iterations); 80 Hz source (315 iterations); 120 Hz source (395 iterations)

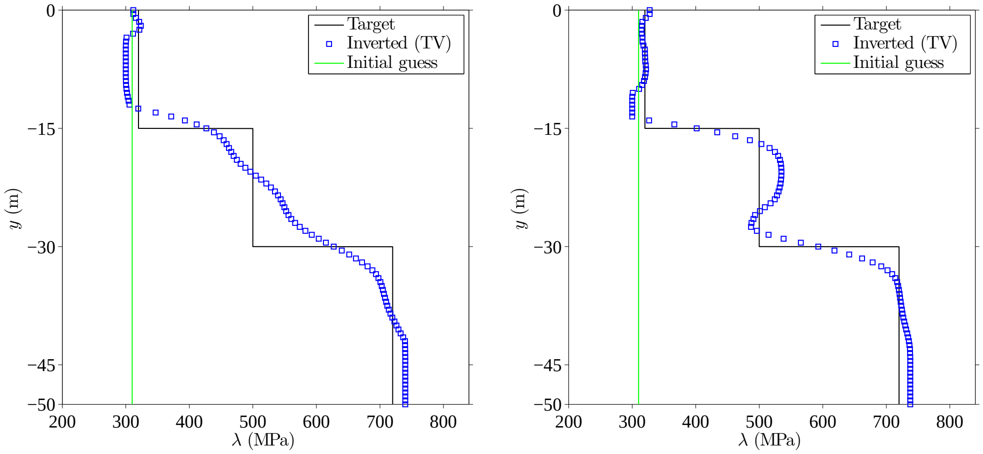

(a) λ profile at $x = -21$m

(b) λ profile at $x = -8$m

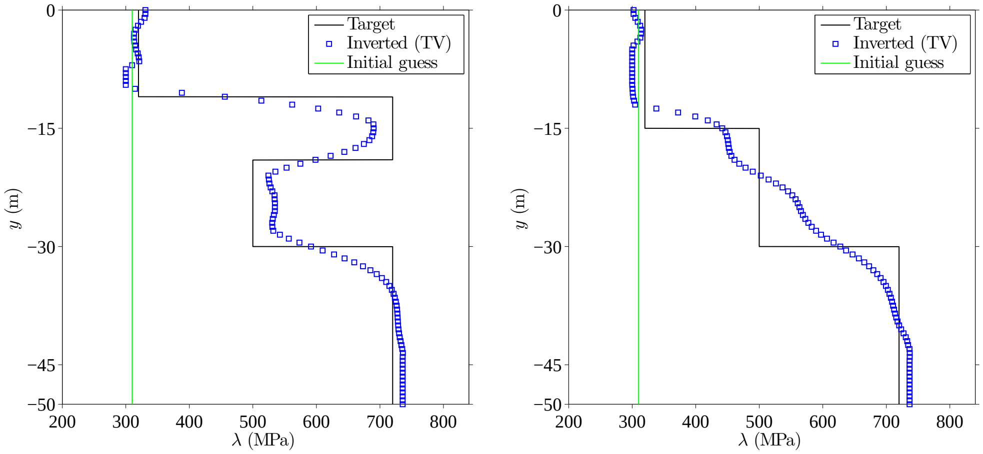

(c) λ profile at $x = 8$m

(d) λ profile at $x = 21$m

Figure 3.25: λ cross-sectional profiles for simultaneously inverted Lamé parameters using Algorithm 3.3

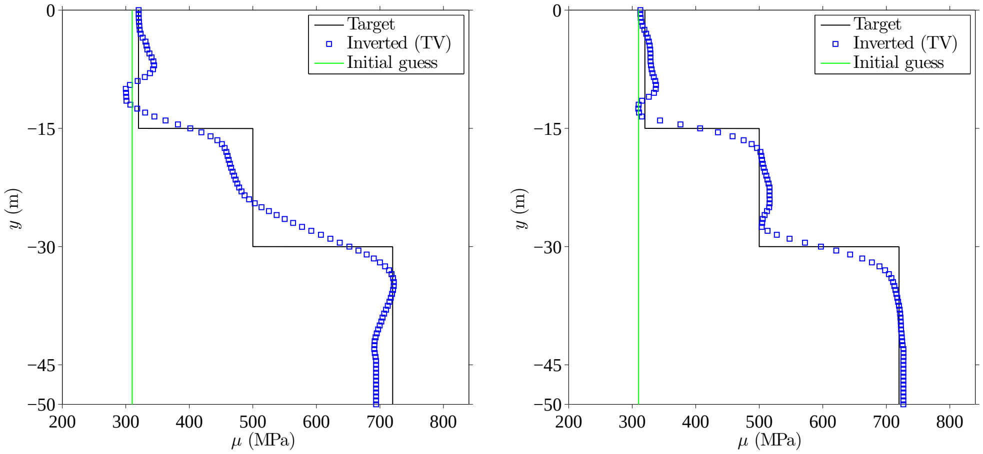

(a) μ profile at $x = -21$m (b) μ profile at $x = -8$m

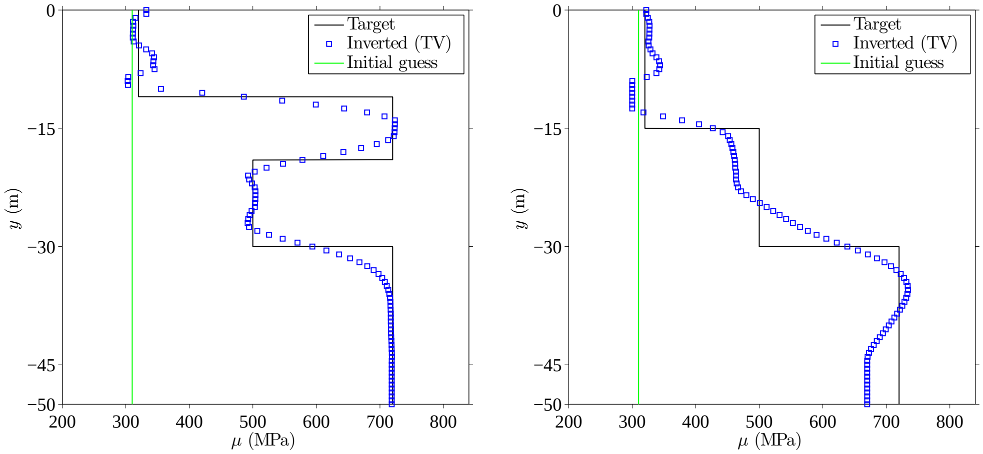

(c) μ profile at $x = 8$m (d) μ profile at $x = 21$m

Figure 3.26: μ cross-sectional profiles for simultaneously inverted Lamé parameters using Algorithm 3.3

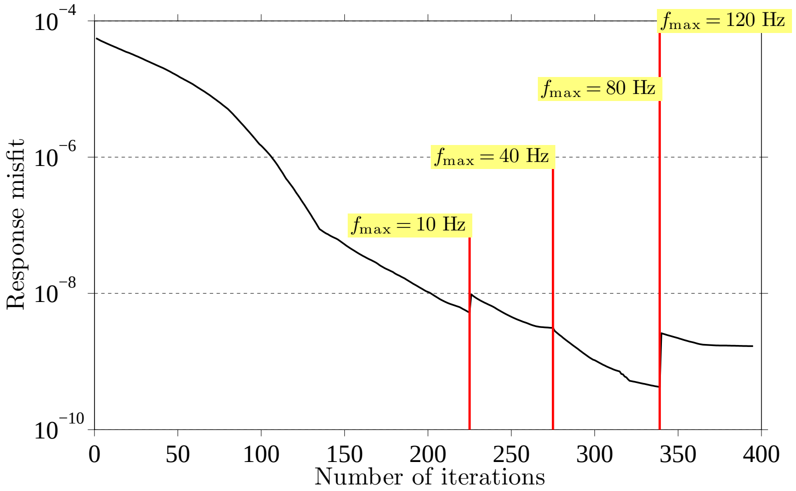

Figure 3.27: Variation of response misfit during simultaneous inversion process with source-frequency continuation

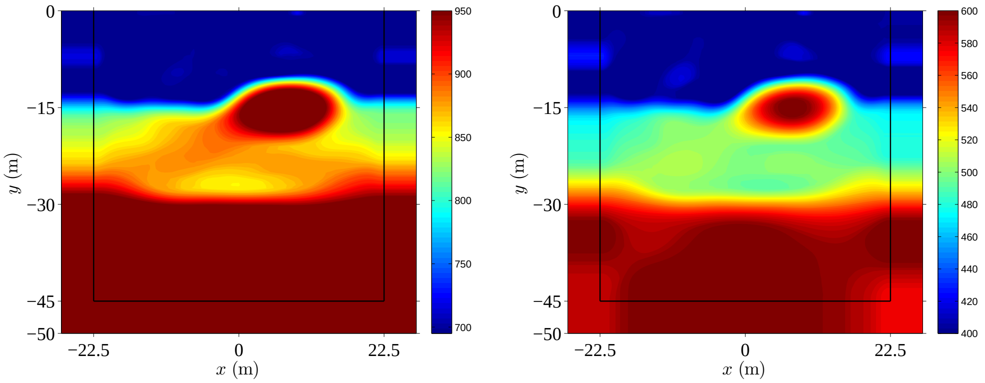

(a) c_p (m/s) (b) c_s (m/s)

Figure 3.28: Velocities computed from the reconstructed Lamé parameters shown in the last row of Fig. 3.24

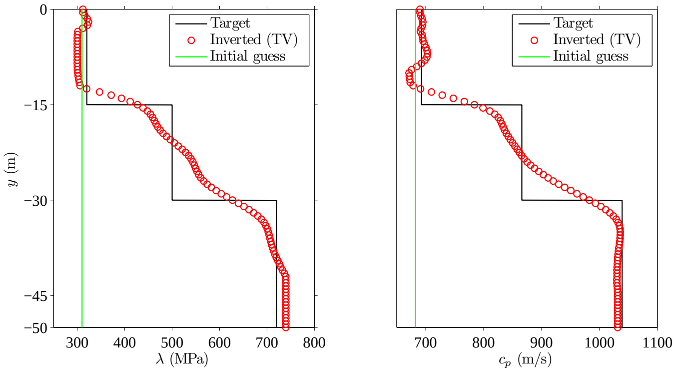

(a) λ vs. c_p profile at $x = -21$m

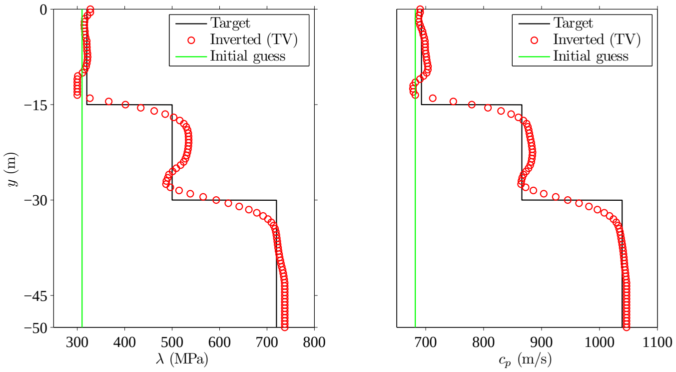

(b) λ vs. c_p profile at $x = -8$m

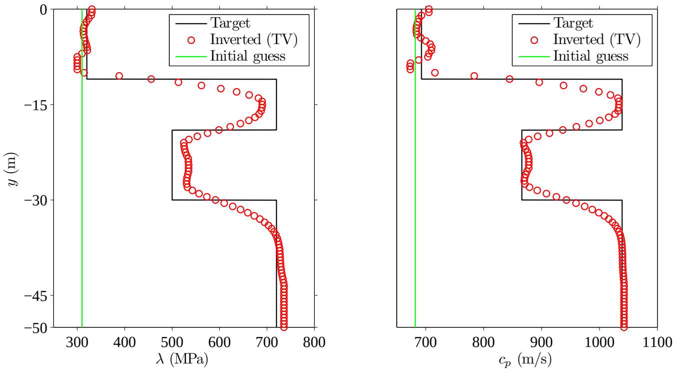

(c) λ vs. c_p profile at $x = 8$m

Figure 3.29: Comparison of cross-sectional profiles using λ (on the left), and c_p (on the right)

Chapter 4

Conclusions

4.1 Summary and contributions

The purpose of this dissertation was to develop a full-waveform-based inversion methodology in PML-truncated elastic media, suitable for geotechnical site characterization purposes, implemented directly in the time-domain, using stress waves for probing, and driven by the measured response at receivers situated on the ground surface.

We have investigated and provided solutions for the two key issues arising in this problem: (a) the numerical simulation of elastic wave motion in PML-truncated arbitrarily heterogeneous semi-infinite media (*forward problem*), and (b) the reconstruction of the spatially-distributed material properties (λ and μ) of the same heterogeneous medium (*inverse problem*).

For the forward problem, we developed and implemented two new formulations. First, a fully-mixed displacement-stress formulation in two dimensions, based on a regularly-stretched and unsplit-field PML. Through the introduction of auxiliary variables (stress memories), the resulting semi-discrete forms are symmetric and second-order in time, thus greatly facilitating time integration. We reported numerical simulations, involving both homogeneous and heterogeneous domains, demonstrating the stability and efficacy of the approach. We then extended the fully-mixed approach to encompass axisymmetric and three-dimensional domains, and reported on numerical results pertaining to axisymmetric media (we have not implemented the three-dimensional case). In these latter cases, the resulting semi-discrete forms were no longer second-order in time but third-order, requiring an extended integration scheme, which we provided herein. Secondly, in an effort to achieve further computational savings, we improved on the earlier formulations by developing a hybrid formulation (mixed unsplit-field PML, coupled with a non-mixed approach for the interior domain) that leads to optimal computational cost. We provided the implementation details for two-dimensional PML-truncated media, and showed that existing displacement-based codes can easily be modified to accommodate PMLs as a means of domain truncation. We numerically studied the stability, efficacy, and cost-effectiveness of the hybrid formulation in both homogeneous and heterogeneous media.

With respect to the inverse problem, we tackled the identification of the soil's material properties in terms of the Lamé parameters within a region of interest resulting from the originally semi-infinite domain through truncation by PMLs. We adopted a PDE-constrained optimization approach, and discussed the implementation of the resulting first-order optimality conditions. These gave rise to: a) a state problem that was treated by the hybrid method developed for the forward wave simulation; b) an adjoint problem that was treated also with the hybrid method similarly to the state problem; and c) control problems that were used to update the material parameters, as described in the preceding chapters.

We discussed continuation schemes for alleviating the solution multiplicity associated with the inverse problem. In particular, we discussed and implemented a source-frequency continuation, and a regularization factor continuation scheme; the latter appears here for the first time in the particular form used herein. The continuation schemes we deployed assisted the optimizer in narrowing the initial feasibility space by presenting subsequent iterations with improved initial guesses.

Lastly, we discussed our experience in reconstructing heterogeneous profiles involving smoothly-varying profiles, as well as layered systems, and layered media with embedded inclusions, in order to demonstrate the performance of the proposed inversion approach. An important finding to emerge from this study is that the objective functional is unequally sensitive to the material properties λ and μ, and accordingly, one should expect difficulties while inverting simultaneously for both λ and μ. This confirms previous findings ([61]) and contributes additional evidence. To address it, we developed and implemented a new search-direction biasing scheme that was shown to significantly improve convergence, both in terms of the quality of the recovered profiles, as well as in terms of the convergence speed.

Parts of the research reported herein have already been published or are currently under review: these include references [88, 97, 102–107].

4.2 Future research

We propose addressing specific issues in future research that escaped the scope of this dissertation, but are viewed as important improvements in the context of the inverse medium problem under consideration.

- Detailed parametric studies are strongly recommended for providing proper guidance on the choice of the PML parameters entering the forward wave simulations. The published literature is rather thin on the topic. More information on these parameters would help one to establish a greater degree of accuracy on designing problem-specific, optimal PMLs.

- In the context of the forward problem, the extension of the hybrid approach reported herein to the axisymmetric and three-dimensional cases, though straightforward, is necessary for computational reasons, if inverse problems implicating such domains are to be efficiently tackled.

- Though the computational cost of the forward problem is optimal in terms of the total number of unknowns involved, the proposed implementation was strictly sequential. Here, even though linear system solutions were provided by an efficient implementation of the SuperLU algorithm, the computational cost per forward solution was strongly dominated by the per-time-step cost. For inverse problem in three-dimensional domains, it is imperative that a parallel solver be used, to reduce the per-time-step cost.

- The issue of varying sensitivity of the objective functional to λ and μ is an intriguing one which could be usefully explored in an effort to design more robust simultaneous inversion schemes. Once the difficulties associated with two-parameter inversion are better understood and tackled appropriately from a theoretical perspective rather than a practical workaround, one could bring in additional control parameters (e.g. density, attenuation characteristics), and seek to address a much more challenging multi-variable inversion that is better suited to realistic problems. In this context, alternative misfit norms should also be explored.
- The structure of the inversion scheme is modular and very flexible. Its performance can be improved by introducing a nonlinear iterative solver that would achieve convergence rates better than the conjugate gradient method used herein, possibly similar to what was proposed in [60].

Appendices

Appendix A

Hybrid formulation semi-discrete form

The global system matrices described in condensed form in (2.129a-2.129b), are expressed in extended form as:

$$
\mathbf{M}^{\mathrm{st}} = \left[\begin{array}{cc|cc|cc|ccc|ccc}
\mathbf{M}^{rr} & \mathbf{0} & \mathbf{M}^{ri} & \mathbf{0} & \mathbf{0} & \mathbf{0} & \mathbf{0} & \mathbf{0} & \mathbf{0} & \mathbf{0} & \mathbf{0} & \mathbf{0} \\
 & \mathbf{M}^{rr} & \mathbf{0} & \mathbf{M}^{ri} & \mathbf{0} & \mathbf{0} & \mathbf{0} & \mathbf{0} & \mathbf{0} & \mathbf{0} & \mathbf{0} & \mathbf{0} \\
\hline
 & & \mathbf{M}^{ii} + \mathbf{M}_a^{ii} & \mathbf{0} & \mathbf{M}_a^{ip} & \mathbf{0} & \mathbf{0} & \mathbf{0} & \mathbf{0} & \mathbf{0} & \mathbf{0} & \mathbf{0} \\
 & & & \mathbf{M}^{ii} + \mathbf{M}_a^{ii} & \mathbf{0} & \mathbf{M}_a^{ip} & \mathbf{0} & \mathbf{0} & \mathbf{0} & \mathbf{0} & \mathbf{0} & \mathbf{0} \\
\hline
 & & & & \mathbf{M}_a^{pp} & \mathbf{0} & \mathbf{0} & \mathbf{0} & \mathbf{0} & \mathbf{0} & \mathbf{0} & \mathbf{0} \\
 & & & & & \mathbf{M}_a^{pp} & \mathbf{0} & \mathbf{0} & \mathbf{0} & \mathbf{0} & \mathbf{0} & \mathbf{0} \\
\hline
 & & & & & & -\mathbf{N}_{1a}^{ii} & \mathbf{N}_{2a}^{ii} & \mathbf{0} & -\mathbf{N}_{1a}^{ip} & \mathbf{N}_{2a}^{ip} & \mathbf{0} \\
 & & & & & & & -\mathbf{N}_{1a}^{ii} & \mathbf{0} & \mathbf{N}_{2a}^{ip} & -\mathbf{N}_{1a}^{ip} & \mathbf{0} \\
 & & & S\ Y\ M & & & & & -\mathbf{N}_{3a}^{ii} & \mathbf{0} & \mathbf{0} & -\mathbf{N}_{3a}^{ip} \\
\hline
 & & & & & & & & & -\mathbf{N}_{1a}^{pp} & \mathbf{N}_{2a}^{pp} & \mathbf{0} \\
 & & & & & & & & & & -\mathbf{N}_{1a}^{pp} & \mathbf{0} \\
 & & & & & & & & & & & -\mathbf{N}_{3a}^{pp}
\end{array}\right]
$$

$$\mathbf{C}^{\mathrm{st}}=\left[\begin{array}{cc:cc:cc:ccc:ccc}
\mathbf{0} & \mathbf{0} & \mathbf{0} & \mathbf{0} & \mathbf{0} & \mathbf{0} & \mathbf{0} & \mathbf{0} & \mathbf{0} & \mathbf{0} & \mathbf{0} & \mathbf{0}\\
 & \mathbf{0} & \mathbf{0} & \mathbf{0} & \mathbf{0} & \mathbf{0} & \mathbf{0} & \mathbf{0} & \mathbf{0} & \mathbf{0} & \mathbf{0} & \mathbf{0}\\
\hdashline
 & & \mathbf{M}_b^{ii} & \mathbf{0} & \mathbf{M}_b^{ip} & \mathbf{0} & \mathbf{A}_{\alpha yx}^{ii} & \mathbf{0} & \mathbf{A}_{\alpha xy}^{ii} & \mathbf{A}_{\alpha yx}^{ip} & \mathbf{0} & \mathbf{A}_{\alpha xy}^{ip}\\
 & & & \mathbf{M}_b^{ii} & \mathbf{0} & \mathbf{M}_b^{ip} & \mathbf{0} & \mathbf{A}_{\alpha xy}^{ii} & \mathbf{A}_{\alpha yx}^{ii} & \mathbf{0} & \mathbf{A}_{\alpha xy}^{ip} & \mathbf{A}_{\alpha yx}^{ip}\\
\hdashline
 & & & & \mathbf{M}_b^{pp} & \mathbf{0} & \mathbf{A}_{\alpha yx}^{pi} & \mathbf{0} & \mathbf{A}_{\alpha xy}^{pi} & \mathbf{A}_{\alpha yx}^{pp} & \mathbf{0} & \mathbf{A}_{\alpha xy}^{pp}\\
 & & & & & \mathbf{M}_b^{pp} & \mathbf{0} & \mathbf{A}_{\alpha xy}^{pi} & \mathbf{A}_{\alpha yx}^{pi} & \mathbf{0} & \mathbf{A}_{\alpha xy}^{pp} & \mathbf{A}_{\alpha yx}^{pp}\\
\hdashline
 & & & & & & -\mathbf{N}_{1b}^{ii} & \mathbf{N}_{2b}^{ii} & \mathbf{0} & -\mathbf{N}_{1b}^{ip} & \mathbf{N}_{2b}^{ip} & \mathbf{0}\\
 & & & & & & & -\mathbf{N}_{1b}^{ii} & \mathbf{0} & \mathbf{N}_{2b}^{ip} & -\mathbf{N}_{1b}^{ip} & \mathbf{0}\\
 & & & S\ Y\ M & & & & & -\mathbf{N}_{3b}^{ii} & \mathbf{0} & \mathbf{0} & -\mathbf{N}_{3b}^{ip}\\
\hdashline
 & & & & & & & & & -\mathbf{N}_{1b}^{pp} & \mathbf{N}_{2b}^{pp} & \mathbf{0}\\
 & & & & & & & & & & -\mathbf{N}_{1b}^{pp} & \mathbf{0}\\
 & & & & & & & & & & & -\mathbf{N}_{3b}^{pp}
\end{array}\right]$$

$$
\mathbf{K}^{\mathrm{st}} = \left[\begin{array}{cc|cc|cc|ccc|ccc}
\mathbf{Q}_1^{rr} & \mathbf{Q}_2^{rr} & \mathbf{Q}_1^{ri} & \mathbf{Q}_2^{ri} & \mathbf{0} & \mathbf{0} & \mathbf{0} & \mathbf{0} & \mathbf{0} & \mathbf{0} & \mathbf{0} & \mathbf{0} \\
 & \mathbf{Q}_3^{rr} & (\mathbf{Q}_2^{T})^{ri} & \mathbf{Q}_3^{ri} & \mathbf{0} & \mathbf{0} & \mathbf{0} & \mathbf{0} & \mathbf{0} & \mathbf{0} & \mathbf{0} & \mathbf{0} \\
\hline
 & & \mathbf{Q}_1^{ii} + \mathbf{M}_c^{ii} & \mathbf{Q}_2^{ii} & \mathbf{M}_c^{ip} & \mathbf{0} & \mathbf{A}_{\beta yx}^{ii} & \mathbf{0} & \mathbf{A}_{\beta xy}^{ii} & \mathbf{A}_{\beta yx}^{ip} & \mathbf{0} & \mathbf{A}_{\beta xy}^{ip} \\
 & & & \mathbf{Q}_3^{ii} + \mathbf{M}_c^{ii} & \mathbf{0} & \mathbf{M}_c^{ip} & \mathbf{0} & \mathbf{A}_{\beta xy}^{ii} & \mathbf{A}_{\beta yx}^{ii} & \mathbf{0} & \mathbf{A}_{\beta xy}^{ip} & \mathbf{A}_{\beta yx}^{ip} \\
\hline
 & & & & \mathbf{M}_c^{pp} & \mathbf{0} & \mathbf{A}_{\beta yx}^{pi} & \mathbf{0} & \mathbf{A}_{\beta xy}^{pi} & \mathbf{A}_{\beta yx}^{pp} & \mathbf{0} & \mathbf{A}_{\beta xy}^{pp} \\
 & & & & & \mathbf{M}_c^{pp} & \mathbf{0} & \mathbf{A}_{\beta xy}^{pi} & \mathbf{A}_{\beta yx}^{pi} & \mathbf{0} & \mathbf{A}_{\beta xy}^{pp} & \mathbf{A}_{\beta yx}^{pp} \\
\hline
 & & & & & & -\mathbf{N}_{1c}^{ii} & \mathbf{N}_{2c}^{ii} & \mathbf{0} & -\mathbf{N}_{1c}^{ip} & \mathbf{N}_{2c}^{ip} & \mathbf{0} \\
 & & & & & & & -\mathbf{N}_{1c}^{ii} & \mathbf{0} & \mathbf{N}_{2c}^{ip} & -\mathbf{N}_{1c}^{ip} & \mathbf{0} \\
 & & & SYM & & & & & -\mathbf{N}_{3c}^{ii} & \mathbf{0} & \mathbf{0} & -\mathbf{N}_{3c}^{ip} \\
\hline
 & & & & & & & & & -\mathbf{N}_{1c}^{pp} & \mathbf{N}_{2c}^{pp} & \mathbf{0} \\
 & & & & & & & & & & -\mathbf{N}_{1c}^{pp} & \mathbf{0} \\
 & & & & & & & & & & & -\mathbf{N}_{3c}^{pp}
\end{array}\right]
$$

Similarly,

$$
\mathbf{d}^{\mathrm{st}} = \left[\mathbf{u}_x^r \;\; \mathbf{u}_y^r \,\vdots\, \mathbf{u}_x^i \;\; \mathbf{u}_y^i \,\vdots\, \mathbf{u}_x^p \;\; \mathbf{u}_y^p \,\vdots\, \mathbf{S}_{xx}^i \;\; \mathbf{S}_{yy}^i \;\; \mathbf{S}_{xy}^i \,\vdots\, \mathbf{S}_{xx}^p \;\; \mathbf{S}_{yy}^p \;\; \mathbf{S}_{xy}^p\right]^T, \tag{A.1}
$$

$$\mathbf{F}^{\mathrm{st}} = \Big[(\mathbf{G}_x^r + \mathbf{Z}_x^r) \ \left(\mathbf{G}_y^r + \mathbf{Z}_y^r\right) \vdots (\mathbf{G}_x^i + \mathbf{Z}_x^i) \ \left(\mathbf{G}_y^i + \mathbf{Z}_y^i\right) \vdots \mathbf{0} \ \mathbf{0} \vdots \mathbf{0} \ \mathbf{0} \ \mathbf{0} \vdots \mathbf{0} \ \mathbf{0} \ \mathbf{0} \Big]^T . \tag{A.2}$$

The various submatrices forming the above global system matrices are defined as follows:

$$\mathbf{M} = \int_{\Omega^{\mathrm{RD}}} \rho \boldsymbol{\Phi} \boldsymbol{\Phi}^T \, \mathrm{d}\Omega, \tag{A.3a}$$

$$\mathbf{M}_k = \int\limits_{\Omega^{\mathrm{PML}}} k \ \rho \boldsymbol{\Phi} \boldsymbol{\Phi}^T \, \mathrm{d}\Omega, \qquad k = a, b, c \tag{A.3b}$$

$$\mathbf{N}_{ik} = \begin{cases} \int\limits_{\Omega^{\mathrm{PML}}} k \frac{\lambda + 2\mu}{4\mu(\lambda+\mu)} \boldsymbol{\Psi} \boldsymbol{\Psi}^T \, \mathrm{d}\Omega, & i = 1, \quad k = a, b, c, \\ \int\limits_{\Omega^{\mathrm{PML}}} k \frac{\lambda}{4\mu(\lambda+\mu)} \boldsymbol{\Psi} \boldsymbol{\Psi}^T \, \mathrm{d}\Omega, & i = 2, \quad k = a, b, c, \\ \int\limits_{\Omega^{\mathrm{PML}}} k \frac{1}{\mu} \boldsymbol{\Psi} \boldsymbol{\Psi}^T \, \mathrm{d}\Omega, & i = 3, \quad k = a, b, c, \end{cases} \tag{A.3c}$$

$$\mathbf{A}_{ijk} = \int\limits_{\Omega^{\mathrm{PML}}} i_j \frac{\partial \boldsymbol{\Phi}}{\partial k} \boldsymbol{\Psi}^T \, \mathrm{d}\Omega, \qquad i = \alpha, \beta, \qquad j, k = x, y, \tag{A.3d}$$

$$\mathbf{Q}_i = \begin{cases} \int_{\Omega^{\mathrm{RD}}} \left[(\lambda + 2\mu) \frac{\partial \boldsymbol{\Phi}}{\partial x} \frac{\partial \boldsymbol{\Phi}^T}{\partial x} + \mu \frac{\partial \boldsymbol{\Phi}}{\partial y} \frac{\partial \boldsymbol{\Phi}^T}{\partial y} \right] \mathrm{d}\Omega, & i = 1, \\ \int_{\Omega^{\mathrm{RD}}} \left[\lambda \frac{\partial \boldsymbol{\Phi}}{\partial x} \frac{\partial \boldsymbol{\Phi}^T}{\partial y} + \mu \frac{\partial \boldsymbol{\Phi}}{\partial y} \frac{\partial \boldsymbol{\Phi}^T}{\partial x} \right] \mathrm{d}\Omega, & i = 2, \\ \int_{\Omega^{\mathrm{RD}}} \left[\mu \frac{\partial \boldsymbol{\Phi}}{\partial x} \frac{\partial \boldsymbol{\Phi}^T}{\partial x} + (\lambda + 2\mu) \frac{\partial \boldsymbol{\Phi}}{\partial y} \frac{\partial \boldsymbol{\Phi}^T}{\partial y} \right] \mathrm{d}\Omega, & i = 3. \end{cases} \tag{A.3e}$$

Moreover, the global load vector submatrices are expressed as:

$$\mathbf{G}_i = \int_{\Gamma_N^{\mathrm{RD}}} \boldsymbol{\Phi} \ g_i(\mathbf{x}, t) \, \mathrm{d}\Gamma, \qquad i = x, y, \tag{A.3f}$$

$$\mathbf{Z}_i = \int_{\Omega^{\mathrm{RD}}} \boldsymbol{\Phi} f_i(\mathbf{x}, t) \, \mathrm{d}\Omega, \qquad i = x, y. \tag{A.3g}$$

The superscripts in the above matrices are used to display the partitions of element submatrices. The ordering is done in such a way that the interior domain nodes come first, followed by the interface nodes, and the PML nodes come last. Thus, any element submatrix could be partitioned as:

$$\Box_{el} = \left[\begin{array}{c:c} \Box^{rr} & \Box^{ri} \\ \hdashline \Box^{ir} & \Box^{ii} \end{array}\right] \qquad \text{where } el \in \Omega^{\mathrm{RD}}, \tag{A.4a}$$

$$\Box_{el} = \left[\begin{array}{c:c} \Box^{ii} & \Box^{ip} \\ \hdashline \Box^{pi} & \Box^{pp} \end{array}\right] \qquad \text{where } el \in \Omega^{\mathrm{PML}}. \tag{A.4b}$$

Similarly, the global load vector submatrices can be partitioned as:

$$\Box_{el} = \left[\begin{array}{c} \Box^{r} \\ \hdashline \Box^{i} \end{array}\right] \qquad \text{where } el \in \Omega^{\mathrm{RD}}. \tag{A.4c}$$

Appendix B

On the 2^{nd} optimality condition

We show here the technical details of obtaining the second optimality condition. The variations of $\mathcal{L}$ with respect to the state variables $(\mathbf{u}, \mathbf{S})$ are quite involved. Here we derive $\delta_{\mathbf{u}}\mathcal{L}$ and $\delta_{\mathbf{S}}\mathcal{L}$ separately; they are added later to obtain

$$\delta_{\mathbf{u}}\mathcal{L} + \delta_{\mathbf{S}}\mathcal{L} = 0. \tag{B.1}$$

B.1 Derivation of $\delta_{\mathbf{u}}\mathcal{L}$

We take first the variation of $\mathcal{L}$ with respect to $\mathbf{u}$:

$$\delta_{\mathbf{u}}\mathcal{L} = \delta\frac{1}{2}\sum_{j=1}^{N_r}\int_0^T\int_{\Gamma_m}\left(\mathbf{u}\cdot\mathbf{u} - 2\mathbf{u}\cdot\mathbf{u}_m + \mathbf{u}_m\cdot\mathbf{u}_m\right)\,\delta(\mathbf{x}-\mathbf{x}_j)\,\mathrm{d}\Gamma_m dt \tag{B.2a}$$

$$+\,\delta\int_{\Omega^{\mathrm{RD}}}\int_0^T \boldsymbol{\theta_{u1}}\cdot\left\{\mathbf{div}\left[\mu\left(\nabla\mathbf{u}+\nabla\mathbf{u}^T\right)+\lambda\,\mathrm{div}\,\mathbf{u}\,\mathcal{I}\right]-\rho\ddot{\mathbf{u}}\right\}\,dt\mathrm{d}\Omega \tag{B.2b}$$

$$+\,\delta\int_{\Omega^{\mathrm{PML}}}\int_0^T \boldsymbol{\theta_{u2}}\cdot\left[-\rho\left(a\ddot{\mathbf{u}}+b\dot{\mathbf{u}}+c\mathbf{u}\right)\right]\,dt\mathrm{d}\Omega \tag{B.2c}$$

$$-\,\delta\frac{1}{2}\int_{\Omega^{\mathrm{PML}}}\int_0^T \boldsymbol{\theta_s} : \left[(\nabla\mathbf{u})\tilde{\Lambda}_p + \tilde{\Lambda}_p(\nabla\mathbf{u})^T + (\nabla\dot{\mathbf{u}})\tilde{\Lambda}_e + \tilde{\Lambda}_e(\nabla\dot{\mathbf{u}})^T\right]\,dt\mathrm{d}\Omega \tag{B.2d}$$

$$+\,\delta\int_{\Gamma_N^{\mathrm{RD}}}\int_0^T \boldsymbol{\theta_{b1}}\cdot\left\{\left[\mu\left(\nabla\mathbf{u}+\nabla\mathbf{u}^T\right)+\lambda\,\mathrm{div}\,\mathbf{u}\,\mathcal{I}\right]\mathbf{n}\right\}\,dt\mathrm{d}\Gamma. \tag{B.2e}$$

To keep track, we compute each term separately. Equation (B.2a) results in

$$\text{Eq.(B.2a)} = \sum_{j=1}^{N_r} \int_0^T \int_{\Gamma_m} \delta\mathbf{u} \cdot (\mathbf{u} - \mathbf{u}_m)\ \delta(\mathbf{x} - \mathbf{x}_j)\, \mathrm{d}\Gamma_m dt \tag{B.3}$$

Let us next compute equation (B.2b). Using the divergence identity[1], we get

$$\begin{aligned} \text{Eq.(B.2b)} = {} & \delta \int_{\Omega^{\mathrm{RD}}} \int_0^T \operatorname{div}\left\{ \left[\mu \left(\nabla\mathbf{u} + \nabla\mathbf{u}^T\right) + \lambda \operatorname{div}\mathbf{u}\, \mathcal{I}\right] \boldsymbol{\theta}_{\boldsymbol{u}\mathbf{1}} \right\}\ dt\mathrm{d}\Omega \\ & - \delta \int_{\Omega^{\mathrm{RD}}} \int_0^T \nabla\boldsymbol{\theta}_{\boldsymbol{u}\mathbf{1}} : \left[\mu \left(\nabla\mathbf{u} + \nabla\mathbf{u}^T\right) + \lambda \operatorname{div}\mathbf{u}\, \mathcal{I}\right]\ dt\mathrm{d}\Omega \\ & - \delta \int_{\Omega^{\mathrm{RD}}} \int_0^T \boldsymbol{\theta}_{\boldsymbol{u}\mathbf{1}} \cdot \rho\ddot{\mathbf{u}}\, dt\mathrm{d}\Omega. \end{aligned} \tag{B.4}$$

Next, we apply the Gauss divergence theorem[2] and also use the definition of a tensor transpose[3] to obtain

$$\begin{aligned} \text{Eq.(B.2b)} = {} & \delta \int_{\Gamma^{\mathrm{RD}}} \int_0^T \left\{ \left[\mu \left(\nabla\mathbf{u} + \nabla\mathbf{u}^T\right) + \lambda \operatorname{div}\mathbf{u}\, \mathcal{I}\right] \mathbf{n} \right\} \cdot \boldsymbol{\theta}_{\boldsymbol{u}\mathbf{1}}\, dt\mathrm{d}\Gamma \\ & - \delta \int_{\Omega^{\mathrm{RD}}} \int_0^T \nabla\boldsymbol{\theta}_{\boldsymbol{u}\mathbf{1}} : \left[\mu \left(\nabla\mathbf{u} + \nabla\mathbf{u}^T\right) + \lambda \operatorname{div}\mathbf{u}\, \mathcal{I}\right]\ dt\mathrm{d}\Omega \\ & - \delta \int_{\Omega^{\mathrm{RD}}} \left\{ \left[\, \boldsymbol{\theta}_{\boldsymbol{u}\mathbf{1}} \cdot \rho\dot{\mathbf{u}}\, \right] \Big|_0^T - \int_0^T \dot{\boldsymbol{\theta}}_{\boldsymbol{u}\mathbf{1}} \cdot \rho\dot{\mathbf{u}}\, dt \right\} \mathrm{d}\Omega. \end{aligned} \tag{B.5}$$

---

[1] $\operatorname{div}\left(\mathcal{A}^T\mathbf{v}\right) = \mathbf{div}\,\mathcal{A} \cdot \mathbf{v} + \nabla\mathbf{v} : \mathcal{A}$

[2] $\int_R \operatorname{div}\mathbf{v}\, dR = \int_{\partial R} \mathbf{v} \cdot \mathbf{n}\, \partial R$

[3] $\left(\mathcal{A}^T\mathbf{u}\right) \cdot \mathbf{v} = \mathcal{A}\mathbf{v} \cdot \mathbf{u}$

We apply integration by parts (the divergence identity) for the second time, use the definition of a tensor trace[4], and the identity $\operatorname{div}\mathbf{v} = \mathrm{tr}(\nabla\mathbf{v})$ to obtain

$$
\begin{aligned}
\text{Eq.(B.2b)} = & \int_{\Gamma^{\mathrm{RD}}}\int_0^T \left\{\left[\mu\left(\nabla\delta\mathbf{u} + \nabla\delta\mathbf{u}^T\right) + \lambda \operatorname{div}\delta\mathbf{u}\,\mathcal{I}\right]\mathbf{n}\right\}\cdot\boldsymbol{\theta}_{\boldsymbol{u1}}\,dt\mathrm{d}\Gamma \\
& - \delta\int_{\Gamma^{\mathrm{RD}}}\int_0^T \left[\mu(\nabla\boldsymbol{\theta}_{\boldsymbol{u1}} + \nabla{\boldsymbol{\theta}_{\boldsymbol{u1}}}^T)\mathbf{n}\right]\cdot\mathbf{u}\,dt\mathrm{d}\Gamma \\
& + \delta\int_{\Omega^{\mathrm{RD}}}\int_0^T \mathbf{div}\left[\mu(\nabla\boldsymbol{\theta}_{\boldsymbol{u1}} + \nabla{\boldsymbol{\theta}_{\boldsymbol{u1}}}^T)\right]\cdot\mathbf{u}\,dt\mathrm{d}\Omega \\
& - \delta\int_{\Omega^{\mathrm{RD}}}\int_0^T \nabla\mathbf{u} : \lambda\ \operatorname{div}\boldsymbol{\theta}_{\boldsymbol{u1}}\,\mathcal{I}\,dt\mathrm{d}\Omega \\
& - \int_{\Omega^{\mathrm{RD}}} \{[\boldsymbol{\theta}_{\boldsymbol{u1}}(\mathbf{x},T)\cdot\rho\delta\dot{\mathbf{u}}(\mathbf{x},T) - \boldsymbol{\theta}_{\boldsymbol{u1}}(\mathbf{x},0)\cdot\rho\delta\dot{\mathbf{u}}(\mathbf{x},0)] \\
& \qquad - \left[\dot{\boldsymbol{\theta}}_{\boldsymbol{u1}}(\mathbf{x},T)\cdot\rho\delta\mathbf{u}(\mathbf{x},T) - \dot{\boldsymbol{\theta}}_{\boldsymbol{u1}}(\mathbf{x},0)\cdot\rho\delta\mathbf{u}(\mathbf{x},0)\right]\Big\}\ \mathrm{d}\Omega \\
& - \int_{\Omega^{\mathrm{RD}}}\int_0^T \delta\mathbf{u}\cdot\rho\ddot{\boldsymbol{\theta}}_{\boldsymbol{u1}}\,dt\mathrm{d}\Omega. && \text{(B.6)}
\end{aligned}
$$

We explicitly impose the initial conditions $\mathbf{u}(\mathbf{x},0) = \mathbf{0}$ and $\dot{\mathbf{u}}(\mathbf{x},0) = \mathbf{0}$. Then, we integrate by parts one more time to obtain

$$
\begin{aligned}
\text{Eq.(B.2b)} = & \int_{\Gamma^{\mathrm{RD}}}\int_0^T \left\{\left[\mu\left(\nabla\delta\mathbf{u} + \nabla\delta\mathbf{u}^T\right) + \lambda \operatorname{div}\delta\mathbf{u}\,\mathcal{I}\right]\mathbf{n}\right\}\cdot\boldsymbol{\theta}_{\boldsymbol{u1}}\,dt\mathrm{d}\Gamma \\
& - \int_{\Gamma^{\mathrm{RD}}}\int_0^T \delta\mathbf{u}\cdot\left\{\left[\mu(\nabla\boldsymbol{\theta}_{\boldsymbol{u1}} + \nabla{\boldsymbol{\theta}_{\boldsymbol{u1}}}^T) + \lambda\ \operatorname{div}\boldsymbol{\theta}_{\boldsymbol{u1}}\,\mathcal{I}\right]\mathbf{n}\right\}\ dt\mathrm{d}\Gamma \\
& + \int_{\Omega^{\mathrm{RD}}}\int_0^T \delta\mathbf{u}\cdot\left\{\mathbf{div}\left[\mu(\nabla\boldsymbol{\theta}_{\boldsymbol{u1}} + \nabla{\boldsymbol{\theta}_{\boldsymbol{u1}}}^T) + \lambda\ \operatorname{div}\boldsymbol{\theta}_{\boldsymbol{u1}}\,\mathcal{I}\right] - \rho\ddot{\boldsymbol{\theta}}_{\boldsymbol{u1}}\right\}\ dt\mathrm{d}\Omega \\
& - \int_{\Omega^{\mathrm{RD}}} \left\{\boldsymbol{\theta}_{\boldsymbol{u1}}(\mathbf{x},T)\cdot\rho\delta\dot{\mathbf{u}}(\mathbf{x},T) - \dot{\boldsymbol{\theta}}_{\boldsymbol{u1}}(\mathbf{x},T)\cdot\rho\delta\mathbf{u}(\mathbf{x},T)\right\}\ \mathrm{d}\Omega. && \text{(B.7)}
\end{aligned}
$$

---

[4] $\mathcal{I} : \mathcal{A} = \mathrm{tr}(\mathcal{A})$

We turn next to equation (B.2c). Using integration by parts in time several times and rearranging terms, one can obtain

$$\begin{aligned}\text{Eq.(B.2c)} = -\int_{\Omega^{\text{PML}}} &\{\, [\boldsymbol{\theta}_{\boldsymbol{u2}}(\mathbf{x},T)\cdot\rho a\delta\dot{\mathbf{u}}(\mathbf{x},T) - \boldsymbol{\theta}_{\boldsymbol{u2}}(\mathbf{x},0)\cdot\rho a\delta\dot{\mathbf{u}}(\mathbf{x},0)] \\ &- \Big[\dot{\boldsymbol{\theta}}_{\boldsymbol{u2}}(\mathbf{x},T)\cdot\rho a\delta\mathbf{u}(\mathbf{x},T) - \dot{\boldsymbol{\theta}}_{\boldsymbol{u2}}(\mathbf{x},0)\cdot\rho a\delta\mathbf{u}(\mathbf{x},0)\Big] \\ &+ [\boldsymbol{\theta}_{\boldsymbol{u2}}(\mathbf{x},T)\cdot\rho b\delta\mathbf{u}(\mathbf{x},T) - \boldsymbol{\theta}_{\boldsymbol{u2}}(\mathbf{x},0)\cdot\rho b\delta\mathbf{u}(\mathbf{x},0)]\,\}\ \mathrm{d}\Omega \\ - \int_{\Omega^{\text{PML}}}\int_0^T &\delta\mathbf{u}\cdot\Big(\rho a\ddot{\boldsymbol{\theta}}_{\boldsymbol{u2}} - \rho b\dot{\boldsymbol{\theta}}_{\boldsymbol{u2}} + \rho c\boldsymbol{\theta}_{\boldsymbol{u2}}\Big)\ dt\mathrm{d}\Omega. \end{aligned} \tag{B.8}$$

Next, we explicitly impose the initial conditions $\mathbf{u}(\mathbf{x},0) = 0$ and $\dot{\mathbf{u}}(\mathbf{x},0) = 0$ that results in

$$\begin{aligned}\text{Eq.(B.2c)} = -\int_{\Omega^{\text{PML}}} &\Big\{\, \rho a\boldsymbol{\theta}_{\boldsymbol{u2}}(\mathbf{x},T)\cdot\delta\dot{\mathbf{u}}(\mathbf{x},T) - \rho a\dot{\boldsymbol{\theta}}_{\boldsymbol{u2}}(\mathbf{x},T)\cdot\delta\mathbf{u}(\mathbf{x},T) \\ &+\rho b\boldsymbol{\theta}_{\boldsymbol{u2}}(\mathbf{x},T)\cdot\delta\mathbf{u}(\mathbf{x},T)\,\}\ \mathrm{d}\Omega \\ - \int_{\Omega^{\text{PML}}}\int_0^T &\delta\mathbf{u}\cdot\Big(\rho a\ddot{\boldsymbol{\theta}}_{\boldsymbol{u2}} - \rho b\dot{\boldsymbol{\theta}}_{\boldsymbol{u2}} + \rho c\boldsymbol{\theta}_{\boldsymbol{u2}}\Big)\ dt\mathrm{d}\Omega. \end{aligned} \tag{B.9}$$

We turn next to equation (B.2d); starting with

$$\begin{aligned}\text{Eq.(B.2d)} = &-\frac{1}{2}\delta\int_{\Omega^{\text{PML}}}\int_0^T \Big[\boldsymbol{\theta}_{\boldsymbol{s}}:(\nabla\mathbf{u})\tilde{\Lambda}_p + \boldsymbol{\theta}_{\boldsymbol{s}}:\tilde{\Lambda}_p(\nabla\mathbf{u})^T\Big]\ dt\mathrm{d}\Omega \\ &-\frac{1}{2}\delta\int_{\Omega^{\text{PML}}}\int_0^T \Big[\boldsymbol{\theta}_{\boldsymbol{s}}:(\nabla\dot{\mathbf{u}})\tilde{\Lambda}_e + \boldsymbol{\theta}_{\boldsymbol{s}}:\tilde{\Lambda}_e(\nabla\dot{\mathbf{u}})^T\Big]\ dt\mathrm{d}\Omega, \end{aligned} \tag{B.10}$$

and using tensor inner product identities[5], we get

$$\begin{aligned}\text{Eq.(B.2d)} = &-\frac{1}{2}\delta\int_{\Omega^{\text{PML}}}\int_0^T \Big[\boldsymbol{\theta}_{\boldsymbol{s}}\tilde{\Lambda}_p:(\nabla\mathbf{u}) + {\boldsymbol{\theta}_{\boldsymbol{s}}}^T\tilde{\Lambda}_p:(\nabla\mathbf{u})\Big]\ dt\mathrm{d}\Omega \\ &-\frac{1}{2}\delta\int_{\Omega^{\text{PML}}}\int_0^T \Big[\boldsymbol{\theta}_{\boldsymbol{s}}\tilde{\Lambda}_e:(\nabla\dot{\mathbf{u}}) + {\boldsymbol{\theta}_{\boldsymbol{s}}}^T\tilde{\Lambda}_e:(\nabla\dot{\mathbf{u}})\Big]\ dt\mathrm{d}\Omega. \end{aligned} \tag{B.11}$$

---

[5] $\mathcal{C}:(\mathcal{A}\mathcal{B}) = (\mathcal{C}^T\mathcal{A}):\mathcal{B}^T = (\mathcal{C}\mathcal{B}^T):\mathcal{A}$

Next, we apply the divergence identity, the Gauss divergence theorem for vectors, and the definition of a tensor transpose to obtain

$$\begin{aligned}\text{Eq.(B.2d)} = &-\frac{1}{2}\delta\int_{\Gamma^{\mathrm{PML}}}\int_0^T\left\{\mathbf{u}\cdot\left(\boldsymbol{\theta_s}\tilde{\Lambda}_p\right)\mathbf{n}+\mathbf{u}\cdot\left({\boldsymbol{\theta_s}}^T\tilde{\Lambda}_p\right)\mathbf{n}\right\}\,dt\mathrm{d}\Gamma\\ &-\frac{1}{2}\delta\int_{\Gamma^{\mathrm{PML}}}\int_0^T\left\{\dot{\mathbf{u}}\cdot\left(\boldsymbol{\theta_s}\tilde{\Lambda}_e\right)\mathbf{n}+\dot{\mathbf{u}}\cdot\left({\boldsymbol{\theta_s}}^T\tilde{\Lambda}_e\right)\mathbf{n}\right\}\,dt\mathrm{d}\Gamma\\ &+\frac{1}{2}\delta\int_{\Omega^{\mathrm{PML}}}\int_0^T\mathbf{div}\left(\boldsymbol{\theta_s}\tilde{\Lambda}_p+{\boldsymbol{\theta_s}}^T\tilde{\Lambda}_p\right)\cdot\mathbf{u}\,dt\mathrm{d}\Omega\\ &+\frac{1}{2}\delta\int_{\Omega^{\mathrm{PML}}}\int_0^T\mathbf{div}\left(\boldsymbol{\theta_s}\tilde{\Lambda}_e+{\boldsymbol{\theta_s}}^T\tilde{\Lambda}_e\right)\cdot\dot{\mathbf{u}}\,dt\mathrm{d}\Omega.\end{aligned}\tag{B.12}$$

Let ${\boldsymbol{\theta_s}}^{sym}$ denote the symmetric part of $\boldsymbol{\theta_s}$, i.e. ${\boldsymbol{\theta_s}}^{sym}=(\boldsymbol{\theta_s}+{\boldsymbol{\theta_s}}^T)/2$, there results

$$\begin{aligned}\text{Eq.(B.2d)} = &-\delta\int_{\Gamma^{\mathrm{PML}}}\int_0^T\left\{\mathbf{u}\cdot\left({\boldsymbol{\theta_s}}^{sym}\tilde{\Lambda}_p\right)\mathbf{n}\right\}\,dt\mathrm{d}\Gamma\\ &-\delta\int_{\Gamma^{\mathrm{PML}}}\int_0^T\left\{\dot{\mathbf{u}}\cdot\left({\boldsymbol{\theta_s}}^{sym}\tilde{\Lambda}_e\right)\mathbf{n}\right\}\,dt\mathrm{d}\Gamma\\ &+\int_{\Omega^{\mathrm{PML}}}\int_0^T\delta\mathbf{u}\cdot\mathbf{div}\left({\boldsymbol{\theta_s}}^{sym}\tilde{\Lambda}_p\right)\,dt\mathrm{d}\Omega\\ &+\delta\int_{\Omega^{\mathrm{PML}}}\int_0^T\mathbf{div}\left({\boldsymbol{\theta_s}}^{sym}\tilde{\Lambda}_e\right)\cdot\dot{\mathbf{u}}\,dt\mathrm{d}\Omega.\end{aligned}\tag{B.13}$$

Applying integration by parts in time and using the initial condition $\mathbf{u}(\mathbf{x},0)=\mathbf{0}$, we simplify further to

$$\begin{aligned}\text{Eq.(B.2d)} = &\int_{\Gamma^{\mathrm{PML}}}\int_0^T\left\{\delta\mathbf{u}\cdot\left(\dot{\boldsymbol{\theta}}_{\boldsymbol{s}}^{sym}\tilde{\Lambda}_e-{\boldsymbol{\theta_s}}^{sym}\tilde{\Lambda}_p\right)\mathbf{n}\right\}\,dt\mathrm{d}\Gamma\\ &-\int_{\Gamma^{\mathrm{PML}}}\left\{\delta\mathbf{u}(\mathbf{x},T)\cdot\left({\boldsymbol{\theta_s}}^{sym}(\mathbf{x},T)\tilde{\Lambda}_e\right)\mathbf{n}\right\}\,\mathrm{d}\Gamma\\ &+\int_{\Omega^{\mathrm{PML}}}\int_0^T\delta\mathbf{u}\cdot\mathbf{div}\left({\boldsymbol{\theta_s}}^{sym}\tilde{\Lambda}_p-\dot{\boldsymbol{\theta}}_{\boldsymbol{s}}^{sym}\tilde{\Lambda}_e\right)\,dt\mathrm{d}\Omega\\ &+\int_{\Omega^{\mathrm{PML}}}\left\{\delta\mathbf{u}(\mathbf{x},T)\cdot\mathbf{div}\left({\boldsymbol{\theta_s}}^{sym}(\mathbf{x},T)\tilde{\Lambda}_e\right)\right\}\,\mathrm{d}\Omega.\end{aligned}\tag{B.14}$$

Lastly, (B.2e) reads

$$\text{Eq.(B.2e)} = \int_{\Gamma_N^{\mathrm{RD}}} \int_0^T \boldsymbol{\theta_{b1}} \cdot \left[\mu\left(\nabla\delta\mathbf{u} + \nabla\delta\mathbf{u}^T\right) + \lambda \operatorname{div}\delta\mathbf{u}\,\mathcal{I}\right]\mathbf{n}\ dt\mathrm{d}\Gamma \tag{B.15}$$

Now, we can combine all, rearrange, and group the terms, in order to write equation (B.2) as

$$\begin{aligned}
\delta_{\mathbf{u}}\mathcal{L} = & \sum_{j=1}^{N_r} \int_0^T \int_{\Gamma_m} \delta\mathbf{u} \cdot (\mathbf{u} - \mathbf{u}_m)\ \delta(\mathbf{x} - \mathbf{x}_j)\,\mathrm{d}\Gamma_m dt \\
& + \int_{\Omega^{\mathrm{RD}}} \int_0^T \delta\mathbf{u} \cdot \left\{ \mathbf{div}\left[\mu(\nabla\boldsymbol{\theta_{u1}} + \nabla\boldsymbol{\theta_{u1}}^T) + \lambda\ \operatorname{div}\boldsymbol{\theta_{u1}}\,\mathcal{I}\right] - \rho\ddot{\boldsymbol{\theta}}_{\boldsymbol{u1}} \right\}\ dt\mathrm{d}\Omega \\
& + \int_{\Omega^{\mathrm{PML}}} \int_0^T \delta\mathbf{u} \cdot \Big[\mathbf{div}\left(\boldsymbol{\theta_s}^{sym}\tilde{\Lambda}_p - \dot{\boldsymbol{\theta}}_{\boldsymbol{s}}^{sym}\tilde{\Lambda}_e\right) - \rho a\ddot{\boldsymbol{\theta}}_{\boldsymbol{u2}} \\
& \qquad\qquad + \rho b\dot{\boldsymbol{\theta}}_{\boldsymbol{u2}} - \rho c\boldsymbol{\theta_{u2}}\Big] dt\mathrm{d}\Omega \\
& - \int_{\Omega^{\mathrm{RD}}} \left\{ \rho\boldsymbol{\theta_{u1}}(\mathbf{x},T) \cdot \delta\dot{\mathbf{u}}(\mathbf{x},T) - \rho\dot{\boldsymbol{\theta}}_{\boldsymbol{u1}}(\mathbf{x},T) \cdot \delta\mathbf{u}(\mathbf{x},T) \right\}\ \mathrm{d}\Omega \\
& + \int_{\Omega^{\mathrm{PML}}} \Big\{ \mathbf{div}\left(\boldsymbol{\theta_s}^{sym}(\mathbf{x},T)\tilde{\Lambda}_e\right) \cdot \delta\mathbf{u}(\mathbf{x},T) - \rho a\boldsymbol{\theta_{u2}}(\mathbf{x},T) \cdot \delta\dot{\mathbf{u}}(\mathbf{x},T) \\
& \qquad + \rho a\dot{\boldsymbol{\theta}}_{\boldsymbol{u2}}(\mathbf{x},T) \cdot \delta\mathbf{u}(\mathbf{x},T) - \rho b\boldsymbol{\theta_{u2}}(\mathbf{x},T) \cdot \delta\mathbf{u}(\mathbf{x},T)\ \Big\}\ \mathrm{d}\Omega \\
& - \int_{\Gamma^{\mathrm{RD}}} \int_0^T \delta\mathbf{u} \cdot \left\{ \left[\mu(\nabla\boldsymbol{\theta_{u1}} + \nabla\boldsymbol{\theta_{u1}}^T) + \lambda\ \operatorname{div}\boldsymbol{\theta_{u1}}\,\mathcal{I}\right]\mathbf{n} \right\}\ dt\mathrm{d}\Gamma \\
& + \int_{\Gamma_N^{\mathrm{RD}}} \int_0^T \boldsymbol{\theta_{b1}} \cdot \left[\mu\left(\nabla\delta\mathbf{u} + \nabla\delta\mathbf{u}^T\right) + \lambda \operatorname{div}\delta\mathbf{u}\,\mathcal{I}\right]\mathbf{n}\ dt\mathrm{d}\Gamma \\
& + \int_{\Gamma^{\mathrm{RD}}} \int_0^T \boldsymbol{\theta_{u1}} \cdot \left[\mu\left(\nabla\delta\mathbf{u} + \nabla\delta\mathbf{u}^T\right) + \lambda \operatorname{div}\delta\mathbf{u}\,\mathcal{I}\right]\mathbf{n}\ dt\mathrm{d}\Gamma \\
& + \int_{\Gamma^{\mathrm{PML}}} \int_0^T \left\{ \delta\mathbf{u} \cdot \left(\dot{\boldsymbol{\theta}}_{\boldsymbol{s}}^{sym}\tilde{\Lambda}_e - \boldsymbol{\theta_s}^{sym}\tilde{\Lambda}_p\right)\mathbf{n} \right\}\ dt\mathrm{d}\Gamma \\
& - \int_{\Gamma^{\mathrm{PML}}} \left\{ \delta\mathbf{u}(\mathbf{x},T) \cdot \left(\boldsymbol{\theta_s}^{sym}(\mathbf{x},T)\tilde{\Lambda}_e\right)\mathbf{n} \right\}\ \mathrm{d}\Gamma.
\end{aligned} \tag{B.16}$$

By splitting the boundary terms into sub-boundaries ($\Gamma^{\mathrm{RD}} = \Gamma_N^{\mathrm{RD}} \cup \Gamma^{\mathrm{I}}$ and $\Gamma^{\mathrm{PML}} = \Gamma_N^{\mathrm{PML}} \cup \Gamma_D^{\mathrm{PML}} \cup \Gamma^{\mathrm{I}}$), we can simplify further and group the boundary integral terms to arrive at

$$
\begin{aligned}
\delta_{\mathbf{u}}\mathcal{L} = &\int_{\Omega^{\mathrm{RD}}}\int_0^T \delta\mathbf{u}\cdot\left\{\mathbf{div}\left[\mu(\nabla\boldsymbol{\theta}_{\boldsymbol{u1}}+\nabla\boldsymbol{\theta}_{\boldsymbol{u1}}{}^T)+\lambda\ \mathrm{div}\,\boldsymbol{\theta}_{\boldsymbol{u1}}\,\mathcal{I}\right]-\rho\ddot{\boldsymbol{\theta}}_{\boldsymbol{u1}}\right\}\,dt\mathrm{d}\Omega \\
&+\int_{\Omega^{\mathrm{PML}}}\int_0^T \delta\mathbf{u}\cdot[\mathbf{div}\left(\boldsymbol{\theta}_{\boldsymbol{s}}{}^{sym}\tilde{\Lambda}_p-\dot{\boldsymbol{\theta}}_{\boldsymbol{s}}{}^{sym}\tilde{\Lambda}_e\right)-\rho a\ddot{\boldsymbol{\theta}}_{\boldsymbol{u2}} \\
&\qquad\qquad +\rho b\dot{\boldsymbol{\theta}}_{\boldsymbol{u2}}-\rho c\boldsymbol{\theta}_{\boldsymbol{u2}}]dt\mathrm{d}\Omega \\
&-\int_0^T\int_{\Gamma_m}\delta\mathbf{u}\cdot\Big\{\left[\mu(\nabla\boldsymbol{\theta}_{\boldsymbol{u1}}+\nabla\boldsymbol{\theta}_{\boldsymbol{u1}}{}^T)+\lambda\ \mathrm{div}\,\boldsymbol{\theta}_{\boldsymbol{u1}}\,\mathcal{I}\right]\mathbf{n} \\
&\qquad\qquad -\sum_{j=1}^{N_r}(\mathbf{u}-\mathbf{u}_m)\ \delta(\mathbf{x}-\mathbf{x}_j)\Big\}\ \mathrm{d}\Gamma_m dt \\
&+\int_{\Gamma_N^{\mathrm{RD}}}\int_0^T(\boldsymbol{\theta}_{\boldsymbol{b1}}+\boldsymbol{\theta}_{\boldsymbol{u1}})\cdot\left[\mu\left(\nabla\delta\mathbf{u}+\nabla\delta\mathbf{u}^T\right)+\lambda\,\mathrm{div}\,\delta\mathbf{u}\,\mathcal{I}\right]\mathbf{n}\ \ dt\mathrm{d}\Gamma \\
&+\int_{\Gamma_N^{\mathrm{PML}}}\int_0^T\left\{\delta\mathbf{u}\cdot\left(\dot{\boldsymbol{\theta}}_{\boldsymbol{s}}{}^{sym}\tilde{\Lambda}_e-\boldsymbol{\theta}_{\boldsymbol{s}}{}^{sym}\tilde{\Lambda}_p\right)\mathbf{n}\right\}\ dt\mathrm{d}\Gamma \\
&-\int_{\Gamma^{\mathrm{I}}}\int_0^T\delta\mathbf{u}\cdot\Big\{\left[\mu(\nabla\boldsymbol{\theta}_{\boldsymbol{u1}}+\nabla\boldsymbol{\theta}_{\boldsymbol{u1}}{}^T)+\lambda\ \mathrm{div}\,\boldsymbol{\theta}_{\boldsymbol{u1}}\,\mathcal{I}\right]\mathbf{n} \\
&\qquad\qquad -\left(\dot{\boldsymbol{\theta}}_{\boldsymbol{s}}{}^{sym}\tilde{\Lambda}_e-\boldsymbol{\theta}_{\boldsymbol{s}}{}^{sym}\tilde{\Lambda}_p\right)\mathbf{n}\Big\}\ dt\mathrm{d}\Gamma \\
&+\int_{\Gamma^{\mathrm{I}}}\int_0^T\boldsymbol{\theta}_{\boldsymbol{u1}}\cdot\left[\mu\left(\nabla\delta\mathbf{u}+\nabla\delta\mathbf{u}^T\right)+\lambda\,\mathrm{div}\,\delta\mathbf{u}\,\mathcal{I}\right]\mathbf{n}\ \ dt\mathrm{d}\Gamma \\
&-\int_{\Omega^{\mathrm{RD}}}\left\{\rho\boldsymbol{\theta}_{\boldsymbol{u1}}(\mathbf{x},T)\cdot\delta\dot{\mathbf{u}}(\mathbf{x},T)-\rho\dot{\boldsymbol{\theta}}_{\boldsymbol{u1}}(\mathbf{x},T)\cdot\delta\mathbf{u}(\mathbf{x},T)\right\}\ \mathrm{d}\Omega \\
&+\int_{\Omega^{\mathrm{PML}}}\Big\{\mathbf{div}\left(\boldsymbol{\theta}_{\boldsymbol{s}}{}^{sym}(\mathbf{x},T)\tilde{\Lambda}_e\right)\cdot\delta\mathbf{u}(\mathbf{x},T)-\rho a\boldsymbol{\theta}_{\boldsymbol{u2}}(\mathbf{x},T)\cdot\delta\dot{\mathbf{u}}(\mathbf{x},T) \\
&\qquad\qquad +\rho a\dot{\boldsymbol{\theta}}_{\boldsymbol{u2}}(\mathbf{x},T)\cdot\delta\mathbf{u}(\mathbf{x},T)-\rho b\boldsymbol{\theta}_{\boldsymbol{u2}}(\mathbf{x},T)\cdot\delta\mathbf{u}(\mathbf{x},T)\ \Big\}\ \mathrm{d}\Omega \\
&-\int_{\Gamma_N^{\mathrm{PML}}}\left\{\delta\mathbf{u}(\mathbf{x},T)\cdot\left(\boldsymbol{\theta}_{\boldsymbol{s}}{}^{sym}(\mathbf{x},T)\tilde{\Lambda}_e\right)\mathbf{n}\right\}\ \mathrm{d}\Gamma \\
&-\int_{\Gamma_D^{\mathrm{PML}}}\left\{\delta\mathbf{u}(\mathbf{x},T)\cdot\left(\boldsymbol{\theta}_{\boldsymbol{s}}{}^{sym}(\mathbf{x},T)\tilde{\Lambda}_e\right)\mathbf{n}\right\}\ \mathrm{d}\Gamma \\
&-\int_{\Gamma^{\mathrm{I}}}\left\{\delta\mathbf{u}(\mathbf{x},T)\cdot\left(\boldsymbol{\theta}_{\boldsymbol{s}}{}^{sym}(\mathbf{x},T)\tilde{\Lambda}_e\right)\mathbf{n}\right\}\ \mathrm{d}\Gamma.
\end{aligned}
\tag{B.17}
$$

B.2 Derivation of $\delta_{\mathbf{S}}\mathcal{L}$

Next, we calculate the variation of $\mathcal{L}$ with respect to $\mathbf{S}$:

$$\begin{aligned}
\delta_{\mathbf{S}}\mathcal{L} = \delta \int_{\Omega^{\mathrm{PML}}} \int_0^T & \boldsymbol{\theta}_{\boldsymbol{u2}} \cdot \mathbf{div} \left(\dot{\mathbf{S}}^T \tilde{\Lambda}_e + \mathbf{S}^T \tilde{\Lambda}_p \right) \, dt \mathrm{d}\Omega \\
& + \delta \int_{\Omega^{\mathrm{PML}}} \int_0^T \boldsymbol{\theta}_{\boldsymbol{s}} : \left\{ \left(\mathcal{D} : a\ddot{\mathbf{S}} \right) + \left(\mathcal{D} : b\dot{\mathbf{S}} \right) + \left(\mathcal{D} : c\mathbf{S} \right) \right\} \, dt \mathrm{d}\Omega \\
& + \delta \int_{\Gamma_N^{\mathrm{PML}}} \int_0^T \boldsymbol{\theta}_{\boldsymbol{b2}} \cdot \left[\left(\dot{\mathbf{S}}^T \tilde{\Lambda}_e + \mathbf{S}^T \tilde{\Lambda}_p \right) \mathbf{n} \right] \, dt \mathrm{d}\Gamma. \qquad \text{(B.18)}
\end{aligned}$$

By using the divergence identity, applying Gauss divergence theorem for vectors, and also shifting the time derivatives of $\mathbf{S}$ over $\boldsymbol{\theta}_{\boldsymbol{s}}$ by using Green's identity, we obtain

$$\begin{aligned}
\delta_{\mathbf{S}}\mathcal{L} = \delta \int_{\Gamma^{\mathrm{PML}}} \int_0^T & \left[\left(\dot{\mathbf{S}}^T \tilde{\Lambda}_e + \mathbf{S}^T \tilde{\Lambda}_p \right)^T \boldsymbol{\theta}_{\boldsymbol{u2}} \right] \cdot \mathbf{n} \, dt \mathrm{d}\Gamma \\
& - \delta \int_{\Omega^{\mathrm{PML}}} \int_0^T \nabla \boldsymbol{\theta}_{\boldsymbol{u2}} : \mathbf{S}^T \tilde{\Lambda}_p \, dt \mathrm{d}\Omega \\
& - \delta \int_{\Omega^{\mathrm{PML}}} \left\{ \left[\nabla \boldsymbol{\theta}_{\boldsymbol{u2}} : \mathbf{S}^T \tilde{\Lambda}_e \right] \Big|_0^T - \int_0^T \nabla \dot{\boldsymbol{\theta}}_{\boldsymbol{u2}} : \mathbf{S}^T \tilde{\Lambda}_e \, dt \right\} \mathrm{d}\Omega \\
& + \delta \int_{\Omega^{\mathrm{PML}}} \left\{ \left[\boldsymbol{\theta}_{\boldsymbol{s}} : \left(\mathcal{D} : a\dot{\mathbf{S}} \right) \right] \Big|_0^T - \int_0^T \dot{\boldsymbol{\theta}}_{\boldsymbol{s}} : \left(\mathcal{D} : a\dot{\mathbf{S}} \right) \, dt \right\} \mathrm{d}\Omega \\
& + \delta \int_{\Omega^{\mathrm{PML}}} \left\{ \left[\boldsymbol{\theta}_{\boldsymbol{s}} : \left(\mathcal{D} : b\mathbf{S} \right) \right] \Big|_0^T - \int_0^T \dot{\boldsymbol{\theta}}_{\boldsymbol{s}} : \left(\mathcal{D} : b\mathbf{S} \right) \, dt \right\} \mathrm{d}\Omega \\
& + \delta \int_{\Omega^{\mathrm{PML}}} \int_0^T \boldsymbol{\theta}_{\boldsymbol{s}} : \left(\mathcal{D} : c\mathbf{S} \right) \, dt \mathrm{d}\Omega \\
& + \delta \int_{\Gamma_N^{\mathrm{PML}}} \int_0^T \boldsymbol{\theta}_{\boldsymbol{b2}} \cdot \left[\left(\dot{\mathbf{S}}^T \tilde{\Lambda}_e + \mathbf{S}^T \tilde{\Lambda}_p \right) \mathbf{n} \right] \, dt \mathrm{d}\Gamma \qquad \text{(B.19)}
\end{aligned}$$

Next, we make use of tensor transpose and tensor inner product identities. Moreover, we split Γ^{PML} into its three boundary components Γ_D^{PML}, Γ_N^{PML}, and

Γ^{I}. Rearranging and grouping terms result in

$$
\begin{aligned}
\delta_{\mathbf{S}}\mathcal{L} = & \int_{\Gamma_D^{\mathrm{PML}}} \int_0^T \boldsymbol{\theta_{u2}} \cdot \left(\delta\dot{\mathbf{S}}^T \tilde{\Lambda}_e + \delta\mathbf{S}^T \tilde{\Lambda}_p \right) \mathbf{n} \, dt \mathrm{d}\Gamma \\
& + \int_{\Gamma_N^{\mathrm{PML}}} \int_0^T \left(\boldsymbol{\theta_{u2}} + \boldsymbol{\theta_{b2}} \right) \cdot \left(\delta\dot{\mathbf{S}}^T \tilde{\Lambda}_e + \delta\mathbf{S}^T \tilde{\Lambda}_p \right) \mathbf{n} \, dt \mathrm{d}\Gamma \\
& + \int_{\Gamma^{\mathrm{I}}} \int_0^T \boldsymbol{\theta_{u2}} \cdot \left(\delta\dot{\mathbf{S}}^T \tilde{\Lambda}_e + \delta\mathbf{S}^T \tilde{\Lambda}_p \right) \mathbf{n} \, dt \mathrm{d}\Gamma \\
& - \int_{\Omega^{\mathrm{PML}}} \int_0^T \delta\mathbf{S} : \left[\tilde{\Lambda}_p \left(\nabla \boldsymbol{\theta_{u2}} \right)^T - \tilde{\Lambda}_e \left(\nabla \dot{\boldsymbol{\theta_{u2}}} \right)^T \right] \, dt \mathrm{d}\Omega \\
& + \delta \int_{\Omega^{\mathrm{PML}}} \left\{ \left[\, \boldsymbol{\theta_s} : \left(\mathcal{D} : a\dot{\mathbf{S}} \right) \right] \big|_0^T + \left[\, \boldsymbol{\theta_s} : \left(\mathcal{D} : b\mathbf{S} \right) \right] \big|_0^T \right. \\
& \qquad \left. - \left[\, \dot{\boldsymbol{\theta}}_{\boldsymbol{s}} : \left(\mathcal{D} : a\mathbf{S} \right) \right] \big|_0^T - \left[\, \nabla \boldsymbol{\theta_{u2}} : \mathbf{S}^T \tilde{\Lambda}_e \right] \big|_0^T \right\} \, \mathrm{d}\Omega \\
& + \delta \int_{\Omega^{\mathrm{PML}}} \int_0^T \ddot{\boldsymbol{\theta}}_{\boldsymbol{s}} : \left(\mathcal{D} : a\mathbf{S} \right) \, dt \mathrm{d}\Omega - \delta \int_{\Omega^{\mathrm{PML}}} \int_0^T \dot{\boldsymbol{\theta}}_{\boldsymbol{s}} : \left(\mathcal{D} : b\mathbf{S} \right) \, dt \mathrm{d}\Omega \\
& + \delta \int_{\Omega^{\mathrm{PML}}} \int_0^T \boldsymbol{\theta_s} : \left(\mathcal{D} : c\mathbf{S} \right) \, dt \mathrm{d}\Omega. \qquad \text{(B.20)}
\end{aligned}
$$

Using the commutative and associative properties of inner product, the definition of compliance tensor[6], and trace identity[7], one obtains

$$
\begin{aligned}
\delta_{\mathbf{S}}\mathcal{L} = & \int_{\Gamma_D^{\mathrm{PML}}} \int_0^T \boldsymbol{\theta}_{\boldsymbol{u2}} \cdot \left(\delta \dot{\mathbf{S}}^T \tilde{\Lambda}_e + \delta \mathbf{S}^T \tilde{\Lambda}_p \right) \mathbf{n} \, dt \mathrm{d}\Gamma \\
& + \int_{\Gamma_N^{\mathrm{PML}}} \int_0^T \left(\boldsymbol{\theta}_{\boldsymbol{u2}} + \boldsymbol{\theta}_{\boldsymbol{b2}} \right) \cdot \left(\delta \dot{\mathbf{S}}^T \tilde{\Lambda}_e + \delta \mathbf{S}^T \tilde{\Lambda}_p \right) \mathbf{n} \, dt \mathrm{d}\Gamma \\
& + \int_{\Gamma^{\mathrm{I}}} \int_0^T \boldsymbol{\theta}_{\boldsymbol{u2}} \cdot \left(\delta \dot{\mathbf{S}}^T \tilde{\Lambda}_e + \delta \mathbf{S}^T \tilde{\Lambda}_p \right) \mathbf{n} \, dt \mathrm{d}\Gamma \\
& + \delta \int_{\Omega^{\mathrm{PML}}} \left\{ \left[\boldsymbol{\theta}_{\boldsymbol{s}} : \left(\mathcal{D} : a \dot{\mathbf{S}} \right) \right] \Big|_0^T + \left[\, \boldsymbol{\theta}_{\boldsymbol{s}} : \left(\mathcal{D} : b \mathbf{S} \right) \right] \Big|_0^T \right. \\
& \qquad \left. - \left[\dot{\boldsymbol{\theta}}_{\boldsymbol{s}} : \left(\mathcal{D} : a \mathbf{S} \right) \right] \Big|_0^T - \left[\nabla \boldsymbol{\theta}_{\boldsymbol{u2}} : \mathbf{S}^T \tilde{\Lambda}_e \right] \Big|_0^T \right\} \mathrm{d}\Omega \\
& + \int_{\Omega^{\mathrm{PML}}} \int_0^T \delta \mathbf{S} : \left[\mathcal{D} : \left(a \ddot{\boldsymbol{\theta}}_{\boldsymbol{s}} - b \dot{\boldsymbol{\theta}}_{\boldsymbol{s}} + c \boldsymbol{\theta}_{\boldsymbol{s}} \right) \right. \\
& \qquad \left. - \tilde{\Lambda}_p \left(\nabla \boldsymbol{\theta}_{\boldsymbol{u2}} \right)^T + \tilde{\Lambda}_e \left(\nabla \dot{\boldsymbol{\theta}}_{\boldsymbol{u2}} \right)^T \right] \, dt \mathrm{d}\Omega.
\end{aligned}
\tag{B.21}
$$

---

[6] $\mathcal{D} : \mathbf{S} = \frac{1}{2\mu}\mathbf{S} - \frac{\lambda}{4\mu(\lambda+\mu)} \left(\mathcal{I} : \mathbf{S} \right) \mathcal{I}$ where the spatial dependence of λ and μ is omitted for notational clarity

[7] $\mathcal{A} : (\mathcal{I} : \mathcal{B}) \mathcal{I} = \mathcal{B} : (\mathcal{I} : \mathcal{A}) \mathcal{I}$

We impose the initial conditions $\mathbf{S}(\mathbf{x},0)=\mathbf{0}$, $\dot{\mathbf{S}}(\mathbf{x},0)=\mathbf{0}$ and the previous expression simplifies to

$$\begin{aligned}
\delta_{\mathbf{S}}\mathcal{L} = &\int_{\Gamma_D^{\mathrm{PML}}}\int_0^T \boldsymbol{\theta_{u2}}\cdot\left(\delta\dot{\mathbf{S}}^T\tilde{\Lambda}_e+\delta\mathbf{S}^T\tilde{\Lambda}_p\right)\mathbf{n}\,dt\mathrm{d}\Gamma \\
&+\int_{\Gamma_N^{\mathrm{PML}}}\int_0^T (\boldsymbol{\theta_{u2}}+\boldsymbol{\theta_{b2}})\cdot\left(\delta\dot{\mathbf{S}}^T\tilde{\Lambda}_e+\delta\mathbf{S}^T\tilde{\Lambda}_p\right)\mathbf{n}\,dt\mathrm{d}\Gamma \\
&+\int_{\Gamma^{\mathrm{I}}}\int_0^T \boldsymbol{\theta_{u2}}\cdot\left(\delta\dot{\mathbf{S}}^T\tilde{\Lambda}_e+\delta\mathbf{S}^T\tilde{\Lambda}_p\right)\mathbf{n}\,dt\mathrm{d}\Gamma \\
&+\int_{\Omega^{\mathrm{PML}}}\Big\{\boldsymbol{\theta_s}(\mathbf{x},T):\left[\mathcal{D}:a\delta\dot{\mathbf{S}}(\mathbf{x},T)\right]+\boldsymbol{\theta_s}(\mathbf{x},T):\left[\mathcal{D}:b\delta\mathbf{S}(\mathbf{x},T)\right] \\
&\qquad -\dot{\boldsymbol{\theta}}_{\boldsymbol{s}}(\mathbf{x},T):\left[\mathcal{D}:a\delta\mathbf{S}(\mathbf{x},T)\right]-\nabla\boldsymbol{\theta_{u2}}(\mathbf{x},T):\delta\mathbf{S}(\mathbf{x},T)^T\tilde{\Lambda}_e\Big\}\,\mathrm{d}\Omega \\
&+\int_{\Omega^{\mathrm{PML}}}\int_0^T \delta\mathbf{S}:\Big[\mathcal{D}:\left(a\ddot{\boldsymbol{\theta}}_{\boldsymbol{s}}-b\dot{\boldsymbol{\theta}}_{\boldsymbol{s}}+c\boldsymbol{\theta_s}\right) \\
&\qquad -\tilde{\Lambda}_p\left(\nabla\boldsymbol{\theta_{u2}}\right)^T+\tilde{\Lambda}_e\left(\nabla\dot{\boldsymbol{\theta}}_{\boldsymbol{u2}}\right)^T\Big]\,dt\mathrm{d}\Omega.
\end{aligned} \tag{B.22}$$

Next, we combine (B.17) and (B.22) in order to obtain $\delta_{\mathbf{u}}\mathcal{L}+\delta_{\mathbf{S}}\mathcal{L}=0$. Since the variations of the state variables ($\delta\mathbf{u}$ and $\delta\mathbf{S}$) are arbitrary, the terms they multiply have to vanish identically. There results the *adjoint problem*[8]

$$\mathbf{div}\left[\mu(\nabla\boldsymbol{\theta_{u1}}+\nabla\boldsymbol{\theta_{u1}}^T)+\lambda\,\mathrm{div}\,\boldsymbol{\theta_{u1}}\,\mathcal{I}\right]=\rho\ddot{\boldsymbol{\theta}}_{\boldsymbol{u1}} \quad \text{on } \Omega^{\mathrm{RD}}\times\mathsf{J} \tag{B.23a}$$

$$\mathbf{div}\left(-\dot{\boldsymbol{\theta}}_{\boldsymbol{s}}\tilde{\Lambda}_e+\boldsymbol{\theta_s}\tilde{\Lambda}_p\right)=\rho\left(a\ddot{\boldsymbol{\theta}}_{\boldsymbol{u2}}-b\dot{\boldsymbol{\theta}}_{\boldsymbol{u2}}+c\boldsymbol{\theta_{u2}}\right) \quad \text{on } \Omega^{\mathrm{PML}}\times\mathsf{J} \tag{B.23b}$$

$$\mathcal{D}:\left(a\ddot{\boldsymbol{\theta}}_{\boldsymbol{s}}-b\dot{\boldsymbol{\theta}}_{\boldsymbol{s}}+c\boldsymbol{\theta_s}\right)=-\tilde{\Lambda}_e\left(\nabla\dot{\boldsymbol{\theta}}_{\boldsymbol{u2}}\right)^T+\tilde{\Lambda}_p\left(\nabla\boldsymbol{\theta_{u2}}\right)^T \quad \text{on } \Omega^{\mathrm{PML}}\times\mathsf{J} \tag{B.23c}$$

---

[8] The symmetry of the stress tensor enforces the symmetry of $\boldsymbol{\theta_s}$ ($\boldsymbol{\theta_s}^{sym}=\boldsymbol{\theta_s}$).

subject to

$$\left\{\mu(\nabla\boldsymbol{\theta}_{\boldsymbol{u1}} + \nabla{\boldsymbol{\theta}_{\boldsymbol{u1}}}^T) + \lambda \ \operatorname{div}\boldsymbol{\theta}_{\boldsymbol{u1}}\,\mathcal{I}\right\}\mathbf{n} = \sum_{j=1}^{N_r}(\mathbf{u}-\mathbf{u}_m)\,\delta(\mathbf{x}-\mathbf{x}_j) \quad \text{on } \Gamma_m \times \mathsf{J} \tag{B.24a}$$

$$\left(-\dot{\boldsymbol{\theta}}_{\boldsymbol{s}}\tilde{\Lambda}_e + \boldsymbol{\theta}_{\boldsymbol{s}}\tilde{\Lambda}_p\right)\mathbf{n} = \mathbf{0} \qquad \text{on } \Gamma_N^{\mathrm{PML}} \times \mathsf{J} \tag{B.24b}$$

$$\boldsymbol{\theta}_{\boldsymbol{u2}} = \mathbf{0} \qquad \text{on } \Gamma_D^{\mathrm{PML}} \times \mathsf{J} \tag{B.24c}$$

$$\boldsymbol{\theta}_{\boldsymbol{u1}} = \boldsymbol{\theta}_{\boldsymbol{u2}} \qquad \text{on } \Gamma^{\mathrm{I}} \times \mathsf{J} \tag{B.24d}$$

$$\left\{\mu(\nabla\boldsymbol{\theta}_{\boldsymbol{u1}} + \nabla{\boldsymbol{\theta}_{\boldsymbol{u1}}}^T) + \lambda \ \operatorname{div}\boldsymbol{\theta}_{\boldsymbol{u1}}\,\mathcal{I}\right\}\mathbf{n} = -\left(-\dot{\boldsymbol{\theta}}_{\boldsymbol{s}}\tilde{\Lambda}_e + \boldsymbol{\theta}_{\boldsymbol{s}}\tilde{\Lambda}_p\right)\mathbf{n} \quad \text{on } \Gamma^{\mathrm{I}} \times \mathsf{J} \tag{B.24e}$$

$$\boldsymbol{\theta}_{\boldsymbol{u1}}(\mathbf{x},T) = \mathbf{0}, \qquad \dot{\boldsymbol{\theta}}_{\boldsymbol{u1}}(\mathbf{x},T) = \mathbf{0} \qquad \text{on } \Omega^{\mathrm{RD}} \tag{B.24f}$$

$$\boldsymbol{\theta}_{\boldsymbol{u2}}(\mathbf{x},T) = \mathbf{0}, \qquad \dot{\boldsymbol{\theta}}_{\boldsymbol{u2}}(\mathbf{x},T) = \mathbf{0} \qquad \text{on } \Omega^{\mathrm{PML}} \tag{B.24g}$$

$$\boldsymbol{\theta}_{\boldsymbol{s}}(\mathbf{x},T) = \mathbf{0}, \qquad \dot{\boldsymbol{\theta}}_{\boldsymbol{s}}(\mathbf{x},T) = \mathbf{0} \qquad \text{on } \Omega^{\mathrm{PML}} \tag{B.24h}$$

while

$$\boldsymbol{\theta}_{\boldsymbol{b1}} = -\boldsymbol{\theta}_{\boldsymbol{u1}} \qquad \text{on } \Gamma_N^{\mathrm{RD}} \times \mathsf{J} \tag{B.25a}$$

$$\boldsymbol{\theta}_{\boldsymbol{b2}} = -\boldsymbol{\theta}_{\boldsymbol{u2}} \qquad \text{on } \Gamma_N^{\mathrm{PML}} \times \mathsf{J}. \tag{B.25b}$$

Appendix C

On the 3^{rd} optimality condition

The variation of $\mathcal{L}$ with respect to the Lamé parameters results in two control problems. Depending on the imposed regularization scheme, the resulting control problems differ. Here, we provide the details on the derivation of the λ- and μ-control problems.

C.1 TN regularization case

C.1.1 λ-control problem

We take variation of $\mathcal{L}$ with respect to λ over the interior domain only since the Lamé parameters at the interface nodes are extended into the PML without any variation along the direction of projection. Starting with

$$\begin{aligned}\delta_\lambda \mathcal{L} = \frac{R_\lambda}{2}\, \delta \int_{\Omega^{\text{RD}}} \nabla\lambda \cdot \nabla\lambda \;\mathrm{d}\Omega \\ + \delta \int_{\Omega^{\text{RD}}} \int_0^T \boldsymbol{\theta_{u1}} \cdot \mathbf{div}\left(\lambda \operatorname{div} \mathbf{u}\, \mathcal{I}\right)\; dt \mathrm{d}\Omega \\ + \delta \int_{\Gamma_N^{\text{RD}}} \int_0^T \boldsymbol{\theta_{b1}} \cdot \left(\lambda \operatorname{div} \mathbf{u}\, \mathcal{I}\right) \mathbf{n}\;\, dt \mathrm{d}\Gamma,\end{aligned} \tag{C.1}$$

and using the divergence identity and the definition of trace, we obtain

$$\begin{aligned}\delta_\lambda \mathcal{L} &= R_\lambda \int_{\Omega^{\mathrm{RD}}} \nabla\delta\lambda \cdot \nabla\lambda \,\mathrm{d}\Omega \\ &\quad + \delta \int_{\Gamma^{\mathrm{RD}}} \int_0^T (\lambda \operatorname{div} \mathbf{u}\, \mathcal{I})\mathbf{n} \cdot \boldsymbol{\theta}_{\boldsymbol{u1}} \, dt\mathrm{d}\Gamma - \delta \int_{\Omega^{\mathrm{RD}}} \int_0^T \nabla\boldsymbol{\theta}_{\boldsymbol{u1}} : (\lambda \operatorname{div} \mathbf{u}\, \mathcal{I}) \; dt\mathrm{d}\Omega \\ &\quad + \int_{\Gamma_N^{\mathrm{RD}}} \int_0^T \boldsymbol{\theta}_{\boldsymbol{b1}} \cdot (\delta\lambda \operatorname{div} \mathbf{u}\, \mathcal{I})\, \mathbf{n} \; dt\mathrm{d}\Gamma. \end{aligned} \tag{C.2}$$

After applying integration by parts to the first term and decomposing Γ^{RD} into $\Gamma_N^{\mathrm{RD}} \cup \Gamma^{\mathrm{I}}$, we obtain

$$\begin{aligned}\delta_\lambda \mathcal{L} &= R_\lambda \int_{\Gamma^{\mathrm{RD}}} \delta\lambda\nabla\lambda \cdot \mathbf{n} \,\mathrm{d}\Gamma - R_\lambda \int_{\Omega^{\mathrm{RD}}} \delta\lambda\Delta\lambda \,\mathrm{d}\Omega \\ &\quad + \delta \int_{\Gamma^{\mathrm{I}}} \int_0^T (\lambda \operatorname{div} \mathbf{u}\, \mathcal{I})\mathbf{n} \cdot \boldsymbol{\theta}_{\boldsymbol{u1}} \, dt\mathrm{d}\Gamma + \delta \int_{\Gamma_N^{\mathrm{RD}}} \int_0^T (\lambda \operatorname{div} \mathbf{u}\, \mathcal{I})\mathbf{n} \cdot \boldsymbol{\theta}_{\boldsymbol{u1}} \, dt\mathrm{d}\Gamma \\ &\quad - \int_{\Omega^{\mathrm{RD}}} \int_0^T \delta\lambda(\operatorname{div} \boldsymbol{\theta}_{\boldsymbol{u1}})(\operatorname{div} \mathbf{u}) \, dt\mathrm{d}\Omega \\ &\quad + \int_{\Gamma_N^{\mathrm{RD}}} \int_0^T \boldsymbol{\theta}_{\boldsymbol{b1}} \cdot (\delta\lambda \operatorname{div} \mathbf{u}\, \mathcal{I})\, \mathbf{n} \; dt\mathrm{d}\Gamma. \end{aligned} \tag{C.3}$$

We impose $\boldsymbol{\theta}_{\boldsymbol{b1}} = -\boldsymbol{\theta}_{\boldsymbol{u1}}$ on Γ_N^{RD} (see Appendix B) to arrive at

$$\begin{aligned}\delta_\lambda \mathcal{L} &= -R_\lambda \int_{\Omega^{\mathrm{RD}}} \delta\lambda\Delta\lambda \,\mathrm{d}\Omega - \int_{\Omega^{\mathrm{RD}}} \int_0^T \delta\lambda(\operatorname{div} \boldsymbol{\theta}_{\boldsymbol{u1}})(\operatorname{div} \mathbf{u}) \, dt\mathrm{d}\Omega \\ &\quad + R_\lambda \int_{\Gamma_N^{\mathrm{RD}}} \delta\lambda\nabla\lambda \cdot \mathbf{n} \,\mathrm{d}\Gamma + R_\lambda \int_{\Gamma^{\mathrm{I}}} \delta\lambda\nabla\lambda \cdot \mathbf{n} \,\mathrm{d}\Gamma \\ &\quad + \int_{\Gamma^{\mathrm{I}}} \int_0^T \boldsymbol{\theta}_{\boldsymbol{u1}} \cdot (\delta\lambda \operatorname{div} \mathbf{u})\mathbf{n} \, dt\mathrm{d}\Gamma. \end{aligned} \tag{C.4}$$

Since the variation of $\delta\lambda$ is arbitrary, the terms it multiplies vanish identically. There results the λ-*control problem*:

$$\begin{aligned} -R_\lambda \Delta\lambda - \int_0^T (\operatorname{div} \boldsymbol{\theta_{u1}})(\operatorname{div} \mathbf{u})\, dt &= 0 && \text{in } \Omega^{\mathrm{RD}}, && \text{(C.5a)} \\ \int_{\Gamma_N^{\mathrm{RD}}} \nabla\lambda \cdot \mathbf{n}\, \mathrm{d}\Gamma &= 0 && \text{on } \Gamma_N^{\mathrm{RD}}, && \text{(C.5b)} \\ R_\lambda \nabla\lambda \cdot \mathbf{n} &= -\int_0^T \boldsymbol{\theta_{u1}} \cdot (\operatorname{div} \mathbf{u})\mathbf{n}\, dt && \text{on } \Gamma^{\mathrm{I}}. && \text{(C.5c)} \end{aligned}$$

C.1.2 μ-control problem

Similarly, we take variation of $\mathcal{L}$ with respect to μ over the interior domain only. Starting with

$$\begin{aligned} \delta_\mu \mathcal{L} = {} & \frac{R_\mu}{2}\, \delta \int_{\Omega^{\mathrm{RD}}} \nabla\mu \cdot \nabla\mu \ \mathrm{d}\Omega \\ & + \delta \int_{\Omega^{\mathrm{RD}}} \int_0^T \boldsymbol{\theta_{u1}} \cdot \mathbf{div} \left[\mu \left(\nabla\mathbf{u} + \nabla\mathbf{u}^T\right)\right] \ dt\mathrm{d}\Omega \\ & + \delta \int_{\Gamma_N^{\mathrm{RD}}} \int_0^T \boldsymbol{\theta_{b1}} \cdot \left[\mu \left(\nabla\mathbf{u} + \nabla\mathbf{u}^T\right)\right] \mathbf{n} \ dt\mathrm{d}\Gamma, \end{aligned} \tag{C.6}$$

and using the divergence identity and the definition of trace, we obtain

$$\begin{aligned} \delta_\mu \mathcal{L} = {} & R_\mu \int_{\Omega^{\mathrm{RD}}} \nabla\delta\mu \cdot \nabla\mu\, \mathrm{d}\Omega \\ & + \delta \int_{\Gamma^{\mathrm{RD}}} \int_0^T \left[\mu \left(\nabla\mathbf{u} + \nabla\mathbf{u}^T\right)\right] \mathbf{n} \cdot \boldsymbol{\theta_{u1}}\, dt\mathrm{d}\Gamma \\ & - \delta \int_{\Omega^{\mathrm{RD}}} \int_0^T \nabla\boldsymbol{\theta_{u1}} : \left[\mu \left(\nabla\mathbf{u} + \nabla\mathbf{u}^T\right)\right] \ dt\mathrm{d}\Omega \\ & + \int_{\Gamma_N^{\mathrm{RD}}} \int_0^T \boldsymbol{\theta_{b1}} \cdot \left[\delta\mu \left(\nabla\mathbf{u} + \nabla\mathbf{u}^T\right)\right] \mathbf{n} \ dt\mathrm{d}\Gamma. \end{aligned} \tag{C.7}$$

After applying integration by parts to the first term and decomposing Γ^{RD} into $\Gamma_N^{\mathrm{RD}} \cup \Gamma^{\mathrm{I}}$, we obtain

$$\begin{aligned}
\delta_\mu \mathcal{L} = R_\mu \int_{\Gamma^{\mathrm{RD}}} \delta\mu \nabla\mu \cdot \mathbf{n} \, \mathrm{d}\Gamma - R_\mu \int_{\Omega^{\mathrm{RD}}} \delta\mu \Delta\mu \, \mathrm{d}\Omega& \\
+ \delta \int_{\Gamma^{\mathrm{I}}} \int_0^T \left[\mu\left(\nabla\mathbf{u} + \nabla\mathbf{u}^T\right)\right] \mathbf{n} \cdot \boldsymbol{\theta}_{\boldsymbol{u}\mathbf{1}} \, dt \mathrm{d}\Gamma& \\
+ \delta \int_{\Gamma_N^{\mathrm{RD}}} \int_0^T \left[\mu\left(\nabla\mathbf{u} + \nabla\mathbf{u}^T\right)\right] \mathbf{n} \cdot \boldsymbol{\theta}_{\boldsymbol{u}\mathbf{1}} \, dt \mathrm{d}\Gamma& \\
- \int_{\Omega^{\mathrm{RD}}} \int_0^T \nabla\boldsymbol{\theta}_{\boldsymbol{u}\mathbf{1}} : \left[\delta\mu\left(\nabla\mathbf{u} + \nabla\mathbf{u}^T\right)\right] \, dt \mathrm{d}\Omega& \\
+ \int_{\Gamma_N^{\mathrm{RD}}} \int_0^T \boldsymbol{\theta}_{\boldsymbol{b}\mathbf{1}} \cdot \left[\delta\mu\left(\nabla\mathbf{u} + \nabla\mathbf{u}^T\right)\right] \mathbf{n} \, dt \mathrm{d}\Gamma.& \qquad \text{(C.8)}
\end{aligned}$$

We impose $\boldsymbol{\theta}_{\boldsymbol{b}\mathbf{1}} = -\boldsymbol{\theta}_{\boldsymbol{u}\mathbf{1}}$ on Γ_N^{RD} (see Appendix B) to arrive at

$$\begin{aligned}
\delta_\mu \mathcal{L} = -R_\mu \int_{\Omega^{\mathrm{RD}}} \delta\mu \Delta\mu \, \mathrm{d}\Omega - \int_{\Omega^{\mathrm{RD}}} \int_0^T \nabla\boldsymbol{\theta}_{\boldsymbol{u}\mathbf{1}} : \left[\delta\mu\left(\nabla\mathbf{u} + \nabla\mathbf{u}^T\right)\right] \, dt \mathrm{d}\Omega& \\
+ R_\mu \int_{\Gamma_N^{\mathrm{RD}}} \delta\mu \nabla\mu \cdot \mathbf{n} \, \mathrm{d}\Gamma + R_\mu \int_{\Gamma^{\mathrm{I}}} \delta\mu \nabla\mu \cdot \mathbf{n} \, \mathrm{d}\Gamma& \\
+ \int_{\Gamma^{\mathrm{I}}} \int_0^T \left[\delta\mu\left(\nabla\mathbf{u} + \nabla\mathbf{u}^T\right)\right] \mathbf{n} \cdot \boldsymbol{\theta}_{\boldsymbol{u}\mathbf{1}} \, dt \mathrm{d}\Gamma.& \qquad \text{(C.9)}
\end{aligned}$$

Since the variation of $\delta\mu$ is arbitrary, the terms it multiplies vanish identically. There results the *μ-control problem*:

$$- R_\mu \Delta\mu - \int_0^T \nabla\boldsymbol{\theta}_{\boldsymbol{u}\mathbf{1}} : \left(\nabla\mathbf{u} + \nabla\mathbf{u}^T\right) \, dt = 0 \qquad \text{in } \Omega^{\mathrm{RD}}, \qquad \text{(C.10a)}$$

$$\int_{\Gamma_N^{\mathrm{RD}}} \nabla\mu \cdot \mathbf{n} \, \mathrm{d}\Gamma = 0 \qquad \text{on } \Gamma_N^{\mathrm{RD}}, \qquad \text{(C.10b)}$$

$$R_\mu \nabla\mu \cdot \mathbf{n} = - \int_0^T \boldsymbol{\theta}_{\boldsymbol{u}\mathbf{1}} \cdot \left(\nabla\mathbf{u} + \nabla\mathbf{u}^T\right) \mathbf{n} \, dt \qquad \text{on } \Gamma^{\mathrm{I}}. \qquad \text{(C.10c)}$$

C.2 TV regularization case

If we replace the TN regularization with the TV regularization in the objective functional, the first terms of (C.1) and (C.6) will be replaced by

$$\frac{R_\lambda}{2}\,\delta\int_{\Omega^{\mathrm{RD}}} \nabla\lambda\cdot\nabla\lambda\;\mathrm{d}\Omega \qquad\rightarrow\qquad R_\lambda\,\delta\int_{\Omega^{\mathrm{RD}}} \left(\nabla\lambda\cdot\nabla\lambda+\epsilon\right)^{\frac{1}{2}}\;\mathrm{d}\Omega, \tag{C.11}$$

$$\frac{R_\mu}{2}\,\delta\int_{\Omega^{\mathrm{RD}}} \nabla\mu\cdot\nabla\mu\;\mathrm{d}\Omega \qquad\rightarrow\qquad R_\mu\,\delta\int_{\Omega^{\mathrm{RD}}} \left(\nabla\mu\cdot\nabla\mu+\epsilon\right)^{\frac{1}{2}}\;\mathrm{d}\Omega, \tag{C.12}$$

respectively. Next, we take variations with respect to λ and μ to obtain

$$R_\lambda\int_{\Omega^{\mathrm{RD}}} \left(\nabla\lambda\cdot\nabla\lambda+\epsilon\right)^{-\frac{1}{2}}\;\left(\nabla\delta\lambda\cdot\nabla\lambda\right)\,\mathrm{d}\Omega, \tag{C.13}$$

$$R_\mu\,\delta\int_{\Omega^{\mathrm{RD}}} \left(\nabla\mu\cdot\nabla\mu+\epsilon\right)^{-\frac{1}{2}}\;\left(\nabla\delta\mu\cdot\nabla\mu\right)\,\mathrm{d}\Omega. \tag{C.14}$$

Applying integration by parts results in

$$\begin{aligned}&R_\lambda\int_{\Gamma^{\mathrm{RD}}} \delta\lambda\;\left(\nabla\lambda\cdot\nabla\lambda+\epsilon\right)^{-\frac{1}{2}}\;\nabla\lambda\cdot\mathbf{n}\,\mathrm{d}\Gamma\\ &\qquad - R_\lambda\int_{\Omega^{\mathrm{RD}}} \delta\lambda\;\nabla\cdot\left[\left(\nabla\lambda\cdot\nabla\lambda+\epsilon\right)^{-\frac{1}{2}}\;\nabla\lambda\right]\,\mathrm{d}\Omega,\end{aligned} \tag{C.15}$$

$$\begin{aligned}&R_\mu\,\delta\int_{\Gamma^{\mathrm{RD}}} \delta\mu\;\left(\nabla\mu\cdot\nabla\mu+\epsilon\right)^{-\frac{1}{2}}\;\nabla\mu\cdot\mathbf{n}\,\mathrm{d}\Gamma\\ &\qquad - R_\mu\int_{\Omega^{\mathrm{RD}}} \delta\mu\;\nabla\cdot\left[\left(\nabla\mu\cdot\nabla\mu+\epsilon\right)^{-\frac{1}{2}}\;\nabla\mu\right]\,\mathrm{d}\Omega.\end{aligned} \tag{C.16}$$

Replacing the first two terms in (C.3) and (C.8) by the above and proceeding accordingly, one can obtain the λ- and μ-control problems associated with the TV regularized least-squares misfit problem.

Appendix D

Adjoint problem semi-discrete form

The global system matrices of the adjoint problem are identical to those derived for the state problem (except for a sign reversal for the damping matrix); their extended form was given in detail in Appendix A. Here, we provided extended forms only for the vectors

$$\mathbf{d}^{\mathrm{ad}} = \left[\boldsymbol{\theta}_{\mathbf{u}}^{xr} \;\; \boldsymbol{\theta}_{\mathbf{u}}^{yr} \,\vdots\, \boldsymbol{\theta}_{\mathbf{u}}^{xi} \;\; \boldsymbol{\theta}_{\mathbf{u}}^{yi} \,\vdots\, \boldsymbol{\theta}_{\mathbf{u}}^{xp} \;\; \boldsymbol{\theta}_{\mathbf{u}}^{yp} \,\vdots\, \boldsymbol{\theta}_{\mathbf{s}}^{xxi} \;\; \boldsymbol{\theta}_{\mathbf{s}}^{yyi} \;\; \boldsymbol{\theta}_{\mathbf{s}}^{xyi} \,\vdots\, \boldsymbol{\theta}_{\mathbf{s}}^{xxp} \;\; \boldsymbol{\theta}_{\mathbf{s}}^{yyp} \;\; \boldsymbol{\theta}_{\mathbf{s}}^{xyp} \right]^T, \tag{D.1a}$$

$$\mathbf{F}^{\mathrm{ad}} = \left[\mathbf{G}_x^r \;\; \mathbf{G}_y^r \,\vdots\, \mathbf{G}_x^i \;\; \mathbf{G}_y^i \,\vdots\, \mathbf{0} \;\; \mathbf{0} \,\vdots\, \mathbf{0} \;\; \mathbf{0} \;\; \mathbf{0} \,\vdots\, \mathbf{0} \;\; \mathbf{0} \;\; \mathbf{0} \right]^T. \tag{D.1b}$$

Moreover, the global load vector submatrix is expressed as:

$$\mathbf{G}_i = \int_{\Gamma_m} \boldsymbol{\Phi} \left[\sum_{j=1}^{N_r} (u_i - u_i^m)\, \delta(\mathbf{x} - \mathbf{x}_j) \right] \mathrm{d}\Gamma_m, \qquad i = x, y. \tag{D.2}$$

Appendix E

Adjoint problem time integration

The obtained semi-discrete form (3.27) is second-order in time, but the time line has been reversed. To resolve the time integration we employ a Newmark-β-like scheme (Algorithm E.1), by, first, making use of the following finite-difference formula describing the evolution of the corresponding quantities

$$\mathbf{d}_{n-1} = \mathbf{d}_n - \Delta\mathrm{t}\ \dot{\mathbf{d}}_n + \left(\frac{1}{2} - \gamma + \beta\right) \Delta\mathrm{t}^2 \ddot{\mathbf{d}}_{n-1} + (\gamma - \beta)\ \Delta\mathrm{t}^2 \ddot{\mathbf{d}}_n, \tag{E.1a}$$

$$\dot{\mathbf{d}}_{n-1} = \dot{\mathbf{d}}_n - (1-\gamma)\,\Delta\mathrm{t}\ \ddot{\mathbf{d}}_{n-1} - \gamma\ \Delta\mathrm{t}\ \ddot{\mathbf{d}}_n, \tag{E.1b}$$

where $\Delta\mathrm{t}$ denotes the time step, and subscripts (n) and $(n-1)$ denote current and previous time step, respectively (β and γ are the usual Newmark-β parameters). For the linear acceleration method, (β, γ) reduce to $(\frac{1}{6}, \frac{1}{2})$, whereas in the case of the constant (average) acceleration method, (β, γ) reduce to $(\frac{1}{4}, \frac{1}{2})$.

Next, after rewriting (3.27) for the $(n-1)$-th time step, and, subsequently, introducing (E.1), there results the following effective system matrix $\{\mathbf{K}^{\mathbf{eff}}\}$, and effective load vector $\{\mathbf{R}^{\mathbf{eff}}\}_{n-1}$

$$\{\mathbf{K}^{\mathbf{eff}}\}\ \ddot{\mathbf{d}}_{n-1} = \{\mathbf{R}^{\mathbf{eff}}\}_{n-1}, \tag{E.2}$$

where

$$\{\mathbf{K}^{\mathbf{eff}}\} = \mathbf{M} + \mathbf{C}(\gamma - 1)\Delta\mathrm{t} + \mathbf{K}\left(\frac{1}{2} - \gamma + \beta\right)\Delta\mathrm{t}^2, \tag{E.3a}$$

$$\begin{aligned}\{\mathbf{R}^{\mathbf{eff}}\}_{n-1} = \mathbf{F}_{n-1} &- \mathbf{C}\left[\dot{\mathbf{d}}_n - \gamma\Delta\mathrm{t}\;\ddot{\mathbf{d}}_n\right] \\ &- \mathbf{K}\left[\mathbf{d}_n - \Delta\mathrm{t}\;\dot{\mathbf{d}}_n + (\gamma - \beta)\,\Delta\mathrm{t}^2\ddot{\mathbf{d}}_n\right].\end{aligned} \tag{E.3b}$$

Equation (E.2) allows for the computation of the second-order terms at every $(n-1)$ time step; lower-order terms for the same time step are then recoverable via (E.1). In the numerical experiments we used the average acceleration scheme.

Algorithm E.1 Time integration with reversed time marching

```
procedure NewmarkRTM($nts$)                          ▷ nts: number of time steps
    Assemble $\mathbf{M}$, $\mathbf{C}$ and $\mathbf{K}$
    Set $\mathbf{d}_f$ and $\dot{\mathbf{d}}_f$                               ▷ final conditions
    Compute $\ddot{\mathbf{d}}_f$                                     ▷ eq. (3.27)
        $\ddot{\mathbf{d}}_f = \mathbf{M}^{-1}\left[\mathbf{F}_f - \mathbf{C}\dot{\mathbf{d}}_f - \mathbf{K}\mathbf{d}_f\right]; n = f + 1$
    Set $\beta$ and $\gamma$                                 ▷ integration parameters
    Assemble $\{\mathbf{K}^{\mathbf{eff}}\}$                                 ▷ eq. (E.3a)
    $n \leftarrow nts$
    while $0 < n$ do                       ▷ integration is complete if $n$ is $nts$
        Assemble $\{\mathbf{R}^{\mathbf{eff}}\}_{n-1}$                           ▷ eq. (E.3b)
        Compute $\ddot{\mathbf{d}}_{n-1}$                                  ▷ eq. (E.2)
        Update $\mathbf{d}_{n-1}$ and $\dot{\mathbf{d}}_{n-1}$                        ▷ eq. (E.1)
        Output $\mathbf{d}_{n-1}$                                     ▷ if desired
        $n \leftarrow n - 1$
    end while
end procedure
```

Bibliography

[1] N. Andrei. Accelerated scaled memoryless BFGS preconditioned conjugate gradient algorithm for unconstrained optimization. *European journal of operational research*, 204(3):410–420, 2010.

[2] D. Appelö and G. Kreiss. A new absorbing layer for elastic waves. *Journal of Computational Physics*, 215:642–660, 2006.

[3] L. Armijo. Minimization of functions having lipschitz continuous first partial derivatives. *Pasific J. Math.*, 16:1–3, 1966.

[4] D. N. Arnold. Mixed finite element methods for elliptic problems. *Computer Methods in Applied Mechanics and Engineering*, 82:281–300, 1990.

[5] D. N. Arnold. Differential complexes and numerical stability. In *International Congress of Mathematicians*, pages 137–157, Beijing, China, August 24 2002. Higher Education Press.

[6] D. N. Arnold and G. Awanou. Rectangular mixed finite elements for elasticity. *Mathematical Models and Methods in Applied Sciences*, 15(9):1417–1429, 2005.

[7] D. N. Arnold, D. Boffi, R. S. Falk, and L. Gastaldi. Finite element approximation on quadrilateral meshes. *Commun. Numer. Meth. Engng.*, 17:805–812, 2001.

[8] D. N. Arnold, F. Brezzi, B. Cockburn, and D. Marini. Discontinuous Galerkin methods for elliptic problems. In B. Cockburn, G. Karniaadakis, and C.-W. Shu, editors, *Discontinuous Galerkin Methods: Theory, Computation and Applications. Lecture Notes in Computational Science and Engineering*, pages 89–101. Springer-Verlag, February 2000.

[9] D. N. Arnold, F. Brezzi, and J. Douglas. PEERS: a new mixed finite element for plane elasticity. *Japan J. Appl. Math*, 1:347–367, 1984.

[10] D. N. Arnold, F. Brezzi, and M. Fortin. A stable finite element for the stokes equations. *Calcolo*, 21:337–344, 1984.

[11] D. N. Arnold, J. Douglas, and C. P. Gupta. A family of higher order mixed finite element methods for plane elasticity. *Numer. Math.*, 45:1–22, 1984.

[12] D. N. Arnold and R. S. Falk. A new mixed formulation for elasticity. *Numer. Math.*, 53:13–30, 1988.

[13] D. N. Arnold, R. S. Falk, and R. Winther. Mixed finite element methods for linear elasticity with weakly imposed symmetry. *Mathematics of Computation*, 76(260):1699–1723, October 2007.

[14] D. N. Arnold and R. Winther. Mixed finite elements for elasticity. *Numer. Math.*, 92:401–419, 2002.

[15] D. N. Arnold and R. Winther. Mixed finite elements for elasticity in the stress-displacement formulation. In Z. Chen, R. Glowinski, and

K. Li, editors, *Current Trends in Scientific Computing, Contemporary Mathematics*, volume 329, pages 33–42. American Mathematical Society, 2003.

[16] A. Bamberger, G. Chavent, and P. Lailly. About the stability of the inverse problem in 1-D wave equation - application to the interpretation of seismic profiles. *Applied Mathematics and Optimization*, 5:1–47, 1979.

[17] U. Basu. Explicit finite element perfectly matched layer for transient three-dimensional elastic waves. *Int. J. Numer. Meth. Engng.*, 77:151–176, 2009.

[18] U. Basu and A. K. Chopra. Perfectly matched layers for time-harmonic elastodynamics of unbounded domains: theory and finite-element implementation. *Computer Methods in Applied Mechanics and Engineering*, 192:1337–1375, 2003.

[19] U. Basu and A. K. Chopra. Perfectly matched layers for transient elastodynamics of unbounded domains. *Int. J. Numer. Meth. Engng.*, 59:1039–1074, 2004.

[20] A. Bayliss and E. Turkel. Radiation boundary conditions for wave-like equations. *Communications on Pure and Applied Mathematics*, 33:707–725, 1980.

[21] E. Bécache, S. Fauqueux, and P. Joly. Stability of perfectly matched layers, group velocities and anisotropic waves. *Journal of Computational*

Physics, 188:399–433, 2003.

[22] E. Bécache, P. Joly, and C. Tsogka. An analysis of new mixed finite elements for the approximation of wave propagation problems. *SIAM Journal on Numerical Analysis*, 37(4):1053–1084, 2000.

[23] E. Bécache, P. Joly, and C. Tsogka. Fictitious domains, mixed finite elements and perfectly matched layers for 2D elastic wave propagation. *J. Comput. Acoust.*, 9(3):1175–1202, September 2001.

[24] E. Bécache, P. Joly, and C. Tsogka. A new family of mixed finite elements for the linear elastodynamic problem. *SIAM Journal on Numerical Analysis*, 39(6):2109–2132, 2002.

[25] E. Bécache, P. G. Petropoulos, and S. D. Gedney. On the long-time behavior of unsplit perfectly matched layers. *IEEE Transactions on Antennas and Propagation*, 52(5):1335–1342, May 2004.

[26] J.-P. Bérenger. A perfectly matched layer for the absorption of electromagnetic waves. *Journal of Computational Physics*, 114:185–200, 1994.

[27] J.-P. Bérenger. Three-dimensional perfectly matched layer for the absorption of electromagnetic waves. *Journal of Computational Physics*, 127:363–379, 1996.

[28] J.-P. Bérenger. Evanescent waves in PML's: origin of the numerical reflection in wave-structure interaction problems. *IEEE Transactions on Antennas and Propagation*, 47(10):1497–1503, October 1999.

[29] J.-P. Bérenger. Application of the CFS PML to the absorption of evanescent waves in waveguides. *IEEE Microwave and Wireless Components Letters*, 12(6):218–220, June 2002.

[30] J.-P. Bérenger. Numerical reflection from FDTD-PMLs: a comparison of the split PML with the unsplit and CFS PMLs. *IEEE Transactions on Antennas and Propagation*, 50(3):258–265, March 2002.

[31] A. J. Brenders and R. G. Pratt. Full waveform tomography for lithospheric imaging: results from a blind test in a realistic crustal model. *Geophysical Journal International*, 168:133–151, 2007.

[32] F. Brezzi. A survey of mixed finite element method. In D.L. Dwoyer, M.Y. Hussaini, and R.G. Voigt, editors, *Finite Elements Theory and Application*, pages 34–49, New York, 1988. Springer-Verlag.

[33] F. Brezzi, J. Douglas, and L. D. Marini. Two families of mixed finite element methods for second order elliptic problems. *Numer. Math.*, 47:217–235, 1985.

[34] F. Brezzi and D. Marini. A survey on mixed finite element approximations. *IEEE Transactions on Magnetics*, 30(5):3547–3551, September 1994.

[35] C. Bunks, F. Saleck, S. Zaleski, and G. Chavent. Multiscale seismic waveform inversion. *Geophysics*, 60:1457–1473, 1995.

[36] G. Chavent and C. A. Jacewitz. Determination of background velocities by multiple migration fitting. *Geophysics*, 60(2):476–490, 1995.

[37] P. Chen, L. Zhao, and T. H. Jordan. Full 3D tomography for the crustal structure of the Los Angeles region. *Bulletin of the Seismological Society of America*, 97:1094–1120, 2007.

[38] Z. Chen. *Finite element methods and their applications.* Springer, New York, 1 edition, 2005.

[39] W. C. Chew, J. M. Jin, and E. Michielssen. Complex coordinate system as a generalized absorbing boundary condition. In *Proc. 13th Annu. Rev. of Prog. Appl. Comp. Electromag.*, pages 909–914, Monterey,CA, 17-21 Mar. 1997. Vol. 2.

[40] W. C. Chew and Q. H. Liu. Perfectly matched layers for elastodynamics: a new absorbing boundary condition. *Journal of Computational Acoustics*, 4(4):341–359, 1996.

[41] W. C. Chew and W. H. Weedon. A 3D perfectly matched medium from modified Maxwell's equations with stretched coordinates. *Micro. Opt. Tech. Lett.*, 7:599–604, 1994.

[42] Y. Choi, D. Min, and C. Shin. Frequency-domain elastic full waveform inversion using the new pseudo-hessian matrix - experience of elastic

marmousi-2 synthetic data. *Bulletin of the Seismological Society of America*, 98(5):2402–2415, 2008.

[43] Y. Choi, C. Shin, D. Min, and T. Ha. Efficient calculation of the steepest descent direction for source-independent seismic waveform inversion: An amplitude approach. *Journal of Computational Physics*, 208:455–468, 2005.

[44] F. Clément, G. Chavent, and S. Gómez. Waveform inversion by MBTT formulation. In *Proceedings of the 3rd International Conference on Mathematical and Numerical Aspects of Wave Propagation*, pages 713–722, Philadelphia, PA, 1995.

[45] G. Cohen and S. Fauqueux. Mixed spectral finite elements for the linear elasticity system in unbounded domains. *SIAM J. Sci. Comput.*, 26(3):864–884, 2005.

[46] F. Collino and P. Monk. The perfectly matched layer in curvilinear coordinates. *SIAM J. Sci. Comput.*, 19(6):2061–2090, November 1998.

[47] F. Collino and P. B. Monk. Optimizing the perfectly matched layer. *Computer Methods in Applied Mechanics and Engineering*, 164:157–171, 1998.

[48] F. Collino and C. Tsogka. Application of the perfectly matched absorbing layer model to the linear elastodynamic problem in anisotropic heterogeneous media. *Geophysics*, 66(1):294–307, February 2001.

[49] D. Correia and J.-M. Jin. On the development of a higher-order PML. *IEEE Transactions on Antennas and Propagation*, 53(12):4157–4163, December 2005.

[50] D. Correia and J.-M. Jin. Performance of regular PML, CFS-PML, and second-order PML for waveguide problems. *Microwave and Optical Technology Letters*, 48(10):2121–2126, October 2006.

[51] Y. Dai and Y. Yuan. A nonlinear conjugate gradient with a strong global convergence properties. *SIAM Journal of optimization*, 10(1):177–182, 1999.

[52] Y. H. Dai. A nonmonotone conjugate gradient algorithm for unconstrained optimization. *J. Syst. Sci. Complex.*, 15:139–145, 2002.

[53] Y. H. Dai and Y. Yuan. A nonlinear conjugate gradient method with a strong global convergence property. *SIAM Journal on Optimization*, 10(1):177–182, 1999.

[54] A. T. de Hoop, R. F. Remis, and P. M. van den Berg. The 3D wave equation and its Cartesian coordinate stretched perfectly matched embedding: A time-domain Green's function performance analysis. *Journal of Computational Physics*, 221:88–105, 2007.

[55] B. Donderici and F. L. Teixeira. Conformal perfectly matched layer for the mixed finite element time-domain method. *IEEE Transactions on Antennas and Propagation*, 56(4):1017–1026, April 2008.

[56] B. Donderici and F. L. Teixeira. Mixed finite-element time-domain method for transient Maxwell equations in doubly dispersive media. *IEEE Transactions on Microwave Theory and Techniques*, 56(1):113–120, January 2008.

[57] F. H. Drossaert and A. Giannopoulos. Complex frequency shifted convolution PML for FDTD modelling of elastic waves. *Wave Motion*, 44(7-8):593–604, August 2007.

[58] F. H. Drossaert and A. Giannopoulos. A nonsplit complex frequency-shifted PML based on recursive integration for FDTD modeling of elastic waves. *Geophysics*, 72(2):T9–T17, March-April 2007.

[59] B. Engquist and A. Majda. Absorbing boundary conditions for the numerical simulation of waves. *Mathematics of Computation*, 31(139):629–651, 1977.

[60] I. Epanomeritakis, V. Akçelik, O. Ghattas, and J. Bielak. A Newton-CG method for large-scale three-dimensional elastic full-waveform seismic inversion. *Inverse Problems*, 24(3):34015–34040, 2008.

[61] I. K. Epanomeritakis. *Identification of elastic basin properties by large-scale inverse earthquake wave propagation*. PhD thesis, Carnegie Mellon University, 2004.

[62] C. Farrell and U. Leonhardt. The perfectly matched layer in numerical simulations of nonlinear and matter waves. *Journal of Optics B:*

Quantum and Semiclassical Optics, 7:1–4, 2005.

[63] G. Festa and S. Nielsen. PML absorbing boundaries. *Bulletin of the Seismological Society of America*, 93(2):891–903, April 2003.

[64] G. Festa and J.-P. Vilotte. The Newmark scheme as velocity-stress time-staggering: an efficient PML implementation for spectral element simulations of elastodynamics. *Geophys. J. Int.*, 161:789–812, 2005.

[65] R. Fletcher. *Practical Methods of Optimization: Unconstrained Optimization*, volume 1. Wiley, New York, 2 edition, 1987.

[66] R. Fletcher and C. Reeves. Function minimization by conjugate gradients. *Comput. J.*, 7(2):149–154, 1964.

[67] L. P. Frasca, T. J. R. Hughes, A. F. D. Loula, and I. Miranda. A new family of stable elements for nearly incompressible elasticity based on a mixed Petrov-Galerkin finite element formulation. *Numer. Math.*, 53:123–141, 1988.

[68] F. Gao, A. Levander, R. G. Pratt, C. A. Zelt, and G.-L. Fradelizio. Waveform tomography at a groundwater contamination site: surface reflection data. *Geophysics*, 72:G45–G55, 2007.

[69] H. Gao and J. Zhang. Implementation of perfectly matched layers in an arbitrary geometrical boundary for elastic wave modelling. *Geophys. J. Int.*, 174:1029–1036, 2008.

[70] S. D. Gedney. An anisotropic perfectly matched layer-absorbing medium for the truncation of FDTD lattices. *IEEE Transactions on Antennas and Propagation*, 44(12):1630–1639, December 1996.

[71] J. C. Gilbert and J. Nocedal. Global convergence properties of conjugate gradient methods for optimization. *SIAM J. Optim.*, 2:21–42, 1992.

[72] D. Givoli and J. B. Keller. A finite element method for large domains. *Computer Methods in Applied Mechanics and Engineering*, 76:41–66, 1989.

[73] D. Givoli and J. B. Keller. Non-reflecting boundary conditions for elastic waves. *Wave Motion*, 12(3):261–279, 1990.

[74] D. Givoli and B. Neta. High-order non-reflecting boundary scheme for time-dependent waves. *Journal of Computational Physics*, 186(1):24–26, 2003.

[75] D. Givoli and S. Vigdergauz. Artificial boundary conditions for 2D problems in geophysics. *Computer Methods in Applied Mechanics and Engineering*, 110:87–101, 1993.

[76] A. A. Goldstein. *Constructive Real Analysis.* Harper & Row, New York, 2 edition, 1967.

[77] W. W. Hager and H. Zhang. A new conjugate gradient method with guaranteed descent and an efficient line search. *SIAM J. Optimization*, 16(1):170–192, 2005.

[78] W. W. Hager and H. Zhang. A survey of nonlinear conjugate gradient methods. *Pacific journal of Optimization*, 2(1):35–58, 2006.

[79] P. Hansen and D. O'Leary. The use of the L-curve in the regularization of discrete ill-posed problems. *SIAM Journal on Scientific Computing*, 14(6):1487–1503, 1993.

[80] I. Harari and U. Albocher. Studies of FE/PML for exterior problems of time-harmonic elastic waves. *Computer Methods in Applied Mechanics and Engineering*, 195:3854–3879, 2006.

[81] F. D. Hastings, J. B. Schneider, and S. L. Broschat. Application of the perfectly matched layer (PML) absorbing boundary condition to elastic wave propagation. *J. Acoust. Soc. Am.*, 100(5):3061–3069, 1996.

[82] J.-Q. He and Q. H. Liu. A nonuniform cylindrical FDTD algorithm with improved PML and Quasi-PML absorbing boundary conditions. *IEEE Trans. on Geoscience and Remote Sensing*, 37(2):1066–1072, March 1999.

[83] M. R. Hestenes and E. Stiefel. Methods of conjugate gradients for solving linear systems. *J. Res. Natl. Bur. Stand.*, 49:409–436, 1952.

[84] R. L. Higdon. Absorbing boundary conditions for elastic waves. *Geophysics*, 56(2):231–241, 1991.

[85] F. Q. Hu. On absorbing boundary conditions for linearized Euler equations by a perfectly matched layer. *Journal of Computational Physics*, 129:201–219, 1996.

[86] Y. F. Hu and C. Storey. Global convergence result for conjugate gradient methods. *J. Optim. Theory Appl.*, 71:399–405, 1991.

[87] T.J.R. Hughes. *The finite element method*. Prentice-Hall, Englewood Cliffs, NJ, 1987.

[88] C. Jeong, S. Kucukcoban, L.F. Kallivokas, and C. Huh. An inverse source problem for focusing wave energy to subsurface inclusions embedded within heterogeneous media. In *Engineering Mechanics Institute 2010*, Los Angeles, CA, USA, 8-11 August 2010. EMI.

[89] C. Johnson and B. Mercier. Some equilibrium finite element methods for two-dimensional elasticity problems. *Numer. Math.*, 30:103–116, 1978.

[90] L. F. Kallivokas, J. Bielak, and R. C. MacCamy. A simple impedance-infinite element for the finite element solution of the three-dimensional wave equation in unbounded domains. *Computer Methods in Applied Mechanics and Engineering*, 147:235–262, 1997.

[91] L. F. Kallivokas and S. Lee. Local absorbing boundaries of elliptical shape for scalar waves. *Computer Methods in Applied Mechanics and Engineering*, 193:4979–5015, 2004.

[92] J. W. Kang. *A mixed unsplit-field PML-based scheme for full waveform inversion in the time-domain using scalar waves.* Doctoral Dissertation, The University of Texas at Austin, Austin, TX, USA, 2010.

[93] J. W. Kang and L. F. Kallivokas. Forward and inverse total wavefield modeling of heteregenous PML-truncated semi-infinite domains. In *8th HSTAM International Congress on Mechanics*, Patras, Greece, 13-16 June 2007.

[94] J. W. Kang and L. F. Kallivokas. Mixed unsplit-field perfectly-matched-layers for transient wave propagation in heterogeneous domains. In *ECCOMAS Thematic Conference on Computational Methods in Structural Dynamics and Earthquake Engineering*, Rethymno, Crete, Greece, 13-16 June 2007.

[95] J. W. Kang and L. F. Kallivokas. Subsurface imaging of PML-truncated semi-infinite domains. In *ECCOMAS Thematic Conference on Computational Methods in Structural Dynamics and Earthquake Engineering*, Rethymno, Crete, Greece, 13-16 June 2007.

[96] J. W. Kang and L. F. Kallivokas. The inverse medium problem in heterogeneous PML-truncated domains using scalar probing waves. *Computer Methods in Applied Mechanics and Engineering*, In press, 2010.

[97] J.W. Kang, S. Kucukcoban, and L.F. Kallivokas. The inverse medium problem in PML-truncated domains. In *ECCM 2010 - IV European*

Conference on Computational Mechanics, Paris, FRANCE, 16-21 May 2010.

[98] Y. Kim and H. Huh. New rectangular mixed finite element method for second-order elliptic problems. *Applied Mathematics and Computation*, 127:375–385, 2002.

[99] L. Knockaert and D. de Zutter. On the stretching of Maxwell's equations in general orthogonal coordinates systems and the perfectly matched layer. *Microwave and Optical Technology Letters*, 24(1):31–34, January 2000.

[100] D. Komatitsch and R. Martin. An unsplit convolutional perfectly matched layer improved at grazing incidence for the seismic wave equation. *Geophysics*, 72(5):SM155–SM167, September-October 2007.

[101] D. Komatitsch and J. Tromp. A perfectly matched layer absorbing boundary condition for the second-order seismic wave equation. *Geophysical Journal International*, 154:146–153, 2003.

[102] S. Kucukcoban and L. F. Kallivokas. A hybrid formulation for transient wave simulations in unsplit-field-PML-truncated heterogeneous media. In *Engineering Mechanics Institute 2010*, Los Angeles, CA, USA, 8-11 August 2010. EMI.

[103] S. Kucukcoban and L. F. Kallivokas. A mixed perfectly-matched-layer for transient wave simulations in axisymmetric elastic media. *Computer*

Modeling in Engineering and Sciences, 64(2):109–146, 2010.

[104] S. Kucukcoban and L. F. Kallivokas. Mixed perfectly-matched-layers for direct transient analysis in 2D elastic heterogeneous media. *Computer Methods in Applied Mechanics and Engineering*, In press, 2010.

[105] S. Kucukcoban and L. F. Kallivokas. A symmetric hybrid formulation for transient wave simulations in pml-truncated heterogeneous media. *Wave Motion*, Under review, 2010.

[106] S. Kucukcoban and L.F. Kallivokas. Perfectly matched layers in axisymmetric elastic media for direct transient analysis. In *EM08 - Inaugural International Conference of the Engineering Mechanics Institute*, University of Minnesota, Minnesota, USA, 18-21 May 2008. ASCE.

[107] S. Kucukcoban and L.F. Kallivokas. Mixed Perfectly-Matched-Layers for Direct Transient Analysis. In *The 2009 ASCE-ASME-SES Joint Conference on Mechanics and Materials*, Blacksburg, VA, USA, 24-27 June 2009.

[108] M. Kuzuoglu and R. Mittra. Frequency dependence of the constitutive parameters of causal perfectly matched anisotropic absorbers. *IEEE Microwave and Guided Wave Letters*, 6(12):447–449, December 1996.

[109] V. Lisitsa. Optimal discretization of PML for elasticity problems. *Electronic Transactions on Numerical Analysis*, 30:258–277, 2008.

[110] Q. H. Liu. Perfectly matched layers for elastic waves in cylindrical and spherical coordinates. *J. Acoust. Soc. Am.*, 105(4):2075–2084, April 1999.

[111] Q. H. Liu and J. Q. He. Quasi-PML for waves in cylindrical coordinates. *Microwave and Optical Technology Letters*, 19(2):107–111, October 1998.

[112] Q. H. Liu and B. K. Sinha. A 3D cylindrical PML/FDTD method for elastic waves in fluid-filled pressurized boreholes in triaxially stressed formations. *Geophysics*, 68(5):1731–1743, Sep-Oct 2003.

[113] Y. Liu and C. Storey. Efficient generalized conjugate gradient algorithms, Part 1: Theory. *Journal of Optimization Theory and Applications*, 69(1):129–137, 1991.

[114] Z. Lou, D. Correia, and J.-M. Jin. Second-order perfectly matched layers for the time-domain finite-element method. *IEEE Transactions on Antennas and Propagation*, 55(3):1000–1004, March 2007.

[115] S. Ma and P. Liu. Modeling of the perfectly matched layer absorbing boundaries and intrinsic attenuation in explicit finite-element methods. *Bulletin of the Seismological Society of America*, 96(5):1779–1794, October 2006.

[116] J. Maloney, M. Kesler, and G. Smith. Generalization of PML to cylindrical geometries. In *Proc. 13th Annu. Rev. of Prog. Appl. Comp. Electromag.*, pages 900–908, Monterey,CA, 17-21 Mar. 1997. Vol. 2.

[117] L. D. Marini. An inexpensive method for the evaluation of the solution of the lowest order Raviart-Thomas mixed method. *SIAM J. Numer. Anal.*, 22(3):493–496, June 1985.

[118] R. Martin, D. Komatitsch, and S. D. Gedney. A variational formulation of a stabilized unsplit convolutional perfectly matched layer for the isotropic or anisotropic seismic wave equation. *CMES: Computer Modeling in Engineering & Sciences*, 37(3):274–304, 2008.

[119] P. McCarthy. Direct analytic model of the L-curve for tikhonov regularization parameter selection. *Inverse Problems*, 19:643–663, 2003.

[120] K. C. Meza-Fajardo and A. S. Papageorgiou. A nonconvolutional, split-field, perfectly matched layer for wave propagation in isotropic and anisotropic elastic media: Stability analysis. *Bulletin of the Seismological Society of America*, 98(4):1811–1836, August 2008.

[121] C. Michler, L. Demkowicz, J. Kurtz, and D. Pardo. Improving the performance of perfectly matched layers by means of *hp*-adaptivity. *Numerical Methods for Partial Differential Equations*, 23(4):832–858, 2007.

[122] M. E. Morley. A family of mixed finite elements for linear elasticity. *Numer. Math.*, 55:633–666, 1989.

[123] S-W. Na and L. F. Kallivokas. Continuation schemes for shape detection in inverse acoustic scattering problems. *Computer Modeling in Engineering and Sciences*, 35(1):73–90, 2008.

[124] J. C. Nédélec. Mixed finite elements in R^3. *Numer. Math.*, 35:315–341, 1980.

[125] J. C. Nédélec. A new family of mixed finite elements in R^3. *Numer. Math.*, 50:57–81, 1986.

[126] J. T. Oden and J. N. Reddy. On mixed finite element approximations. *SIAM J. Numer. Anal.*, 13(3):393–404, June 1976.

[127] S. Operto, C. Ravaut, L. Improta, J. Virieux, A. Herrero, and P. Dell'Aversana. Quantitative imaging of complex structures from dense wide-aperture seismic data by multiscale traveltime and waveform inversions: a case study. *Geophysical Prospecting*, 52(6):625–651, 2004.

[128] R.-E. Plessix. Introduction: Towards a full waveform inversion. *Geophysical Prospecting*, 56(6):761–763, 2008.

[129] R.-E. Plessix, Y.-H. De Roeck, and G. Chavent. Waveform inversion of reflection seismic data for kinematic parameters by local optimization. *SIAM Journal of Scientific Computing*, 20(3):1033–1052, 1999.

[130] E. Polak and G. Ribiere. Note sur la convergence de méthodes de directions conjuguées. *Revue Française d'Informatique et de Recherche Opérationnelle*, 3e Année 16:35–43, 1969.

[131] B. T. Polyak. The conjugate gradient method in extremal problems. *USSR Computational Mathematics and Mathematical Physics*, 9(4):94–112, 1969.

[132] R. G. Pratt. Seismic waveform inversion in the frequency domain, part 1: Theory, and verification in a physical scale model. *Geophysics*, 64:888–901, 1999.

[133] R. G. Pratt and R. M. Shipp. Seismic waveform inversion in the frequency domain, part 2: Fault delineation in sediments using crosshole data. *Geophysics*, 64(3):902–914, 1999.

[134] R. G. Pratt, Z.-M. Song, P. R. Williamson, and M. R. Warner. Two-dimensional velocity models from wide angle seismic data by waveform inversion. *Geophysical Journal International*, 124:323–340, 1996.

[135] P. A. Raviart and J. M. Thomas. A mixed finite element method for second order elliptic problems. In I. Galligani and E. Magenes, editors, *Mathematical Aspects of the Finite Element Method, Lecture Notes in Mathematics*, volume 606, pages 292–315, New York, 1977. Springer-Verlag.

[136] Y. S. Rickard and N. K. Nikolova. Enhancing the PML absorbing boundary conditions for the wave equation. *IEEE Transactions on Antennas and Propagation*, 53(3):1242–1246, March 2005.

[137] J. A. Roden and S. D. Gedney. Convolutional PML (CPML): an efficient FDTD implementation of the CFS-PML for arbitrary media. *Microwave and Optical Technology Letters*, 27(5):334–339, 2000.

[138] J. A. Roden and S. D. Gedney. An efficient FDTD implementation of the PML with CFS in general media. *IEEE Antennas and Propagation Society International Symposium*, 3:1362–1265, July 2000.

[139] L. Rudin, S. Osher, and E. Fatemi. Nonlinear total variation based noise removal algorithms. *Physica D*, 60:259–268, 1992.

[140] T. Rylander and J.-M. Jin. Perfectly matched layer for the time domain finite element method. *Journal of Computational Physics*, 200:238–250, 2004.

[141] T. Rylander and J.-M. Jin. Perfectly matched layer in three dimensions for the time-domain finite element method applied to radiation problems. *IEEE Transactions on Antennas and Propagation*, 53(4):1489–1499, April 2005.

[142] Y. Shi and C.-H. Liang. A strongly well-posed PML with unsplit-field formulations in cylindrical and spherical coordinates. *J. of Electromagn. Waves and Appl.*, 19(13):1761–1776, 2005.

[143] Z. J. Shi and J. Guo. A new family of conjugate gradient methods. *Journal of Computational and Applied Mathematics*, 224(1):444–457, 2009.

[144] C. Shin and D.-J. Min. Waveform inversion using a logarithmic wavefield. *Geophysics*, 71:R31–R42, 2006.

[145] R. M. Shipp and S. C. Singh. Two-dimensional full wavefield inversion of wide-aperture marine seismic streamer data. *Geophysical Journal International*, 151(2):325–344, 2002.

[146] L. Sirgue and R. G. Pratt. Efficient waveform inversion and imaging: a strategy for selecting temporal frequencies. *Geophysics*, 69(1):231–248, 2004.

[147] E. A. Skelton, S. D. M. Adams, and R. V. Craster. Guided elastic waves and perfectly matched layers. *Wave Motion*, 44:573–592, 2007.

[148] R. Stenberg. A family of mixed finite elements for the elasticity problem. *Numer. Math.*, 53:513–538, 1988.

[149] W. W. Symes. Migration velocity analysis and waveform inversion. *Geophysical Prospecting*, 56(6):765–790, 2008.

[150] A. Tarantola. Inversion of seismic reflection data in the acoustic approximation. *Geophysics*, 49:1259–1266, 1984.

[151] F. L. Teixeira and W. C. Chew. Perfectly matched layer in cylindrical coordinates. In *Antennas and Propagation Society International Symposium Digest*, pages 1908–1911, Montreal, Canada, 13-18 July 1997. IEEE. Vol. 3.

[152] F. L. Teixeira and W. C. Chew. PML-FDTD in cylindrical and spherical grids. *IEEE Microwave and Guided Wave Letters*, 7(9):285–287, 1997.

[153] F. L. Teixeira and W. C. Chew. Systematic derivation of anisotropic PML absorbing media in cylindrical and spherical coordinates. *IEEE Microwave and Guided Wave Letters*, 7(11):371–373, November 1997.

[154] F. L. Teixeira and W. C. Chew. On causality and dynamic stability of perfectly matched layers for FDTD simulations. *IEEE Transactions on Microwave Theory and Techniques*, 47(6):775–785, June 1999.

[155] F. L. Teixeira and W. C. Chew. Complex space approach to perfectly matched layers: a review and some new developments. *Int. J. Numer. Model.*, 13:441–455, 2000.

[156] A. Tikhonov. Solution of incorrectly formulated problems and the regularization method. *Soviet Math. Doklady*, 4:1035–1038, 1963.

[157] D. Toutai-Ahmed and C. Storey. Efficient hybrid conjugate gradient techniques. *J. Optim. Theory Appl.*, 64:379–397, 1990.

[158] S. V. Tsynkov. Numerical solution of problems on unbounded domains. a review. *Appl. Numer. Math.*, 27(4):465–532, 1998.

[159] E. Turkel and A. Yefet. Absorbing PML boundary layers for wave-like equations. *Applied Numerical Mathematics*, 27:533–557, 1998.

[160] R. Versteeg. The Marmousi experience: Velocity model determination on a synthetic complex data set. *The Leading Edge*, 13:927–936, 1994.

[161] C. Wang. Some remarks on conjugate gradient methods without line search. *Applied Mathematics and Computation*, 181(1):370–379, 2006.

[162] J. Wang, Y. Wang, and D. Zhang. Truncation of open boundaries of cylindrical waveguides in 2.5-dimensional problems by using the convolutional perfectly matched layer. *IEEE Transactions on Plasma Science*, 34(3):681–690, June 2006.

[163] S. Wang, R. Lee, and F. L. Teixeira. Anisotropic-medium PML for vector FETD with modified basis functions. *IEEE Transactions on Antennas and Propagation*, 54(1):20–27, January 2006.

[164] T. Wang and X. Tang. Finite-difference modeling of elastic wave propagation: A nonsplitting perfectly matched layer approach. *Geophysics*, 68(5):1749–1755, 2003.

[165] P. Wolfe. Convergence conditions for ascent methods. *SIAM Rev.*, 11:226–235, 1969.

[166] P. Wolfe. Convergence conditions for ascent methods II: some corrections. *SIAM Rev.*, 13:185–188, 1971.

[167] Y. Xiao and Y. Lu. The hybrid perfectly matched layer and finite element solution for open region problems. *IEEE Transactions on Magnetics*, 36(4):1635–1639, July 2000.

[168] A. Younes, R. Mose, P. Ackerer, and G. Chavent. A new formulation of the mixed finite element method for solving elliptic and parabolic PDE

with triangular elements. *Journal of Computational Physics*, 149:148–167, 1999.

[169] G. Yu, L. Guan, and Z. Wei. Globally convergent Polak-Ribiére-Polyak conjugate gradient methods under a modified Wolfe line search. *Applied Mathematics and Computation*, 215(8):3082–3090, 2009.

[170] G. Yu, Y. Zhao, and Z. Wei. A descent nonlinear conjugate gradient method for large-scale unconstrained optimization. *Applied mathematics and computation*, 187(2):636–643, 2007.

[171] G. Yuan. Modified nonlinear conjugate gradient methods with sufficient descent property for large-scale optimization problems. *Optimization Letters*, 3(1):11–21, 2009.

[172] M. Zampolli, A. Tesei, and F. B. Jensen. A computationally efficient finite element model with perfectly matched layers applied to scattering from axially symmetric objects. *J. Acoust. Soc. Am.*, 122(3):1472–1485, September 2007.

[173] Y. Q. Zeng, J. Q. He, and Q. H. Liu. The application of the perfectly matched layer in numerical modeling of wave propagation in poroelastic media. *Geophysics*, 66(4):1258–1266, 2001.

[174] L. Zhang. A new liu-storey type nonlinear conjugate gradient method for unconstrained optimization problems. *Journal of Computational and Applied Mathematics*, 225(1):146–157, 2009.

[175] L. Zhang, W. Zhou, and D. Li. A descent modified Polak-Ribiére-Polyak conjugate gradient method and its global convergence. *IMA Journal of Numerical Analysis*, 26(4):629–640, 2006.

[176] L. Zhang, W. Zhou, and D. Li. Global convergence of a modified Fletcher-Reeves conjugate gradient method with Armijo-type line search. *Numerische Mathematik*, 104(4):561–572, 2006.

[177] L. Zhao. The generalized theory of perfectly matched layers (GT-PML) in curvilinear co-ordinates. *Int. J. Numer. Model.*, 13:457–469, 2000.

Vita

Sezgin Kucukcoban was born in Zile, Tokat, Turkey on September 23, 1980, the son of Hayri Küçükçoban and Gülümser Küçükçoban. After completing secondary education at the Zile Anatolian High School in 1998, he attended the Middle East Technical University in Ankara, Turkey. He graduated in 2002 with a Bachelor of Science degree in Civil Engineering. He subsequently enrolled for graduate studies also at the Middle East Technical University from which he received the Master of Science degree with the *Best Thesis Award* in June 2004. Soon after graduation, in August 2004, he enrolled in the doctoral program in the Department of Civil, Architectural and Environmental Engineering at the University of Texas at Austin. In August 2010, he was presented with an Award for the Best Student Paper in Computational Mechanics by the Engineering Mechanics Institute of ASCE, following an international student competition conducted under the auspices of the EMI 2010 Conference held at the University of Southern California.

Permanent address: Yunus Emre Mah. Stad Cad.
No: 37/A Zile, Tokat 60400, TURKEY

This dissertation was typeset with LaTeX[†] by the author.

[†] LaTeX is a document preparation system developed by Leslie Lamport as a special version of Donald Knuth's TeX Program.